Tungsten Oxide and Tungsten Oxide Based Heterogeneous Nanostructure thin films: Synthesis *via* AACVD, Characterisation, Growth Mechanism, and Application in Photocatalysis

Min Ling

A thesis presented for the degree of

Doctor of Philosophy

Supervised by:

Dr. Christopher S. Blackman

Dr. Robert G. Palgrave

Department of Chemistry

Mathematical and Physical Sciences Faculty

University College London, UK

July, 2016

I, Min Ling confirm that the work presented in this thesis is my own. Where information has been derived from other sources, I confirm that this has been indicated in the thesis.

ACKNOWLEDGMENTS

First and foremost I would like to thank my supervisor Dr Chris Blackman for giving me the opportunity to undertake this project and his unconditional trust upon me over the last three years, and also thank my secondary supervisor Dr Robert Palgrave for support and scientific insights. The huge amount of stuffs I learnt from them has been an inspiration to pursue a career in chemistry.

Special thanks to my friends and colleague Francesco Di Maggio and Carlos Sotelo-Vazquez for collaborative spirit and general enthusiasm for science and life made working with a joy.

I would like to thank Drs Sanjay Sathasivam, Andreas Kafizas and Nuruzzaman Noor for their encouragement, help and scientific guidance.

I would like to thanks Dr Steven Firth, Dr Kevin Reeves and Dr Tom Gregory for SEM and TEM training, and Dr Martin Vickers for XRD traning.

I would like to thanks all my friends and group memeber (Kaipei Qiu, Yi Shi, Liying Wang, Haitang Luo, Ya Hu, Yaomin Li, Yiyun Zhu) for their collaborative inputs and burden sharing.

Finally, I wish to dedicate this thesis to my family and especially to my wife Qing Qin and the new coming member Little Yumi.

ABSTRACT

Tungsten oxide thin films with one-dimensional (1D) nanostructure (e.g. nanorod (NR)) show enhanced performances for gas sensing, catalysis and photocatalysis due to a large surface-to-volume ratio, high crystallinity, reduction of light reflection and relative high collection efficiency of charge carriers.

This thesis details the use of aerosol assisted chemical vapour deposition (AACVD) to deposit tungsten oxide NR array thin films *via* optimising the deposition conditions (e.g temperature, solvent, precursor and substrate). The tungsten oxide NR array thin films were able to be grown directly on glass, quartz, silica and alumina substrates.

Based on observation of the change of tungsten oxide morphologies from planar to NR on traversing from the inlet to outlet of an AACVD reactor, where the actual substrate temperature changed from 339 to 358 ℃, a 'kinetic competition' mechanism was proposed to describe the relation between deposition parameters and the morphology formed during AACVD. In this mechanism the formation of planar and wave-like morphologies is due to the competition between r_{perp} (perpendicular growth rate) and r_i (parallel growth rate contributed by nucleation rate). When r_{perp} is around 7 times faster than r_i, the formation of tungsten oxide NR is favoured.

The difference between r_{perp} and r_i is attributed to planar defects which appear in the direction perpendicular to the NR growth suppressing r_i. These planar defects induced by oxygen vacancy may also be responsible for the observed dislocation loops with size (~0.4 to 1.5 nm) providing with the associated strain field generated leading to a quantum-spatial-confinement effect which modifies the band structure of WO_3 NR array thin films. During photodegradation of stearic acid (SA) WO_3 NR with length around 1200 nm (deposited for 5 mins) gave the highest photocatalytic activity, and the WO_3 NR were more than 2 μm in length reduced tungsten states (W^{4+}) were observed *via* NIR and in XPS spectra which lead to lower photocatalytic activity.

In order to improve photocatalytic activity of plain WO_3 NR arrays, AACVD was used to grow noble metal (Au, Pt, Pd and Ru) and metal oxide (PdO, RuO_2, Co_2O_3, CuO_x and TiO_2)

NPs supported on 1D WO_3 nanorod arrays with size of the NPs (1.9 to 7.3 nm) is directly controlled by the deposition time (0.5 to 36 minutes). Hybrid nanostructures of Au/WO_3 (1 min, with particle mean size 3.0 nm), Pt/WO_3 (10 min, 3.0 nm) and PdO/WO_3 (5 min, 5.6 nm) increased photocatalytic activity by 40 to 50% compared to undecorated plain WO_3 NR array thin films.

KEYWORDS: Tungsten oxide, Nanorods, AACVD, Photocatalysis, 1D growth mechanism, Defect engineering.

Contents

LIST OF FIGURES

Chapter 1

Chapter 2

Chapter 3

Chapter 4

Chapter 5

LIST OF TABLES

NOMENCLATURE

1D	One-dimension
2D	Two-dimension
3D	Three-dimension
Å	Angstrom
AACVD	Aerosol assisted chemical vapour deposition
APCVD	Atmospheric pressure chemical vapour deposition
CB	Conduction band
CBM	Conduction band minimum
CNT	Carbon nanotubes
CTAB	Cetyltrimethylammonium bromide
CVD	Chemical vapour deposition
DCI	Double charge injection
EC	Electrochromism
EDX	Energy dispersive X-ray
E_f	Fermi level or Fermi energy
E_g	Bandgap
eV	Electronvolt
FCC	Face-centred cubic
FM	Frank–van der Merwe
FQE	Formal quantum efficiency
FT-IR	Fourier transform infrared spectroscopy
GC	Gasochromism
HCP	Hexagonal close packed
HER	Hydrogen evolution reaction
HOR	Hydrogen oxidation reaction
IVCT	Intervalence charge transfer
k	Boltzmann's constant
LSPR	Localized surface plasmon resonance
ML	Mono-layer
MO	Molecular orbital
MOCVD	Metalorganic chemical vapour deposition
NN	Nanoneedle
NP	Nanoparticle

NR	Nanorod
OER	Oxygen evolution reaction
ORR	Oxygen reduction reaction
PECVD	Plasma enhanced chemical vapour deposition
PVD	Physical vapour deposition
QCE	Quantum confinement effect
QD	Quantum dot
Rf magnetron	Radio frequency magnetron
SA	Stearic acid
sccm	Standard cubic centimetres per minute
SCE	Saturated calomel electrode
SEM	Scanning electron microscopy
SK	Stranski–Krastanov
SMSI	Strong metal-support interaction
SPH	Small polaron hopping
SPR	Surface plasmon resonance
TEM	Transmission electron microscopy
TOF	Turn over frequency
TSK	Terrace-step-kink
UV	Ultraviolet
UV-Vis	Ultraviolet-visible
VB	Valence band
VBM	Valence band maximum
VL	Vapour-liquid
VLS	Vapour-liquid-solid
V_O	Oxygen vacancy
VW	Volmer–Weber
XPS	X-ray photoelectron spectroscopy
XRD	X-ray diffraction

CHAPTER 1: INTRODUCTION

This chapter presents a literature review of the synthesis, characterisation, properties, growth mechanism and applications of tungsten oxide and tungsten oxide based hetero-junction materials, aerosol assisted chemical vapour deposition, thin film characterisation techniques and the motivation, aims and purpose of this thesis.

1.1 Background of Tungsten Oxide

1.1.1 Structure of Tungsten Oxide

The crystal structures of WO_3 are formed by corner-sharing networks of WO_6 octahedra. The prototype crystal structure of WO_3 is cubic ReO_3.[1] However, the cubic structure of WO_3 is rarely observed in experiment. Since the triclinic (pseudo-monoclinic) phase of WO_3 was investigated by Braekken in 1931,[2] six additional phases have subsequently been characterised: monoclinic II (ε-WO_3), triclinic (δ-WO_3), monoclinic I (γ-WO_3), orthorhombic (β-WO_3), tetragonal (α-WO_3) and hexagonal (h-WO_3),[3,4] as shown in Table 1.1. The seven phases of WO_3 are differentiated by tilting angles and distortions of the WO_6 octahedra from the ideal cubic structure resulting in lower symmetry, as presented in Figure 1.1.[3] The crystal phase transitions take place at various temperatures in the following sequence: monoclinic II (ε-WO_3, < -43 ℃), triclinic (δ-WO_3, $-43\ to\ 17$℃), monoclinic I (γ-WO_3, $< 17\ to\ 330$ ℃), orthorhombic (β-WO_3, $< 330\ to\ 740$ ℃), tetragonal (α-WO_3, > 740 ℃).[3]

Table 1.1. Lattice constant of different WO_3 phases.

Crystal	Space Group	Lattice constant						Calc. Density g/cm^3	Reference
		a	*b*	*c* (Å)	α	β	γ (°)		
ε-WO_3	*Pc*	5.278	5.156	7.664	90	90.76	90	7.39	PDF 88-545[5]
δ-WO_3 Triclinic	*P-1*	7.313	7.525	7.689	88.85	90.91	90.94	7.28	PDF 20-1323[6]
γ-WO_3 Monoclinic	*P2$_1$/c*	7.306	7.540	7.692	90	90.88	90	7.27	PDF 72-0677[7]
β-WO_3 Orthorhombic	*Pmnb*	7.341	7.570	7.754	90	90	90	7.15	PDF 71-131 [8]
α-WO_3 Tetragonal	*P4/nmm*	5.272	5.272	3.920	90	90	90	7.07	PDF89-1287[9]
Cubic WO_3 (ReO_3)	*Pm-3m*	3.834	3.834	3.834	90	90	90	6.83	[10]
h-WO_3 Hexagonal	*P6/mmm*	7.298	7.298	3.899	90	90	120	6.42	PDF 01-075-2187[4]

Without oxidative treatment such as annealing, oxygen deficient tungsten oxide (WO_x) is usually formed *via* liquid or gas phase methods.[11,12] The mechanisms for formation of WO_x are discussed in Section 1.1.3. WO_x varies from $WO_{2.625}$ ($W_{32}O_{84}$) to $WO_{2.96}$ arising from corner-sharing networks of WO_6 octahedra as shown in Table1.2. Compared to fully oxidized WO_3, WO_x phases possess larger unit cells, and crystal structures transition from monoclinic to orthorhombic as the x value decreases (Table 1.2).

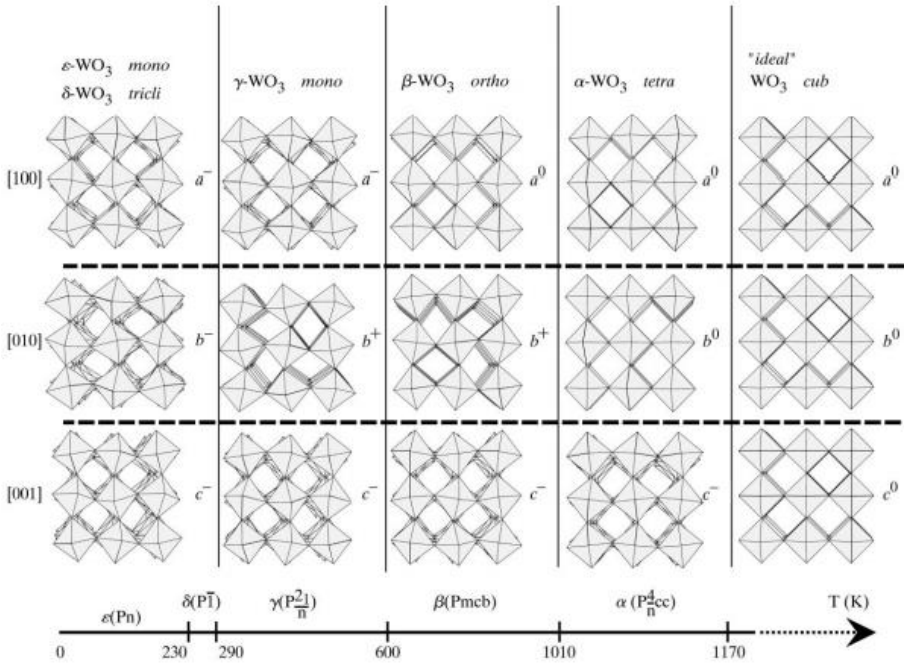

Figure 1.1. Tilt patterns and stability temperature domains of the different polymorphs of WO_3.[13]

Tungsten oxide with different crystal phases or/and various oxygen defects presents varying symmetry of the crystal lattice described by space group as shown in Table 1.1 and 1.2. There are a total of 230 possible space groups for crystal (2 triclinic, 13 monoclinic, 59 orthorhombic, 68 tetragonal, 25 trigonal, 27 hexagonal and 36 cubic) combining 32 crystallographic point groups with the 14 Bravais lattices designated by the Hermann-Mauguin space group symbol to describe the crystal structure of a particular substance.[14] The first letter of that symbol refers to the Bravais centering e.g. P for Primitive, F for Face-centred, I for body centred, A for (100) face centred, B for (010) face centred and C for (001) face centred, and the remaining three letters refer to the symmetry elements in the lattice. As an example, monoclinic γ-WO_3 with $P2_1/c$ space group (Table 1.1) is a very common tungsten oxide phase stable at room temperature. This space group consist of a primitive monoclinic unit cell, a twofold screw axis and a c-glide plane perpendicular to the screw axis.

Table 1.2. Lattice constant of different oxygen content of WO_x.

Crystal	Space Group	Lattice constant						Calc. Density g/cm^3	Reference
		a	b	c (Å)	α	β	γ (°)		
$W_{32}O_{84}$ ($WO_{2.63}$)	*Pbam*	21.43	17.77	3.78	90	90	90	8.33	PDF 01-077-0810[15]
W_3O_8 ($WO_{2.67}$)	*C222*	6.39	10.43	3.80	90	90	90	8.92	PDF 01-081-2262[16]
$W_{18}O_{49}$ ($WO_{2.72}$)	*P2/m*	18.32	3.78	14.03	90	115.2	90	7.73	PDF 01-084-1516[17]
$W_{17}O_{47}$ ($WO_{2.76}$)	*P2/m*	18.84	3.79	12.33	90	102.7	90	7.50	PDF 01-079-0171[18]
W_5O_{14} ($WO_{2.80}$)	*P-42m*	23.33	23.33	3.80	90	90	90	7.35	PDF 01-071-0292[19]
$W_{10}O_{29}$ ($WO_{2.90}$)	*P2/m*	12.05	3.77	23.59	90	85.3	90	7.17	[20]
$W_{25}O_{73}$ ($WO_{2.92}$)	*P2/c*	11.93	3.82	59.72	90	98.3	90	7.11	PDF 01-071-0070[21]
$WO_{2.92}$	*P2/c*	11.90	3.83	59.65	90	98.4	90	7.15	PDF 30-1387[22]

1.1.2 Properties and Applications of Tungsten Oxide

Tungsten metal has a very high meting point and enthalpy of atomization, reacting with O_2 at high temperature to form yellow WO_3.[23] WO_3 does not react with acid, but reacts with alkali forming $[WO_4]^{2-}$ polyoxometallate ions.[23] Among transition metals oxide, tungsten oxide indicates properties similar to non-metal oxide and acids with the strongest Brønsted acid sites owing to the high oxidation state, W^{VI}, showing very high electronegativity.[24] Therefore, tungsten oxide has been used as a support in catalysis, with applications in the petrochemical and refining industry including catalytic reaction such as ethylene polymerization, alkane oxidative dehydrogenation, alkene metathesis and reduction of NO_x with ammonia.[25]

Tungsten oxide is a semiconductor material presenting an electronic bandgap (E_g) (gap of forbidden energies) between the valence band maximum (VBM) and the conduction band minimum (CBM). The energy bands are constructed by an infinite number of molecular orbitals (MO) formed by an infinite number of atoms within the crystal lattice which are so close to each other blurring discrete MOs.[14] There must be N/2 available states for N electron to house the electron density based on the Pauli Exclusion Principle.[14] The VB of tungsten oxide is the electron-occupied band formed through overlap of O 2p orbitals, whereas the CB of tungsten oxide is the unfilled band formed through overlap of W 5d orbitals.

WO_3 is also a wide bandgap n-type semiconductor (larger electron concentration than hole concentration, and fermi level locates close to CBM), presenting an E_g around 3.25 and 2.62 eV

corresponding to amorphous and monoclinic WO_3 respectively.[3] The bandgap of nanostructured WO_3 increases with reducing crystallite size due to the quantum confinement effect (QCE),[26] which when the crystallite size approaches the Bohr radius causing the change of wavefunctions and hence expands the E_g.[27] Recently, sub-nano-sized WO_3 quantum dots were synthesized via a template method with sub-nano porous silica giving a crystallite size of 0.70 nm and E_g 3.69 eV (Figure 1.2).[28]

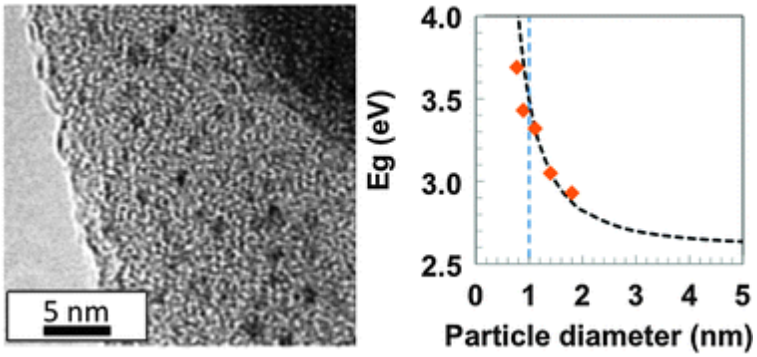

Figure 1.2. TEM image of WO3 quantum dots and their bandgap dependence on particle size.[28]

Tungsten oxide has been used to photosensitize the oxidation of water and for destruction of toxic pollutants.[29–31] Previous report have showed that WO_3 has very high activity for water oxidation (with a suitable electron acceptor) under visible light radiation (reaction scheme in Figure 1.3) but it is unable to reduce water to H_2, due to its valence band (VB) and conduction band (CB) being more positive than the oxidation and reduction potentials of water respectively.[29,32] Degradation of organic contaminants is tested by photo-degradation of stearic acid which are significantly decomposed by WO_3 under ultraviolet (UV) light radiation with either 254 or 365 nm wavelength.[33]

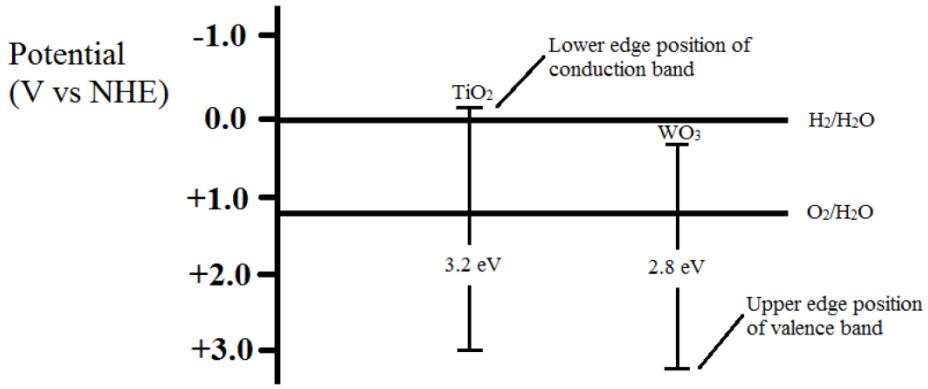

Figure 1.3. The reaction scheme of water oxidation by WO_3 in presence of electron acceptors.[34]

WO_3 thin films are also used in smart windows due to the unique optical properties in the visible region, which are dominated by the absorption threshold defined by the bandgap.[35] As the bandgap decreases, the colour of WO_3 shifts to yellow due to absorption in part of the blue spectrum.[35] The colour of WO_3 thin films can also be changed by applied voltage or reducing gases (such as H_2), corresponding to electrochromism (EC) or gasochromism (GC). The double injection of protons and electrons forming M_xWO_3 (M=H,Na,Li) was widely accepted to explain the coloration process of EC.[36] As shown in Figure 1.4, the typical EC device is composed of five-layers, two transparent conductor layers, an ion storage film, an ion conductor and an electrochromic film. When an electrical field is applied between two transparent conductors, ions transport via electrolyte from the ion storage film, and then insert into electrochromic film causing a colour change in the electrochromic film.[37] For GC, there were two models widely accepted to define this phenomenon. The first model is the double injection of ions which is similar to the mechanism of EC.[38] The other model is *via* the generation of Oxygen vacancy (V_O).[39]

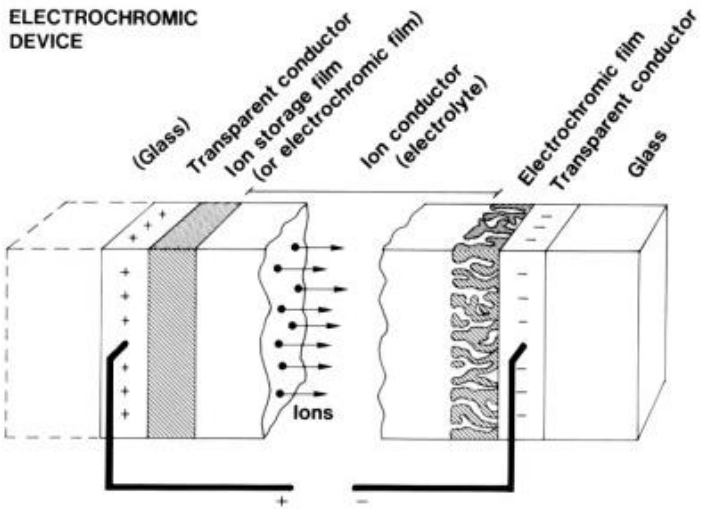

Figure 1.4. Generic five-layer EC device design.[37]

The fundamental mechanism of gas sensors or detectors is based on the electrical resistance of a thin film that changes due to the ambient gas chemical composition. WO_x can be used as the active material for gas sensors. The electrical conductivity depends on the concentration of free electrons in the CB, which is determined by oxygen vacancies in WO_x and results in an electrical conductivity in the range from 10 to 10^{-4} S cm^{-1}. [40,41] In order to improve its gas sensing performance, an effective way is to increase the surface-to-volume ratio of tungsten oxide.[42] For instance in nanostructured tungsten oxide, by reducing grain size or modifying the surface with high porosity. Porosity is enhanced by synthesising tungsten oxide with nanorod structure which shows a dramatic increase in gas sensitivity to ethanol, hydrogen, carbon monoxide, ammonia and nitrogen dioxide (Figure 1.5).[43]

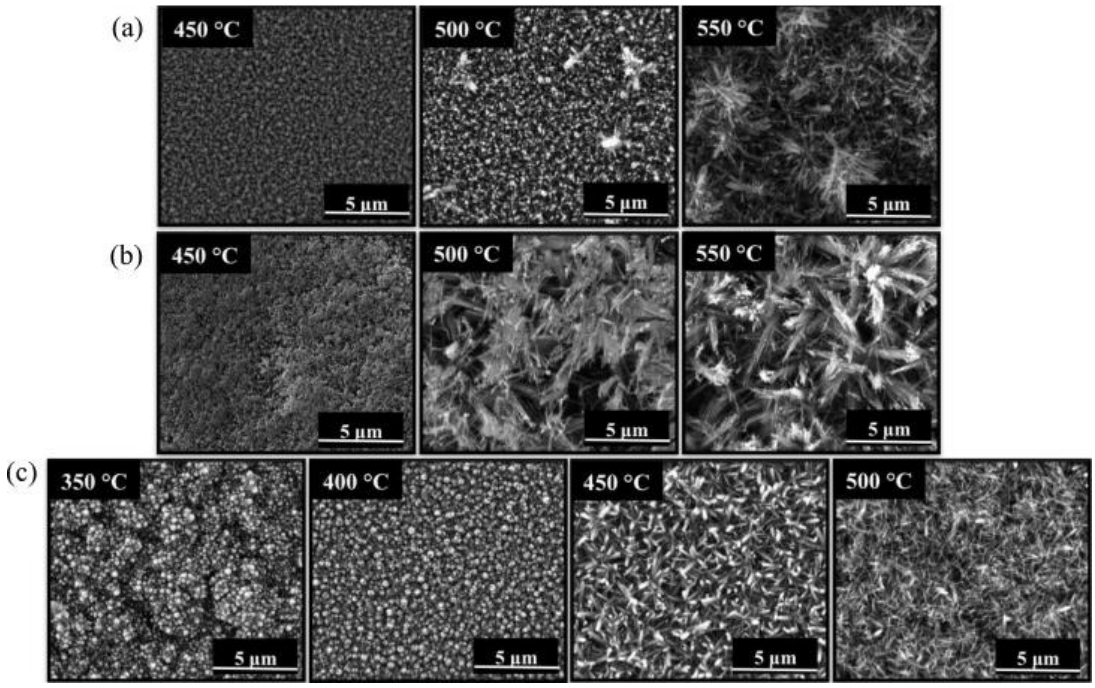

Figure 1.5. SEM images of tungsten oxide films grown at various deposition temperatures using acetone (a), toluene (b) and acetone/toluene 50:50 (c).[43]

1.1.3 Synthesis of Nanostructured Tungsten Oxide

Fabricating WO_3 nanostructures, which provide unique properties due to increased surface to volume ratio and quantum confinement effects, has attracted increasing interest[3]. There are various approaches to synthesis of nanostructured WO_3 including vapour phase and liquid phase based methods.[3]

Liquid phase synthesis methods include sol-gel, templating, hydrothermal, electrochemical anodization and electrodeposition.

Sol-gel processes normally begin with a precursor solution (sol). During the aging process (gelation), hydrolysis and polycondensation occur to form discrete particles or a network structure, and then the "sol-gel" is dip-coated, spun or drop-cast on the substrate to form the thin film.[44] As shown in Figure 1.6, when the reagent WO_4^{2-} from Na_2WO_4 mixes with H^+ from nitric acid, then H_2WO_4 is formed. Consequently, partial condensation polymerisation occurs eliminating molecules of H_2O to form a shared oxygen bond between two tungsten atoms. As more acid is added, the tungsten oxo ligands can be hydrated to dihydroxy ligands (W-$(OH)_2$)

which experience further condensation action to form a 3D network structure until six shared oxygen bonds form in a similar structures to a polyoxotungstate.[45]

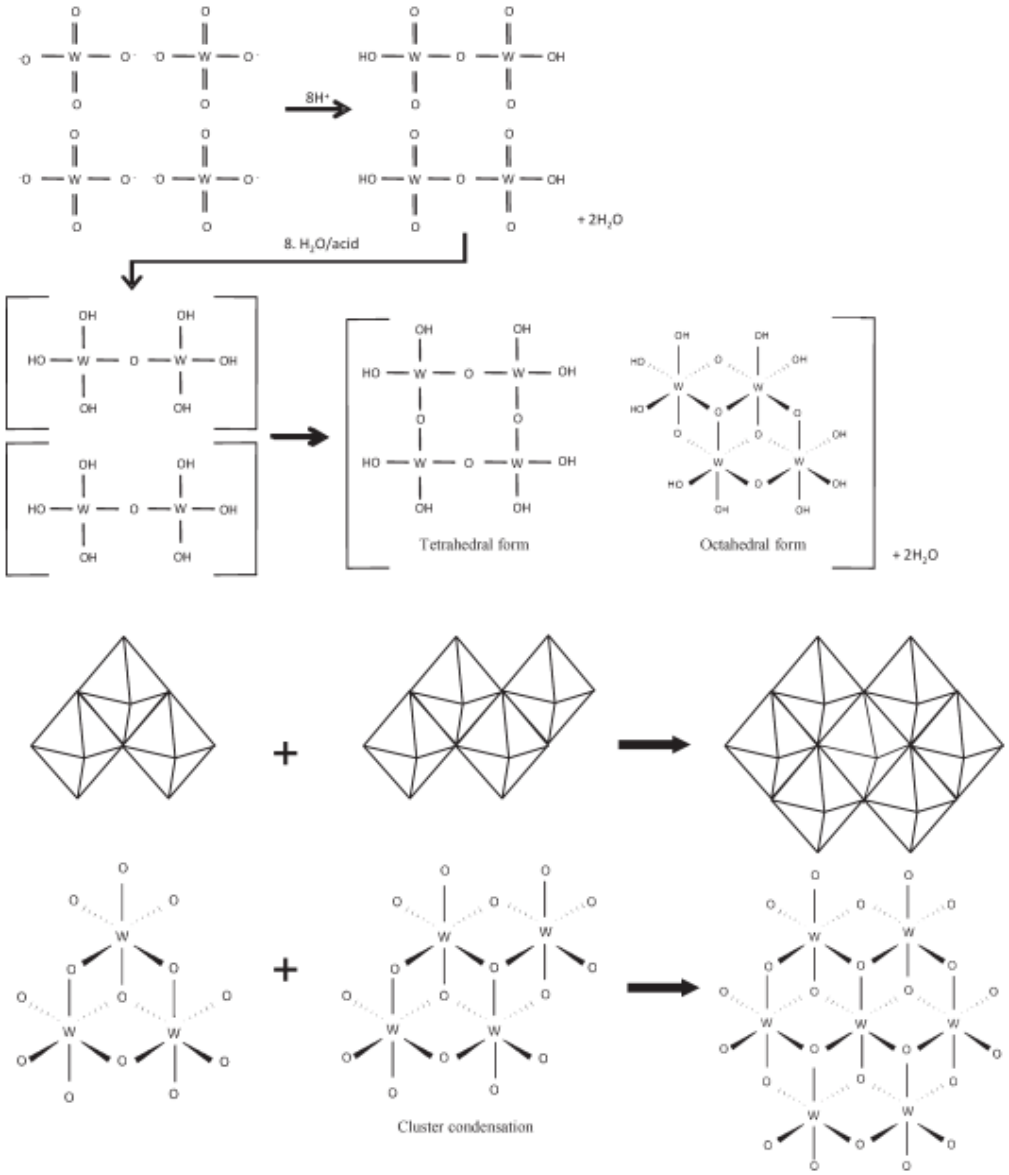

Figure 1.6. Sol-gel condensation polymerization reaction and cluster condensation of Tungsten oxide.[45]

Templating is a modification method of the sol-gel synthesis divided into two types based on the templates used, e.g. anodic alumina for hard templating and polyethylene glycol for soft templating.[46,47] Recently, Sadakane etc. reported that $(NH_4)_6H_2W_{12}O_{40}$ ammonium meta-tungstate, which is inexpensive and air-stable was found to be suitable tungsten source for constructing 3D ordered macro-porous WO_3 using a colloidal template (mono-disperse

poly(methyl methacrylate) with size 490 and 180 nm), which when calcined at 773 k or 873 k resulted in different morphologies as shown in Figure 1.7.[48]

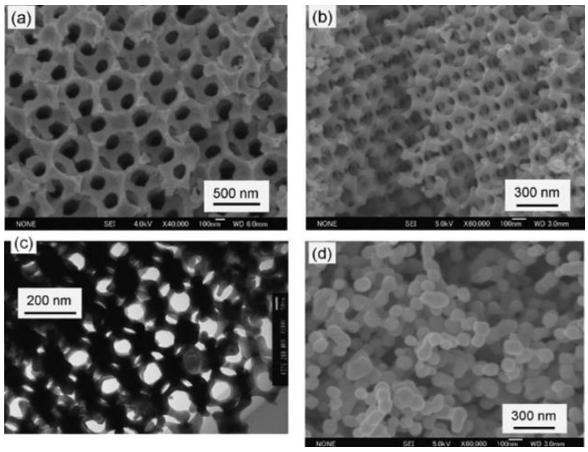

Figure 1.7. SEM (a,b,d) and TEM (c) images of WO3 prepared using a colloidal crystal template. (a) PMMA diameter, 490 nm; calcination temperature, 773 K. (b,c) 180 nm; 773 K. (d) 180 nm, 873 K.[48]

Hydrothermal synthesis is performed in autoclaves as shown in Figure 1.8.[49] The feeding mixture reactants include selected precursors (which are normally not dissolved in water in room temperature), mineralizer, solvent (e.g. water) and additives (e.g. surfactant). After transferring the mixture into the autoclave, the temperature is raised to 100 ~ 300 ℃.[50] The hydrothermal synthesis of nanostructured WO_3 starts with a tungsten precursor, typically a tungstic acid solution (e.g. H_2WO_4, $(NH_4)_6H_2W_{12}O_{40}$) which is dissolved into deionized water with additives such as HCl and surfactant of cetyltrimethylammonium bromide (CTAB), and then aged at temperature (180-200 ℃) for 12 to 24 hours in order to allow the nucleation and crystal growth to take place. The synthesized precipitates are finally washed by deionized water and then dried in air at 70-80 ℃.[51,52]

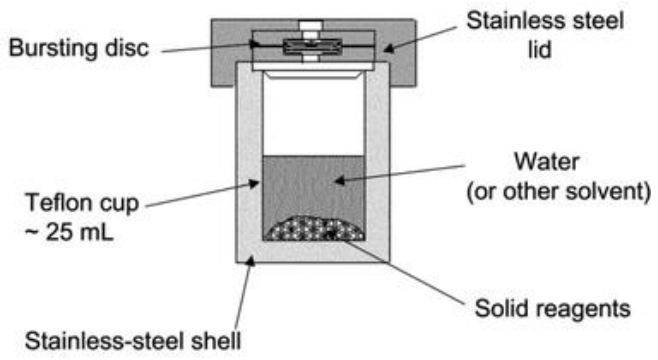

Figure 1.8. A schematic of a Teflon lined stainless steel autoclave used for hydrothermal synthesis.[49]

A typical schematic setup for electrochemical anodization to fabricate nano-porous Al is shown in Figure 1.9.[53] During the anodization the formation of a porous structure depends on polyprotic acid or electrolyte, temperature and anodic voltage.[53] The first use of electrochemical anodization to produce nanostructured WO_x was reported by Grimes et al. who used a pure tungsten foil in an oxalic acid *via* a galvanostatic (constant current) method at room temperature where the morphologies of tungsten oxide were found to be dependent on the current density, with 6.5 to 8 mA/cm^2 found to produce nano-porous tungsten oxide.[54]

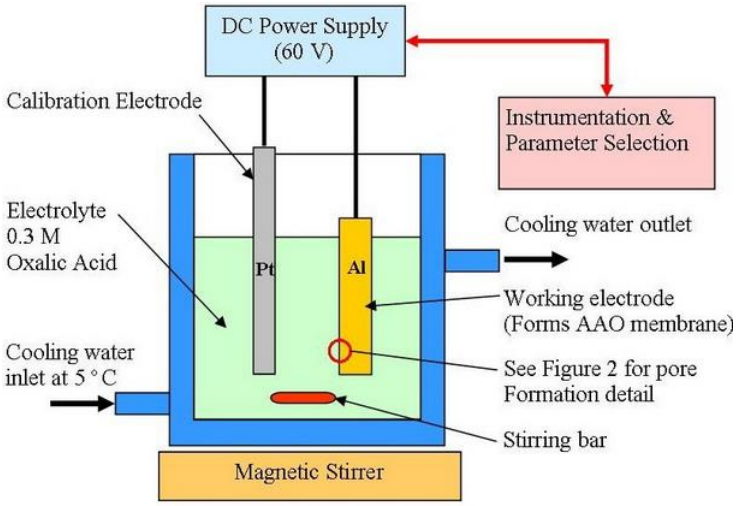

Figure 1.9. Schematic of a typical experimental setup for anodization of aluminium.[53]

Electrodeposition is the reverse of electrochemical anodization requiring only a small applied potential in order to form a metal film by accumulating metal ions in the electrolyte (Figure 1.10).[55] Previously, Baeck fabricated nanoparticles (NPs) tungsten oxide via pulsed electrodeposition using a conventional three-electrode system with Pt as a counter electrode, saturated calomel electrode (SCE) as a reference electrode, and both Ti foil and ITO-coated glass as cathodic substrates, in electrolytes prepared by dissolving tungsten powder into hydrogen peroxide.[56]

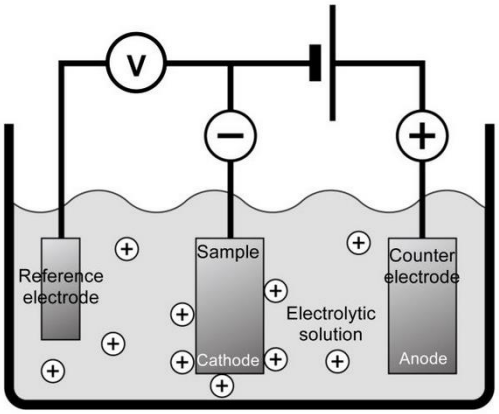

Figure 1.10. Schematic of an electrolytic cell used in the electrodeposition.[55]

Vapour phase synthesis methods are generally divided to physical vapour deposition (PVD) and chemical vapour deposition (CVD). PVD use physical process to transform the target into the gaseous state by either thermal evaporation or an impact process, as shown in Figure 1.11.[57]

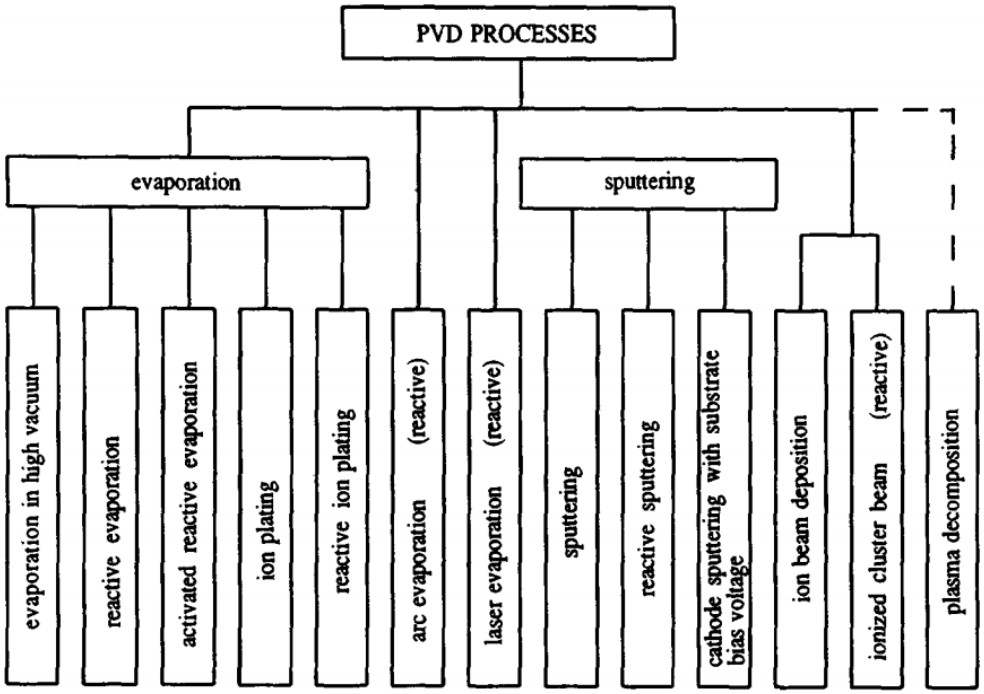

Figure 1.11. Overview of PVD process.[57]

The thermal evaporation technique is a simple process where source materials (condensed or powder) are vaporized by heating, and then the resultant vapour condensed to form the desired product.[58] The depositions are usually conducted in a tube furnace (Figure 1.12).[58] The morphology and phase of products depend on the deposition conditions and source materials.[58]

Previously, Smith successfully prepared nanowires of WO_3 via a thermal evaporation process at 500 mTorr with WO_3 powders on tungsten substrate, with the temperature set to 675 ℃ in the substrate zone and 685 ℃ in the source zone with a flow rate of air from 0.1 to 5 sccm (standard cubic centimetres per minute).[59]

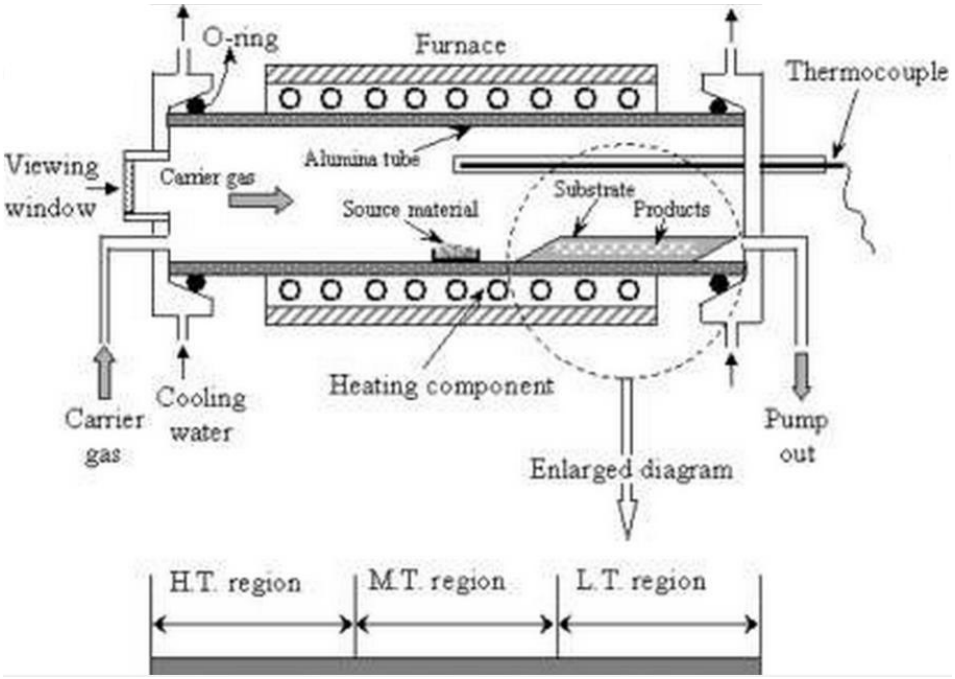

Figure 1.12. Schematic diagram of experimental apparatus for thermal evaporation. An enlarged diagram of the substrate enclosed in the dotted-line circles shown at the bottom, where several alumina strip plates were placed downstream. The temperature decreases gradually from left to right, giving three temperature regions (high (H.T.), medium (M.T.) and low (L.T.)).[58]

Sputtering is a very common PVD process in which desired atoms are ejected from a target bombarded by energetic particles (e.g. plasma) (Figure 1.13).[60] The general mechanism of sputtering deposition is that single atoms, molecules or clusters are produced from a target solid bombarded by ions or atoms with keV energy, and then deposited on the substrate.[57] A glow discharge or radio frequency magnetron (Rf magnetron) is used as the ion source.[57] Previously, Nanba reported that Rf magnetron sputtering method has been used to prepare WO_3 thin films on ITO coated glass substrates using a metallic tungsten target in a mixture of Ar and O_2 at a total pressure of 7.0×10^{-3} Torr.[61]

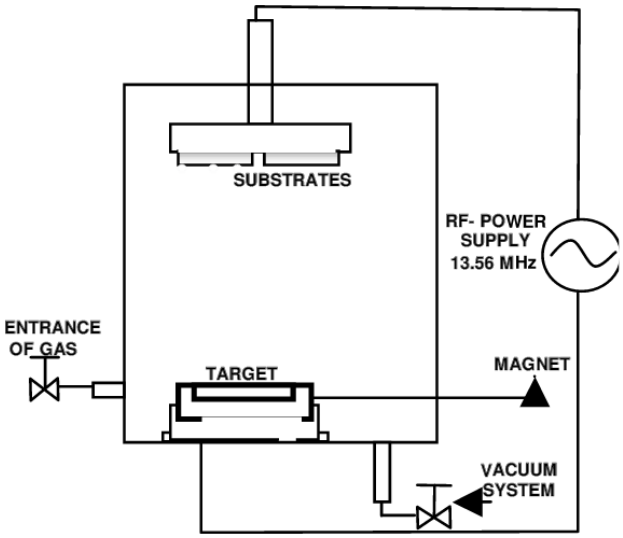

Figure 1.13. Schematic diagram of Rf-magnetron sputtering system.[60]

The CVD process involves the dissociation and/or chemical reactions of gaseous reactants in an activated (heat, light, plasma) environment, followed by the formation of a stable solid product.[62] The depositions are conducted in a cold wall or hot wall reactor (Figure 1.14 and 1.15 respectively).[63,64] There are various CVD methods including thermally activated chemical vapour deposition, plasma enhanced chemical vapour deposition (PECVD), photo-assisted chemical vapour deposition, atomic layer epitaxy, metalorganic chemical vapour deposition (MOCVD), pulsed injection MOCVD, aerosol assisted chemical vapour deposition (AACVD), flame assisted chemical vapour deposition and electrochemical vapour deposition.[62]

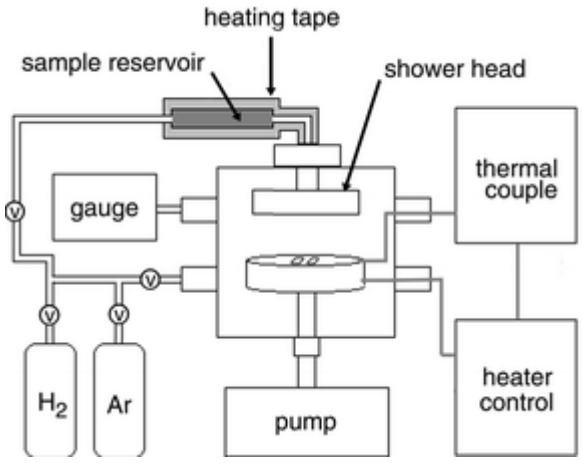

Figure 1.14. Schematic diagram of the set-up of the cold-wall CVD apparatus.[63]

C.Blackman and I.Parkin fabricated WO_3 films by atmospheric pressure chemical vapour deposition (APCVD) reaction of WCl_6 with various reactants including ethanoic anhydride, ethanoic acid, ethyl ethanoate, methanol, ethanol, 2-propanol, 2-methyl-2-propanol and water on glass substrate obtaining monoclinic WO_3 with different morphogies.[65]

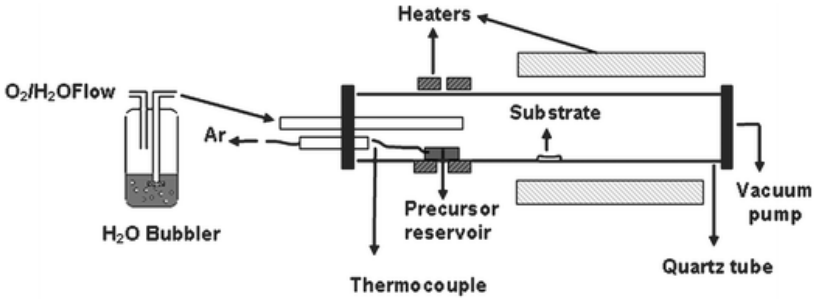

Figure 1.15. MOCVD hot-wall reactor scheme.[64]

PECVD has been used to fabricate WO_3 thin films due to the advantages of low temperature and relative high deposition rate (Figure 1.16).[66] The precursor source of gaseous WF_6, O_2 and H_2 were excited and reacted in the plasma chamber which was supplied by a 300w rf power operating at 13.56 MHz:[67]

$$WF_6 + 2O_2 + 3H_2 \rightarrow WO_3 + 6HF + H_2O \quad (1.1)$$

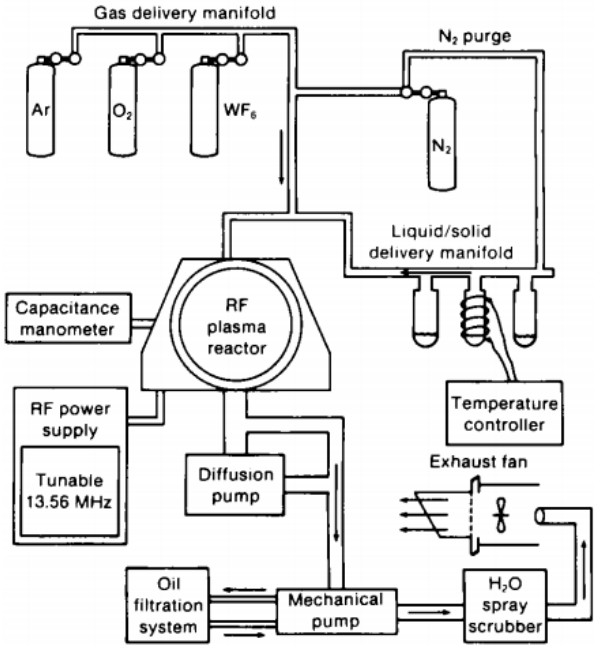

Figure 1.16. Simplified schematic diagram of the PE-CVD apparatus illustrating the essential components of the system.[66]

1.1.4 Growth Mechanism of Tungsten Oxide Nanorods

The study of film growth has produced several growth modes and theories based on thermodynamics and kinetics. In the 1870s and 1880s, J.W. Gibbs applied the idea of thermodynamic reasoning to a surface to give a description of the concentration profile of any elemental or molecular species varying from one level at phase 1 to another level at phase 2 using thermodynamic potentials from the contributing phases 1, 2 plus a surface term.[68] An imaginary dividing surface can be defined between a surface of bulk material and a vapour on that surface whose thermodynamic properties scale with its area.[68] Therefore a specific shape of a small crystal at a particular temperature depends on minimisation of total energy of each crystal faces based on Wulff theorem.

Subsequently, there are three growth modes which were introduced by Bauer in 1958 as shown in Figure 1.17.[69] Frank–van-der-Merwe (FM) or layer-by-layer growth arises when the adatoms favour depositing on the substrate rather than themselves. In the opposite case, the adatoms prefer to deposit on themselves rather than the substrate as described by Volmer–Weber (VW) or island mode. In a much more common case, layers formed at first, and then formation of islands occurs on that layer are described by Stranski–Krastanov (SK) or layer-plus-island growth mode.[68] Originally, Bauer judged which growth modes occurred by surface energies of deposited materials A (γ_A) and B (γ_B) and the interface energy (γ^*).[68] If $\gamma_A < \gamma_B + \gamma^*$, thin films grow based on VW layer mode, and vice versa for FM island mode, and if the interface energy increases with increasing of film thickness, SK layer-plus-island occurs e.g. formed layer is strained to fit the substrate.[68] Venables showed these three growth modes have their thermodynamic counterpart corresponding to various adsorption isotherms.[69] In FM island mode, due to fast re-evaporation from weak bond formation with the substrate, low concentrations of absorbed atoms need a large positive chemical potential change, $\Delta\mu > 0$ (saturation) to nucleate before occupying one mono-layer (ML); during VW layer growth, the process of layer depositing on layer always occurs under negative $\Delta\mu < 0$ (under saturation); in

SK layer-plus-island growth, after finite layers are formed under saturation, the super saturation is reached causing the deposit to nucleate.[69]

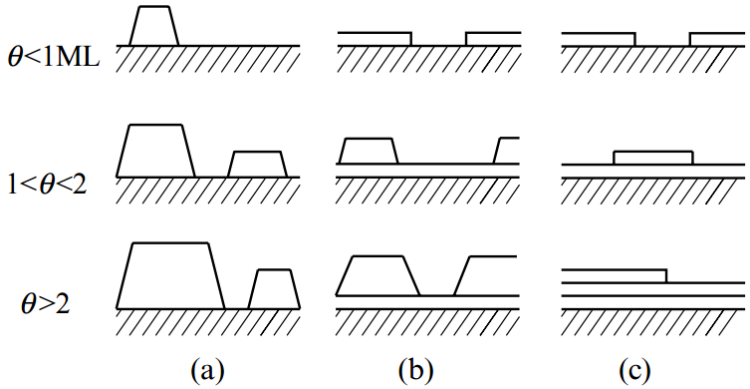

Figure 1.17. Schematic representation of the three growth modes, as a function of the coverage (θ) in ML (Mono-layer): (a) island, or Volmer–Weber growth; (b) layer-plus-island, or Stranski–Krastanov growth; (c) layer-by-layer, or Frank–van der Merwe growth.[69]

In order to understand which growth mode is selected, the terrace-step-kink (TSK) model has been used to describe the atomistic mechanism of crystal growth. It is based on the idea that atoms on the crystal surface in different sites (terrace, step and kink) have various numbers of bonds with neighbouring atoms, which results in different energy required to remove an atom and hence influence atom diffusion, nucleation and crystal growth (Figure 1.18).[68,70] Therefore, in this model, compared to bulk atoms, atoms in different sites of terrace, step and kink have an extra energy of e_t, e_s and e_k respectively (normally $e_t < e_s < e_k$). Moving the kink around the surface maintain the surface energy unchanged due to unchanged amount of terrace, step and kink atoms, and hence it is a repeatable step of constructing a crystal.[68] Practically, crystals were considered growing on a vicinal or stepped surface which consists of many flat terraces separated by steps of atomic height.[71] Burton, Cabrera, and Frank (BCF) discussed crystal growth on vicinal surface developing an analytical model for growth of crystals by step movement.[72,73] The mechanism was that adatoms diffusing on a terrace were captured and incorporated into the step edge subject to the following assumptions: 1) the effect of the moving boundary was ignored, 2) at the step edge, the concentration was at equilibrium and 3) between atoms there was no interaction and reaction.[72,73]

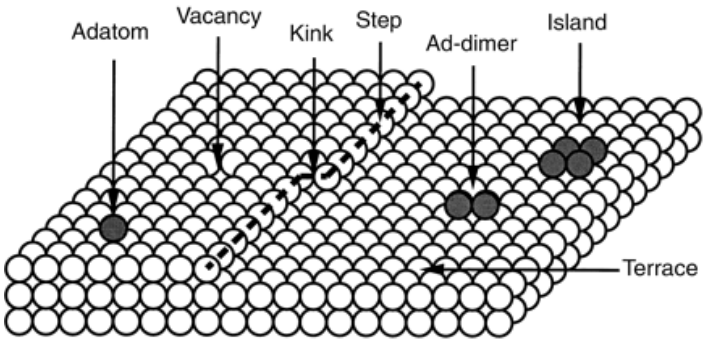

Figure 1.18. The TSK model of a surface defined for a simple cubic crystal. The white circles represent atoms of the substrate. The dashed line indicates the location of a step separating the upper and the lower terraces, with a kink along the step. The step-down direction is from left to right. The black circles are atoms adsorbed on the terraces.[70]

Venables introduced a kinetic theory to describe atomic processes of the nucleation and growth in thin films concentrating on activation energies for every step occurring on a defect-free surface.[68,74] The schematic diagram of atomic processes shown in Figure 1.19 show the following processes:

(a) Atoms from vapour arrive on substrate with an arrival rate *R* in units of molecules $m^{-2}s^{-1}$ given by[71,75]

$$R = \tfrac{1}{4}\rho_n v_m = \tfrac{1}{4}\frac{P}{kT}\sqrt{\frac{2kT}{\pi m}} = \frac{P}{\sqrt{2\pi m k T}} \quad (1.2)$$

where ρ_n is number density of atoms in vapour (treated as an ideal gas) calculated by $\frac{P}{kT}$ based on equation of state for ideal gases ($PV = nRT$). v_m is the mean speed of atoms in vapour determined by the Maxwell Boltzmann distribution equalling to $\sqrt{\frac{2kT}{\pi m}}$. *P* is the vapour pressure, *m* is the atomic mass, *k* is Boltzmann's constant and *T* the absolute temperature of vapour.

(b) At high temperature those adatoms can only stay for a short time the substrate, (adsorption residence time, τ_a) before re-evaporation[68,75]

$$\tau_a^{-1} = \upsilon_a exp(-E_a/kT) \quad (1.3)$$

where υ_a is an atomic vibration frequency with order 1 to 10 THz and E_a is the adsorption energy.

(c) During the absorption residence time, these adatoms migrate over the substrate with diffusion coefficient D[75]

$$D = (\upsilon_d a^2/4)\exp(-E_d/kT) \quad (1.4)$$

where α is the jump distance with the order of the surface repeat distance 0.2 to 0.5 nm. The adatoms diffuse with diffusion energy of E_d and frequency of υ_d.

(d) The diffusing adatoms can meet each other or attach to an existing island to nucleates forming cluster with rate J[68]

$$J = \sigma_i D n_1 n_i \quad (1.5)$$

where σ_i is the capture number describing the adatoms diffusing to the critical or sable cluster, n_1 is the number density of adatoms which is equal to $R\tau_a$ when only re-evaporation is considered, n_i the density of critical nuclei is equal to[68]

$$n_i = C_i n_1 \exp(E_i/kT) \quad (1.6)$$

where C_i is a statistical weight of order 1-10 and E_i is the free energy of the critical cluster when on the perfect substrate.[68,69,71,76]

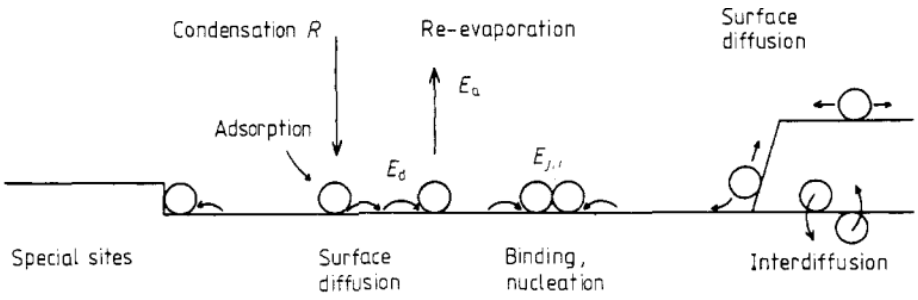

Figure 1.19. Schematic diagram of processes and characteristic energies in nucleation and growth on surfaces.[69]

Generally, 1D nanorod growth is achieved by anisotropic material deposition or growth with relative fast growth along one axis or/and a plane based on two main mechanisms: vapour-liquid-solid (VLS) and vapour-solid (VS).[77] The mechanism of VLS has been well studied as a catalyst assisted method, though the fundamental understanding of VS is still controversial.[77]

Recently, the planar-defect-driven growth mechanism was introduced as a supplement to the screw-dislocation-driven VS method.[78]

The VLS mechanism was introduced by Wagner and Ellis (1964) who fabricated Si whiskers using small Au particles deposited on a {111} surface of a Si wafer as a catalyst, forming small droplets of Au-Si alloy at 950 ℃ as shown in Figure 1.20a.[79] Consequently, the liquid alloy acted as a favoured site or a catalyst for the deposition of Si atoms produced by reaction of H_2 and $SiCl_4$, with the Si atoms forming a crystal at the interface between the solid Si and the liquid alloy droplet.[79] As these processes repeat, the Si crystal grows along the <111> direction until the Au is consumed or the growth conditions varied as presented in Figure 1.20b.[79] Fabrication of WO_3 nanowires based on a VLS mechanism has been reported using a thin Au film (5 nm) as a catalyst, growing on W films (0.5 μm) on Si substrate via CVD at 450 to 600 ℃ and 5000 – 9000 Pa.[80]

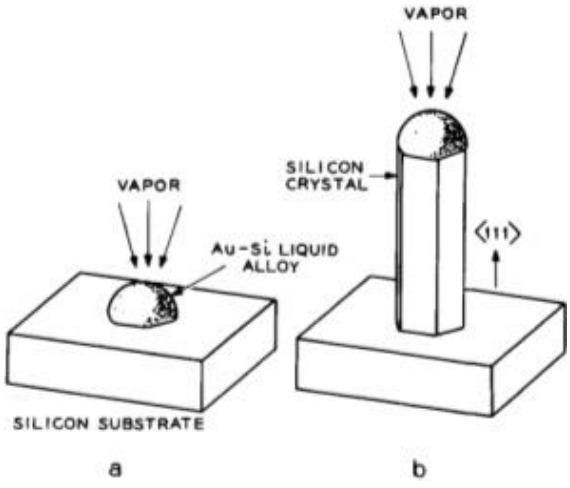

Figure 1.20. VLS mechanism of growth of a silicon crystal: a) Initial condition with liquid droplet on substrate; b) Growing crystal with liquid droplet at the tip[79].

The difference between VLS and VS is that in VS mechanism there is no catalyst to form a liquid alloy, atoms are deposited from vapour directly on the crystal.[81] The VS process is not fully understand, although there are many mechanisms used to explain the mechanism of VS such as screw-dislocation-driven, solid-phase growth and planar-defect-driven growth mechanisms.

As shown in Figure 1.21, crystal growth based on screw dislocations can lead to 1D structure due to the spiral growth perpendicular to surface. Burton et al. considered that when new layers are added, the direction of the dislocation remains perpendicular to the surface to minimize the elastic energy.[82] The growing spiral forms a low cone if the speed of advance of a step is independent of its orientation, otherwise the growing spiral forms a pyramid as the speed of advance of a step depends on its orientation.[82] The step winds up in a spiral due to dislocation occurring at a faster rate as supersaturation increases.[82] When the curvature at the centre gets to a critical value, the rate of step advance decreases to zero resulting in spiral rotation with stationary shape.[82] Recently, screw dislocation-driven growth was evoked to explain development of PdS and CdS NWs *via* CVD.[83]

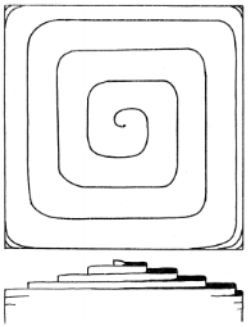

Figure 1.21. Growth pyramid due to a single screw dislocation.[82]

The solid-phase growth mechanism of WO_3 nanowires was proposed by Kojima etc. who prepared NWs *via* Rf-magnetron sputtering.[84] As shown in Figure 1.22, an amorphous WO_3 layer was formed on the surface of a W layer due to annealing in O_2, and then nucleation of nanowires occurred at irregular sites on the W surface, and subsequently WO_3 molecules diffused onto the nucleus leading to nanowires growth.[84]

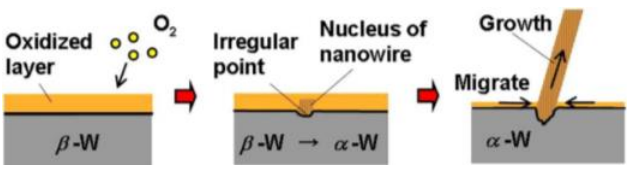

Figure 1.22. Schematic of the solid-phase growth model proposed in this study.[84]

A planar-defect-driven growth mechanism was proposed by Smith. whereby the metallic tungsten layer was oxidized, and then a substoichiometric tungsten oxide film formed with defects which can coalesce to form the nucleus of tungsten oxide nanowires which subsequently promote deposition of vapour species leading to NW growth (Figure 1.23a).[59] As the saturation of vapour species increase and O_2 is introduced, polycrystalline growth was observed due to the formation of fully oxidised tungsten oxide depleting the defects in the film as shown in Figure 1.23bc.[59]

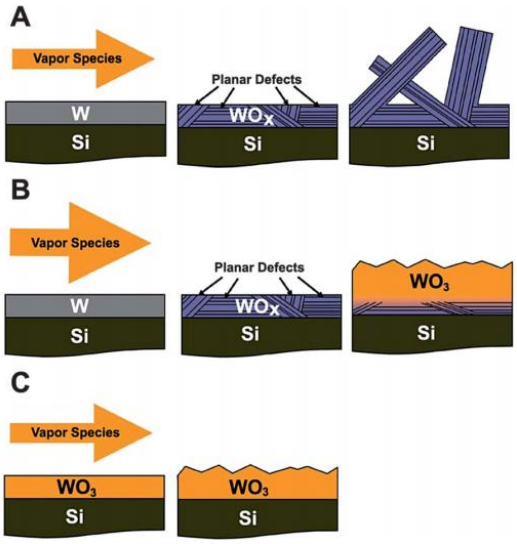

Figure 1.23. Schematic of a proposed growth mechanism. (A) NW synthesis illustrating defect-driven growth. (B) Growth of polycrystalline films under increased supersaturation or oxygen partial pressure. (C) Growth of polycrystalline films on WO_3.[59]

To understand the mechanism of 1D nanostructure growth *via* a VS mechanism, the key point is to find out the driving force for anisotropic growth. In the screw-dislocation driven mechanism the driving force is the generation of a dislocation spiral step due to the velocity of the step at the dislocation core being greater than that at the outer edge.[83] However the screw-dislocation driven mechanism for explaining the VS process of tungsten oxide NW growth during CVD is controversial. Recently, Z. Zhang et al. showed a real-time observation of tungsten oxide NW growth *via* an environmental transmission electron microscopy (TEM). In that observation, during NW growth no step was found on the tip terrace as expected for the screw-dislocation driven mechanism, instead, the 1D growth of $W_{18}O_{49}$ was attributed to the minimization of surface free energy resulting in a higher growth rate along the [010] direction

((010) with higher surface free energy -33.03 eV) than other directions such as [100] and [001] ((100) -33.44 eV, (001) -33.25 eV).[85] In the planar-defect-driven mechanism, the nuclei of substoichiometric tungsten oxide such as $W_{18}O_{49}$ are formed *via* partial oxidation of a metallic W film resulting in planar defects appearing and limiting the growth rate in the directions perpendicular to the NW growth direction.[59] Alternatively, in the solid-phase growth mechanism, the NW nuclei are formed at irregular points on the metallic W thin film and at the interface between metallic W and a tungsten oxide thin film.[84]

1.2 Aerosol Assisted Chemical Vapour Deposition

1.2.1 Overview of AACVD

CVD technology has been widely used to synthesise thin films, coatings and powders.[62] However, traditional CVD can be limited by the lack of volatile precursors and the difficulty of controlling the stoichiometry of the deposition.[86] Compared to traditional CVD, AACVD has several potential advantages as following: a wide choice of commercially available precursors whose primary requirement is to be able to dissolve in solvent rather than to be volatile at relatively low temperature; simplification of the delivery and vaporization of precursors due to aerosol delivery; high reaction rate; a more flexible reaction environment; simplification of the synthesis of multicomponent products with precise stoichiometric control.[62]

As demonstrated in Figure 1.24, the process of AACVD involves the atomization of a liquid precursor solution into aerosol droplets by ultrasonic aerosol generation, pneumatic aerosol jet or electrostatic aerosol atomization, distribution throughout a gaseous medium, and then transportion by carrier gas into a heated reaction zone where the solvent rapidly evaporates and/or decomposes and the precursor evaporates. Finally, the desired products (under moderate temperature heterogeneous reaction occurs in order to form a film with good adhesive strength, whilst at higher temperature homogeneous reaction is favoured to form powders) are able to be synthesized via decomposition or other chemical reactions of the vaporized precursor.[86]

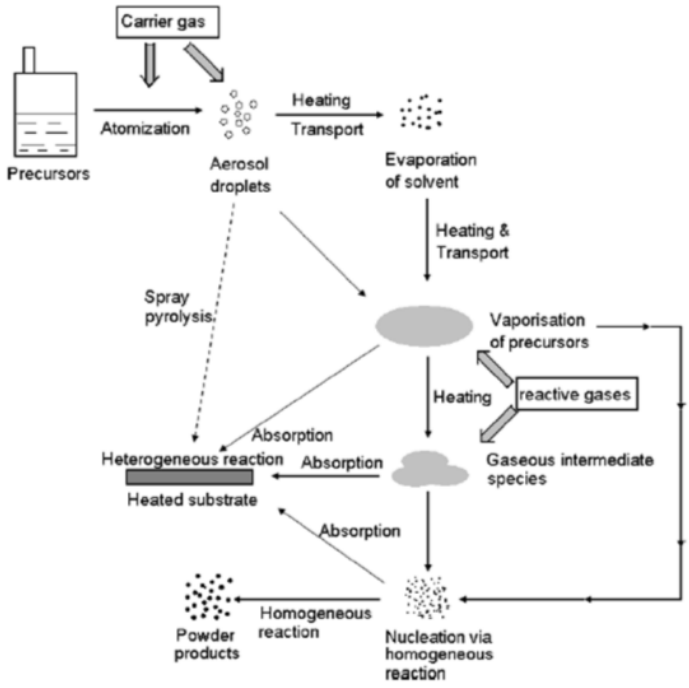

Figure 1.24. Schematic diagram of the AACVD process for the deposition of films and powders.[86]

The most popular equipment for aerosol generation in AACVD is ultrasonic, using a high-frequency electrical field to vibrate a transducer to physically form fine droplets of solution with diameter *d* described as

$$d = k\left(\frac{2\pi\gamma}{\rho f^2}\right)^{\frac{1}{2}} \quad (1.7)$$

where *f* is the excitation frequency of the transducer, *k* is a constant, ρ is density of solution and γ is the surface tension of the solution.[79]

AACVD is particularly suitable to fabricate simple and multicomponent metal oxides with various surface morphologies for potential application in optics, electronics, solid oxide fuel cells, superconductors, catalyst and biomaterials.[86] Highly oriented crystalline metal chalcogenide films were able to be produced by AACVD using single source precursors.[86] In addition, metallic alloy films with controllable composition have been deposited by AACVD.[86] Nano composite thin films have been formed by co-deposit of particles and matrix simultaneously. Recently, AACVD has been used to synthesize carbon-nanotubes (CNT) due to the simplicity of obtaining good quality CNT.[86]

1.2.2 Synthesis of Nanostructured Tungsten Oxide *via* AACVD

Many different types of precursors for fabrication of tungsten oxide thin films via AACVD have been reported. Two polyoxotungstate anions $[n\text{-}Bu_4N]_2[W_6O_{16}]$ and $[n\text{-}Bu_4N]_4H_3[PW_{11}O_{39}]$ were used to deposit blue tungsten oxide (WO_x) films at 410 and 480 ℃ respectively *via* AACVD as shown in Figure 1.25.[31] Tungsten hexaaryloxide complexes of formula $W(OAr)_6$ (Ar = C_6H_5, C_6H_4F-4 and C_6H3F_2-3, 4) synthesized by the reaction of $W(O)Cl_4$ and ArOH, were used to produce WO_x at 300 to 500 ℃.[87] Monomeric tungsten oxo-aminoalkoxides $W(O)(OR)_3(L)$ [L = $O(CH_2)_nNMe_2$; n = 2 (dmae) and 3 (dmap)] deposited WO_x thin films via AACVD at 260 to 450 ℃.[88] In addition $W(CO)_6$ has been used to deposit nanostructured tungsten oxide thin films showing various morphologies with different solvents as shown in Figure 1.26.[11]

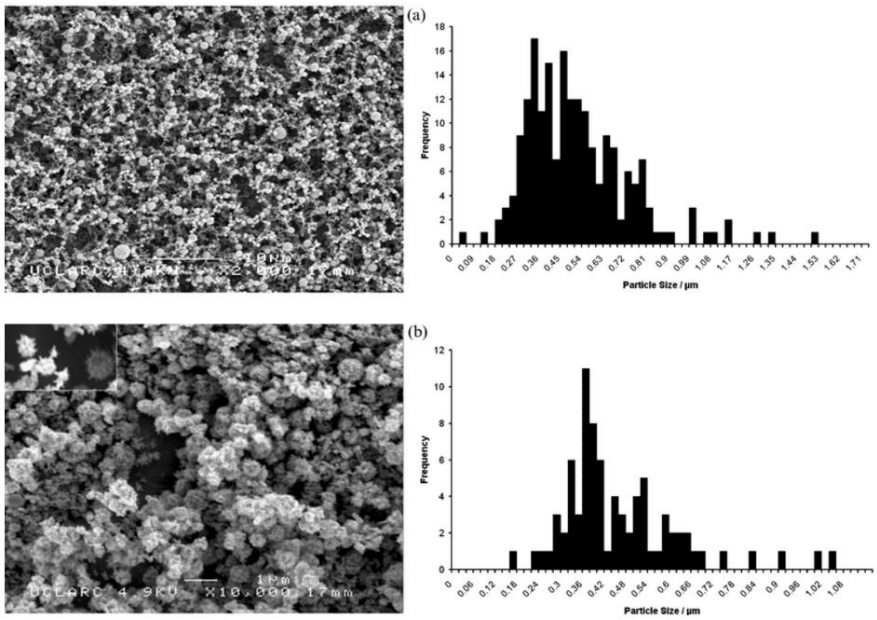

Figure 1.25. Scanning electron micrographs of tungsten oxide films deposited from AACVD reactions of $[^nBu_4N]_3[WO_4]$ (a), and $[^nBu_4N]_2[W_6O_{19}]$ (b) at 550 ℃ and 0.5 L min^{-1}, including inset at higher magnification showing the needle-like agglomerates, and their corresponding size-distributions..[11]

Vallejos etc. conducted a series of depositions of tungsten oxide thin films by AACVD with different parameters such as temperature and solvents showing the change of morphologies as presented in Figure 1.26.[89] The conclusion revealed that solvents played a very important role for the morphologies of formation of tungsten oxide and deposition temperature affected the crystal orientation and crystalline phases.[89]

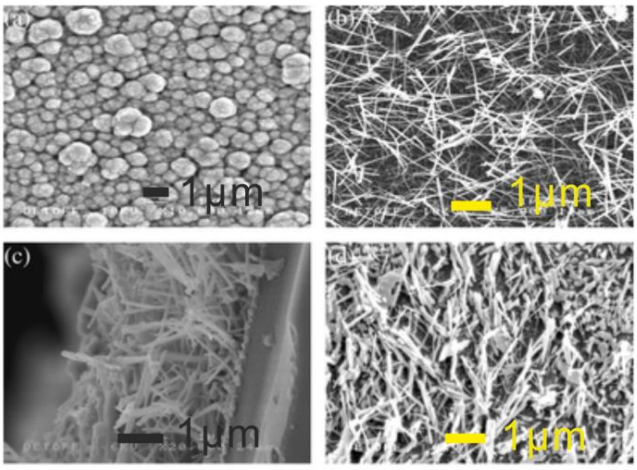

Figure 1.26. Scanning electron micrographs of tungsten oxide films deposited from the AACVD reactions of $[W(CO)_6]$ in acetone, a, and methanol, b, at 400 °C and 2 L min^{-1}. The film deposited using acetone, a, has a microstructure composed of spherical particles coalesced together and is similar to the morphology of films deposited using acetonitrile, toluene and a 50:50 mixture of toluene. The film deposited from methanol, b, has a microstructure comprising a network of needles randomly orientated with respect to the substrate. Part c and d show a cross-section of the film and the film post-annealing respectively.[11]

Kim etc. reported growth of WO_x films and nanorods using oxo-alkoxide tungsten (IV) compounds, $WO[OCCH_3(CF_3)_2]_4$ and $WO[OC(CH_3)_2CF_3]_4$ as precursors via AACVD.[90] At different deposition temperature (200 to 400 ℃) by using different precursors the tungsten oxide thin films presented varying morphologies as shown in Figure 1.27.[90] It revealed that substoichiometric amorphous tungsten oxide thin films were grown below 250 ℃ and between 300 to 350 ℃, nanorods (NRs) with long straight sides and flat circular end were observed on the amorphous films, and above 400 ℃ the fully developed tungsten oxide NR structure was found.[90]

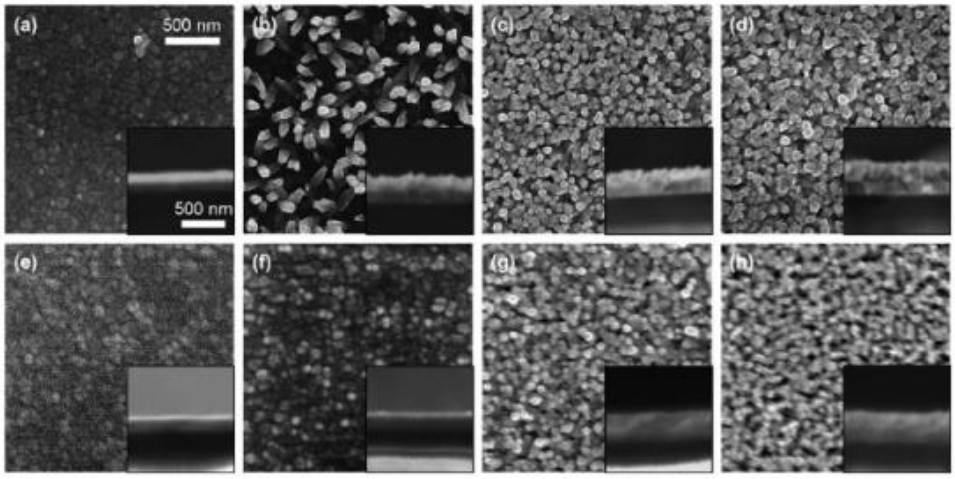

Figure 1.27. Top-view and cross-sectional (insect) SEM images of materials grown with precursor at $WO[OCCH_3(CF_3)_2]_4$ at (a) 250 ℃, (b) 300 ℃, (c) 350 ℃, (d) 400 ℃ and $WO[OC(CH_3)_2CF_3]_4$ at (e) 250 ℃, (f) 300 ℃, (g) 350 ℃, (h) 400 ℃ with diglyme and N_2 carrier gas (all the scale is the same).[90]

1.2.3 Synthesis and application of Tungsten Oxide based heterogeneous Junction thin film material via AACVD

Applications of metal particles supported on a semiconductor for CO oxidation, water splitting and environmental protection have shown better performance than a plain semiconductor.[91] However, typical synthesis methods use organic agents such as polymers and surfactants which form an organic layer at the interface between the metal particles and the supports, leading to poor interfacial contact and resulting in poor charge separation efficiency and transport.[91] To remove that organic layer, thermal treatment has been used to oxidise the layer, though this method normally results in a change in either the size or morphology of particles and reduces the catalytic efficiency.[91] Therefore, Xi et al proposed a new method for growth of metal particles on WO_3 via an in-situ reduction of oxidative metal salt precursors on weakly reductive $WO_{2.72}$, as shown in Figure 1.28.[91]

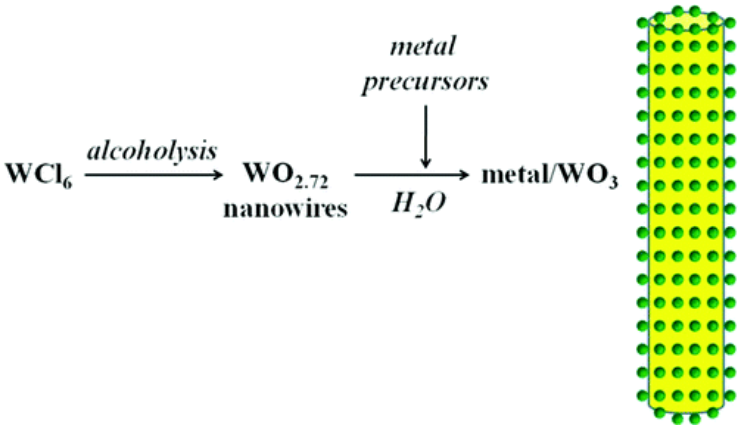

Figure 1.28. Schematic Procedure for in Situ Loading of Metal Particles on WO_3.[91]

As presented in Figure 1.29, Pt/WO_3, Ag/WO_3, Rh/WO_3 and Au/WO_3 have been successfully synthesized *via* this in-situ growth method in the liquid phase providing improved photocatalytic degradation of toxic pollutant.[91]

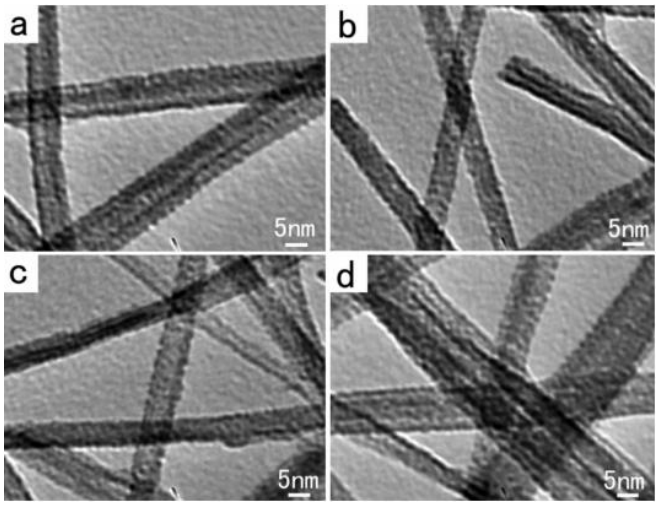

Figure 1.29. TEM images of metal/WO_3 composites: (a) Pt/WO_3 (0.9 wt%, <1 nm), (b) Au/WO_3 (1.1 wt%, <1 nm), (c) Rh/WO_3 (1.0 wt%, <1 nm), (d) Ag/WO_3 (0.8 wt%, <1 nm).[91]

Vallejos and Blackman etc. reported a single step deposition of noble metal nanoparticles (NP) functionalised tungsten oxide nanoneedles (NN) with a sharp point at top end via AACVD.[92,93] In comparison to liquid phase synthesis, the advantages of AACVD method includes greater purity, continuous mode operation and higher throughput, providing better homogenous coverage of the metal particles on the oxide supports compared to physical methods such as sputtering or thermal vapour deposition.[92] As shown in Figure 1.30, Au and Pt NPs functionalized tungsten oxide have been successfully synthesized via single step deposition by AACVD with the materials providing improved sensing characteristics to H_2 and CO.[93]

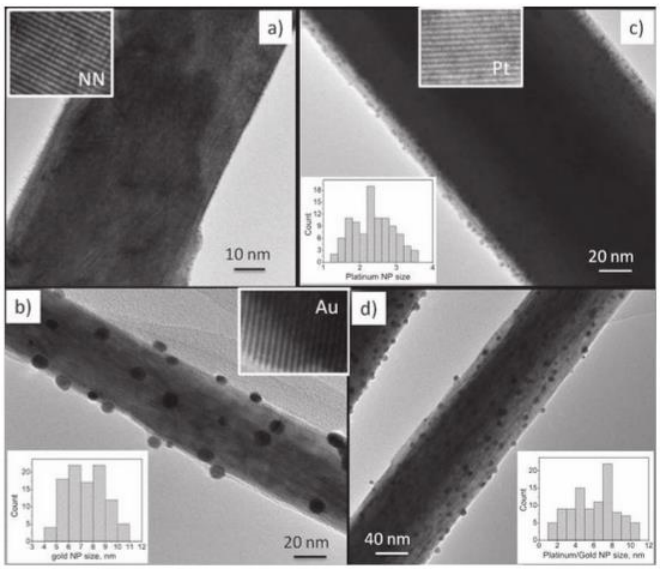

Figure 1.30. HR-TEM and size distribution of the non-functionalized (a) and functionalized samples with gold (b), platinum (c), and gold/platinum (d) NPs after annealing.[93]

Recently, Annanouch et al firstly reported Cu_2O NP decorated WO_3 NNs via AACD with precursors $W(CO)_6$ and $Cu(acac)_2$ dissolved into methanol and chloroform respectively, demonstrating improved gas sensing to H_2S, as shown in Figure 1.31.[94]

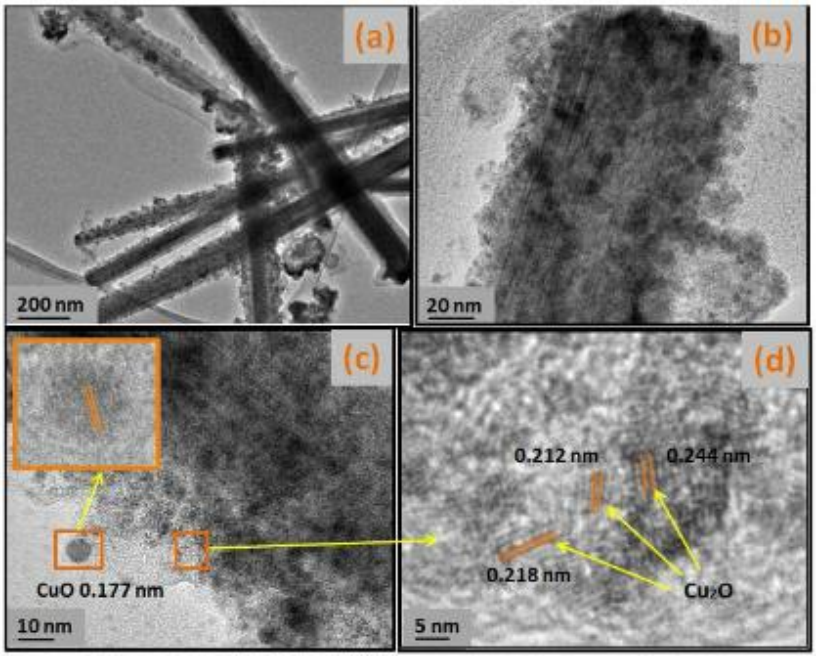

Figure 1.31. TEM and HRTEM images of the obtained Cu_2Ofunctionalized WO_3 NNs: (a and b) low magnification; (c and d) high magnification.[94]

1.3 Catalyst and Photocatalyst

1.3.1 Catalyst Properties of Noble Metals and Noble metal/Metal Oxide heterogeneous Materials and Their Applications

1.3.1.1 Platinum (Pt)

Since 1831 Pt has been used as a catalyst for sulphuric acid manufacture and it plays an important role as a catalyst in a wide variety of applications in the petrochemical industry, automobile exhaust purification, and fuel cells.[95] In terms of the low abundance and high cost researchers around the world are working on finding out effective alternatives to Pt as a catalyst or efficient utilisation of Pt, and in particular the relationship between the size/shape of Pt nanoparticles/nanocrystals and their catalytic activity, selectivity and stability.

H_2 is a clean energy source, which combusts to produce only water. One way to produce H_2 involves 'hydrogen evolution reaction' (HER) in which protons chemisorbed on the surface of a

metal electrode (also acts as a catalyst) transport from an electrolyte solution and then are reduced to produce H_2. The performance of the catalyst relies on the Gibbs energy of proton absorption on the surface of catalyst, ΔG_H, for which the absolute value approaching to zero corresponds to better performance.[96] Pt has $\Delta G_H = -0.1\ eV$ and is a very good catalyst for HER. Greeley et al. used DFT calculations to search for potential and effective alternatives to Pt as a catalyst by calculating ΔG_H for 736 binary alloys, proposing the BiPt is one of most promising candidates with $\Delta G_H = -0.04\ eV$.[97] Therefore, Pt is still one of best catalysts for HER.

The control of grain size and shapes of Pt nanocrystals are able to be achieved via different synthesis techniques by varying precursor, solvent, and reaction condition and parameters.[98] The catalytic and electrocatalytic activity depends on not only the grain size (smaller grain size increase the ratio of surface area to volume), but also the structure of nanocrystals on the surface.[99] Pt, as well as Au, Pd, Pt, Rh and Ir, has a face-centred cubic (FCC) structure,[99] and normally Pt nanocrystals with surface defined by high-index planes demonstrate greater catalytic activity than those defined by low-index planes. This is because high-index planes have a high density of atomic steps, leading to low-coordinated atoms which serve as active sites where the reactant molecules more easily interact to break chemical bonds, whereas low-index plane result in close packed atoms with less catalytic activity.[100]

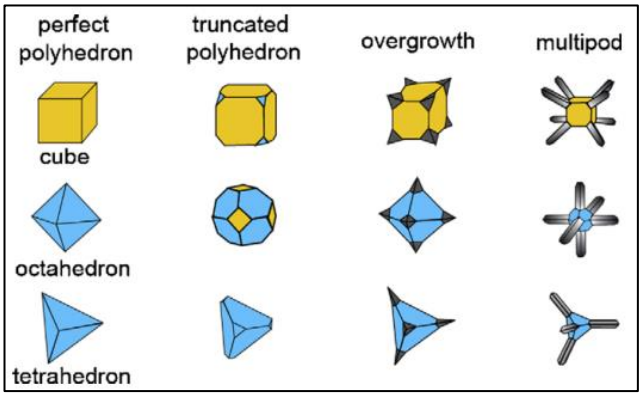

Figure 1.32. Schematic illustration of different shapes of Pt nanocrystals derived from conventional single-crystal polyhedrons enclosed by the low-index planes (100) and (111).The first column represents the perfect polyhedrons, while the second column contains the truncated forms of the perfect polyhedrons. The third and fourth columns compromise the overgrown nanostructures and highly branched nanostructures grown from the corners of the perfect polyhedrons, respectively. The yellow and blue colours represent the (100) and (111) facets, respectively.[100]

1.3.1.2 Gold (Au)

Au has an FCC structure which is commonly terminated by (100), (110), (111) facets, similar to Pt.[99] In the previous century gold was neglected from applications in catalysis due to two prejudices, firstly that gold is too expensive to be affordable to be applied in catalysis, and secondly that gold has the highest normal potential (1.48 eV) towards oxidation among all other metals.[101] But since 1973, after a paper of the hydrogenation of olefins over supported gold catalysts was published, this changed was dramatically.[102] Haruta et al. firstly reported that gold acted as a catalyst for CO oxidation showing activity even at temperatures as low as -70 ℃.[103] Hutchings showed gold was a potential catalyst for selective acetylene hydrochlorination.[104] When the diameter is below 3.5 nm, gold particles show catalytic activity, for instance Au NPs with diameter ~1.4nm demonstrate efficient catalytic activity for the selective oxidation of styrene by dioxygen.[105] This is attributed to the Au NPs being able to dissociate chemisorbed O_2 to yield oxygen adatoms for subsequent reactions.[105]

1.3.1.3 Palladium (Pd)

Pd also crystallizes in an FCC unit with frequent exposure of (100), (110) and (111) facet, which produce different catalytic activity and selectivity.[106] For instance, due to a more open surface and higher sticking probability the (110) facet provides better adsorption and activation of hydrogen, leading to the turn over frequency (TOF) for selective hydrogenation of 1,3-butadiene on (110) planes increasing five times over that on (111) planes.[107,108] When the diameter is approximately 1.3 – 1.9 nm, Pd NPs show better catalytic properties for alkene hydrogen *via* the Horiuti-Polanyi mechanism involving dissociating adsorbed H_2.[109] Pd NPs have also been reported to promote the hydrogen oxidation reaction and the oxygen reduction reaction (ORR) in alkaline media rather than OER and HER which is less reported.[110–112] Growth of the shapes of Pd nanocrystals largely depend on the crystallinity of Pd seeds.[113] After nucleation, each type of Pd seed is able to still grow into a nanocrystals with several possible shapes depending on various experimental processes and conditions.[113]

1.3.1.4 Ruthenium (Ru)

Ru crystallises in a hexagonal close packed (HCP) structure. A Ru based catalyst was used as the main catalyst in manufacture of cyclohexene *via* partial hydrogenation of benzene developed by the Asahi Chemical Company in 1988.[114] A second famous example is that Kellogg, in cooperation with British Petroleum (BP), developed breakthrough ammonia synthesis technology known as the Kellogg Advanced Ammonia Process (KAAP) which introduced Ru as the main catalyst, achieving 20 times higher catalytic activity than the iron based catalyst used for over 80 years.[115]

The catalytic activity and selectivity of Ru-based catalysts depends on: (1) the precursors used for synthesis, for example, a Ru catalyst prepared by the precursor $Ru(CO)_{12}$ give two times higher catalytic activity for ammonia synthesis than a catalyst prepared usin $RuCl_3$;[116] (2) promoters used for modification of the surface of Ru, for example alkali metal nitrates used as promoters on a Ru/MgO catalyst in ammonia synthesis were shown to be more effective than alkali earth metal nitrates due to the lower electronegativity of the alkali metal applied;[117] (3) the support used for dispersing the catalyst, which increase the ratio of surface area to volume, helps to avoid catalyst aggregation and provide a strong metal-support interaction; (4) preparative variables.[118]

1.3.1.5 Palladium Oxide (PdO)

Okamoto et al. demonstrated PdO showing it is a p-type semiconductor, which has an optical band gap in the range from 0.1 to 5.4 eV based on various reports.[119][120] Recently, PdO is found with CBM (-5.27 eV) and VBM (-6.29 eV) reference to TiO_2 nanobelts (-4.21 *vs.* -7.41 eV), and the fermi energy value of PdO has been reported as -7.9 eV.[121] PdO has also been reported as a catalyst for ORR (rather than OER).[122]

1.3.1.6 Ruthenium Oxide (RuO_2)

RuO_2 and RuO_2-based catalysts have been reported for applications in low-temperature dehydrogenation of small molecules, catalysing gas phase oxidation of HCl, as a electrocatalyst for CO oxidation reaction, and for OER.[123] RuO_2 has been found with metallic character with a work function around 6.2 eV.[124] Recently RuO_2 was used as a co-catalyst on PtO_x/WO_3 playing a role for promoting hole-extraction from WO_3 VB to improve OER rather than water oxidation catalysis.[125]

1.3.1.7 Metal Supported on Metal oxide Heterogeneous catalysts

Supported-metal heterogeneous catalysts play an import role in automotive exhaust purification and gasoline octane improvement amongst other applications.[126] The porous metal oxide support normally has a surface area of 200 m^2/g or more, thus increasing the surface-to-volume of supported metal particles and hence providing greater catalytic utilization.[126] In addition, the appearance of interaction between the particle metal and support, called the 'strong metal-support interaction' (SMSI), as used in CO-H_2 (Fischer-Tropsch) synthesis.[126] SMSI was first reported by Roland Ward et al. who observed cations of noble metals incorporated into the lattice of $BaTiO_3$ form strong bonds with titanium cations leading to 'guest cations' with flexible oxidation states in the range from +2 and +4 instead of forming metal-metal bonds, advantages for petroleum-related processes.[126] The catalytic properties of supported metal particles are altered *via* changing the chemisorption properties by the SMSI state between metal particles and supports.[126] In the case of the Fischer-Tropsch reaction the chemisorption of CO and H_2 is strongly suppressed due to SMSI on support oxides of titanium, niobium, vanadium and manganese resulting in the change of the catalytic activities of metals Ru, Rh, Pd, Os, Ir and Pt.[126] For example, the catalyst Ni/TiO_2 showed 10 times greater activity than Ni/Al_2O_3, Ni/SiO_2,

or Ni/C catalysts, and greater selectivity for formation of higher molecular weight products and less formation of nickel carbonyl.[127]

Supported metal catalysts normally consist of two components, the active metal particles and the support which are commonly oxides such as Al_2O_3, MgO, TiO_2, WO_3, SiO_2, Fe_2O_3, CeO_2.[99] Wet impregnation is a widely used method to prepare metal/metal oxide heterogeneous catalysts in which the metal oxide support soaks into a solution of metal salt, and then drying and treating by calcination are used to decompose the metal salt to form nanoparticles on the support.[128]

Maiyalagan reported fabrication of a film of platinum nanoparticles supported on tungsten oxide NRs by a hybrid method of template synthesis with an anodisc alumina membrane and conventional impregnation on a glassy carbon electrode.[129] The Pt/WO_3 NRs (Figure 1.33) showed 2 times greater activity of methanol oxidation than the commercial Pt/C, possibly due to the oxo-philic nature of WO_3 cleaning the Pt surface by chemisorbing the intermediates (such as methanol) by forming hydrogen tungsten oxide bronzes, as following:[129]

$$1)\quad WO_3 + xPt - H \rightarrow H_xWO_3 + xPt \quad (1.10)$$

$$2)\quad H_xWO_3 \rightarrow +xH^+ + xe^- + WO_3 \quad (1.11)$$

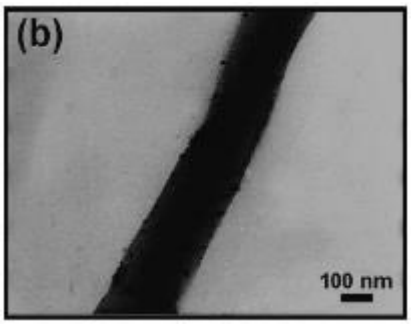

Figure 1.33. TEM images of Pt/WO_3 nanorods[129].

An alloy of Au and Pd, discovered by Hutchings, led to a 25 times greater activity and selectivity than Au or Pd mono-metallic catalysts for oxidation of primary alcohols to aldehydes.[130] Enhong Cao et al. studied oxidation of benzyl alcohol on 1 % Au–Pd /TiO_2

catalysts using a micropacked-bed reactor where 95.5 % of benzyl alcohol was converted with 78 % selectivity to benzaldehyde with catalyst sizes of 53-63 μm at 120 ℃.[131]

1.3.2 Photocatalyst Properties of Metal Oxide and Metal Oxides Heterogeneous Materials and Their Applications

There is great interest in photodegradation of organic pollutants with oxygen, for example by titania particles dispersed in aqueous solution according to following the reaction:[132]

$$\text{Organic} + O_2 \xrightarrow[h\upsilon \geq E_g]{TiO_2} CO_2 + H_2O + \text{minal acides} \quad (1.12)$$

Semiconductor photocatalysis is activated by absorbing photos with energy > E_g promoting an electron from VB into CB and generating of an electron and a hole in the CB and VB respectively, with these charge carriers (an electron or/and a hole) reacting with absorbed organic species before deactivation *via* electron-hole recombination.[133]

Consequently, semiconductor photocatalysis could potentially be applied in water purification. Compared to the predominant technologies currently used such as air-stripping and carbon absorption with problems of air pollution and production of hazardous solids respectively, water purification by semiconductor photocatalysis could be incorporated into existing UV water purification systems avoiding those problems and producing only carbon dioxide, water and mineral acids.[133]

However, scaling up of semiconductor photocatalysis is not simple due to photocatalyst particle filtration and recovery.[132] Therefore, the creation of self-cleaning surfaces on glass, tiles and tent fabric has been essential for many large commercial products, especially, self-cleaning glass with a photocatalytic surface layer of titania manufactured by Pilkington glass (Activ^{TM}), St-Gobanin (Bioclean^{TM}) and PPG (SunClean^{TM}).[132] To assess the activity of a self-cleaning photocatalyst film, Mills et al. introduced the stearic acid (SA) test. SA is an ideal chemical for photocatalyst testing due to its stability under UV irradiation without a photocatalyst, easy

deposition from a methanol or chloroform solution and the zero order kinetics of decomposition which can be monitored by FT-IR.[132] The general reaction of SA destruction by a titania thin film,

$$CH_3(CH_2)_{16}CO_2H + 26O_2 \xrightarrow{TiO_2}_{h\upsilon \geq E_g} 18CO_2 + 18H_2O \quad (1.13)$$

is commonly studied through FT-IR absorption to monitor the disappearance of the SA film, which strongly absorbs in the region 2700 to 3000 cm^{-1} with peaks at 2958 (C-H asymmetric stretching in the CH_3 group), 2923 (C-H asymmetric stretching in the CH_2 group) and 2853 cm^{-1} (C-H symmetric stretching in the CH_2 group).[132] In order to compare activity of SA destruction by various photocatalyst films the initial formal quantum efficiency (FQE) is calculated *via*

$$FQE\ (SA) = \frac{rate\ of\ removal\ of\ SA\ (molecules/s)}{rate\ of\ incident\ light\ (photons/s)} \quad (1.14)$$

with a conversion factor 9.7×10^{15} molecules of SA in 1 cm^{-1} integrated areas of SA peaks (2700 – 3000 cm^{-1}) in the FT-IR.[132]

Mills et al. proposed that Pilkington Activ™ used for SA test can be a reference for semiconductor thin film photocatalyst, with FQE (SA), 0.7×10^{-5} molecules per photon, under 365 nm UV irradiation, (compared to commercial P25 TiO_2 (mixture of anatase 70% and rutile 30%)), 15.3×10^{-5} molecules per photon.[134] Quesada-Cabrera et al. prepared N-doped TiO_2 (N-TiO_2) thin films by CVD with FQE (SA) up to 2.77×10^{-4} molecules per photon possibly due to a highly oxidising N-O radical being involved in the photodegradation reaction.[135] Subsequently, N-TiO_2 multiple layer stratified thin films fabricated via APCVD by Sotelo-Vazquez et al. gave FQE (SA) close to 2.5×10^{-3} molecules per photon attributed to the combined effects of high charge carrier photogeneration and mobility, and also low carrier recombination between doped and undoped regions of the stratified films.[136] However, not all the non-metal dopants can improve photodegradation of SA on TiO_2, e.g. phosphorus doped TiO_2 (P-TiO_2) synthesized by APCVD containing both P^{5+} and P^{3-} reported by Sotelo-Vazquez et al. demonstrated higher electrical conductivity relating to P^{5+} species but lower photocatalytic

activity due to the fast recombination of photogenerated charges attributed to P^{3-} species doped in TiO_2.[137]

Enhancing charge carrier separation is an effective way to improve photocatalytic activity of thin films. Noimark et al. functionalised titania nanoparticles with gold providing two times greater activity than plain titania thin films.[138] Layered anatse-rutile titania thin films with defect free contact between two phases, was successfully synthesized via APCVD by Quesada-Cabrera et al. promoting electron transport from the rutile phase to the anatase phase and hence enhancing the photocatalytic activity (FQE (SA) about 1.2×10^{-3} molecules per photon).[139] The photogradation of SA involves two photoreactions: (1) the intermediate hydroxyl (OH) radicals which are generated by photo-oxidising H_2O, and (2) the hydroperoxy (HO_2 ·) radicals which is generated by photo-reducing O_2.[133] Photocatalytic degradation of organic pollutants can proceed indefinitely when both of these radicals are able to participate in degradation reactions.[140] The VB maximum potential of tungsten oxide is sufficiently positive (vs. NHE) to photo-oxidise H_2O to ·OH, but the CB minimum potential is insufficiently negative (vs. NHE) to photo-reduce O_2 to HO_2 ; as a result that bulk tungsten oxide is inactive for photodegradation of SA.[133,141] Consequently, a TiO_2/WO_{3-x} (x=0 to 0.3) heterojunction thin film, which was synthesized via CVD with sequential steps by Quesada-Cabrera et al., demonstrated enhanced photocatalytic activity in SA test compared to those single layer titania or substoichiometric tungsten oxide respectively, due to enhanced charge separation by the heterojunction by transporting electrons from the higher energy CB of titania and holes from the lower energy VB of the tungsten oxide to higher energy VB of titania.[142]

1.4 Thin Film Characterisation Techniques

1.4.1 X-ray Diffraction

XRD is an analytical technique normally non-destructive used to determine the atomic and molecular structure of a crystal, chemical composition and physical properties by observing the intensity and the angles of characteristic X-ray beam scattering from crystalline material.[143]

Bragg's proposed the simple expression:

$$n\lambda = 2d_{hkl}sin\theta \quad (1.8)$$

where λ is the wavelength, n is the order of reflection, d_{hkl} is the lattice plane spacing and θ is the angle of incidence/reflection to the planes envisaging that crystals comprise of layers of atoms which strongly reflect incident X-ray with the path differences between those reflections being equal to an integer number of wavelengths.[143] Actually, it is the electrons in the atoms that scatter the X-rays.[143]

1.4.2 X-ray Photoelectron Spectroscopy

XPS is a surface chemical analysis technique that is used to do quantitative and qualitative analysis of the surface of materials, and the chemical and electronic states of the elements in materials. The mechanism of XPS is that the X-ray is directed onto the surface of the samples (≤10 nm) ejecting core electrons from each element with the kinetic energy and number of photoelectrons with that energy recorded in the XPS spectrum. The binding energy of the peak is unique for each element when the chemical and electronic state is constant.[144] The binding energy E_B can be obtained from the expression

$$E_B = h\upsilon - E_k - W \quad (1.9)$$

where $h\upsilon$ is the energy of photon, E_k is the kinetic energy of electron and W is the spectrometer work function.[144]

1.4.3 Ultraviolet-Visible Spectroscopy

UV-Vis spectroscopy is applied in analytical chemistry for the quantitative analysis of different analytes, such as transition metal ions, highly conjugated organic compounds, and biological macromolecules. Spectroscopic analysis is commonly carried out in solutions but solids and

gases may also be studied.[145] The π-electrons or non-bonding electrons of molecules can absorb the energy in the range of ultraviolet and/or visible light exciting those electrons to higher energy orbitals, hence the absorption spectrum of semiconductors obtained from UV-Vis spectroscopy can be used to determine the bandgap or optical gap. The Tauc plot, $(\alpha h\nu)^n$ vs $h\nu$ where α is absorption coefficient and n=1/2 for a direct band gap, n=2 for indirect bandgap, is constructed to estimate the band gap of a semiconductor.[146]

1.4.4 Scanning Electron Microscopy

SEM is an electron microscope that records images of surface topography of materials by non-contacted scanning of the surface of samples with a focused beam of electrons. In a typical SEM an electron beam, which is produced by thermionic or field emission methods, is focused by one or two electromagnetic lens in order to interact with the sample in a high vacuum environment. The signals produced by SEM include secondary electrons (SE), back-scattered electrons (BSE), characteristic X-rays and light (cathodoluminescence) (CL). The most common image of SEM is formed by the collecting secondary electrons inelastic scattering from interaction between the electron beam and the suface of the constituent atoms.[147]

1.4.5 Transmission Electron Microscopy

TEM is also an electron microscope technique, however compared to SEM the image is formed from electrons transmitted through an ultra-thin specimen rather than being scattered from its surface.[148] The contrast of TEM images is formed when transmitting through an ultra-thin sample, the flux of electron lose a part of intensity proportional to the thickness of sample and the atomic number of the elements in the sample.[148] If the objective aperture filters out the scattered electrons thicker samples or those with higher atomic number appear darker colour. Due to its high resolution the crystal lattice in a sample is able to be examined in order to identify the crystal structures by matching with database references.[148]

1.4.6 Energy Dispersive X-ray spectroscopy

EDX, which is usually built in to a SEM or TEM, is used to analyse elemental composition of a sample. The mechanism is to collect the signals of the characteristic X-rays ejected from the elements present in the sample produced by interaction between the electron beam and constituted atoms. This causes the inner shell electrons (lower energy) to be excited and ejected from of the sample, creating electron holes which are filled by the outer shell electrons (higher energy) resulting in release of an unique X-ray spectrum, which can be used to determine the elemental composition of sample.[149]

1.4.7 Fourier Transform Infrared Spectroscopy

IR spectroscopy is used to determine the infrared spectrum of a sample in order to obtain their structure from the characteristic absorbed frequencies corresponding to the transition energy of bonds.[150]

FT-IR irradiates the sample by a beam with many frequencies of light at once to obtain the IR absorption spectrum of sample at each wavelength.[150] The advantages of Fourier translation (FT) spectrometer include Fellegtt's advantage, which is the fact that all the information from all wavelengths can be collected simultaneously resulting in a higher ratio of signal to noise for a given scan time or a shorter scan time for a given resolution, and Jacquinot's advantage, which is the fact that the amount of light passing through samples only depends on the diameter of the collimated beam from the source rather than both the entrance and slit of the monochromator.[150]

1.5 Motivation, Aim and Purpose

First of all the synthesis of nanostructured tungsten oxide thin films *via* different techniques in both liquid phase and solid phase and their mechanism have been reviewed. Compared to liquid

phase, the vapour phase process including physical vapour deposition (PVD) and chemical vapour deposition (CVD) is proved to be better in case of purity (without introducing organic agents such as stabilisers, dendrimer templates and reducing agents during synthesis process) and continuous processes (no batch form process required).[62,151] The PVD method shows limitations of low deposition rate, incapable for complex shape components and large area deposition, relatively high-cost compared to CVD method.[62] Consequently, nowadays CVD is still a versatile deposition technique for metallic, metal oxide, ceramic or perovskite thin films with well-controlled morphologies, size and stoichiometry, and with the advancement of CVD variants such as aerosol-assisted CVD (AACVD) which is a variant of the conventional chemical vapour deposition (CVD) process, is crucial because it utilises solvent aerosols to transport precursors and hence can be used with many relatively cheap commercially available metal precursors not suitable for traditional CVD (only required the precursor soluble in sovlent). However, the vapour-solid growth mechanism of 1D structure (e.g. tungsten oxide nanorods (NRs)) prepared by CVD is still not fully understood, and characterising the deposition conditions resulting in formation of tungsten oxide NR is not clear.

Consequently, my thesis will start with depositing tungsten oxide thin films under various conditions (temperature, solvent, and precursor) on different substrates via AACVD in order to identify optimal deposition parameters for growth of tungsten oxide NR array thin films. Subsequently the relationship between deposition parameters (substrate temperature and precursor concentration) and morphologies of tungsten oxide thin films will be present in order to find ideal conditions to deposit different nanostructure of tungsten oxide thin films. Afterwards, the effect of the growth of tungsten oxide NR arrays on their band structure of WO_3 is studied in order to investigate the 1D quantum-confinement effects and defect chemistry of 1D tungsten oxide NR arrays.

As reviewed previously Au, Pt or Cu nanoparticles supported on WO_3 NNs have been synthesized via AACVD with demonstrated improved performance for applications in gas sensors. In my thesis noble metal (Au, Pt, Pd and Ru) NPs supported on WO_3 NRs thin films

were fabricated by AACVD, and the relationship of deposition parameters to NP size and concentration studied. Those as-synthesized metal nanoparticle functionalized WO_3 NRs thin film were tested for activities in photocatalysis in order to reveal if the activities depend on the NP size and concentration to find out the optimal size for best activities and to study the mechanism of photocatalysis enhancement. Subsequently, metal oxide (PdO, RuO_x, CuO_x and CoO_x)/WO_3 heterostructure thin films fabricated by AACVD will be presented along with their activity for photocatalysis to investigate where heterojunction formation can help enhance their activity.

In summary, the first part of this thesis focuses on tungsten oxide thin films prepared by AACVD and the relationship between deposition parameters and morphologies, and the relationship between morphologies and properties. Subsequently, I will present work on deposition of WO_3 based heterojunction thin films by AACVD, and their application in photocatalysis (SA test).

CHARPTER 2: NANOSTRUCTRED TUNGSTEN OXIDE: SYNTHESIS, CHARATERISATION, GROWTH MECHANISM AND APPLICATION

In this chapter the relation between deposition parameters and obtained morphologies of tungsten oxide thin films are investigated. Subsequently, the growth mechanism of nanostructured tungsten oxide is discussed.

2.1 Introduction

The synthesis of tungsten oxide thin films *via* AACVD using different temperature and solvents was reviewed in section 1.2, with the morphologies of the deposited tungsten oxide changing as the temperature and solvent were varied. However, the effects of some alternative solvents and use of different substrates on the growth is not fully investigated, and more importantly an understanding of why these parameters change the morphology has not been developed. Many growth mechanisms of 1D structured material have been investigated (see section 1.1), though the mechanism is still not fully understood, especially for AACVD.

Therefore, in this chapter, the depositions of tungsten oxide thin films are conducted on different substrates with different solvents and at different temperature, and as-synthesized thin films are characterised in order to elucidate the growth mechanism of tungsten oxide. Subsequently, the characterisation of the as-synthesized thin films will be discussed to find out which tungsten oxide phases are presented within the thin films, and with more than 9 different phases of substoichiometric tungsten oxide with similar XRD pattern the accurate phase identification is highly challenging. This is further complicated because the as-synthesized thin film possibly comprises of more than two substoichiometric phases. Hence, different techniques such as XRD, XPS, EDX, TEM, and etc. are used to combine different information from those techniques to elucidate the phases present.

2.2 Synthesis of Nanorod structured Tungsten Oxide Thin Films via AACVD

2.2.1 Introduction

To obtain NR structured tungsten oxide thin films, deposition on different substrates (alumina, micro slide glass, SiO_2 coated barrier glass and quartz) with various solvents (acetone, methanol, toluene and mixture solvent of acetone, methanol and/or toluene in varying ratios) and at different temperatures ranging from 350 to 500 ℃ was conducted.

2.2.2 Experimental

Film deposition conditions are shown in Table 2.1 below. The precursor $W(OPh)_6$ was synthesised according to the literature[152] and the precursor $W(CO)_6$ was bought from Aldrich (99% purity), dissolved in solvent, and an aerosol created by an ultrasonic humidifier operated at 2 MHz (Liquifog). The aerosols were transported to the reactor by a N_2 carrier gas (99.99%, BOC, flow rate 300 cm^3/min) controlled by a mass flow controller (MFC, Brooks), and reacted on a substrate (e.g. SiO_2 coated barrier glass with 2 mm thickness, microscope glass with 1 mm thickness, alumina 0.5 mm thickness or quartz 1 mm thickness) (all the substrates were cleaned by acetone, 2-propanol and methanol before deposition) at elevated temperature to form the thin film (reaction 2.1). Annealing of samples was carried out in air at 500 ℃ for 2 hours. The annealed sample is denoted as [sample name]-ann e.g. AM375-ann.

$$W(CO)_6 + [O] \rightarrow WO_x + CO_2 \quad (2.1)$$

Table 2. 1 Deposition conditions of thin films.

Name	Precursor (g)	Solvent (mL)	Substrate	Deposition Temp.(°C)
A450g	$W(OPh)_6$ (0.075)	Acetone (15)	Glass	450
A450b	$W(OPh)_6$ (0.075)	Acetone (15)	B-glass	450
A450a	$W(OPh)_6$ (0.075)	Acetone (15)	Alumina	450
AT450b	$W(OPh)_6$ (0.075)	Acetone (10) and Toluene (5)	B-Glass	450
T450b	$W(OPh)_6$ (0.075)	Toluene (15)	B-Glass	450
A450b	$W(OPh)_6$ (0.075)	Acetone (15)	B-Glass	450
T300b	$W(OPh)_6$ (0.150)	Toluene (15)	B-glass	300
T325b	$W(OPh)_6$ (0.150)	Toluene (15)	B-glass	325
T350b	$W(OPh)_6$ (0.150)	Toluene (15)	B-glass	350
T375b	$W(OPh)_6$ (0.150)	Toluene (15)	B-glass	375
T400b	$W(OPh)_6$ (0.075)	Toluene (15)	B-glass	400
T425b	$W(OPh)_6$ (0.075)	Toluene (15)	B-glass	425
T450b	$W(OPh)_6$ (0.075)	Toluene (15)	B-glass	450
T500b	$W(OPh)_6$ (0.075)	Toluene (15)	B-glass	500
T375q	$W(CO)_6$ (0.06)	Toluene (15)	Quartz	375
A375q	$W(CO)_6$ (0.06)	Acetone (15)	Quartz	375
M375q	$W(CO)_6$ (0.06)	Methanol (15)	Quartz	375
AM375q	$W(CO)_6$ (0.06)	Acetone (10) and Methanol (5)	Quartz	375
AT375q	$W(CO)_6$ (0.06)	Acetone (10) and Toluene (5)	Quartz	375
MT375q	$W(CO)_6$ (0.06)	Methanol (10) and Toluene (5)	Quartz	375
AM350q	$W(CO)_6$ (0.06)	Acetone (10) and Methanol (5)	Quartz	350
AM400q	$W(CO)_6$ (0.06)	Acetone (10) and Methanol (5)	Quartz	400

The design of the AACVD reactor used is demonstrated in Figure 2.1. A water jacket is equipped at the inlet of the cold wall reactor of the AACVD system in order to avoid precursor

heating and decomposition prior to entering the reactor chamber.[153] The exhaust was directly vented into the extraction system of the fume cupboard.[153]

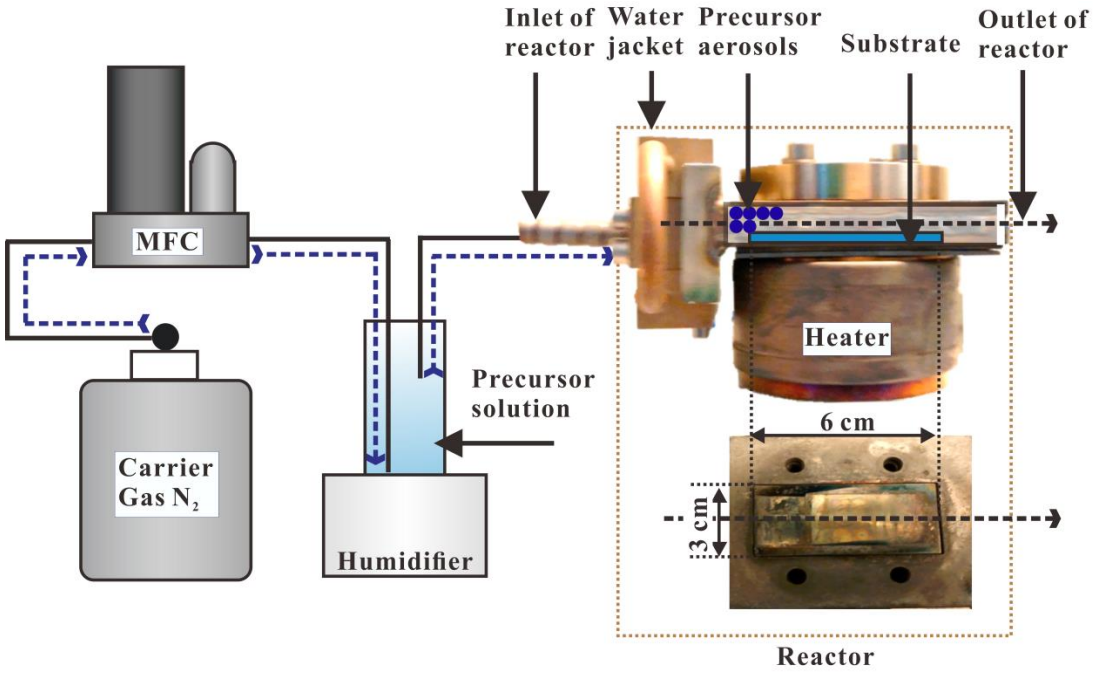

Figure 2.1. Schematic flow diagram of the AACVD reactor.[153]

The crystalline structures of samples were determined by X-Ray diffraction (XRD) (Bruker, AXD D8-Discover) equipped with a LinxEye silicon strip detector using Cu Kα radiation operated at 40 kV and 40 mA. The microstructure of the films was examined by Field-Emission Scanning Electron Microscope (FE-SEM) (Jeol 6310F, 5 keV). Samples were coated with gold and scanned at 5 kV. The X-ray photoelectron (XPS) analysis was carried on a Thermo Scientific K-Alpha instrument equipped with a monochromatic Al Kα radiation (1486.6 eV) with charge compensation by a beam charge neutralization argon-ion gun (≤10 eV), and calibrated by the C 1s peak at 284.8 eV. The W 4f region were recorded from the samples showing two peaks at 35.4 ($\pm$0.4) eV and 37.5 ($\pm$0.3) eV which were fitted by using software "CasaXPS" showing two components at 35.4 and 34.2 eV (binding energy) attributed to W $4f_{7/2}$ of W^{6+} and W^{4+} respectively. Transmission electron microscopy (TEM) and scanning TEM (STEM) analysis was performed on a JEOL 2100 at 300 KV equipped with energy dispersion X-ray (EDX) detector (X-MaxN 80, Oxford Instruments). UV/vis spectroscopy was performed

using a double monochromated PerkinElmer Lambda 950 UV/vis/NIR spectrophotometer with integrating sphere in the 250−2500 nm range recording the transmittance % and reflectance % of tungsten oxide NR arrays on quartz. The absorbance % is estimated by:

$$\text{Absorbance \%} = 100\% - (\text{Transmittance \%} + \text{Reflectance \%}) \quad (2.2)$$

The band gap of tungsten oxide NR arrays is estimated by Tauc plot with the following equation:

$$\alpha = A\,[(h\nu - E_g)^{\frac{n}{2}}/h\nu] \quad (2.3)$$

where $\alpha, A, E_g, \nu \; and \; n$ are the absorption coefficient, constant, band gap, incident light frequency and an integer respectively, whilst the value of integer n depends on the characteristics of the optical transition (n = 1 or 4 for direct or indirect band transition respectively).[154]

2.2.3 Results and Discussions

2.2.3.1 Deposition on Various Substrates

Glancing angle X-ray diffraction revealed only two peaks at 23.4 °and 47.8° 2θ from thin films deposited on various substrates, including glass (A450g), barrier glass (A450b) and alumina (A450a) (neglecting peaks of Al_2O_3) at 450 ℃ (details in Table 2.1), as shown in Figure 2.2, possibly attributed to the (020) and (040) reflections of monoclinic tungsten oxide (ICDD 20-1324) due to preferred orientation of as-synthesized thin films.[152] However, those two strong diffraction peaks also could be attributed to (010) and (020) reflections of substoichiometric tungsten oxide according to previous deposition by other techniques such as thermal evaporation (see section 1.2). The assignment of those two strong peaks to reflections of stoichiometric or substoichiometric tungsten oxide will be discussed later in section 2.4 and 2.5. Therefore, thin films deposited on glass, barrier glass or alumina did not show significant difference between XRD patterns.

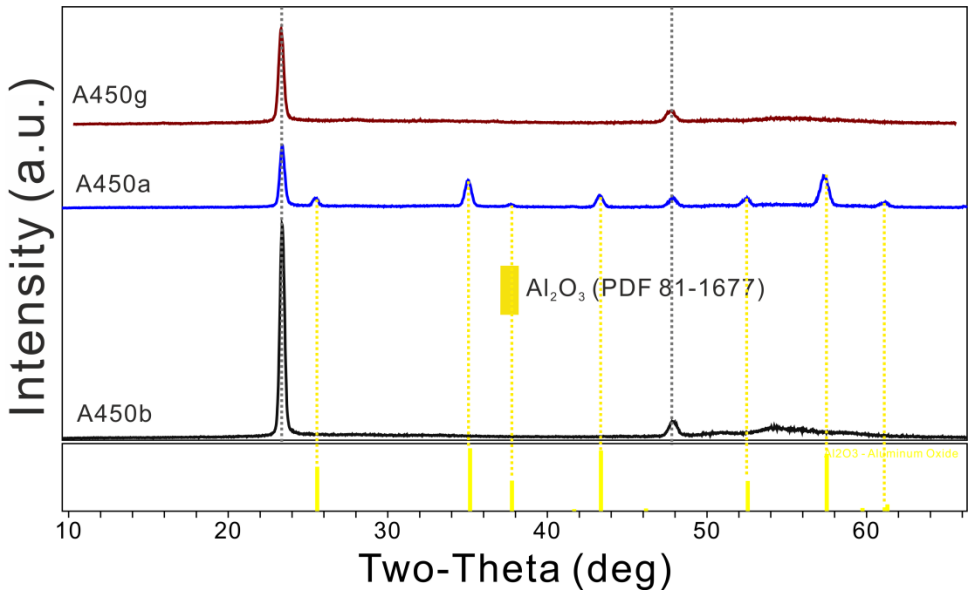

Figure 2.2. Glancing angle XRD pattern of as-synthesized thin films A450g A450b and A450a prepared by AACVD on glass, barrier glass and alumina substrates, yellow stick pattern Al_2O_3 (PDF 81-1667).

SEM was used to examine the morphology of the as-synthesized thin films. SEM (Figure 2.3) showed that nanostructured thin films deposited on barrier glass (A450b) were similar to those on alumina (A450a) under similar conditions, with hollow pipe-like structures and tiny particles grown on the wall of pipe. The diameter of these rods was close to 800 nm. However, the morphology of films deposited on plain glass (A450g) was distinct from those on barrier glass and alumina, featuring nano-needles with sharp end structures with diameters ranging from 16-135 nm, similar to NNs grown on Si substrates by AACVD at 500 °C reported previously.[155]

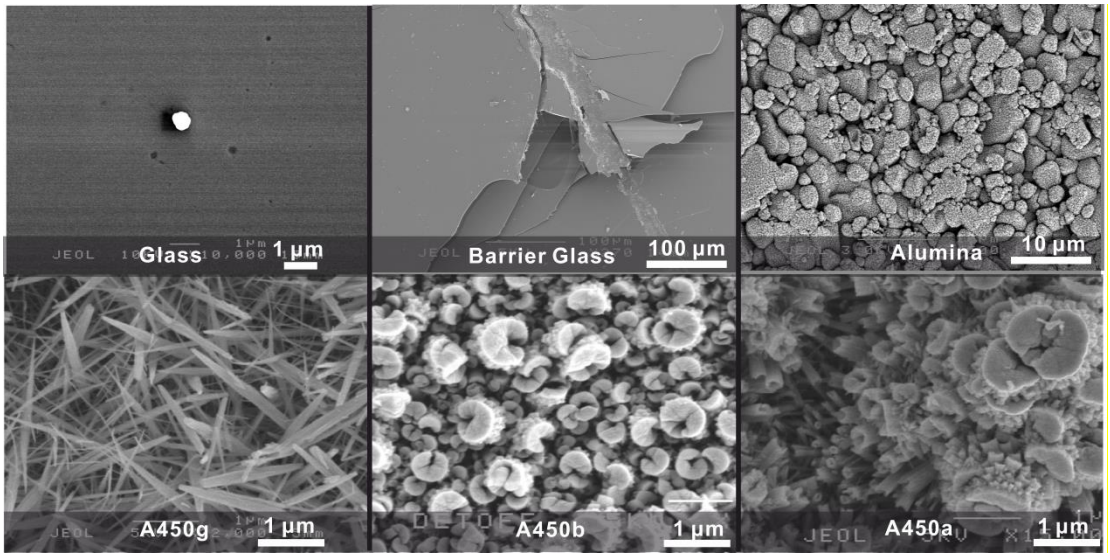

Figure 2.3. SEM of substrates (glass, Barrier glass and alumina) and films deposited from $W(OPh)_6$ and Acetone at 450 ℃ on those substrates.

From XRD patterns, the thin films deposited on various substrates presented similar crystal structure, though NNs could only be found by SEM in thin films deposited on glass at 450 ℃ with acetone (A450g).

After annealing 2 hours at 500 ℃ in air, there were more peaks present in XRD pattern as seen in Figure 2.4. The XRD patterns of annealed as-synthesized thin films on barrier glass or alumina matched monoclinic WO_3 (PDF 72-0677). The pattern for thin films on barrier glass (A450b-ann) had strong (002) and (020) peaks and relative weak (200) peak showing preferred orientation along the (002) and (020) directions, but the pattern for thin films on alumina (A450a-ann) had one strong peak (002) and two relatively weak peaks (020) and (200) showing preferred orientation in the (002) direction. However, after annealing films deposited on plain glass (A450g) a totally different pattern was observed, which matched a reference pattern of sodium tungsten oxide $Na_2W_4O_{13}$ (PDF 70-2022) rather than any phases of pure WO_3. This is probably due to migration of sodium ions from the glass substrate while annealing in air at high temperature, entering into the unit cell of WO_3.

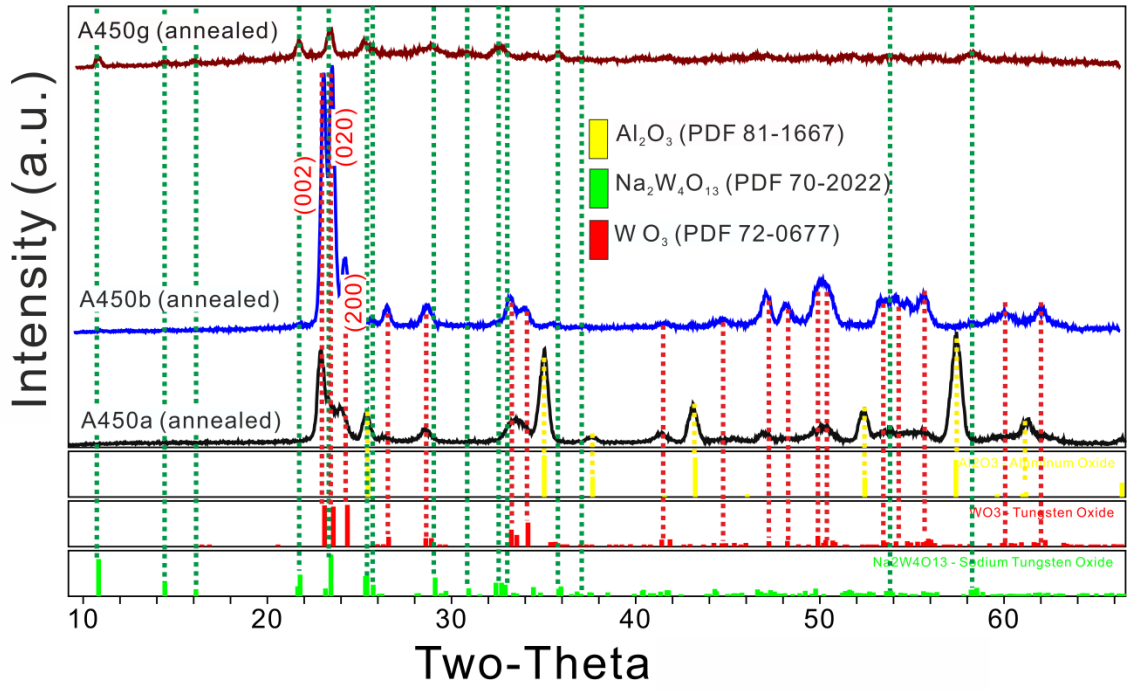

Figure 2.4. Glancing angle XRD pattern of WO_3 films deposited from $W(OPh)_6$ and Acetone at 450 ℃ on glass, Barrier glass and alumina annealed at 500 ℃ in air for 2 hours, red stick pattern monoclinic WO_3 (PDF 72-0677), yellow stick pattern Al_2O_3 (PDF 81-1667) and green stick pattern $Na_2W_4O_{13}$ (PDF 70-2022).

The microstructure of as-synthesized thin films deposited on glass (A450g-ann), barrier glass (A450b-ann) and alumina (A450a-ann) after annealing at 500 ℃ for 2 hours in air varied from those pre-annealing, as shown in Figure 2.5. For A450g-ann, the NNs fused to form bigger rod-like structures with diameters around 300 nm, and the sharp end disappears. For A450b-ann, the hollow in the pipe-like structures became bigger. But the wall of pipes became thinner, resulting in a diameter decrease to 400 nm from around 800 nm. For A450a-ann the walls of the pipe-like structures decomposed to form short branched structures, and the diameter had not significantly changed.

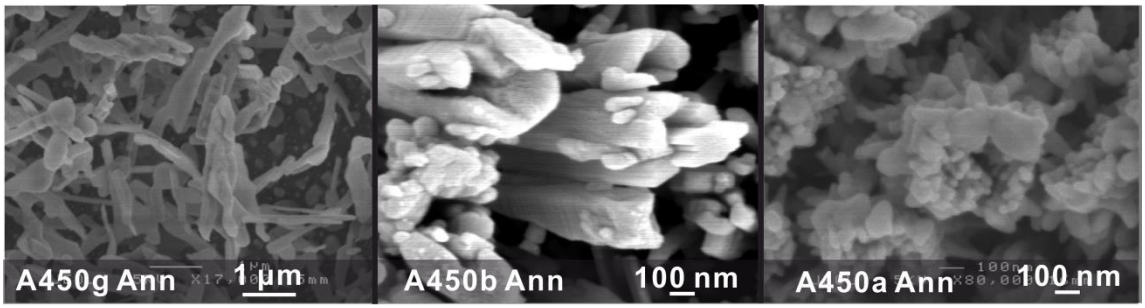

Figure 2.5. SEM of films deposited from $W(OPh)_6$ and Acetone at 450 ℃ on glass, Barrier glass and alumina and annealing at 500 ℃ for 2 hours in air.

Therefore, as-synthesized thin films deposited on different substrates (with the same other conditions) present various morphologies. Before annealing, A450g, A450b and A450a show similar XRD pattern, but present varying morphologies from NNs to hollow pipe-like structures. After annealing, XRD patterns of A450g-ann and A450b-ann match the m-WO_3 though with different orientation and A450a-ann match sodium tungsten oxide $Na_2W_4O_{13}$ due to sodium ion immigrating from glass substrate. Therefore, the substrate is able to affect the morphologies and crystal structure of deposited thin films attributed to ion diffusing and also possibly properties of substrate and its surface (e.g. roughness, surface energy, heat or electron conductivity, terminated elements). Moreover, according to previous reports of the solid-phase growth model, irregular points on the substrate can lead to nucleation of nanowires.[84] However, A450b and A450a with barrier glass and alumina substrate respectively show similar morphology, and hence the different substrate has not resulted in a different morphology, but we note that if pure tungsten oxide thin film is the desired product, the plain glass substrate should not be used. In

the following section the effect of solvents and temperature on morphology of tungsten oxide will be studied.

2.2.3.2 Deposition with Various Solvents

The solvents used for deposition were varied, including mixtures of solvents, in order to target formation of NR structure on barrier glass (deposition on plain glass suffers from sodium ion migration, and alumina substrates are opaque and not suitable for optical and photocatalytic applications).

Glancing angle XRD patterns of as-synthesized thin films prepared using acetone (A450b), a mixture solvent of acetone and toluene (2:1) (AT450b), or toluene (T450b) all show two peaks at 23.4 ° and 47.8° 2θ, hence indicating a similar crystal structure (Figure 2.6), also similar to those deposited on alumina and glass substrates (A450a and A450g) (Figure 2.2).

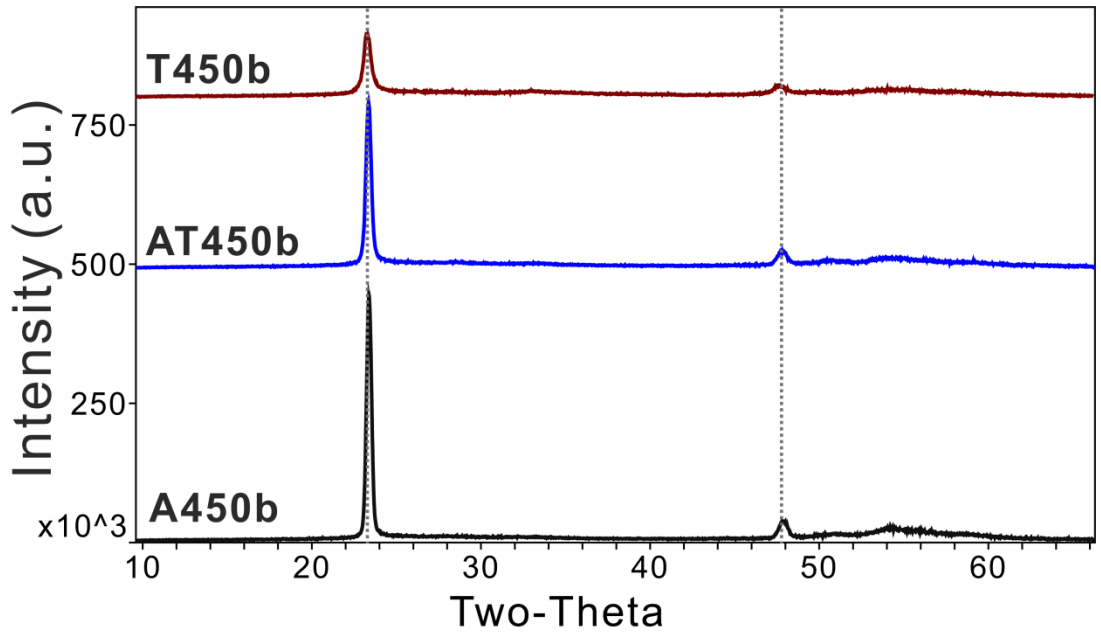

Figure 2.6. Glancing angle XRD pattern of as-synthesized films prepared by AACVD using solvent acetone (A450b), a mixture solvent of acetone and toluene (2:1) (AT450b), or toluene at 450 ℃ (T450b).

SEM image (Figure 2.7) was used to characterise the morphology of the as-synthesized thin films with the nanostructures obtained using acetone (A450b) alone having been discussed in the previous section (2.2.3.1). When toluene is added in the ratio of acetone: toluene = 2: 1, the

nano-structure had a high density of rod-like structures without hollows, with diameter in range from 50 to 100 nm, similar to previous research on deposition from WCl_6 and ethanol at 625 ℃ by APCVD.[156] When using pure toluene, narrow NNs with diameter below 20 nm were observed. Although, samples (A450a, A450b, A450g, AT450b and T450b) present the similar XRD patterns, the morphologies of those thin films vary. A possible mechanism will be discussed later.

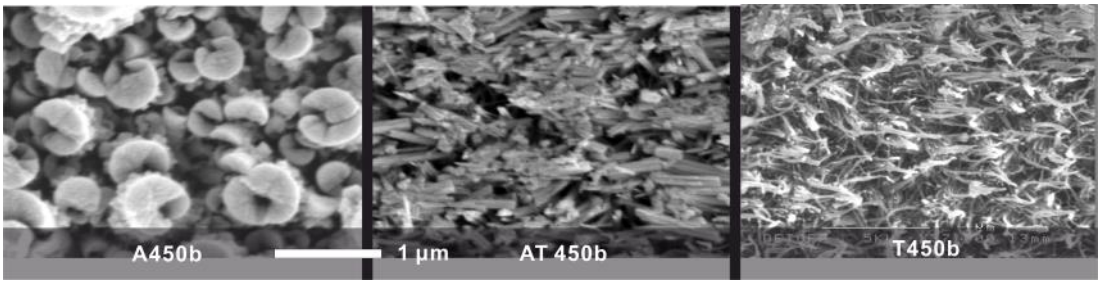

Figure 2.7. SEM of films deposited from $W(OPh)_6$ at 450 ℃ using solvent acetone (A450b), a mixture solvent of acetone and toluene (2:1) (AT450b), or toluene (T450b) on barrier glass.

After annealing for 2 hour at 500 ℃ in air, the XRD pattern of the as-synthesized thin films were similar irrespective of the initial solvent (Figure 2.8), with all patterns showing more peaks than the two strong peaks at 23.4° and 47.8° 2θ seen in the pre-annealed thin films, matching the monoclinic phase of WO_3 (PDF 72-0677), similar to the XRD pattern of A450a. The diffraction peaks of A450b-ann showed high intensity when pure acetone had been used as the solvent. However, when the solvent mixture of acetone and toluene was used (AT450b-ann) the strength of diffraction peaks decreased. These annealed thin films had very weak diffraction peaks (T450b-ann), after pure toluene was used.

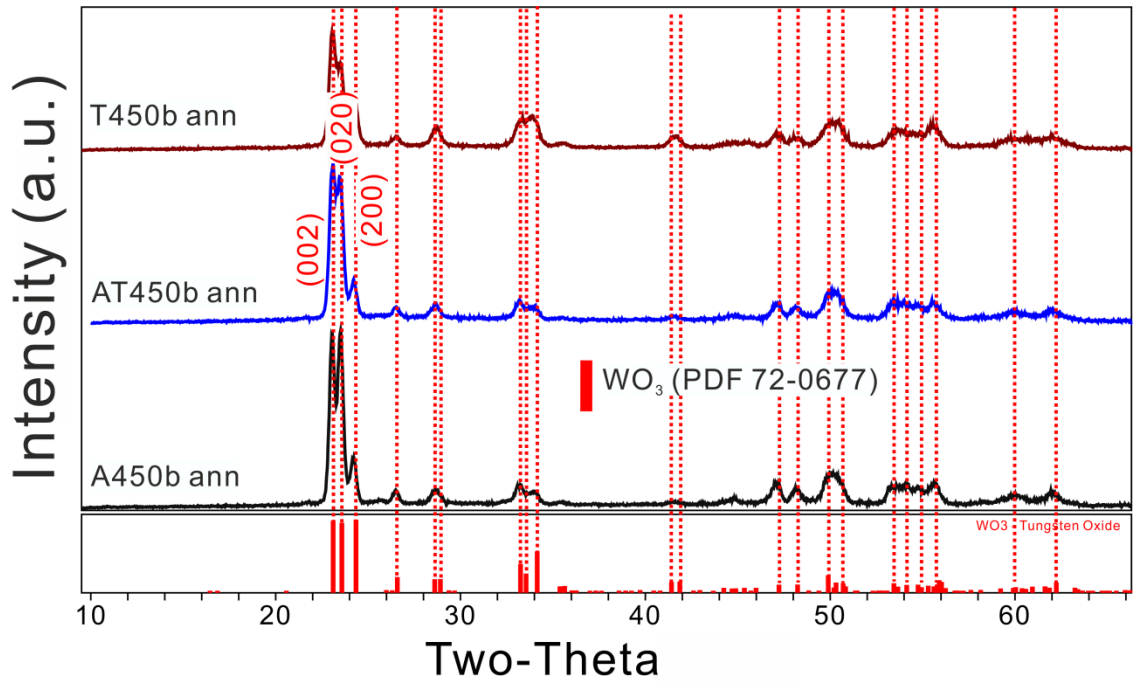

Figure 2.8. Glancing angle XRD pattern of as-synthesized films prepared by AACVD using solvent Acetone (A450b-ann), a mixture solvent of Acetone and toluene (2:1) (AT450b-ann) and Toluene (T450b-ann) at 450 ℃, and annealing for 2 hours at 500 ℃ in air, red stick pattern monoclinic WO3 (PDF card no.72-0677).

The morphologies of the annealed films had slightly changed from the as-deposited films are shown in Figure 2.9. The rod-like structure observed in a film prepared using a mixture solvent (acetone: toluene=2:1) became shorter and thicker. The structure of a film deposited from pure toluene showed no significant change after annealing.

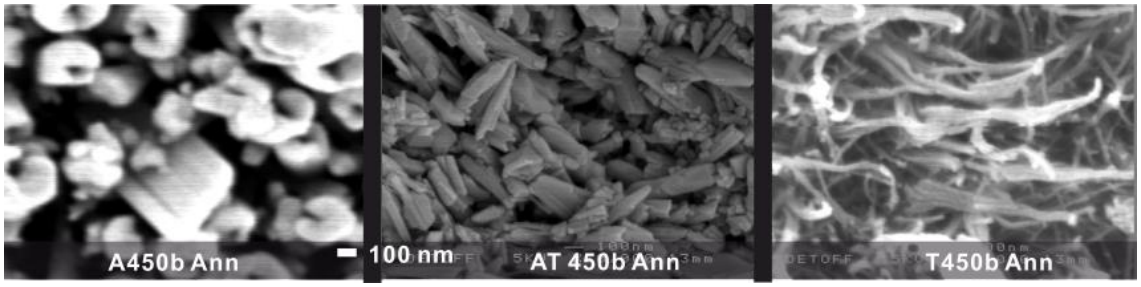

Figure 2.9. SEM of films deposited from $W(OPh)_6$ at 450 ℃ using solvent acetone (A450b-ann), a mixture solvent of acetone and toluene (2:1) (AT450b-ann), or toluene (T450b-ann) on barrier glass, and annealing for 2 hours at 500 ℃ in air.

In summary, as-synthesized thin films possessed a NN-like structure when a solvent mixture of acetone and toluene (2:1) or pure toluene was used, though adding toluene seemed to reduce

the crystallinity of the thin film. Therefore, the solvent used for deposition of tungsten oxide thin films by AACVD affects the morphology of thin film growth.[89]

Based on previous literatures and observation made in this thesis, the solvent used for AACVD deposition affects the thin film formation *via* three main paths: (1) the solubility of different precursors in various solvents varies (e.g. $W(CO)_6$ with high solubility in acetone and low in methanol) resulting in different concentration of precursor in solution and generated aerosols; (2) the diameter of generated aerosols delivered into AACVD reactor depends on the type of solvent due to surface tension, viscosity and density; (3) in certain cases, the solvent could participate in reactions for thin film formation, though those reactions are complex to characterise due to a lack of detection techniques and the participation of deposited material acting as a catalyst. For example, acetone contains oxygen which could be donated at elevated temperature, whereas toluene cannot provide oxygen, and hence the deposited thin film (T450b) may have relatively low crystallinity due to a lack of a sufficiently oxidising environment.

2.2.3.3 Deposition at Various Temperatures

In the previous section, the as-synthesized thin films possessed a NN structure when toluene was used as a solvent and a deposition temperature of 450 ℃. Herein the deposition temperature was changed from 300 to 500 ℃ to identify conditions giving a NR structure.

Glancing angle XRD patterns of as-synthesized thin films deposited at various temperatures vary as shown in Figure 2.10. At a deposition temperature 300 ℃, diffraction peaks of T300b match the reference pattern of tetragonal WO_3 (PDF 85-0808). When the deposition temperature increases from 325 to 400 ℃, the diffraction peak of T300b at 22.6 °(2θ) shifts to 23.1 ° (T325b, T350b, T375b and T400b) matching the (002) facet of monoclinic WO_3 (PDF 72-0677), and the intensity of peak at 24.0 °(matching tetragonal WO_3 reference) reduces to zero. At deposition temperatures above 425 ℃, there is only a peak appearing at 23.5 °in 2θ range of 22 to 25 ° matching the (020) facet of monoclinic WO_3 (PDF 72-0677). Those XRD patterns suggest that T300b presents in tetragonal phase, and when the deposition temperature increases

the monoclinic phase appears and tetragonal phase gradually vanish, with the preferred orientation of the monoclinic phase changing from (002) to (020).

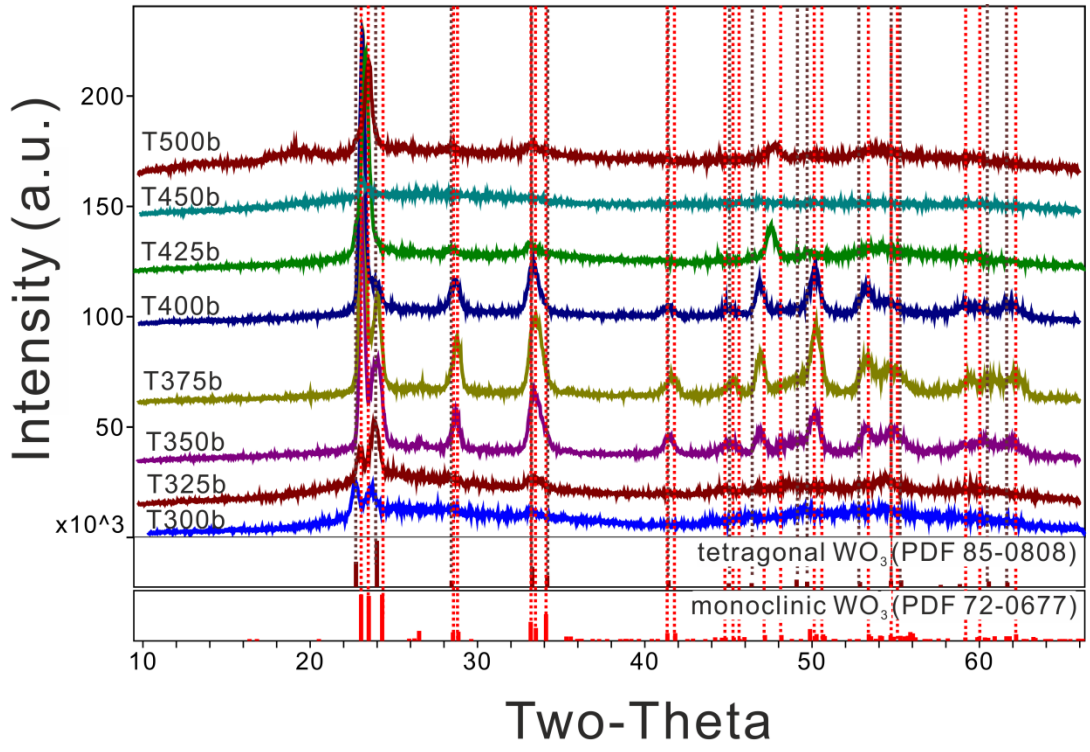

Figure 2.10. Glancing angle XRD pattern of as-synthesized films prepared from toluene by AACVD from 300 to 500 ℃ with red stick reference pattern monoclinic WO_3 (PDF card no.72-0677) and brown stick tetragonal WO_3 (PDF card no.85-0808).

SEM was used to measure the nano-structure of the as-synthesized thin films as shown in Figure 2.11. With deposition temperature between 300 and 325 ℃, particles agglomerate to form islands with quasi-square shape and diameter 10 μm with wide gaps between each island at 350 ℃. Also, size of the islands became smaller and connected by wire-like structures. At 375 ℃, the island structure disappears and wire-like structures interweaving each other were observed. Increasing the deposition temperature to 400 and 425 ℃ caused NR structures to be observed with diameter 100 – 150 nm. When the deposition temperature increased to 450 ℃ NN were observed instead of rod-like structures and at 500 ℃ NN mat-like morphologies were observed.

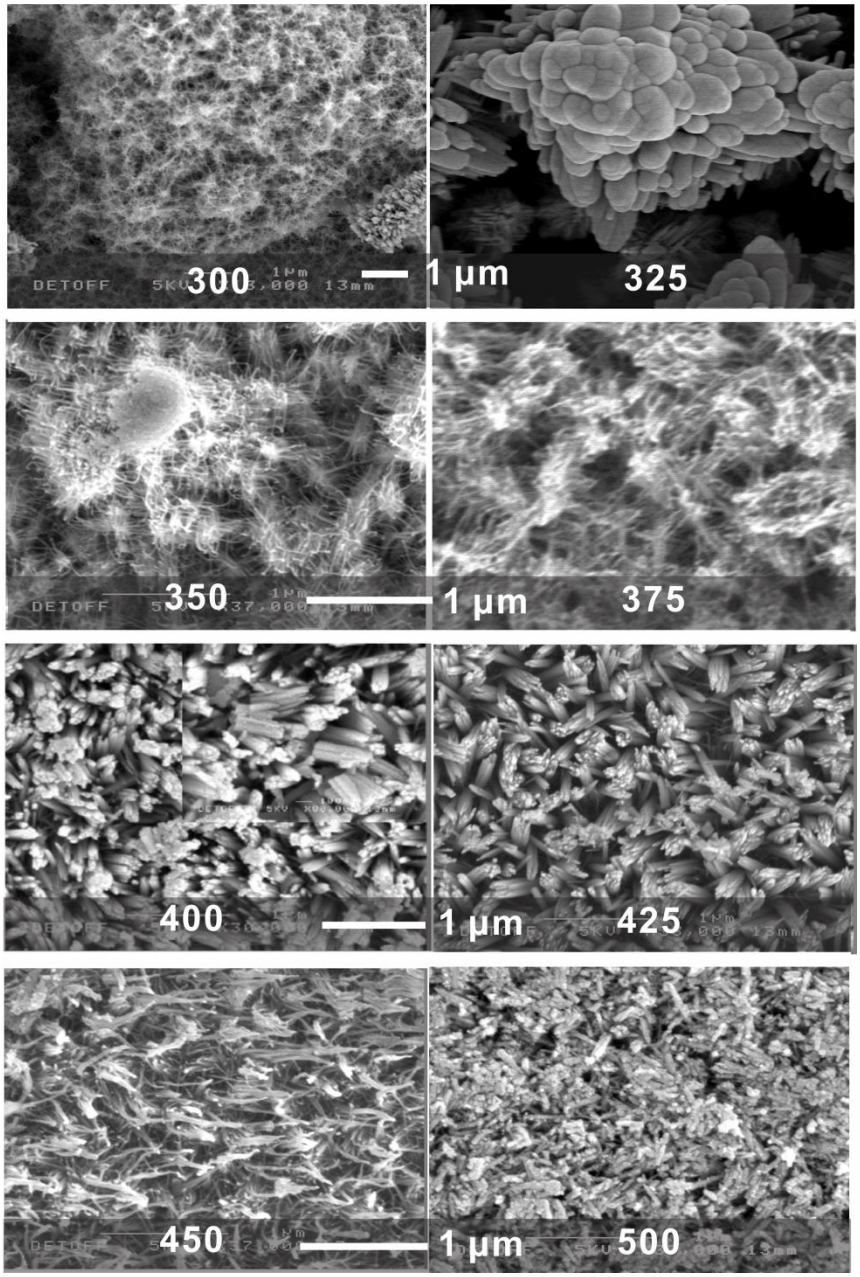

Figure 2.11. SEM of as-synthesized thin films deposited from $W(OPh)_6$ and toluene at 300-500 ℃.

After annealing samples for 2 hours in air, more peaks were present in the diffraction pattern as seen in Figure 2.12. After annealing, XRD patterns of films deposited above 375 ℃ matched the reference pattern of the monoclinic form of WO_3 (PDF 72-0677) however when the deposition temperature as below 375 ℃ the peaks of the annealed films shifted to lower 2θ matching the orthorhombic form of WO_3 (PDF 71-0131). According to previous reports, the orthorhombic form of WO_3 is stable from 330 to 740 ℃ (See section 1.1.1) with the monoclinic

form being stable at room temperature.[3] The reason why the orthorhombic phase is stabilised at room temperature after annealing at 500 ℃ for samples deposited below 375 ℃ is not clear.

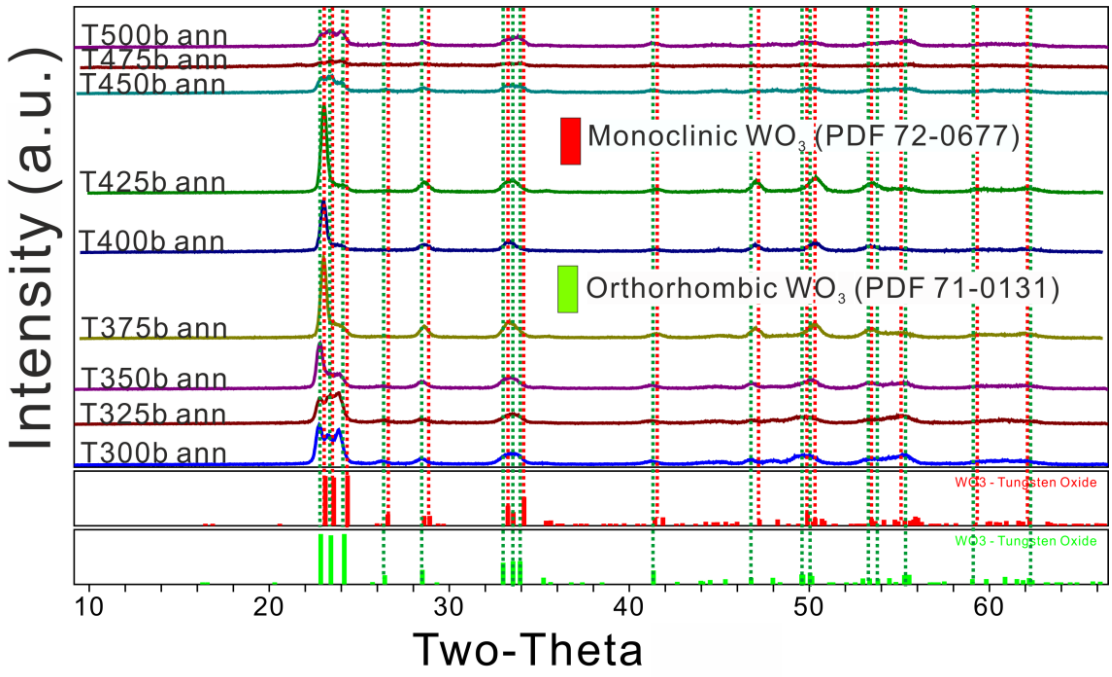

Figure 2.12. Glancing angle XRD pattern of the as-synthesized thin films prepared from toluene by AACVD at 300-500 ℃ and annealing at 500 ℃ for 2 hours in air, red reference pattern of monoclinic WO_3 (PDF 72-0677) and green reference pattern of orthorhombic WO_3 (PDF 71-0131).

After annealing at 500 ℃ for 2 hours in air, the morphologies of films deposited at temperature up to 375 ℃ was significantly altered, specifically, the wire-like structure appeared to 'melt' during the annealing process as shown in figure 2.13. For deposition temperatures between 400 and 425 ℃ the surface of the NR became smoother after annealing, and when the deposition temperature was above 450 ℃, the morphologies underwent no significant change.

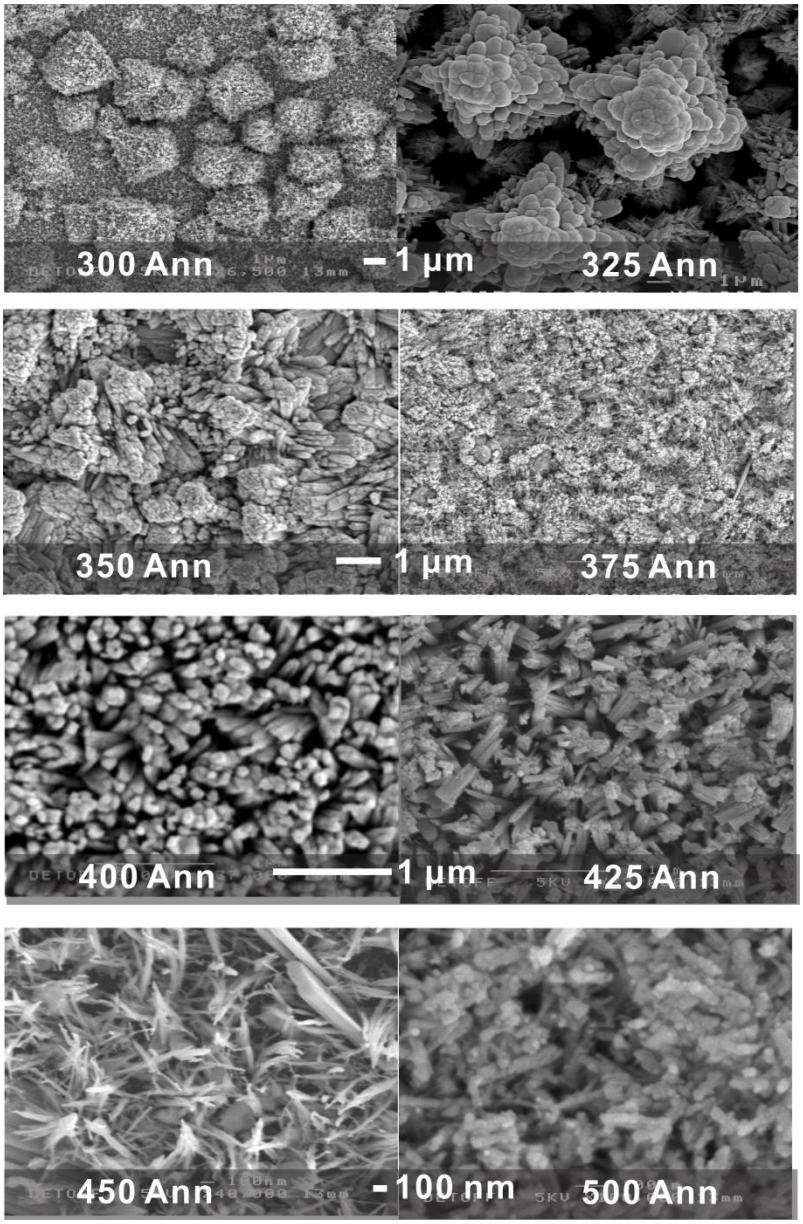

Figure 2.13. SEM of as-synthesized thin films deposited from $W(OPh)_6$ and toluene at 300-500 ℃ and annealing at 500 ℃ for 2 hours in air.

In summary, thin films fabricated with $W(OPh)_6$ dissolved in toluene at the deposition temperature ≥ 375 ℃ produced NN (with sharp point at the top end) or NR (with long straight sides and flat circular end) structure. After annealing at 500 ℃ in air for two hours, all the as-synthesized thin films demonstrated orthorhombic (deposited temperature < 375 ℃) or monoclinic (deposited temperature ≥ 375 ℃) phases of WO_3 based on the XRD patterns. However, after annealing, the NNs of thin films prepared at 375 ℃ and below agglomerated together. Therefore the deposition temperature influenced on the crystal structure and

morphology of the as-synthesized tungsten oxide thin films observed by XRD and SEM during AACVD likely *via* two main routes: (1) elevated temperature is needed to initiate decomposition of the precursor or/and the reaction between precursor and solvent; (2) the temperature also affects the adsorption, diffusion and nucleation of adatoms of decomposed precursor molecules, and growth rate along certain facets (details discussed in following section).

2.2.3.4 Deposition on Quartz with Optimal Deposition Conditions

Quartz has low absorption in the region from UV to NIR and hence is an ideal substrate for optical characterisation and photocatalytic tests. Therefore, deposition conditions for growth of NR structured tungsten oxide on quartz were studied.

In the previous section, NR structures can be found in thin films prepared from $W(OPh)_6$, which was synthesized based on reaction 2.4,[152] dissolved in toluene at 375 ℃ on barrier glass substrates.

$$W(O)Cl_4 + 6PhOH \rightarrow W(OPh)_6 + H_2O \quad (2.4)$$

Subsequently, the commercially available precursor $W(CO)_6$ was used to fabricate tungsten oxide thin films with toluene at 375 ℃ on quartz (T375q) *via* AACVD to compare with $W(OPh)_6$ (T375b.P). As shown in Figure 2.14, the sample T375q presents conjugated ball-like structure and the sample T375b.P gives a wire-like structure.

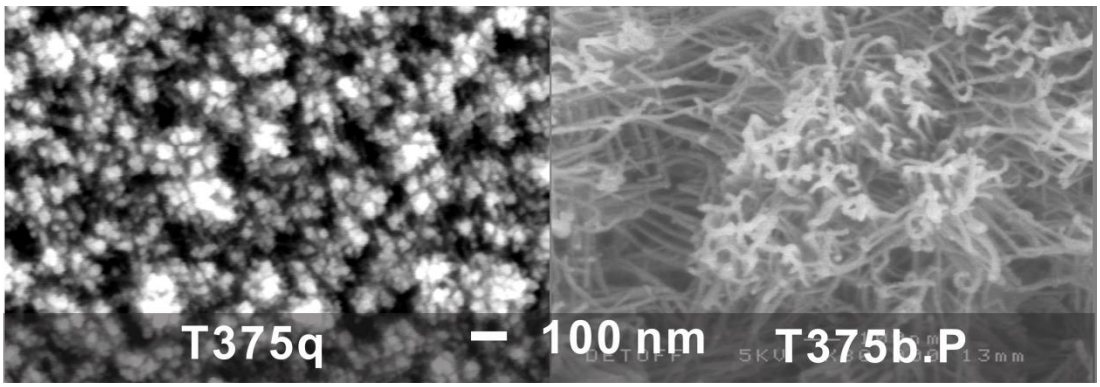

Figure 2.14. SEM of as-synthesized thin films deposited from $W(CO)_6$ on quartz (T375q) and $W(OPh)_6$ (T375b.P) with toluene at 375 °C.

Subsequently toluene was replaced by acetone, methanol, a mixture of acetone and methanol (2:1), a mixture of acetone and toluene (2:1), and a mixture of methanol and toluene (2:1) for depositions with $W(CO)_6$ at 375 ℃ on quartz. As shown in Figure 2.15, when using the solvent methanol, a mixture of acetone and toluene, or acetone and methanol, the NN or NR like structure is obtained at 375 ℃ in contrast to toluene alone. Specifically, the NN can be obtained with average diameter 50 nm using pure methanol as the solvent. If the methanol was mixed with acetone in a (1:2) ratio, the NR structure was obtained with increased diameter 130 nm. If acetone was mixed with toluene in a (1:2) ratio, the NN became thicker with average diameter 220 nm. However, $W(CO)_6$ is less soluble in pure methanol than in acetone and as a result a mixture of acetone and methanol was used to obtain 'thicker' (longer NR) films.

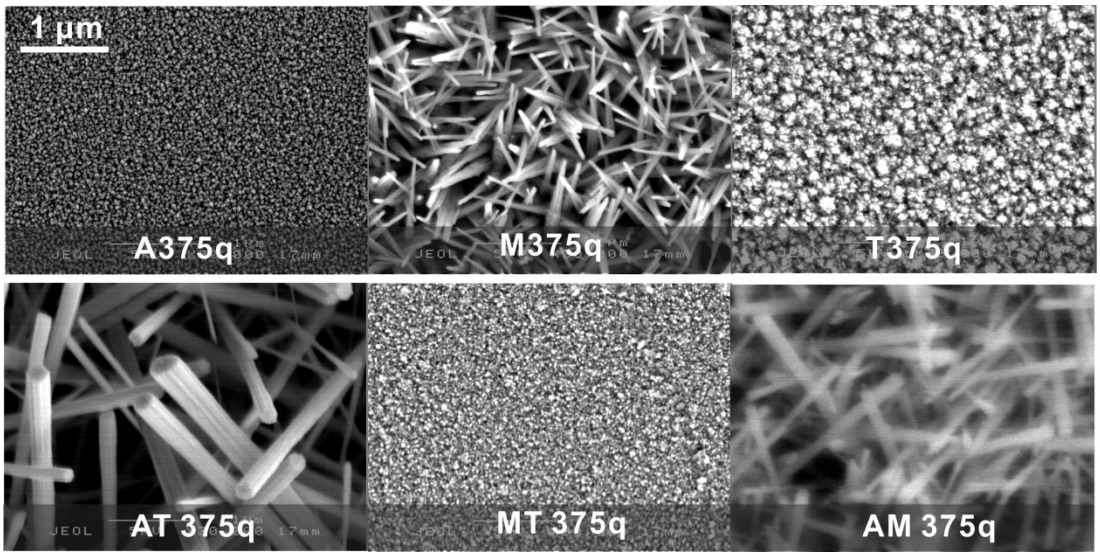

Figure 2.15. SEM of as-synthesized thin films deposited from $W(CO)_6$ on quartz at 375 ℃ with acetone (A375q), methanol (M375q), toluene (T375q), a mixture solvent of acetone and toluene (2:1) (AT375q), a mixture solvent of methanol and toluene (2:1) (MT375q) and a mixture solvent of acetone and methanol (2:1) (AM375q) (all the same magnification × 30,000).

2.2.3.5 Characterisation of Tungsten Oxide NR Arrays Thin Films Deposited on Quartz via AACVD

In the above section, conditions for obtaining NR structured tungsten oxide on quartz (AM375q) were identified. Subsequently, crystal structure, morphologies, composition, element state and

band structure of the as-synthesized thin films were characterised *via* SEM, TEM, XRD, EDX, XPS and UV-Vis.

The as-synthesized thin films were dark blue in colour, becoming yellow-white after annealing at 500 ℃ in air for 2 hour, as shown in Figure 2.16. SEM indicated the NR structure is maintained after annealing, but the NRs become thicker.

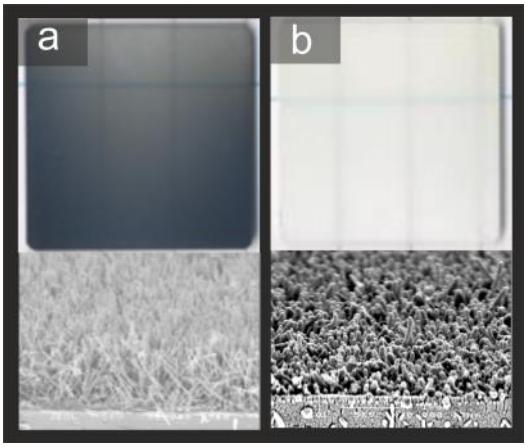

Figure 2.16. Images and SEM images of as-synthesized thin films prepared with $W(CO)_6$ with a mixture solvent of acetone and methanol (2:1) at 375 ℃ on quartz (a) AM375q and annealed at 500 ℃ in air for 2 hours (b) AM375q-ann.

In section 2.2.3, most thin films prepared with $W(OPh)_6$ presented two strong peaks in the XRD patterns(at 23.4 ° and 47.8 ° 2θ) before annealing at 500 ℃. Warren B. Cross et al. suggested that the preferred growth of tungsten oxide deposited by AACVD from $W(OPh)_6$ gave rise to two strong peaks in the XRD pattern attributed to (020) and (040) reflections of γ-WO_3 (monoclinic).[152] As shown in Figure 2.17, an as-synthesized thin film deposited from $W(CO)_6$ (AM375q) also presents two relatively strong peaks (at 23.5 and 48.0 °), but also several other diffraction peaks. To assign these, the as-synthesized thin film was assumed to be substoichiometric tungsten oxide (WO_x) due to the blue colour.[157] The common XRD references for WO_x are listed in Table 1.2, however the peaks corresponding to (100), (010) or (001) of all substoichiometric tungsten oxides appeared at 23.4 °(± 0.2 °) therefore making it difficult to match these peaks, especially considering preferred orientation and/or multiple phases. By comparing both strong peaks (23.4° and 47.8° 2θ) to reference patterns, the best matches were

provided by $W_{32}O_{84}$ (PDF 77-0810, a=21.43 Å, b=17.77 Å, c=3.79 Å, α=90 °, β=90 °, γ=90 °) with two peaks at 23.5 and 48.1 ° corresponding to (001) and (002) reflections, and $W_{25}O_{73}$ (PDF 71-0070, a=11.93 Å, b=3.82 Å, c=59.72 Å, α=90 °, β=98.3 °, γ=90 °) with two peaks at 23.5 and 48.0 ° attributed to (010) and (020) reflections. The lower intensity peaks from the as-synthesized film also matched those peaks from reference of $W_{32}O_{84}$ and $W_{25}O_{73}$. Therefore, the phase of as-synthesized thin film AM375q is most likely consisting of two phases of $W_{25}O_{73}$ and $W_{32}O_{84}$.

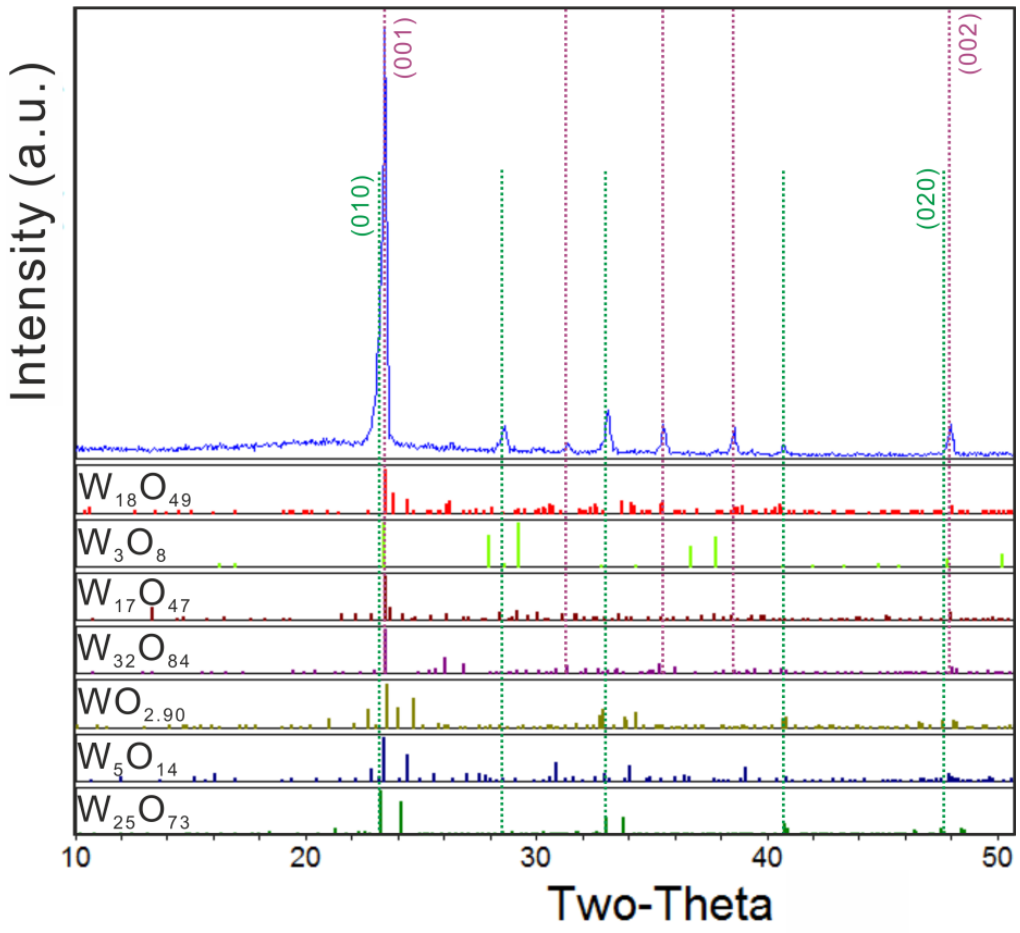

Figure 2.17. Glancing angle XRD pattern of the as-synthesized thin films (AM375q) comparing with the reference XRD patterns of substoichiometric tungsten oxide WO_x (x=2.72 to 2.92).

After annealing at 500 ℃ in air for 2 hours, the two relatively strong peaks shifted to lower 2θ from 23.5 to 23.1 °, and 48.0 to 47.1 ° matching the reference peaks of monoclinic WO_3 (PDF 72-0677, a=7.31 Å, b=7.54 Å, c=7.70 Å, α=90 °, β=90.88 °, γ=90 °) at 23.1 and 47.2 ° attributed to (002) and (004) reflections, as shown in Figure 2.18. Therefore, it seems the as-

synthesized thin film is dominated by $W_{32}O_{84}$ before annealing and transform to monoclinic WO_3 after annealing. Diffraction peaks of (020) and (200) did not clearly demonstrate in AM375q, consisted with the change in colour from blue (WO_x) to yellow (WO_3) (Figure 2.16).

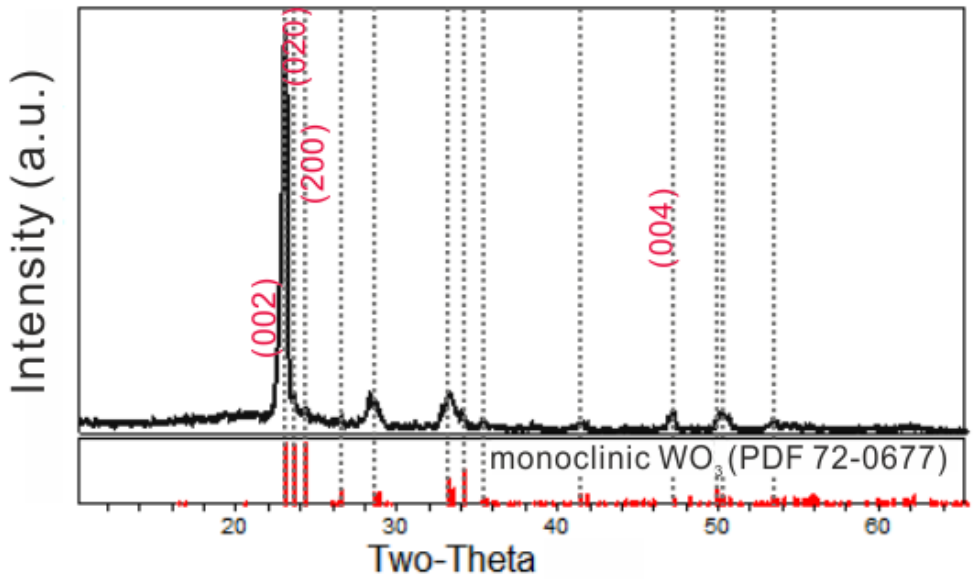

Figure 2.18. Glancing angle XRD pattern of AM375q annealed at 500 ℃ for 2 hours in air, red reference pattern of monoclinic WO_3 (PDF 72-0677).

STEM image of a single as-deposited NR with length 4.9 μm, which was removed from the substrate by sonication, showed an increase of diameter from 40 nm (bottom) to 170 nm (top) along the growth direction perpendicular to the substrate (Figure 2.19a). Element linear scanning shows the amount of tungsten and oxygen increases along the NR growth direction as expected for the NR diameter increasing. However oxygen appears to increase slower than tungsten i.e. this suggests the presence of more reduced tungsten cations along the NR length possibly leading to oxygen defects or oxygen vacancy (V_O). This is possibly due to formation of crystallographic shear planes causing substoichiometric planar defects.[78,153] The HRTEM image and corresponding Fast Fourier Transform (FFT) pattern (inset) in Figure 2.19b, which corresponds to the square-enclosed area in Figure 2.19a, revealed d-spacings along the growth direction of 0.37 ± 0.01 nm, which can be attributed to the (001) planes of monoclinic $W_{32}O_{84}$ ($WO_{2.63}$) (0.378 nm). It can be concluded that the growth direction of WO_x NRs was along the [001] direction. Streaks were observed in the FFT pattern (Figure 2.19b, inset) perpendicular to

[001], which can be attributed to planar defects within the NRs caused by V_O.[153,158] The presence of planar V_O perpendicular to the growth direction [001] could suppress the growth along e.g. [100] and [010].[153] An EDX spectrum line-scan from the bottom to top of the single NR gave an average ratio (%) of O to W equalling to 2.88 ($WO_{2.88}$) between the $W_{32}O_{84}$ ($WO_{2.63}$) and $W_{25}O_{73}$ ($WO_{2.92}$) phases identified by XRD. Therefore, AM375q prepared by AACVD is substoichiometric tungsten oxide (WO_x) with the NR growing along the [001] direction, in agreement with the observed strong XRD reflection peak (001) of $W_{32}O_{84}$.

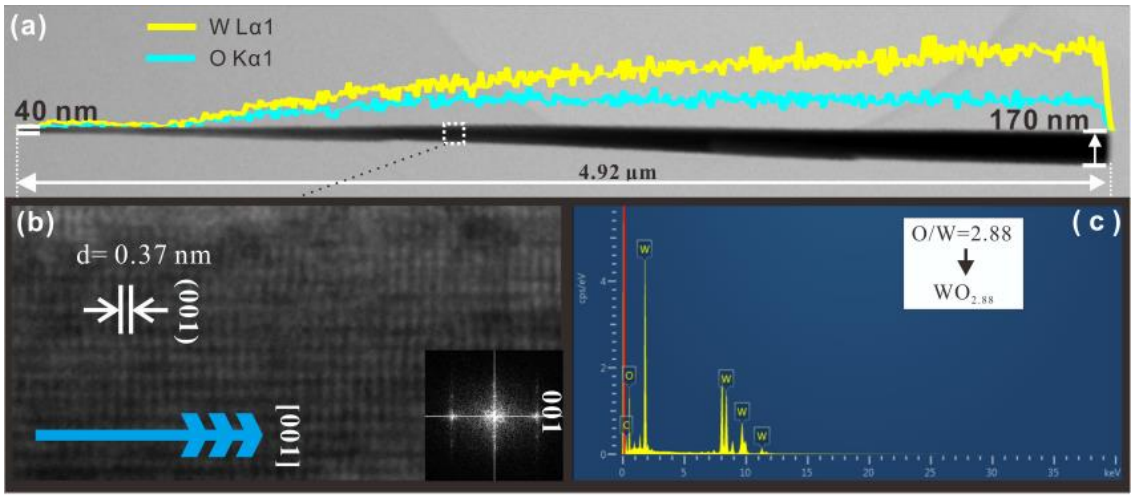

Figure 2.19. (a) STEM images of a single WO_x NR with a length 4.92 µm and the corresponding STEM-EDX elements linear scanning of tungsten and oxygen. (b) HRTEM image of selected section of NR and corresponding FFT pattern (inset). (c) EDX spectrum.[153]

The NR structure of AM375q-ann was maintained after annealing at 500 ℃ in air for 2 hour as observed by STEM (Figure 2.20a), but the surface of the NR appeared rough. The d-spacing along the [001] growth direction increased from 0.37 to 0.38 nm, attributed to the (002) plane of monoclinic WO_3 (PDF 072-0677) as presented in Figure 2.20b. This again suggests that during annealing the WO_x is oxidised resulting in the increase of the lattice parameter. However, streaks still appeared in the FFT pattern (Figure 2.20c) along [100] and [010] directions perpendicular to growth direction ([001]) owing to the presence of defects possibly formed by grain boundaries during annealing, which may explain why peaks attributed to (020) and (200) were low intensity in XRD patterns (Figure 2.18).

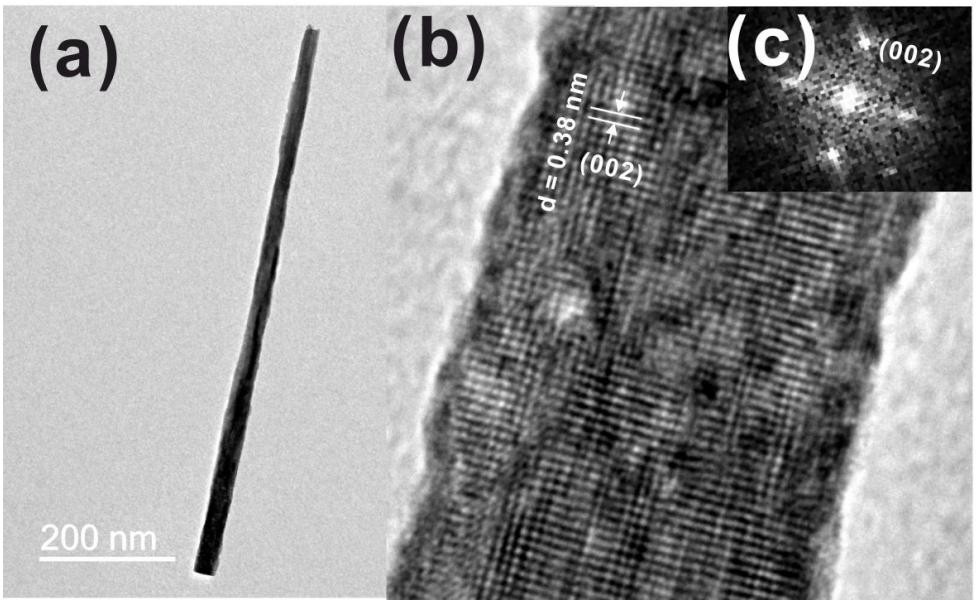

Figure 2.20. (a) STEM images of a single WO_3 NR with a length 4.9 μm. (b) HRTEM image of selected section of NR and (c) corresponding FFT pattern.

X-ray photoelectron spectra were recorded for samples AM375q and AM375q-ann. By fitting the spectrum obtained from AM375q (Figures 2.21a), the main peaks (in red) at 36.0 and 38.1 eV can be assigned to W $4f_{7/2}$ and W $4f_{5/2}$ peaks of W^{6+} respectively.[159] The lower binding energy peaks (in blue) at 34.6 and 36.9 eV correspond to W^{4+}.[160] The ratio of W^{6+} to W^{4+} was calculated *via* the ratio of areas of those peaks, which was 2.9 ± 0.01, e.g. $WO_{2.9}$. The XPS analysis, which only measures around 10 nm depth of samples, suggests that the surface of NRs are comprised of $WO_{2.9}$ phase, agreeing with the XRD pattern reflections of $W_{25}O_{73}$ found before annealing. After annealing (Figures 2.21b) in air at 500 ℃, two peaks at 36.4 and 38.6 eV (in red) are observed corresponding to W $4f_{7/2}$ and W $4f_{5/2}$ peaks of W^{6+}, with lower concentration (9 %) of W^{4+} due to the oxidation of W^{4+} to W^{6+} during annealing, but the crystal structure is similar to monoclinic-WO_3 (Figure 2.18), and the lower concentration of reduced cations (W^{4+}) leading to the colour change from blue to yellow as shown in Figure 2.16.

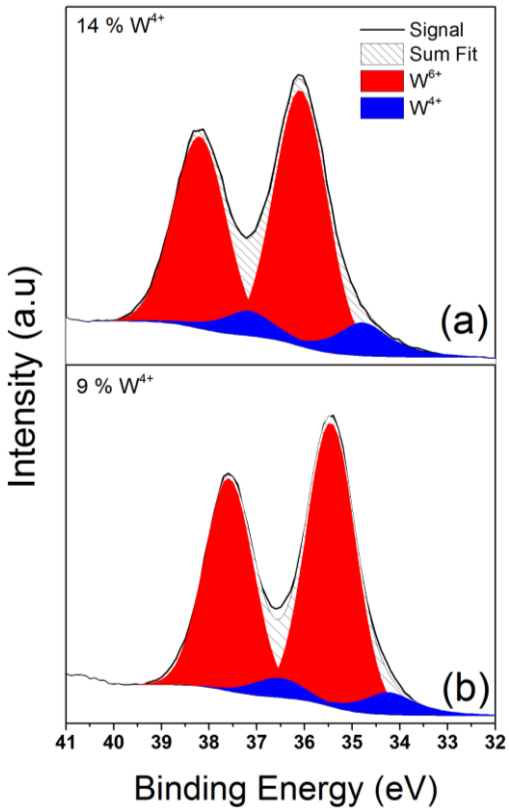

Figure 2.21. X-ray photoelectron spectrum of W 4f region recorded from (a) sample AM375q and (b) AM375q-ann. By fitting this spectrum, the oxidation states of W^{4+} (in blue) and W^{6+} (in red) were obtained.

As shown in Figure 2.22, the XPS VB scan of the as-synthesized thin film before WO_x (AM375q) and after annealing WO_3 (AM375q-ann), are both located at 2.4 eV with respect to the fermi level (E_f =0 eV equal to spectrometer). In sample AM375q there is an energy tail extending into E_f labelled as *d*-band (Figure 2.22), partially occupied with a low number of electrons due to the presence of reduced cations (W^{4+}).[161] After annealing, the intensity in the *d*-band decreased, corresponding with a reduction in concentration of W^{4+} to 4.2 % (AM375q-ann) from 9.8 % (AM375q) (Figure 2.21). Therefore, according to the XPS results AM375q contained both W^{6+} and W^{4+} which leads to *d*-band occupation. After annealing some W^{4+} is oxidised to W^{6+} resulting in a lower intensity in the *d*-band, though reduced cations (W^{4+}) were still found in sample. The presence of W^{4+} can be attributed to V_O,[162] as expressed by the Kröger–Vink notation,

$$W_W^{\times} + O_O^{\times} \leftrightarrows V_O^{\circ\circ} + \frac{1}{2}O_2 + W_W'' \quad (2.5)$$

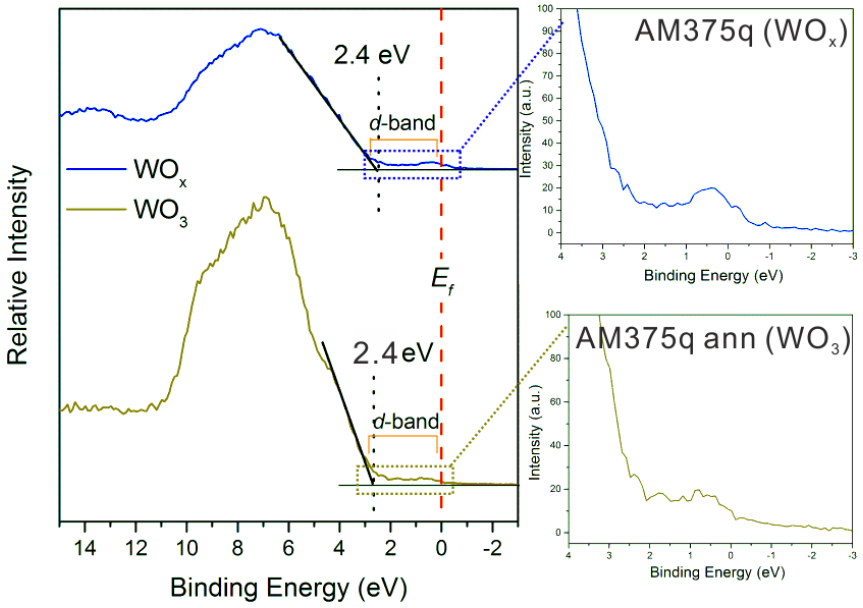

Figure 2.22. XPS valence band (VB) spectra of the as-synthesized thin film WO_x (AM375q) before annealing (blue) and after annealing WO_3 (AM375q-ann in dark yellow).

Figure 2.23. shows that the sample AM375q (WO_x) has about 30 % transmission in visible region, a reflectance peak at 430 nm, strong UV absorption peak at 337 nm and NIR absorption of 80 % at around 2500 nm. After annealing AM375q-ann (WO_3) showed increased transmission of about 65 % in the visible region, increased reflectance with a peak at 460 nm and strong UV absorption below 320 nm.

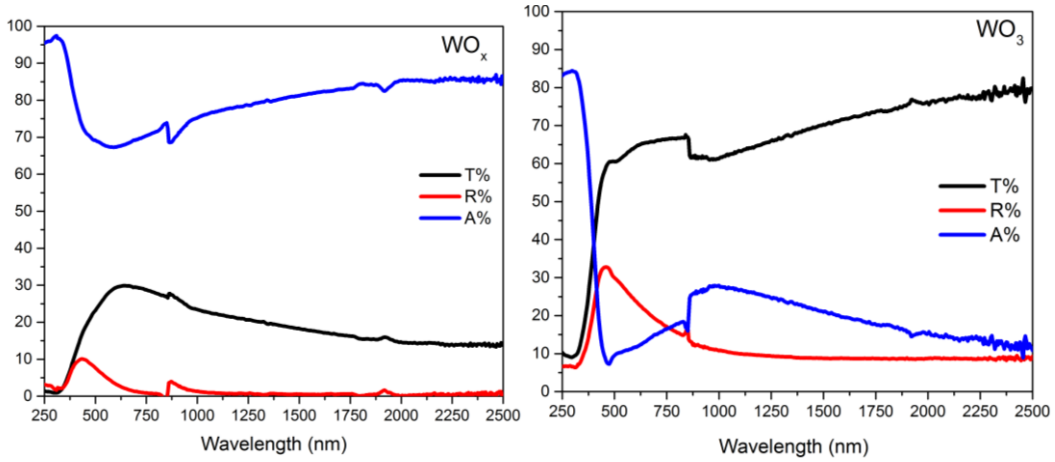

Figure 2.23. Transmittance, reflectance and absorbance spectra of WO_x (AM375q) and WO_3 NRs (AM375q-ann) thin film deposited for 30 mins (aberant data due to grating change of the UV-Vis spectrometer).

According to a previous report,[163] bulk WO_3 has an indirect band gap (E_g) at 2.62 eV and direct E_g at 3.53 and 3.74 eV (recorded by photoelectrolysis spectra which is based on the

measurements of the quantum efficiency photoelectrolysis of water using semiconducting oxide anodes), thus bulk WO_3 is considered as an indirect bandgap semiconductor. Based on UV-Vis data, the Tauc plot gave the indirect E_g of WO_3 (AM375q-ann) at 2.6 eV is in good agreement with indirect E_g from photo-electrolysis spectra (Figure 2.24).[163] As the V_O increased WO_x (AM375q) showed a lower indirect E_g = 0.4 eV indicating metal-like properties attributed to the *d*-band being located around E_f, which increases free-carriers from ~10^{19} cm^{-3} (WO_3) to ~10^{21} cm^{-3} (WO_x) based on the previous study of Mott-Schottky plot and Hall effect.[30,164] Therefore, indirect E_g reduced after sample annealing which is ascribed to the levels of oxygen deficiency decreasing as reported in previous literature.[165]

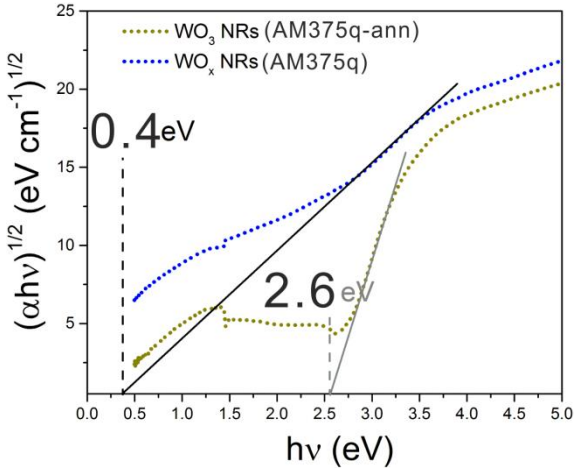

Figure 2.24. Tauc plot of WO_x (AM375q) and WO_3 NRs (AM375q-ann) thin film deposited for 30 mins gave the optical indirect bandgap 0.4 and 2.6 ± 0.05 eV.

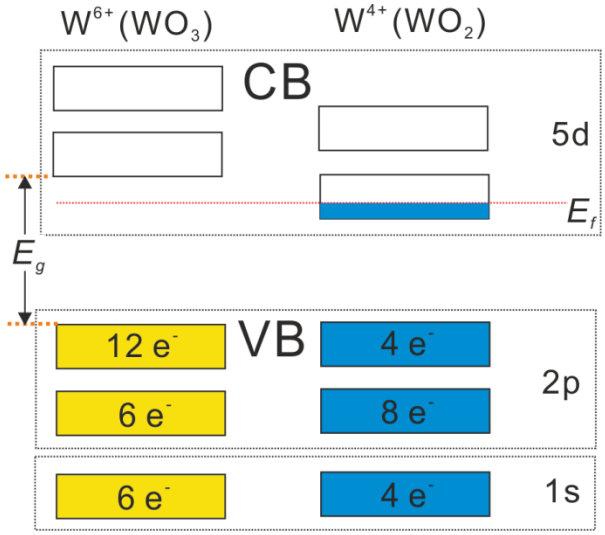

Figure 2.25. Schematic illustration of band structure of WO_3 (W^{6+}) and WO_2 (W^{4+}) based on previous literature.[166]

The mechanism of colour change between blue (AM375q) and more transparent yellow-white (AM375q-ann) is similar to that seen for the elecrochromic (EC) properties of WO_3, which are attributed to a double-charge-injection (DCI) mechanism.[165] The DCI process is described by reaction 2.6 where the injection of electrons and anions into tungsten oxide lattice produce a tungsten bronze.[167]

$$WO_{3-y} + xe^- + xM^+ \Leftrightarrow M_xWO_{3-y} \quad (M = H^+, Li^+, Na^+) \quad (2.6)$$

Subsequently, the injected electrons localized at W atoms are able to alternate the valence of W^{6+} to W^{5+}, and then absorbed light excites electrons from W^{5+} species in site "a" to a neighbouring W^{6+} site "b" leading to coloured tungsten oxide as presented by reaction 2.7.[167] This electron transition process has been described by intervalence charge transfer (IVCT) mode or small polaron hopping absorption (SPH) mode which considers the excess "hopping" electron and corresponding lattice distortion as the polaron.[165,168] Those two modes are widely accepted to explain the tungsten oxide colour change from colourless to dark blue. However either IVCT or SPH modes featuring photoelectrons transition between W^{5+} and W^{6+} site are unable to explain the colourless of WO_x ($x>2.7$) and a decrease of colouring efficiency in relation to a reducing oxygen deficiency. Therefore, zhang et al. (1994) proposed a modified IVCT and SPH mode that instead of balanced cation W^{5+}, the W^{4+} species (generated by oxygen deficiency) and W^{6+} species play the role of host cations, and then the colour change of tungsten oxide *via* photoelectrons transition process is presented by reaction 2.8.[169] Hence, when the oxygen deficiency is low (WO_x, $3.0>x>2.7$), the colouring efficiency is very low attributed to colourless nature of WO_x ($x>2.7$) films. Alternatively, when the oxygen deficiency increases (WO_x when $x<2.7$) an increased amount of W^{4+} species raise the colouring efficiency. However, the formation of W^{5+} or W^{4+} by V_O in W^{6+} background is still under debate. In the computational modelling of amorphous WO_3 by G. A. de Wijs et al. (1999), the appearance of W^{4+} was energetically unlikely, and hence W^{5+} is favourable.[168] In the computational modelling

of WO_3 with *P*21-c system by Chatten et al. (2005), W^{4+}/ W^{6+} polarons are likely to form in strongly oxygen deficient WO_3 and W^{5+}/ W^{5+} in less oxygen deficient conditions.[165]

$$W_a^{5+} + W_b^{6+} \xrightarrow{h\upsilon} W_a^{6+} + W_b^{5+} \quad (2.7)$$

$$W_a^{4+} + W_b^{6+} \xrightarrow{h\upsilon} W_a^{6+} + W_b^{4+} \quad (2.8)$$

For AM375q, the dominate phase is monoclinic $W_{32}O_{84}$ ($WO_{2.63}$) with strong (001) facet observed by XRD, with a concentration of W^{4+} of 14 % given by XPS. After annealing, AM375q-ann was monoclinic WO_3 phase with (002) preferred orientation, with a W^{4+} concentration of 9 % and measured composition as $WO_{2.91}$. Therefore, based on the transition due to W^{4+}/ W^{6+},[165] AM375q ($WO_{2.63}$) which has high oxygen deficient was dark blue colour, whilst after annealing the colour of thin film (AM375q-ann) bleached to be white /pale yellow due to the low oxygen deficients ($WO_{2.91}$).

The optical absorption peak in the NIR due to IVCT/SPH was studied and fitted based on different models. In the Bryksin model, the optical absorption depends on three parameters, the fermi level, E_f (determined from the maximum of Gaussian density of states), the electron activation energy E_a and the band width σ, and then the optical coefficient was given in three different frequency regions from low to high energy as following:[170]

a. When the absorbed light with energy $\hbar\omega < 4E_a(1 - \frac{2E_fKT}{\sigma^2})$, the absorption coefficient *α(ω)* is given by

$$\alpha(\omega) \propto \exp(-\frac{E_f^2}{\sigma^2} - \frac{(\hbar\omega - 4E_a)^2}{16E_akT}) \quad (2.9)$$

b. When the absorbed light with energy $4E_a\left(1 - \frac{2E_fKT}{\sigma^2}\right) < \hbar\omega < 4E_a\left(1 + \frac{2E_fKT}{\sigma^2} + 2E_f\right)$, the absorption coefficient *α(ω)* is given by

$$\alpha(\omega) \propto \exp(-\frac{E_f^2}{2\sigma^2} - \frac{\left(\hbar\omega - 4E_a - E_f\right)^2}{16E_akT} + 2\sigma^2) \quad (2.10)$$

c. When the absorbed light with energy $\hbar\omega > 4E_a\left(1 + \frac{2E_f KT}{\sigma^2} + 2E_f\right)$, the absorption coefficient *α(ω)* is given by

$$\alpha(\omega) \propto \exp(-\frac{(\hbar\omega - 4E_a)^2}{16E_a kT} + 4\sigma^2) \quad (2.11)$$

Therefore, the maximum absorption coefficient peak at $\hbar\omega_{max}$ between $4E_a$ and $4E_a + E_f$ obtained from the derivative of the function (2.9 to 2.11). The E_a was reported lying at ~ 0.28 to 3.0 eV and an increase in E_f by ~ 0.12 to 0.22 eV, and then $\hbar\omega_{max}$ was obtained around 1.30 to 1.36 eV corresponding to wavelength 954 to 912 nm. The maximum optical NIR peak of sample AM375q-ann centred at around 1000 nm (Figure 2.23) with E_a estimated by the energy difference of ~0.2 eV between *d*-band around fermi level and minimum of CB (Figure 2.22 and 2.24).

As the concentration of small polarons increases, the interaction between them needs to be considered. After the concentration of small polarons reachs a critical level, large polarons are formed and the optical absorption will contain a free-electron-like Drude term, in analogy with non-metal to metal transition.[171] Based on large polaron theory, Larsson et al. proposed that the energy needed to excite the self-trapped electrons in a potential well formed by polarons was $2E_p$ with consideration of a change in potential of an atom. The E_p is the polaron binding energy given by

$$E_p = (\frac{1}{\varepsilon_0} - \frac{1}{\varepsilon_\infty})\frac{me^4}{6\pi\hbar^2} \quad (2.12)$$

where ε_0 and ε_∞ are the static and high frequency dielectric constants, respectively, and E_p is 179 meV.[171] The phonons can also be excited *via* a 'shake-up' effect, due to the energy of a photon being much larger than that of a phonon, thus the optical absorption spectrum would give a maximum peak at $4E_p$ (0.72 eV corresponding to wavelength 1722 nm) from the start point of $2E_p$.[171] The maximum NIR absorption peak of sample AM375q was measured at around 2000 nm.

In summary, the optical absorption peak at NIR of samples AM375q before and after annealing was attributed to the formation of V_O leading to IVCT/SPH. With low V_O concentration, the IVCT/SPH absorption peak can be estimated *via* the Bryksin model with a maximum absorption peak at $4E_a + E_f$ in agreement with our sample of AM375q-ann with E_a around 0.2 eV and maximum absorption peak at 1000 nm. With high V_O concentration, the IVCT/SPH absorption peak can be estimated by large polaron theory with maximum absorption peak at $4E_p$. The sample of AM375q gave a maximum absorption peak at around 2000 nm close to the theoretical peak maximum at 1722 nm calculated *via* large polaron theory.[171]

2.3 Growth Mechanism of Nanostructured Tungsten Oxide Thin Films Deposited via AACVD

2.3.1 Introduction

Varying morphologies of tungsten oxide thin films have been prepared on different substrates, by varying solvent and temperature during AACVD (in section 2.3). However, how these various parameters alter the morphology of tungsten oxide was not fully understand. To resolve this, we deposited tungsten oxide thin films using tungsten hexacarbonyl $W(CO)_6$ in a mixture of acetone (10 mL) and methanol (5 mL) (AM375q) at a substrate of 375 ℃. The morphologies of the tungsten oxide thin films obtained were analysed from the inlet (5 mm) of the reactor to the outlet (45 mm) (total reactor length = 60 mm) at 10 mm intervals. The morphology change is related to the competition between nucleation and perpendicular growth for tungsten adatoms and a mathematical description made by combining kinetic factors and statistical mechanical arguments. Hence, the change of substrate temperature and the number density of precursor molecules in the vapour affected the nucleation rate and perpendicular growth rate, resulting in a change from planar to NR structure.

2.3.2 Growth Mechanism of Planar or Nanorod Structured Tungsten Oxide Thin Films

2.3.2.1 Experimental

The sample of tungsten oxide thin film (AM365q) prepared by AACVD has been described in experimental section 2.2.2.

The temperature of the substrate was determined at 5, 15, 25, 35 and 45 mm along the quartz by a type-k thermocouple which was stuck to the surface of the quartz using copper metal tape and the temperature recorded by a temperature controller (EUROTHEM 2116). It is acknowledged that this setup is unlikely to provide the absolute temperature and therefore all our results are relative.[153]

2.3.2.2 Results and Discussions

The as-synthesized WO_x thin film, as presented in Figure 2.26, showed the morphology transitions from planar to NR structure from the inlet to the outlet of reactor. The NR structure was found at a distance between 25 and 50 mm from the inlet where the temperature was recorded between 351 to 358 ℃ on the surface of a quartz substrate. A dense planar structure appeared within the first 25 mm of the thin film where the temperature was below 351 ℃ on the surface of substrate, as demonstrated in Figure 2.26. The blue colour was darker at the front of substrate, but the mean thickness of thin film increased at 5 (800 ± 100), 15 (1100 ± 400), 25 (1500 ± 200), 35 (3800 ± 300) and 45 mm (4000 ± 500 nm) from the inlet, as shown in SEM images in Figure 2.26. This may be due to formation of a more dense planar structure near the inlet and a less dense NR structure further from the inlet. Moreover, the NRs 'forest' at 35 and 45 mm occupied 50 and 38 % area of substrate respectively, estimated by counting the areas of white (NRs) and black pixels (gaps) from SEM images in Figure 2.26.[153]

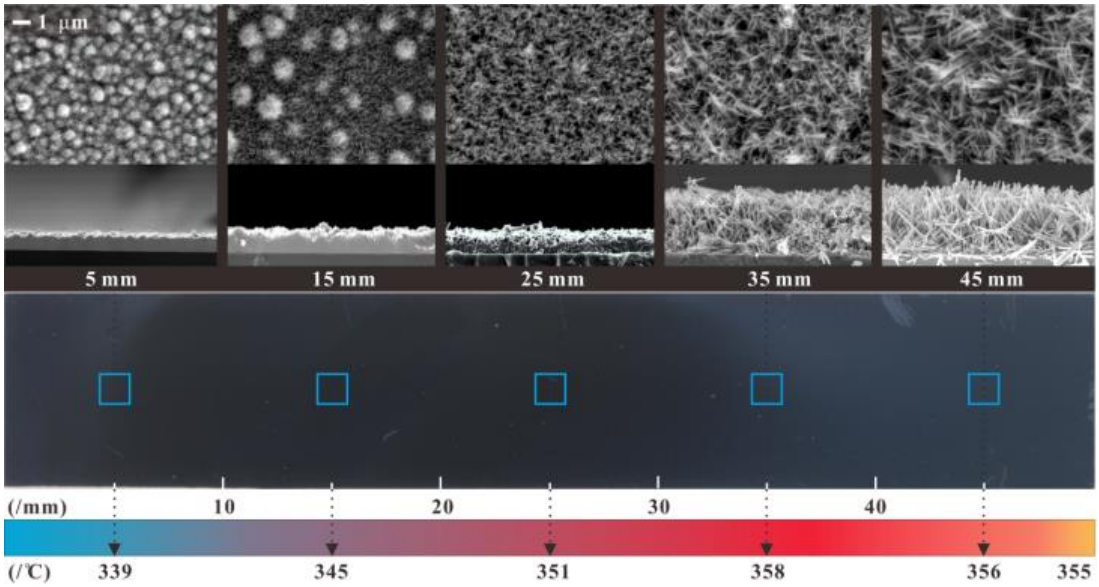

Figure 2.26. Determination of the morphology of various points on the WO_x thin film deposited for 30 min by SEM demonstrating that structures from planar to NRs are obtaining at different distances from (5, 15, 25, 35, 45 mm) and the measured temperature distribution along the length of a quartz substrate.[153]

Glancing angle X-ray diffraction shows two relatively intense peaks at 23.5 and 48.0 °(2θ) on all points within the thin film as shown in Figure 2.27. These two peaks can be attributed to the (001) and (002) reflections of $W_{32}O_{84}$ (PDF 77-0810, a=21.43 Å, b=17.77 Å, c=3.79 Å, α=90 °, β=90 °, γ=90 °) with two peaks at 23.5 and 48.1 °. As the distance from the inlet of the reactor increases, the intensity of the two peaks (001) and (002) becomes stronger, and other less intense peaks emerge corresponding to other reflections of $W_{32}O_{84}$. Reflections of the monoclinic $W_{25}O_{73}$ structure (PDF 071-0070, P12/c, a=11.93 Å, b=3.82 Å, c=59.72 Å, β=98.30°) are also observed. Therefore the as-synthesized WO_x thin film is comprised of $W_{25}O_{73}$ and $W_{32}O_{84}$. Moreover, the increase of relative intensity of diffraction peaks (001) and (002) with increasing distance from the inlet strongly suggests the growth direction of the NR was along [001], which correlates with SEM since the NR structure appears and the length of NRs increase as the distance from the inlet increases above 25 mm (Figure 2.19). However, the total intensity of each diffraction peak decreased between 25 and 45 mm, where the length of NRs increases, possibly due to the decrease in NR occupied surface area between 25 and 45 mm.

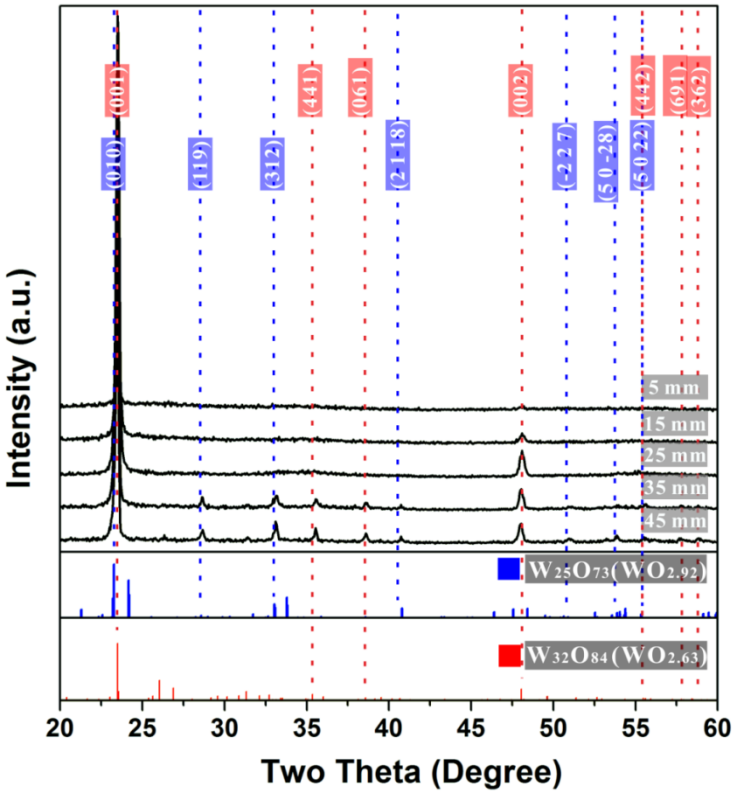

Figure 2.27. Glancing angle XRD patterns of various points within a WO_X thin film deposited for 30 min at various distance (5, 10, 15, 25, 35 and 45 mm) from the inlet of the reactor with reference patterns for $W_{32}O_{84}$ ($WO_{2.63}$) in red and $W_{25}O_{73}$ ($WO_{2.92}$) in blue.

Generally, deposition of thin films usually proceeds via nucleation and growth stages which include three modes: Frank van-der-Merwe (FM) (layer-by-layer), Stranski-Krastanov (SK) (layer plus island) and Vollmer-Weber (VM) (island). If the adatoms prefer to bond with the substrate rather than the growing material, the VM mode is favoured, otherwise FM is selected, or SK mode is preferred in the intermediate situation. Hence, the growth mode selected is normally dependent on a thermodynamic change (change of substrate), but the morphologies change in Figure 2.26 can also be explained using kinetic arguments. The competition between nucleation rate (growth rate parallel to substrate) and growth rate (perpendicular to substrate) results in a wave-like morphology on the surface of the thin film as shown schematically in Figure 2.28. The gap between wave crest and trough of thin film surface (cross-section view Figure 2.28) varies based on 'kinetic competition', when the gap is wide enough the NR structure will be formed.

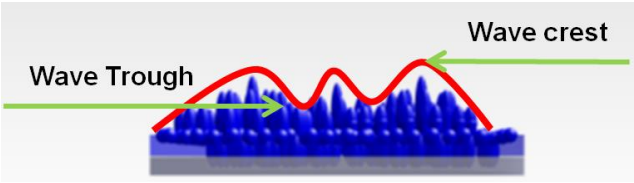

Figure 2.28. Simulation of wave-like morphology of the surface of WO_x thin film.

To confirm the theory of 'kinetic competition', a nucleation rate and perpendicular growth rate were measured from the as-synthesized thin film. The nucleation rate was abstracted from the SEM images from Figure 2.29. At a point 5 mm from the inlet of the reactor the nucleation rate was very fast, and after 180 seconds, spherical islands with average size 53 ± 3 nm occupied all available space on the substrate surface. At 25 mm, needles and spherical islands (average size 46 ± 3 nm) were found after 60 seconds deposition, and after 180 seconds the surface of the substrate was occupied by NRs. At 45 mm, the density of NR islands was lower than 5 mm or 25 mm for the same deposition time, and after depositing for 1800 seconds island coalescence can be seen when the film is viewed from the back, i.e. from the substrate side. Abstracting from the SEM images, the plots of island density dependent on deposition time at different positions are shown in Figure 2.29a in order to obtain a nucleation rate (J in unit of island m^{-2} s^{-1}). The slopes of these plots show J decreases along the distance from the inlet to the outlet of the reactor.

Subsequently, the perpendicular growth rate r_{perp} was estimated by the thickness of the thin film measured by cross-sectional SEM (Figure 2.26). It depends on substrate temperature, as shown in Figure 2.30b, where the Arrhenius plot gives an activation energy of 29.4 ± 3.8 kJ/mol, slightly higher than previously reported 0.22 eV (21.2 kJ/mol) from the precursor tungsten (IV) oxo fluoroalkoxide.[172]

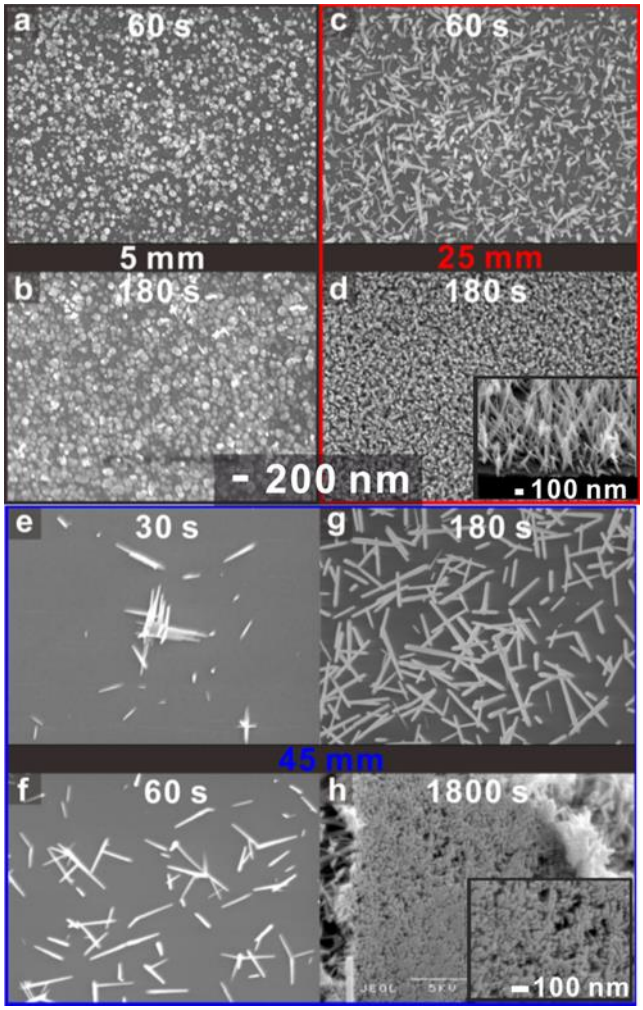

Figure 2.29. Determination of the number of nucleus of WOx thin film deposited by SEM for (a,b) 60 and 180 seconds at 5 mm; (c,d) 60 and 180 seconds at 25 mm (higher magnification inset); (e,f,g) 30, 60, 180 seconds at 45 mm. (h) the back side of an as-synthesized thin film at 45 mm delaminated from the substrate (higher magnification inset).[153]

As shown in Figure 2.30c, as the nucleation rate J rises, the perpendicular growth rate r_{per} reduces from the inlet to the outlet of reactor. At point 25 mm J and r_{per} were around 1.4×10^{12} $m^{-2}s^{-1}$ and 1.6×10^{-9} ms^{-1} respectively. When J was lower than 1.4×10^{12} $m^{-2}s^{-1}$ and r_{per} higher than 1.6×10^{-9} ms^{-1}, NR structure is favoured, otherwise planar was favoured.

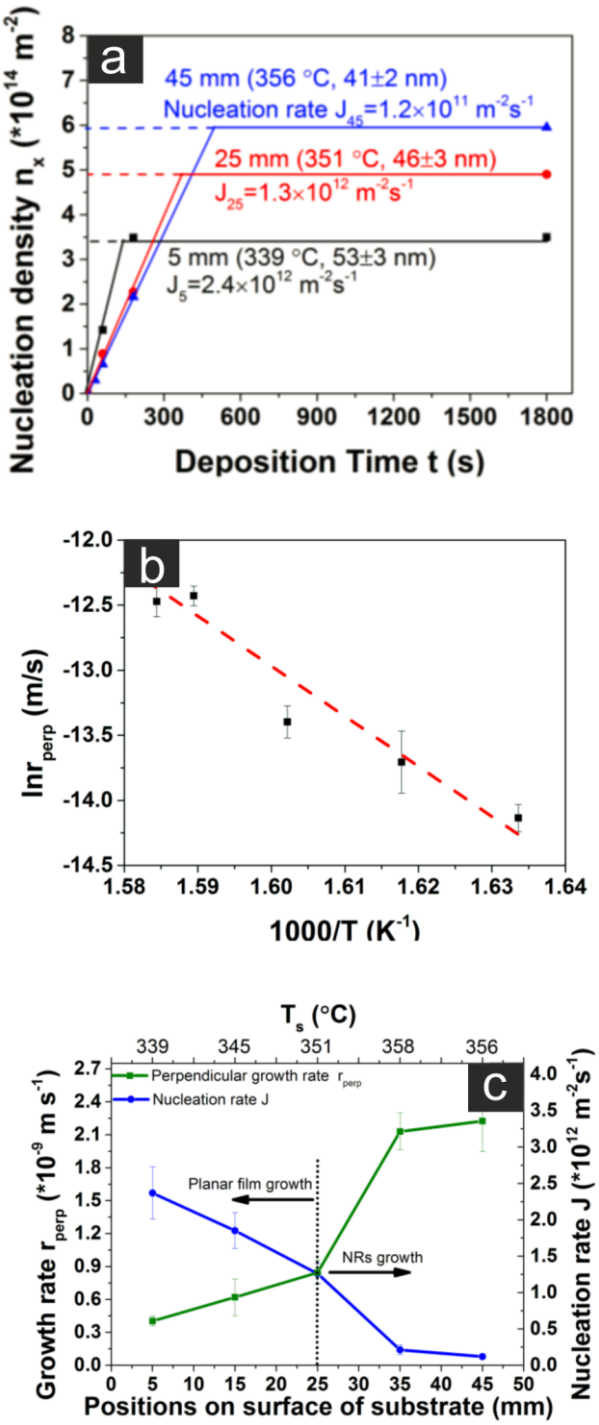

Figure 2.30. (a) Nucleation density n_x and average size of nucleation islands (obtained from SEM images of WO_x thin film deposited at 5, 25 and 45 mm) for 60, 180 and 1800 seconds, with the calculation of nucleation rate J; (b) Arrhenius plot of growth rate along the direction perpendicular to substrate versus inverse temperature of substrate; (c) the plot of growth rate r_{perp} (green) and the nucleation rate J (blue) at various positions from inlet to outlet of reactor.[153]

However, the units for J ($m^{-2}\,s^{-1}$) and r_{per} ($m\,s^{-1}$) were different. If nucleation is considered as thin film growth parallel to substrate, and the area each island cluster can occupy is d^2, where d is the average side-length of an island assumed to be a cube (volume d^3), then time t, which is

represented by $1 / (J \times d^2)$, is the time taken for clusters to occupy a unit 1 m^2 area of the substrate surface, forming a thin film with thickness *d*. In other words, the nucleation of islands contributes to thin film perpendicular growth with thickness *d* in the period of time *t*. Subsequently, the contribution of the nucleation rate *J* to thin film perpendicular growth at rate r_i is represented by $d / t = J \times d^3$, and so $r_i \propto J$, as shown in Figure 2.31.

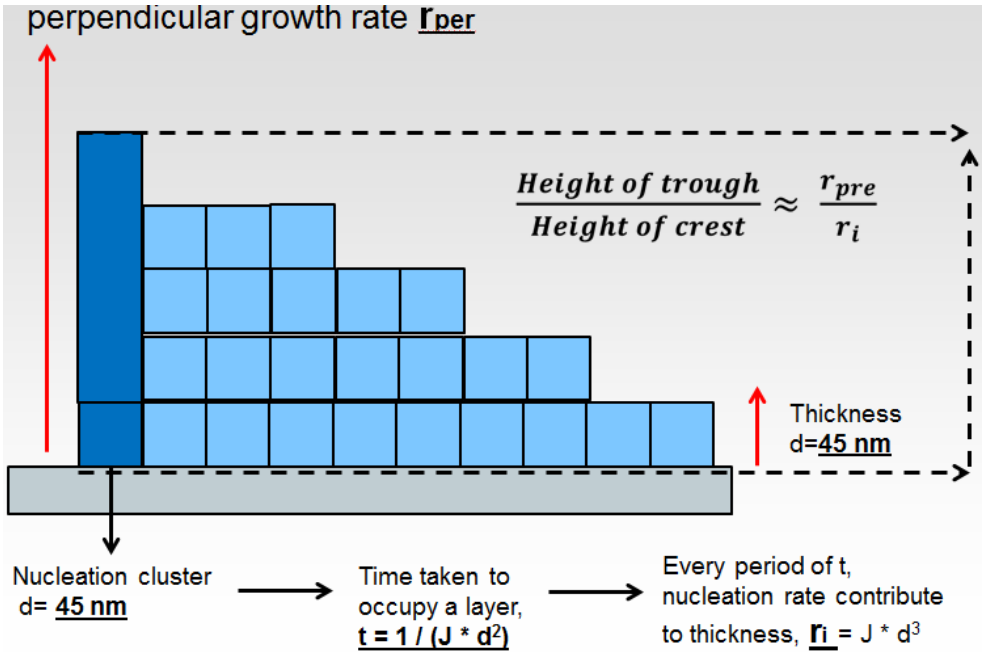

Figure 2.31. The processes of conversion of nucleation rate *J* to thickness increase rate contributed by *J*, r_i, and then the ratio of height of wave trough to that of crest equals to ratio of perpendicular rate r_{per} to r_i.

As shown in Figure 2.29a and 2.30a, the diameter of each nucleation cluster was about 40 to 50 nm at different points. Hence, the average size of clusters was ~ 45 nm, and then the thickness increase rate r_i contributed by *J* can be calculated as shown in Figure 2.31. Therefore, the ratio of r_{per} to r_i was obtained which matched the ratio of the height of a wave trough to that of a crest at points 5 mm and 15 mm (Figure 2.32). Consequently, the wave-like morphology of the as-synthesized thin film prepared by AACVD can be considered as attributed to the 'Kinetic competition' between nucleation rate *J* and perpendicular rate r_{per} and when the ratio of r_{per} to r_i is larger than 7.1 the NR structure is obtained. However, when the rate of perpendicular growth (r_{per}) increases rapidly, the ratio of r_{per} to r_i did not correlate well ratio of the height of the wave trough to that of the crest.

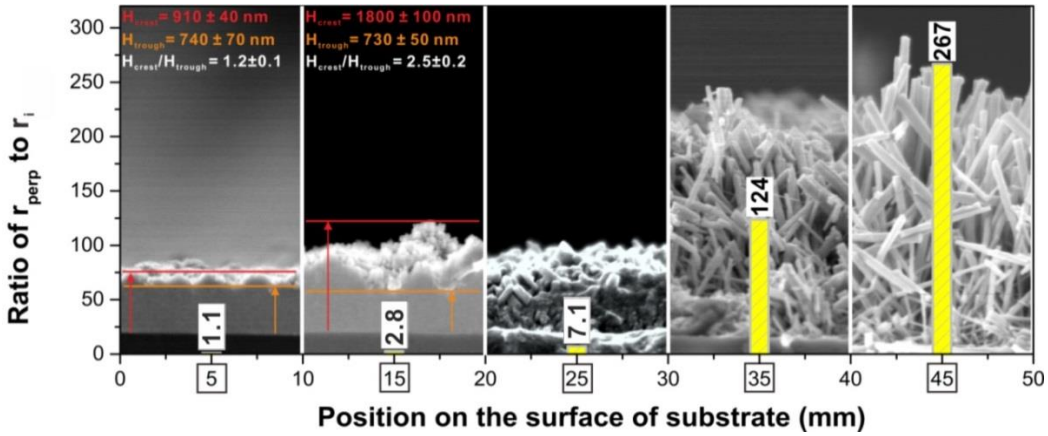

Figure 2.32. The increase of ratio of r_{perp} and r_i at position from 5 to 50 mm (yellow bar) resulting in the distance between the crest and trough larger. NR structure emerges after 25 mm with ratio above 7.1.[153]

Therefore, the different growth modes resulting in morphologies transitioning from planar to NR structure can be explained by kinetic competition between nucleation rate (parallel) and perpendicular rate (growth). As shown in Figure 2.33, when the nucleation rate was extremely fast and perpendicular rate was low, the nucleation clusters were produced very quickly, forming a relatively flat surface similar to that seen in layer-by-layer growth. As the nucleation rate reduced and perpendicular rate increased, the wave-like morphology was formed similar to a growth mode of Layer-plus-island. When the nucleation was extremely low and perpendicular growth rate high, NR structure can be found similar to a growth mode of island growth.

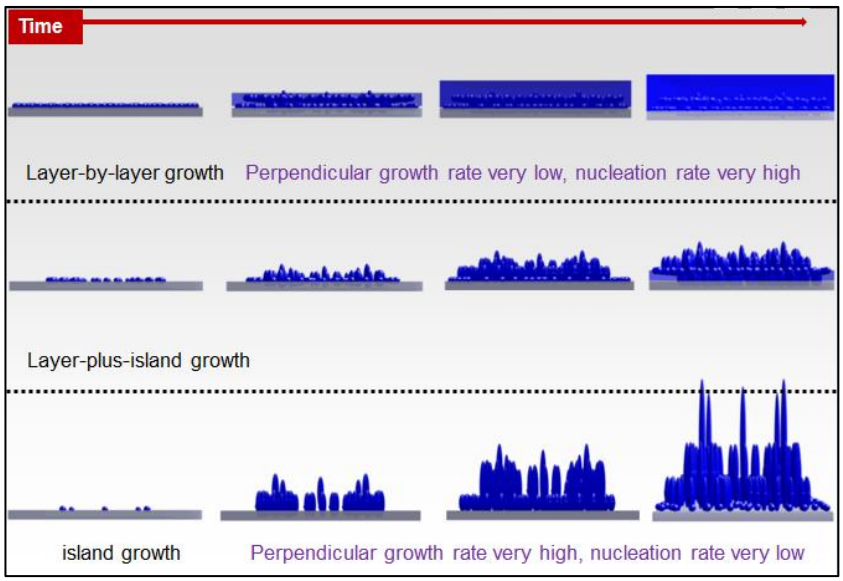

Figure 2.33. The simulation of different growth processes base on different growth modes due to kinetic competition.

To understand how the deposition conditions relate to the kinetic competition between nucleation rate and perpendicular growth rate an atomistic description of the tungsten oxide thin film deposition by AACVD was considered (Figure 2.34). Six main steps occur: transportation of precursor onto the surface of the substrate, adsorption/desorption of precursor molecules on the substrate, pyrolysis of the precursor, tungsten atom diffusion, reaction for tungsten oxide/nucleation and finally thin film growth with three growth modes: FM (layer-by-layer) growth, SK (layer plus island) growth and VM (island) growth.[153] To determine the competition amongst different growth modes, we considered the impact of various deposition conditions at each step.[153]

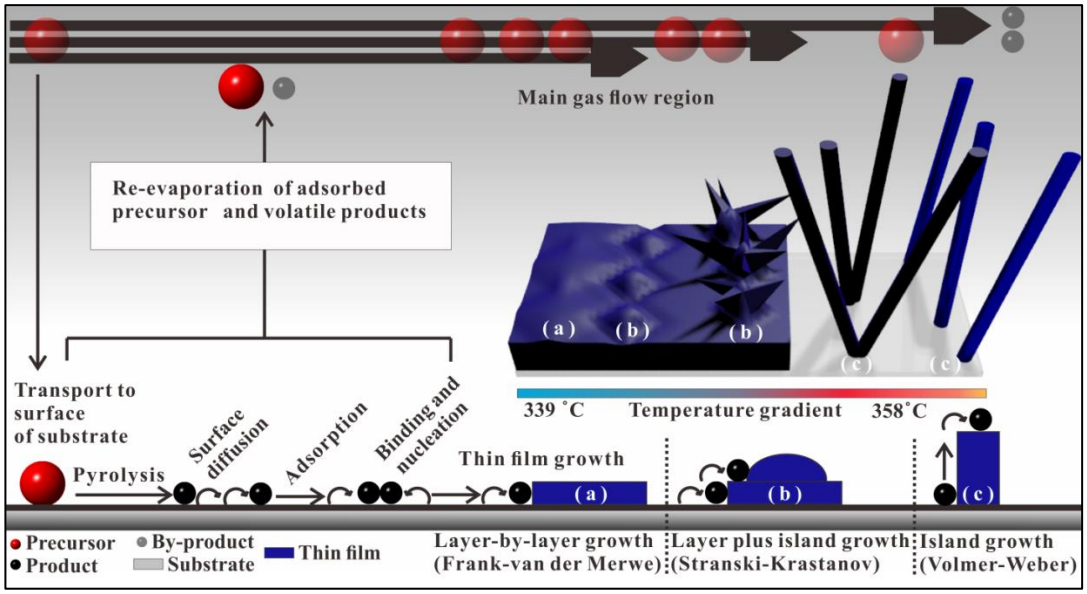

Figure 2.34. Typical atomistic processes during thin film growth via AACVD with three growth modes: (a) FM growth, (b) SK growth and (c) VM growth corresponding to various structures from planar to NR of WO_x.[153]

Firstly, the precursor $W(CO)_6$ solution was transported by carrier gas (such as N_2) as an aerosol over the surface of a heated substrate at a flux R_{pre} (in units of molecules $m^{-2}s^{-1}$) given by (see Equation 1.2)

$$R_{pre} = \frac{p}{\sqrt{2\pi mkT}} \quad (2.13)$$

where p is precursor vapour pressure, m is the molecular weight of precursor, k is Boltzmann's constant and T is the temperature of the vapour source (considered as the surface temperature of the substrate, T_s).[69]

If the flow of precursor aerosols is considered as an incompressible ideal fluid, and therefore gravity ignored, *p*, which is the static pressure on the substrate, can be estimated by a simplified form of Bernoulli's equation:

$$p = (C_{cons} - v_w^2/2)\rho_{pre} \quad (2.14)$$

where ρ_{pre} is the density of precursor aerosols in the vapour (in units of molecules m^{-3}) calculated by $\frac{m}{v}$, (m is the mass of an aerosol, v is the volume of an aerosol estimated by $\frac{4}{3}\pi r^3$ where r is the radius of an aerosol calculated by $\frac{k}{2}(\frac{2\pi\gamma}{\rho f^2})^{\frac{1}{2}}$ (see section 1.2.1)), C_{cons} is the constant of Bernoulli's equation and v_w is flow speed (in unit of m s^{-1}). Hence, Equation 2.13 can be written as

$$R_{pre} = \frac{(C_{cons} - \frac{1}{2}v_w^2)\rho_{pre}}{\sqrt{2\pi mkT_s}} \quad (2.15)$$

After arriving at the heated substrate, $W(CO)_6$ molecules on the surface will only stay for a finite time before re-evaporation, which is described as the adsorption residence time τ_a:

$$\tau_a = \frac{\exp(E_a/kT_s)}{v_a} \quad (2.16)$$

where E_a is the adsorption energy of $W(CO)_6$ molecules on a quartz surface and v_a is an absorption vibration frequency in the order of 1-10 THz.[69] Hence the rate of mass transport (R_w) of $W(CO)_6$ onto the surface of the substrate before desorption can be expressed by

$$R_w = R_{pre}\tau_a = \frac{(C_{cons} - \frac{1}{2}v_w^2)\rho_{pre}\tau_a}{\sqrt{2\pi mkT_s}} \quad (2.17)$$

Subsequently, the adsorbed $W(CO)_6$ precursor decomposes above 250 ℃ producing tungsten atoms.[173] The rate of pyrolysis is controlled by the dissociation of the first CO ligand after which the dissociation of the other five CO bonds is rapid.[174] Hence, the pyrolysis of $W(CO)_6$ is suggested to be a first order reaction, and the pyrolysis rate, r_{pre} (in unit of atoms m^{-2} s^{-1}) is[75,175]

$$r_{pre} = R_{pre}\left[A\exp\left(-E_p/RT_s\right)\right] \quad (2.18)$$

where R is the gas constant, A is the pre-exponential and E_p is the activation energy of $W(CO)_6$ pyrolysis (159 to 192 kJ/mol).[176,177] As the temperature increases, the rate constant of precursor pyrolysis increase, and consequently when the rate constant is equal to 1, r_{pre} equals R_w and the pyrolysis rate depends only on the arrival of precursor due to extremely rapid rate of pyrolysis. Hence, the temperature required to make the rate constant equall to 1 attributing to the maximum mass transport of W atoms, is represented by T^* which can be calculated by

$$T^* = \frac{E_p}{R \ln A} \quad (2.19)$$

where E_p is 44.3 kcal/mol (185.5 kJ/mol), $logA$ is 15.5 (lnA = 36.7), and then T^* is estimated as 352 ℃, which is similar to the substrate temperature at 25 mm where the NR structure start to be found (Figure 2.26).[178]

Therefore, n_w, the density of the adatoms W (in unit of atoms m^{-2}) condensed on the surface of the substrate, can be calculated via an expression:

$$\begin{cases} n_w = R_w A \exp(-E_p/RT_s) = R_{pre}\tau_a A \exp(-E_p/RT_s) \quad (T_s < T^*) \\ n_w = R_w = R_{pre}\tau_a \quad (T_s \geq T^*) \end{cases} \quad (2.20)$$

when T_s is below T^* then n_w is limited by the pyrolysis rate of $W(CO)_6$ on the substrate. If T_s is above T^*, and then n_w is limited by the rate at which $W(CO)_6$ (R_w) arrives at the substrate.

To estimate the n_w and ρ_{pre} at various positions of the surface of substrate, we assumed the as-synthesized WO_x thin film only consists of the $W_{32}O_{84}$ (PDF 77-0810, a=21.43 Å, b=17.77 Å, c=3.79 Å, α=90 °, β=90 °, γ=90 °) phase, and the precursor $W(CO)_6$ deposited equally on the walls of the reactor and on the surface of the substrate. Therefore, the adsorption energy E_a is calculated as 1.2 eV (115 kJ/mol), and profiles of n_w and n_w^2 against T_s and ρ_{pre} are shown in Figure 2.35. In Figure 2.35a and b, peak maxima n_w and n_w^2 appear at $T_s = T^*$=352 ℃ corresponding to the maximum mass transport of W.[153]

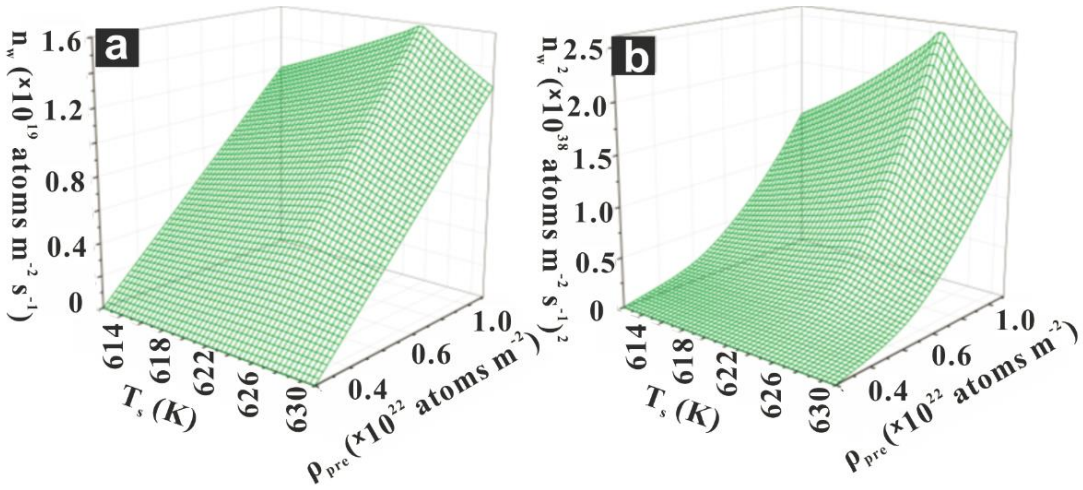

Figure 2. 35 The scaled density profile of W atoms absorbed and deposited on the surface of the substrate before evaporation, n_w and its square n_w^2 for (a,b) temperature of substrate surface, T_s (612 to 631 k) and the density of precursor aerosols, ρ_{pre} (11.2 to 4.4 × 10^{21} m^{-2}).

The oxidation of W atoms occurs rapidly to nucleate WO_x islands.[179] Moreover, the sources of oxygen likely come from the solvent (acetone and/or methanol), or from air leaking into the reactor.[78] Consequently, the nucleation rate of tungsten oxide can be simplified to the nucleation rate of tungsten adatoms. If only re-evaporation and a perfect substrate surface are considered, and only single W adatoms can move, then the nucleation rate, *J*, can be given by[153]

$$J = \frac{dn_x}{dt} = \sigma D n_w n_i \quad (2.21)$$

where n_w is the density of stable islands with size larger than a critical nucleus size (smaller than which are unstable and decay) and σ is a capture number representing the competition between islands for available adatoms.[180] The diffusion coefficient *D* can be written by

$$D = \frac{\upsilon_d a^2}{4} \exp\left(-\frac{E_d}{kT_s}\right) \quad (2.22)$$

where E_d is the diffusion energy and υ_d the diffusion frequency (which smaller than υ_a) and α is the jump distance which is of the same order as the surface repeat distance[75,181]. The n_i is the density of critical nuclei on a perfect surface, which can be written by an atomistic expression as

$$n_i = C_i n_w \exp\left(\frac{E_i}{kT_s}\right) \quad (2.23)$$

where C_i is a statistical weight of order 1-10, and the critical nuclei is defined as when the nuclei with size above critical size i , the nuclei is more likely to grow than decay.[181]

Therefore, Equation 2.22 and 2.23 are substituted in Equation 2.21, and then the nucleation rate J can be given by

$$J = \sigma D n_w n_i = \frac{\sigma C_i \upsilon_d a^2}{4} n_w^2 \exp\left(\frac{E_i - E_d}{kT_s}\right) \quad (2.24)$$

Subsequently, Equation 2.15, 2.16 and 2.20 can be substituted in Equation 2.24, and then the nucleation rate J can be calculated by

$$\begin{cases} J = \frac{\sigma C_i \upsilon_d a^2 A^2 (C_{cons} - \frac{1}{2}\upsilon_w^2)^2 \rho_{pre}^2}{8 v_a^2 \pi m k T_s} \exp\left(\frac{2E_a + E_i - E_d - 2E_p'}{kT_s}\right) \quad (T_s < T^*) \quad (2.25) \\ J = \frac{\sigma C_i \upsilon_d a^2 (C_{cons} - \frac{1}{2}\upsilon_w^2)^2 \rho_{pre}^2}{8 v_a^2 \pi m k T_s} \exp\left(\frac{2E_a + E_i - E_d}{kT_s}\right) \quad (T_s \geq T^*) \quad (2.26) \end{cases}$$

Where E_p' equals to $\frac{E_p'}{N_A}$, N_A is Avogadro constant. To simplified Equation 2.25 and 2.26, the change of υ_d and v_a^2 are considered to be counteracting as varies T_s. Hence, the pre-factor can be treated as a constant Ω:

$$\Omega = \frac{\sigma C_i \upsilon_d a^2 (C_{cons} - \frac{1}{2}\upsilon_w^2)^2}{8 v_a^2 \pi m k} \quad (2.27)$$

When $T_s > T^*$ (352 ℃), based on Equation 2.27 the nucleation rate J relating to the square of W adatoms density $n_w{}^2$ and substrate temperature T_s (Figure 2.36a), and relating to density of precursor ρ_{pre} and T_s (Figure 2.36b) shows that a high nucleation rate appears in regions of lower temperature and/or higher density of adatoms or precursor.

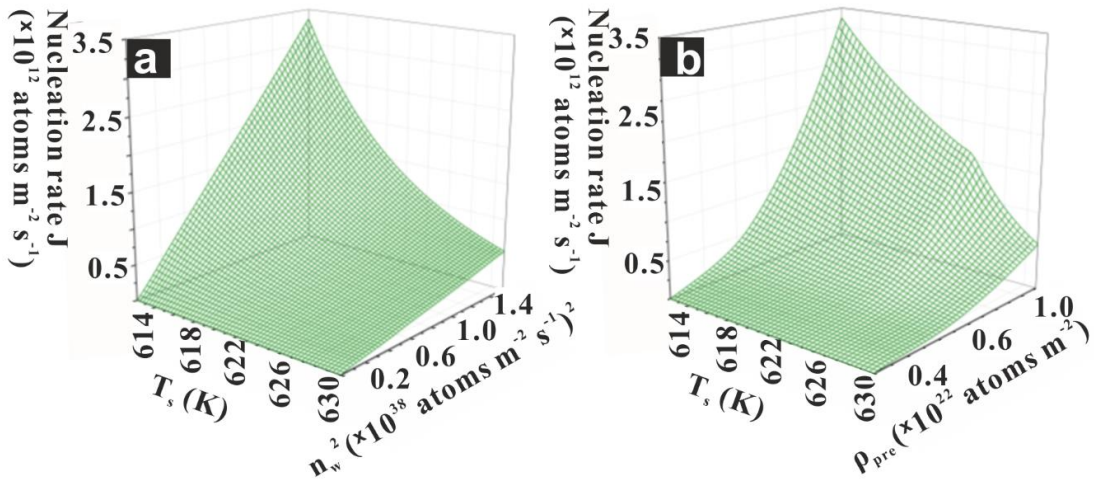

Figure 2.36. The scaled profile of nucleation rate J as a function of substrate temperature T_s and square of W adatoms density, n_w^2 (a), or precursor density ρ_{pre} (b).[153]

Due to the starting point of NR growth being around 25 mm, where the temperature is close to $\boldsymbol{T}^*$, we conclude that NR can be found above $\boldsymbol{T}^*$ at which point the mass transport of W atoms is a maximum. Hence the nucleation J for NR structure can be simplified as

$$J = \Omega \frac{\rho_{pre}^2}{T_s} \exp\left(\frac{E_{NR}}{kT_s}\right) \quad (2.28)$$

where E_{NR} represent the energy for nucleation of the NR structure expressed by $2E_a + E_i - E_d$. Finally, the kinetic competition for NR growth can be estimated by the ratio (R_{KC}) of perpendicular growth to thickness increase rate contributed by nucleation rate ($J \times d^3$) as follows

$$R_{KC} = \frac{r_{Per}}{r_i} = \frac{r_{per}}{Jd^3} = \frac{A_{per} \exp\left(-\frac{E_{act}}{kT_s}\right)}{d^3 \Omega \frac{\rho_{pre}^2}{T_s} \exp\left(\frac{E_{NR}}{kT_s}\right)}$$

$$\therefore R_{KC} = C_{KC} \frac{T_s}{\rho_{pre}^2} \exp\left(-\frac{E_{KC}}{kT_s}\right) \quad (2.29)$$

where r_{per} is the perpendicular growth rate which is usually a zero order reaction.[182] The constant C_{KC} and energy E_{KC} of kinetic competition ratio are represented by $\frac{A_{per}}{d^3\Omega}$ and $E_{act} + E_{NR}$ respectively. As shown in Figure 2.33, when the R_{KC} is not smaller than 7.1, the NR structure can be found in the as-synthesized tungsten oxide thin film prepared by AACVD.

2.3.3 Growth Mechanism of Tungsten Oxide Nanorods

In the previous section, the controlled growth of tungsten oxide NRs *via* deposition parameters such as temperature and concentration of precursor was discussed. Herein, we describe the growth mechanism of tungsten oxide NRs as a function of deposition time during AACVD *via* observation of their growth process by microscopy e.g. SEM and TEM.

A schematic diagram for tungsten oxide NR growth is shown in Figure 2.37 describing four steps: (1) nucleation; (2) NR growing and extruding from nucleus; (3) the growing NR coalesces with neighbouring NR; (4) as the NR grows, more NRs coalesce leading to increasing in the diameter of the NR. Finally, this leads to a NR array (Figure 2.38a) with a smaller number of NR at the top of the film on the bottom.

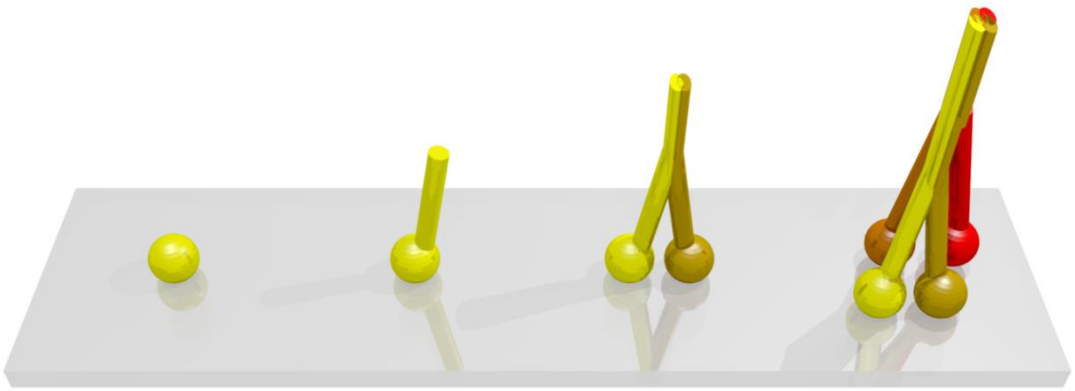

Figure 2.37. Schematic diagram of the growth process of the tungsten oxide NR arrays (a) is following (1) nucleation, (2) NR growth along [001] direction, (3) NRs coalescence and (4) more NRs coalescence attributing to diameter increase.

The nucleus was observed by HRTEM (Figure 2.38b) where defects were observed in the [010] and [100] directions which may be ascribed to an absent of bridging O ions which would result in an increase of the W-W distance and shortening of W-O bonds (~ 0.2 Å) at the V_O site.[165] This could lead to the observed formation of dislocation loops with diameter around 0.4 to 1.5 nm, and hence the formation of these suppresses the crystal growth in those directions. Subsequently, the NR grows along the [001] direction extruding from the nucleus a shown in Figure 2.38c. As the NR grows, the coalescence of randomly oriented NRs occurs giving rise to

an increase in the NR diameter. This coalescence is supported by observation of crystallographic shear planes (CSPs) which gradually disappear as the NRs grows, with a reduction in angles between lattices from different NRs (5.4 and 4.3 ° at interface I and II respectively, Figure 2.38d). The NR diameter growth was able to be described as layer growth along direction [010] and [100] (thickness 1st layer > 2nd > 3rd > 4th, Figure 2.38e).

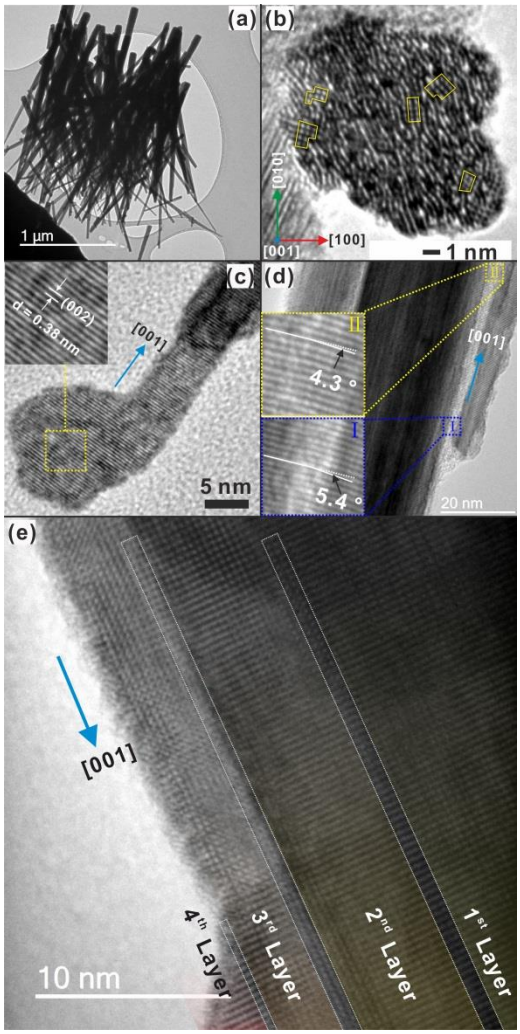

Figure 2.38. TEM image of the NR array (a). HRTEM of top view of a nucleus (b) showing dislocation loops (yellow circles) in direction [010] and [100] with diameter (~ 0.4 to 1.5 nm). A NR extruding from a nucleus and growth along direction [001] (d). Onset of two NRs coalescence at the interface I with the angle 5.4 °between lattices reducing to 4.3 °as NRs growth (d). A NR formed from coalescence of other four NRs demonstrating four layer with interfaces (white rectangle) (e).

As shown in Figure 2.39, the diameter of the NR top increased from e.g. 75 ± 5, 80 ± 5, 85± 5, 90 ± 5, 115 ± 10, 170 ± 15 and 170 ± 15 nm measured according to the length of NRs growth corresponding to deposition times of 0.5, 1, 3, 5, 10, 20, 30 min (Figure 2.40).

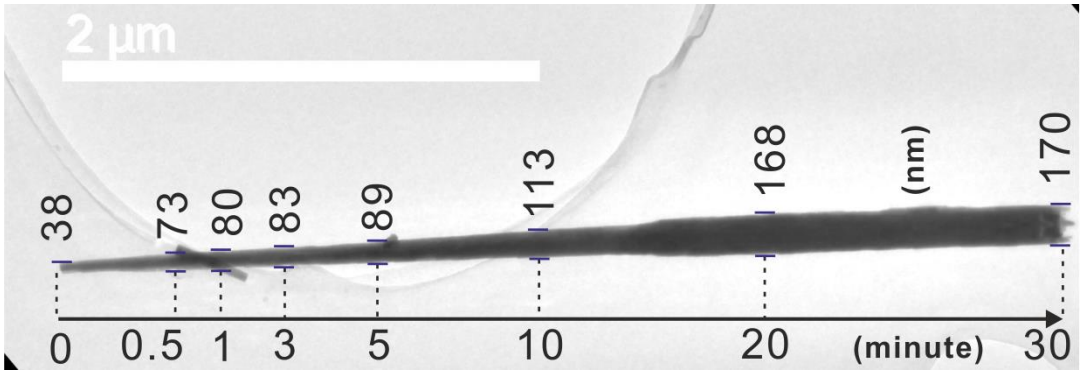

Figure 2.39. A typical single NR (a), abstracted from as-synthesized thin film with randomly orientated NRs (c), used to estimate the NR diameter as a function of increasing deposition time.

The growth rate of the NR was estimated by measuring the thickness of as-synthesized thin film determined by cross-section SEM. As shown in Figure 2.40, the cross-section SEM images of the as-synthesized thin films for 30 seconds to 30 minutes illustrated the thickness (which were measured at the point 30 mm from the inlet of reactor) increase from 430 (±70) nm (30 s) to 2300 (±100) nm (30 mins) as demonstrated in Figure 2.40. The NR length of those thin films deposited for 30s to 3 mins rose from 430 (± 70) nm to 760 (± 90) nm, and the density of NRs increased similar to the prediction for the island growth mode (Figure 2.30) due to kinetic competition between nucleation rate (low) and perpendicular growth rate (high).

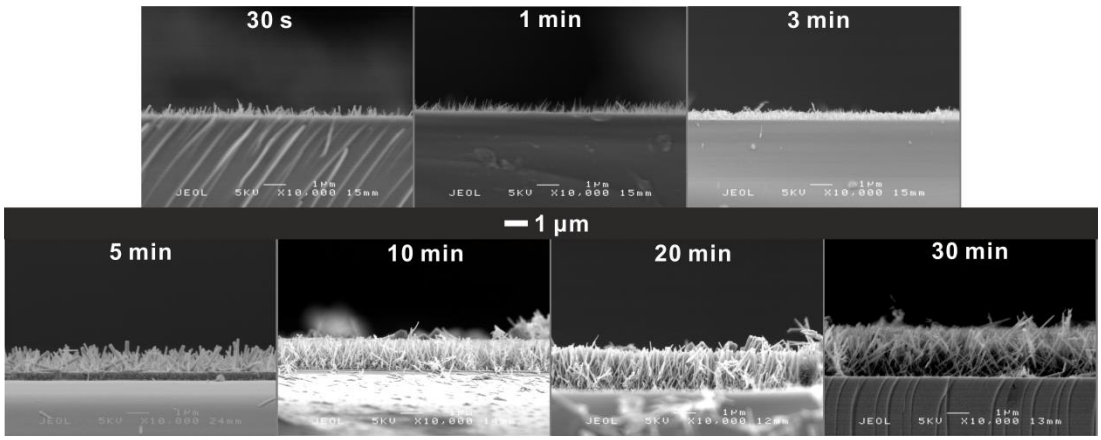

Figure 2.40. The cross-sessional SEM images of WO_x thin films with NR structure were prepared by AACVD for various deposition times such as 30 s, 1 min, 3 min, 5 min, 10 min and 30 min.

The thickness increase of the as-synthesized thin film is not linear with deposition time. As shown in Figure 2.41, the thickness of the thin films, *D*, abstracted from the measurement of the

thickness from cross-section SEM images in Figure 2.40 can be related to the deposition time, *t*, expressed by

$$D = 102t^{0.42} \quad (2.30)$$

where that equation implies the NR growth rate, r_{per}, varies as the thickness changes. Therefore, the change of r_{per} at different thickness can be estimated by the derivative of Equation 2.30

$$r_{per} = \frac{dD}{dt} = 43t^{-0.58} \quad (2.31)$$

In Section 2.4.2.3, the perpendicular growth rate can be expressed by a zero order Arrhenius equation $r_{per} = A_{per} \exp\left(-\frac{E_{act}}{RT_s}\right)$ where the pre-factor A_{per} and activation energy E_{act} was obtained from an Arrhenius plot (Figure 2.30b), 1771 and 29.4 ± 3.8 kJ/mol respectively, when the excessive adatoms arrived at NR growth point.

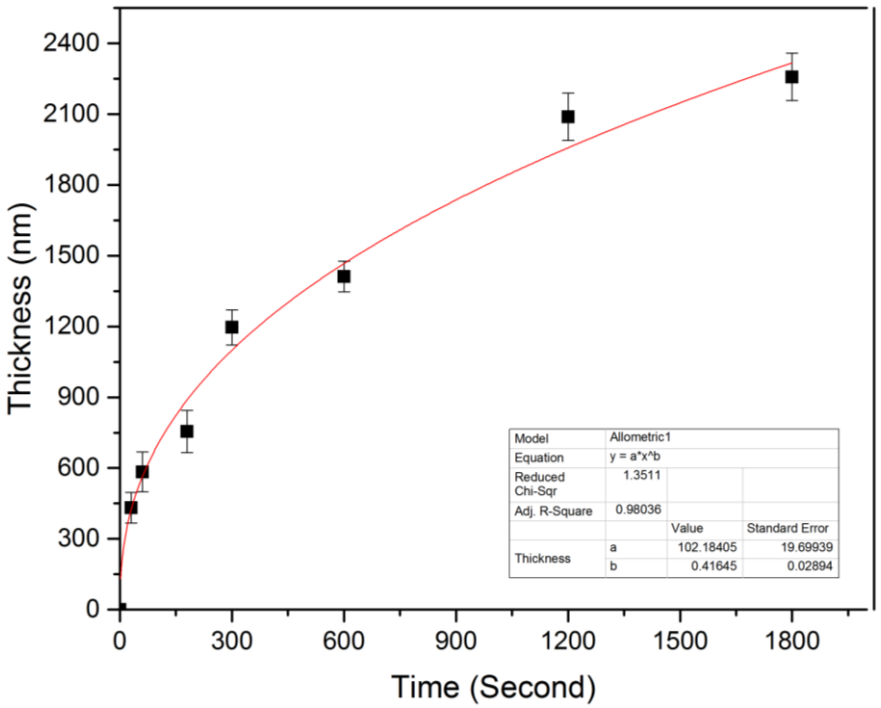

Figure 2.41. The thickness of the as-synthesized WO_x thin film against time was fitted by simulated line.

The change of thickness *D* and growth rate r_{per} as a function of deposition time *t* was extrapolated based on Equation 2.30 and 2.31 as shown in Figure 2.42. The thickness increased with deposition time, though the growth rate decreased. When the deposition time was between

0 to 320 second, r_{per} experienced a sharp reduction, as the deposition time is extrapolated to infinity, the growth rate will be zero. Therefore, after reaching 3600 nm, the thickness is expected to increase at a very slow rate.

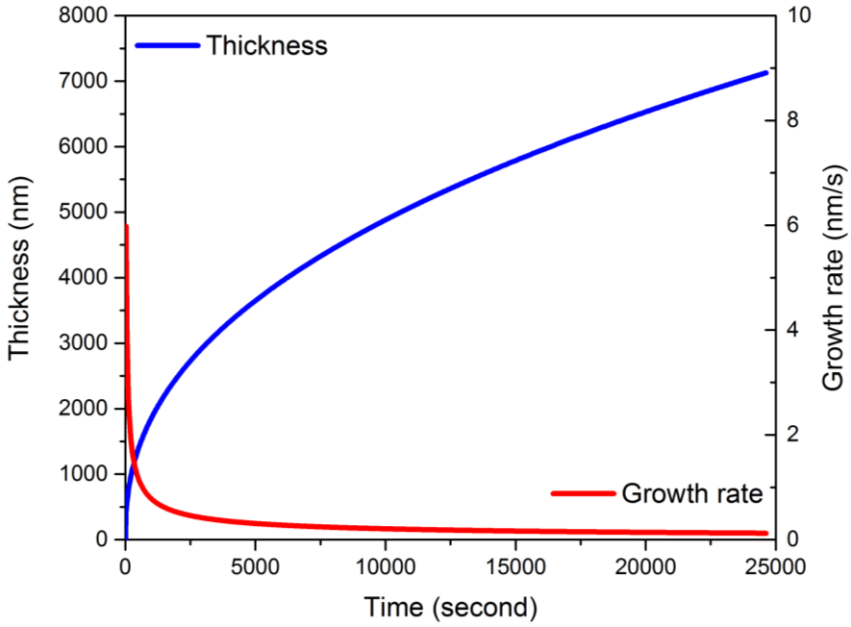

Figure 2.42. The scaled profile of Thickness, *D*, and growth rate, r_{per}, as a function of deposition time based on Equation 2.30 and 2.31.

2.4 Conclusion

In this chapter, an optimisation of the deposition parameters for tungsten oxide NR growth *via* AACVD was presented. When using pure methanol as a solvent, a mixture of acetone and toluene or acetone and methanol, the NN or NR like structure can be deposited on alumina, silicon, glass or quartz substrates. The effects of solvent include: (1) solubility of precursor attributing to different concentration precursor in solution and aerosols; (2) diameter of aerosols; (3) reactions with precursor, substrate and/or the formed thin films by donating oxygen or forming interstitial or substitutional carbon in the unit cell at elevated temperature.

This leads to the question of how the deposition parameters affect the morphologies of tungsten oxide. In the previous literatures, The VLS and VS mechanism studied on the driven force attributing to the 1D nanostructure growth (e.g. screw-dislocation driven mechanism and defect-driven mechanism) without correlating the deposition parameters to the formation of

various nanostructures (1D, 2D or 3D). Therefore, the limits of previous growth models were failed to predict the morphologies of thin films formed with varying the deposition parameters during AACVD.

Herein the morphologies of as-synthesised tungsten oxide thin film were observed changing from planar to NR structure along the distance from the inlet to the outlet of the reactor, I ascribed this to the competition for adatoms on the substrate between perpendicular growth with rate r_{perp} and nucleation (parallel growth) with rate J resulting in various ratios of r_{perp} to r_i (film thickness increase rate contributed by J, $r_i \propto J$). That competition was ascribed to kinetic competition estimated by a kinetic competition ratio calculated by Equation 2.29 for predicting NR structure. As that ratio increases, the cross-section morphology of the surface of the planar as-synthesised thin film appears to be wave-like; when that ratio is larger than 7.1 the structure transitions to NR (Figure 2.32). The r_{perp} is dependent on the substrate temperature T_s, and the r_i is proportional to J, which is dependent on the density of precursor vapour ρ_{pre} and T_s (J is proportional to ρ_{pre}^2 and T_s^{-1}). As the distance from the inlet to the outlet of the reactor increases, the change of deposition conditions of T_s (increase) and ρ_{pre} (decrease) results in r_{perp} (increase) and r_i (decrease), and an increase in the ratio of r_{perp} to r_i leading to a transition in growth mode from Frank-van der Merwe (FM) (layer-by-layer) and Stranski-Krastanov (SK) (layer plus island) to Volmer-Weber (VM) (island), and hence the morphology from planar to NR. Therefore, if the planar structure is desired, the preferred deposition conditions are relatively low T_s for compressing perpendicular growth, and high ρ_{pre} for accelerating the nucleation rate J (parallel growth) e.g. low substrate temperature and high precursor flux. For NR structure, not only does the nucleation growth rate need to be compressed (relatively low ρ_{pre}), but the most important factor is an increase in r_{perp} which is dependent on T_s and activation energy E_{act}. In other words, when E_{act} is high, extremely high T_s would be required to obtain NR structure. Consequently, several methods and mechanisms have been introduced to decrease E_{act} in order to fabricate NR structures at relatively low temperatures, i.e. VLS and VS mechanisms introduce catalysts to reduce E_{act} for NR growth, the use of plasma can reduce E_{act}, use of different precursors can also impact on the E_{act} such as $W(CO)_6$ (E_{act} = 29.4 kJ/mol),

$WO[OCCH_3(CF_3)_2]_4$ (21.2 kJ/mol, NR expected to appear at around 300 ℃) and $WO[OC(CH_3)_2CF_3]_4$ (32.8 kJ/mol, NR expected to appear at around 350 ℃) resulting in the required T_s for NR structure increasing as E_{act} increases.[153]

After nucleation, the defects and dislocation loops were found in the [100] and [010] directions suppress the crystal growth in those directions. Alternatively, NRs are able to grow in the [001] direction without defects by extruding from nucleus. Afterward, the NRs coalesce with neighbouring NRs leading to the observed increase of NR diameter from 73 to 170 nm with deposition time from 30 s to 30 min.

The NRs growth rate was estimated from the observation of thin film thickness change by SEM. When the deposition time was between 0 to 320 second, r_{per} experienced a sharp reduction, because as the deposition time is extrapolated to infinity the growth rate will be zero, which corresponds to the thickness above 3600 nm increasing at a very slow rate.

Finally, based on the Venables' kinetic theory and the observation of different morphologies of tungsten oxide thin films with various deposition parameters during AACVD, the 'Kinetic competition' equation was deduced (Equation 2.29) which could use to estimate temperature for the 1D structure formation of other metal oxides during AACVD, after conducting a small series deposition to work out the constant in that equation.

CHARPTER 3: NANOSTRUCTRED TUNGSTEN OXIDE: FUNCTIONAL PROPERTIES AND APPLICATIONS

In this chapter, the potential applications of the as-synthesized thin film as a solar light filter and for photodegradation of stearic acid are explored.

3.1 Solar Heat-Filter Coating (NIR Absorption Thin Film)

3.1.1 Introduction

J.M. Berak et al. reported Hall effect studies on WO_3 and WO_x revealing that as the oxygen-deficiency increased, the density and mobility of charge carriers (free electron) increase.[164] In previous sections, the synthesis and growth mechanism of substoichiometric tungsten oxide NR ($W_{32}O_{84}$) *via* AACVD have been studied. Substoichiometric tungsten oxide contains oxygen vacancies (V_O) that lead to intervalence charge transfer (IVCT) / small polaron hopping (SPH) absorption and the observation of an absorption band.

Based on this NIR absorption property of WO_x, an NIR shielding coating fabricated from WO_x nanoparticles and NR was proposed in order to save energy from air conditioning by avoiding IR heating of sunlight into indoor enviroments.[183,184] However, one of the challenges of a solar heat-shielding coating is to show high NIR absorption as well as high visible light transmittance. Herein, NR structured WO_x thin films with different thickness were prepared by AACVD on quartz in order to study the relationship between NR length and NIR absorption by estimating which thickness of WO_x thin films balance NIR absorption and visible light transmittance.

3.1.2 Experimental

Substoichiometric tungsten oxide NR array thin films (AM375q) were prepared by AACVD with conditions described in section 2.2.2 in 30 s to 30 min denoted as WO_x ("t") where "t" represents the deposition time e.g. WO_x (30 min).

To test the NIR filtering of the as-synthesized thin films, a simulated experiment was performed at room temperature around 20 to 22 ℃ (Figure 3.1). A 25 W halogen lamp bought from EXO-TERRA was used as light source. The temperature changes dependent on time were recorded by type-K thermocouple for 1 hour.

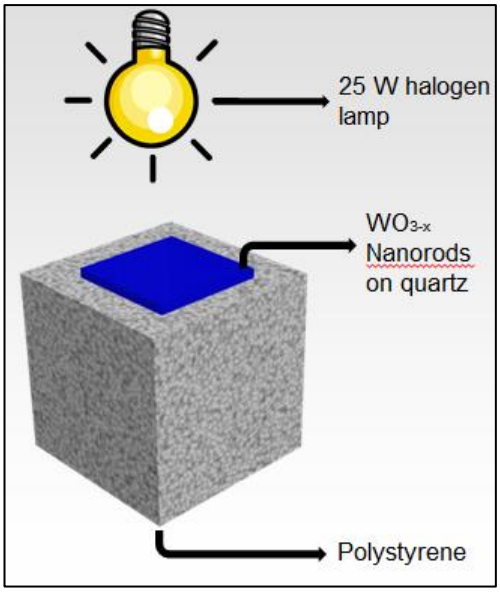

Figure 3.1. Schematic demonstration of simulated experiment of NIR absorption where a WO_x thin film on quartz was placed on top of a polystyrene box irradiated by a 25 W halogen lamp and the temperature changes dependent on time were recorded by K-type thermocouple and thermometer from inside that box.

3.1.3 Results and Discussions

WO_x thin films with NR structure were prepared by AACVD with the same conditions of AM375q (see section 2.2.2) for various time from 30 s to 30 min. As deposition time increased, the as-synthesized thin films became dark blue and less transparent as shown in Figure 3.2.

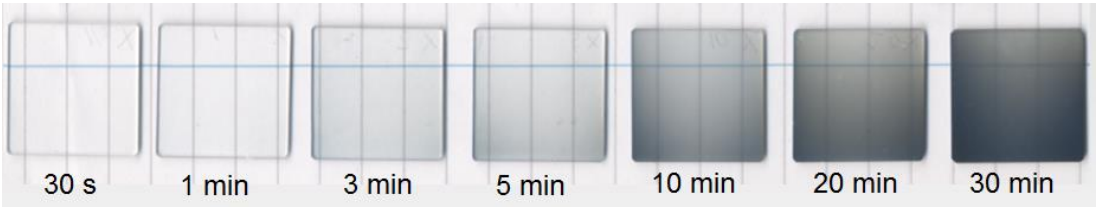

Figure 3.2. The WO_x thin films with NR structure were prepared by AACVD for various deposition time such as 30 s, 1 min, 3 min, 5 min, 10 min and 30 min.

As shown in Figure 3.3, the SEM images of the as-synthesized thin films for 30 seconds to 30 minutes showed the length of NR increasing from 430 (±70) nm (30s) to 2300 (±100) nm (30 min), and the density of NRs also increased. Therefore, as length and density of NRs increase with the deposition time, the colour of those as-synthesized WO_x thin films became darker and less transparent due to higher density of nucleation sites and greater amount of absorbing material.

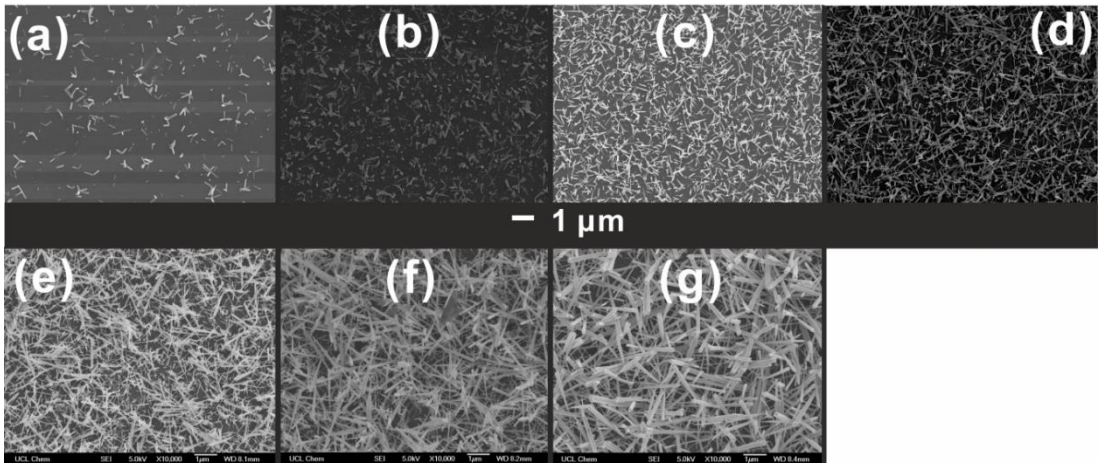

Figure 3.3. The SEM images of WO_x thin films with NR structure were prepared by AACVD for various deposition times: (a)30 s, (b)1 min, (c)3 min, (d)5 min, (e)10 min, (f)20 min and (g)30 min.

Glancing angle X-ray diffraction shows two relatively intense peaks at 23.5 and 48.0 ° (2θ) in the XRD patterns of all WO_x thin films deposited from 30s to 30 mins as shown in Figure 3.4. These two peaks can be attributed to the (001) and (002) reflections of $W_{32}O_{84}$ (PDF 77-0810, a=21.43 Å, b=17.77 Å, c=3.79 Å, α=90 °, β=90 °, γ=90 °) with two peaks at 23.5 and 48.1 °, and the reflections of the mono-clinic $W_{25}O_{73}$ structure (PDF 071-0070, P12/c, a=11.93 Å, b=3.82 Å, c=59.72 Å, β=98.30°) are also observed. Therefore the as-synthesized WO_x thin film is comprised of $W_{25}O_{73}$ and $W_{32}O_{84}$ which was discussed in Section 2.3.2 .As the deposition time increases, the length of NR became longer and the intensity of the two peaks (001) and (002) becomes stronger, and other less intense peaks emerge corresponding to other reflections of $W_{32}O_{84}$, possibly due to NRs growing along the [001] direction and becoming thicker which is in agreement with observation by SEM and TEM in Section 2.3.2.

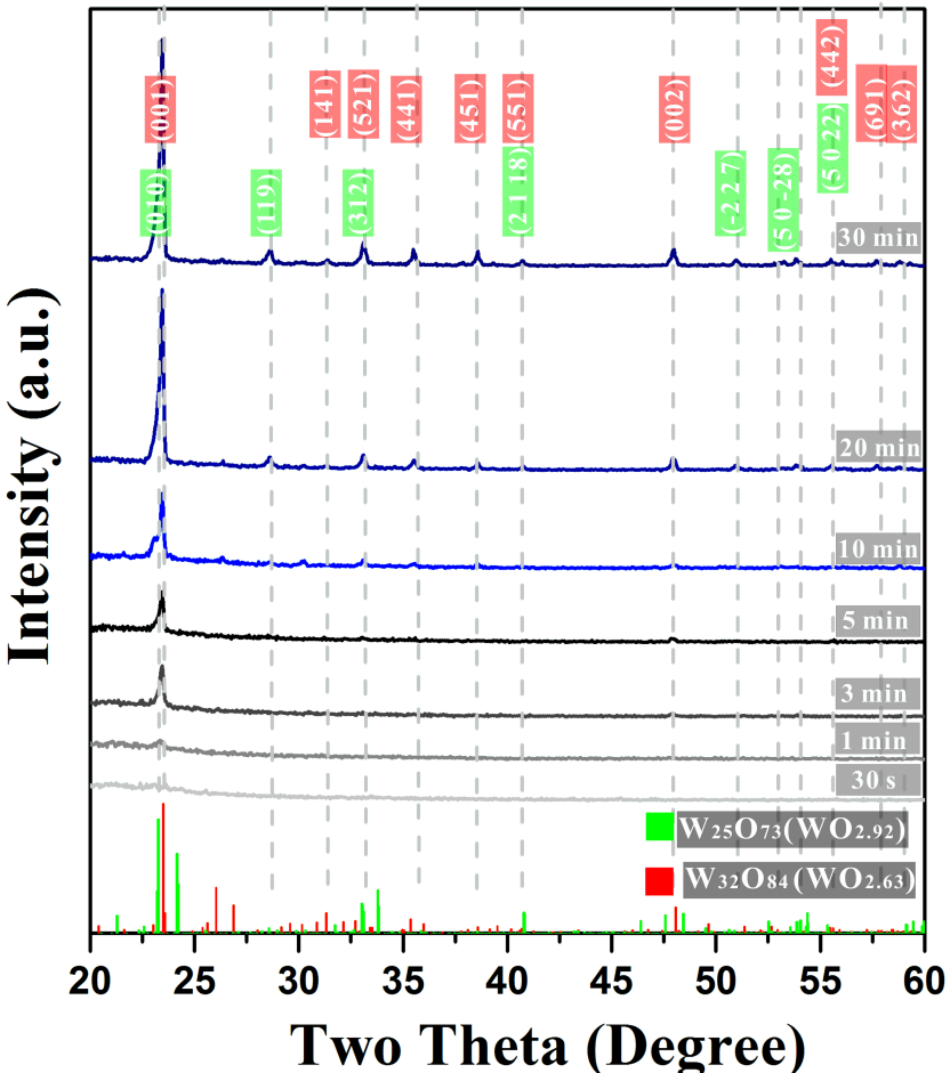

Figure 3.4. Glancing angle XRD patterns of WO_X thin films deposited for 30s to 30 min with reference patterns for $W_{32}O_{84}$ ($WO_{2.63}$) in red and $W_{25}O_{73}$ ($WO_{2.92}$) in green.

Figure 3.5 shows the transmittance reduces in all regions as deposition time increases due to the length of NRs increasing. In the UV region, the WO_x thin film deposited for 1 min demonstrates 15 % less transmittance compared to that for a film deposited for 30 s, mainly attributed to the density of NRs increasing. The transmittance peak starts to appear at 364 nm for 1 min deposition, and then progressively red shifts to 384 nm (3 min), 396 nm (5 min), 468 nm (10 min), 588 nm (20 min) and 620 nm (30 min).

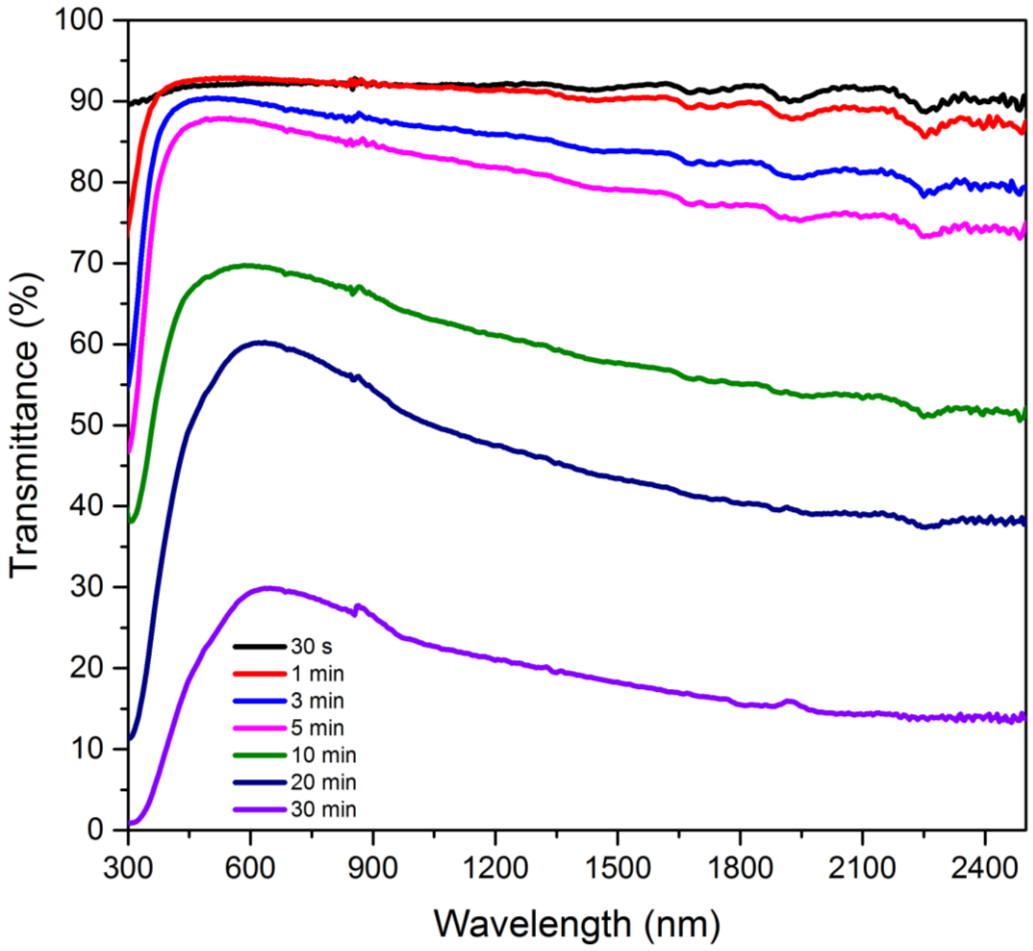

Figure 3.5. Transmittance spectra of WO_x thin films deposited for 30s, 1 min, 3 min, 5 min, 10 min, 20 min, and 30 min respectively (aberant data due to grating change of the UV-Vis spectrometer).

The reflectance of all those WO_x thin films were low in NIR (less than 5%), UV (less than 15 %) and visible (less than 15 %) as shown in Figure 3.6. The sharp peak appearing around 900 nm is due to the grating change by the spectrometer. The peak appearing at about 450 nm corresponds with the blue colour of the as-synthesized thin films. The reflectance peaks started to appear at 315 nm for 1 min deposition, and then red shifts to 319 nm (3 min), 356 nm (5 min), 413 nm (10 min), 433 nm (20 min) and 433 nm (30 min).

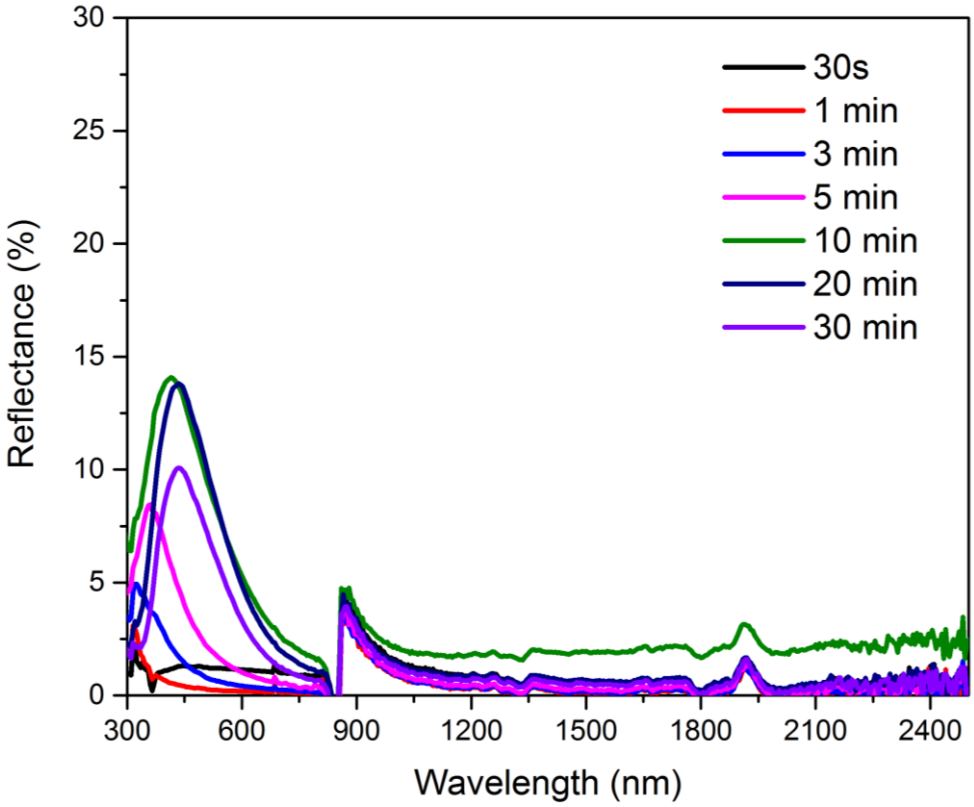

Figure 3.6. Reflectance spectra of WO_x thin films deposited for 30s, 1 min, 3 min, 5 min, 10 min, 20 min, and 30 min respectively (aberant data due to grating change of the UV-Vis spectrometer).

The calculated absorbance spectra of the WO_x thin films were obtained from the expression $A\% = 100 - T\% - R\ \%$ as shown in Figure 3.7. The absorbance in all regions showed an increase as the length of NRs increase. The absorbance generally increases eight and six times in the NIR and visible regions respectively from deposition for 30s (430 ($\pm$ 70) nm) to 30 mins (2300 ($\pm$100) nm). The NIR peak of samples WO_x (30 s) and WO_x (1 min) was difficult to find. As the deposition time increased and the length and density of the NR increased, the intensity and curvature of the NIR peak increased.

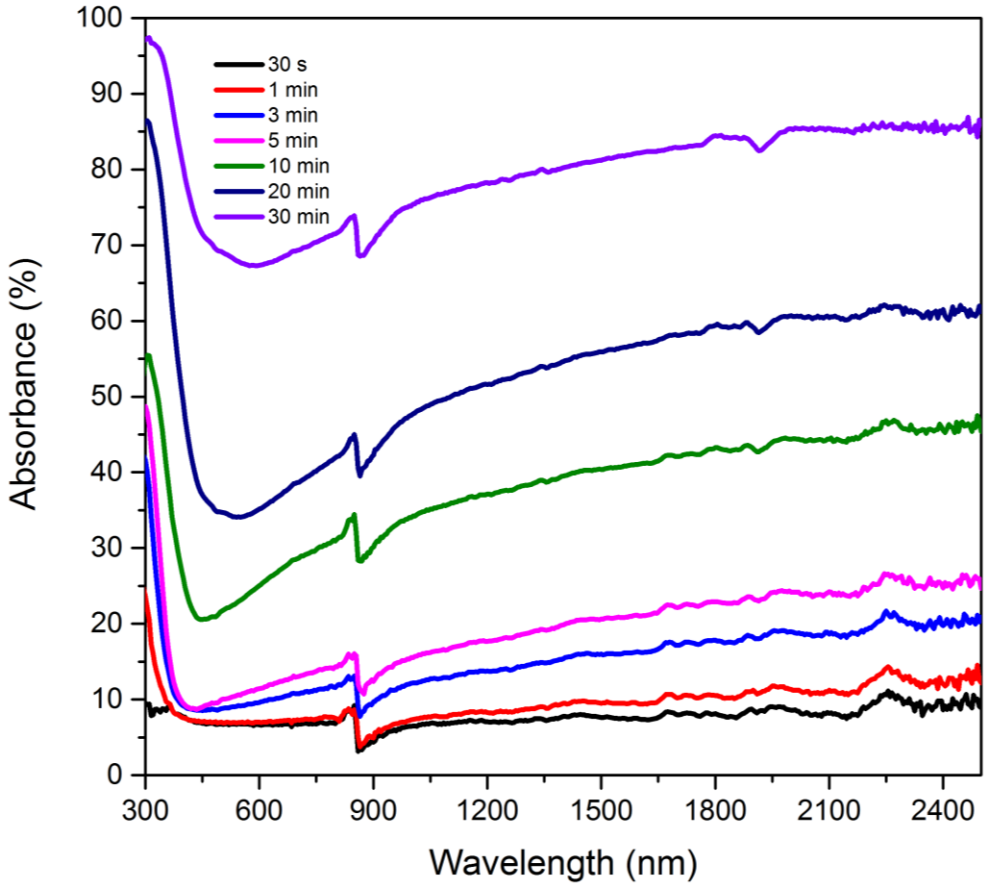

Figure 3.7. Calculated absorbance spectra of WO_x thin films deposited for 30s, 1 min, 3 min, 5 min, 10 min, 20 min, and 30 min respectively (aberant data due to grating change of the UV-Vis spectrometer).

In order to investigate the NIR shielding property of WO_x thin films deposited for 30 s to 30 min on quartz, compared with a plain quartz substrate, the WO_x thin films were put on the top of a polystyrene box shielding the irradiation from 25 W halogen light, and the temperature change of that box was recorded as shown in Figure 3.1. After being irradiated by the halogen light for one hour, the temperature of that box shielded by WO_x thin film deposited for various times was 47.6 (30 s), 47.5 (1 min), 46 (3 min), 45.6 (5 min), 43.5 (10 min), 43 (20 min) and 39.2 ℃ (30 min) compared to 48.0 ℃ for plain quartz as shown in Figure 3.1. The result agrees with NIR absorption increasing as the length of the NRs increase owing to stronger IVCT/SPH absorption. Therefore, balancing visible light transmittance and NIR absorption, the WO_x thin film deposited for 10 min is a potential candidate for NIR shielding coating with around 70 % visible light transparently and 40 % NIR absorption (1500 nm), reducing temperature by 4.5 ℃ in a simulated NIR absorption experiment.

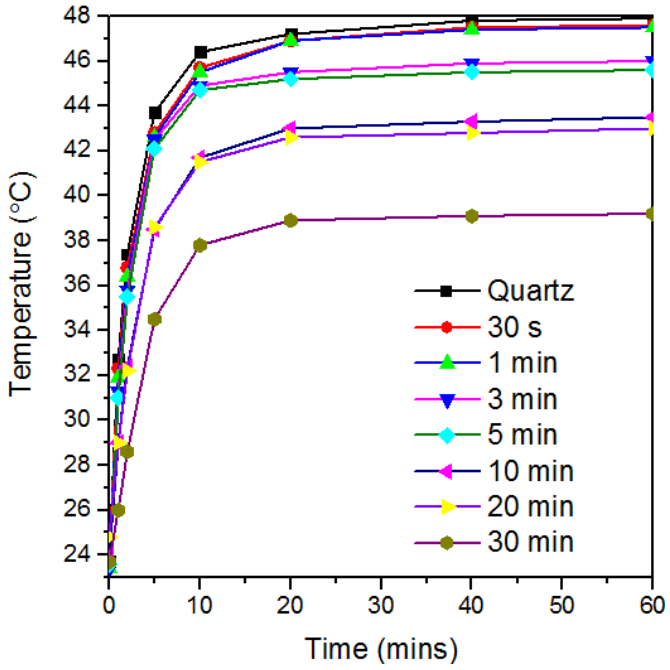

Figure 3.8. The inside temperature of polystyrene box with a lid which is the WO_x thin films deposited for 30s to 30 mins dependence on the irradiation time.

3.2 Photocatalytic Degradation of Toxic Pollutant

3.2.1 Introduction

The band gap (E_g) and band edge positions of metal oxide semiconductors are crucial in photocatalytic applications and heterojunction design. Although the valence band (VB) maxima (vs. NHE) of many metal oxide semiconductors, e.g. bulk WO_3 with indirect band gap 2.6 ~ 2.8 eV, are sufficiently positive to oxidise H_2O, the conduction band (CB) minima are insufficiently negative to reduce O_2/H^+. This results in low photocatalytic activity compared to anatase (TiO_2) as shown in Figure 3.9.[3,133,185,186] A potential strategy to enhance photocatalytic activity is therefore to shift the conduction band (CB) level more negative than the O_2/H+ reduction potential whilst at least maintaining the valence band (VB) level more positive than the H_2O oxidation potential. This has previously been achieved by doping with metals and/or non-metals, or via the quantum size effect,[28,187,188] although reproducible preparation of particles sufficiently small (< 2 nm) to exploit quantum size effects has proved synthetically challenging.

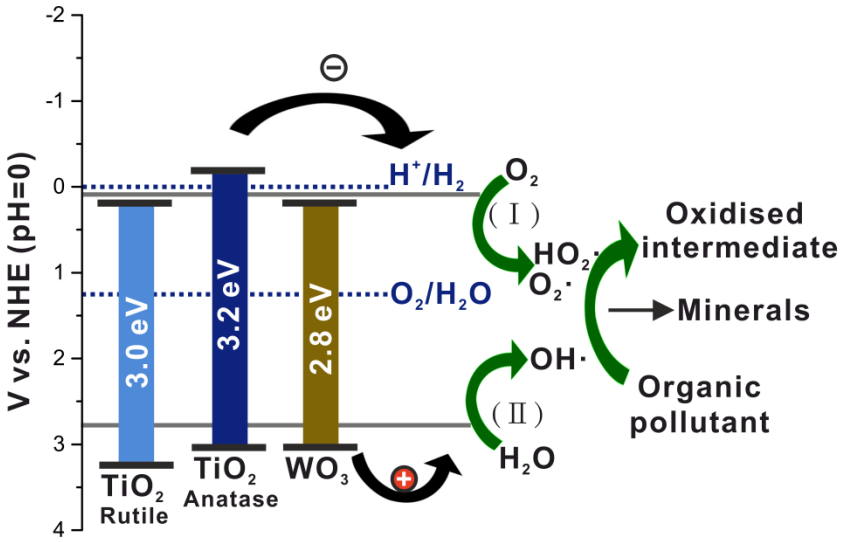

Figure 3.9. Relationship between band structures of WO_3, Rutile (TiO_2) and Anatase (TiO_2), and the redox potential of water splitting (vs. NHE at pH=0); the redox potential and general reactions for the photocatalytic degradation of organic pollutant: (I) the reduction reaction of O_2 producing superoxide radicals (O_2 ·) and/or hydroperoxy radical (HO_2 ·), (II) the oxidation reaction of H_2O creating hydroxyl radical (OH ·).[133,141,189]

In the previous section, the growth mechanism of tungsten oxide was studied. The formation of a WO_3 NRs array was attributed to the V_O created in the directions [100] and [010] leading to defects suppressing crystal growth but driving the crystal growth along direction [001] (without defects). In this section, the WO_3 NR array thin films were prepared by AACVD for various deposition times from 30 s to 30 min in order to investigate if their band structure and photocatalytic varied.

3.2.2 Experimental

The WO_3 NR array thin films were prepared by AACVD with the same conditions of AM375q-ann (see section 2.2.2) for deposition times from 30 s to 30 min were denoted as WO_3 ("t" min) where "t" represents for deposition time.

The photodegradation of stearic acid (SA) was tested via Fourier transform infrared (FTIR) (Perkin Elmer RX-I) spectroscopy scanning in the range 2700–3000 cm^{-1}. A thin layer of stearic acid was dip-coated onto the as-synthesized WO_3 films from a 0.05 M stearic acid solution in chloroform (Figure 3.10), and then irradiated by UV light in spectra range of 340 to 410 nm

(maximum at 365 nm) (4 mW cm^{-2}) (Figure 3.11) with area of samples 0.78 cm^2. Consequently, the IR spectra were recorded in absorbance mode and the integrated areas of typical C - H bands of the acid at 2958, 2923 and 2853 cm^{-1} for a serial of radiation time. These bands give an estimation of the number of molecules of stearic acid degraded using a conversion factor reported in the literature (1 $cm^{-1} \equiv 9.7 \times 10^{15}$ mol)[134]. Finally, the formal quantum efficiency (FQE) value can be obtained as $FQE\ (SA) = \frac{rate\ of\ removal\ of\ SA\ (molecules/s)}{rate\ of\ incident\ light\ (photons/s)}$ in order to compare the photocatalytic efficiency of different samples.

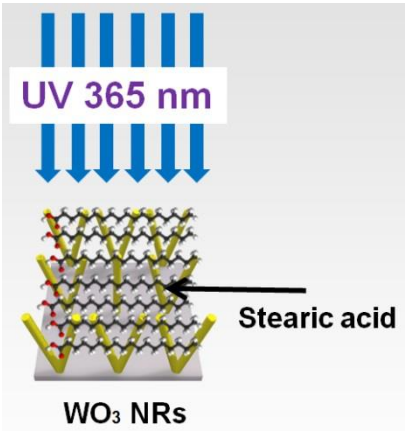

Figure 3.10. Schematic outline of degradation SA test. A thin layer of stearic acid was dip-coated onto the as-synthesized WO_3 films, and then irradiated under UV light with 365 nm.

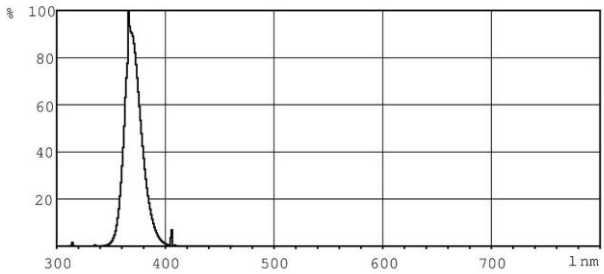

Figure 3.11. Spectra of UVA light (Philips, TL-D 18W BLB) present the range from 340 to 410 nm.[190]

3.2.3 Results and Discussions

The colour of as-synthesized thin films changed as the deposition time increased form 30 s to 30 min as shown in Figure 3.12. WO_3 (30 s) was transparent becoming white with lower transparency when deposited for 10 min and after deposition for 30 min sample became yellow white.

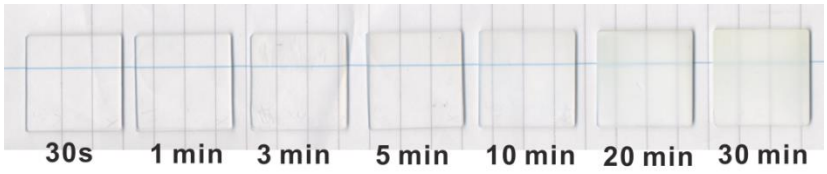

Figure 3. 12 The WO_3 thin films with NR structure were prepared by AACVD for various deposition time such as 30 s, 1 min, 3 min, 5 min, 10 min and 30 min.

As shown in Figure 3.13, the cross-section SEM images of the as-synthesized WO_3 thin films for 30 seconds to 30 minutes illustrated the thickness (which were measured at a point 45 mm from the inlet of reactor) increased from 430 ($\pm$70) nm (30s) to 4200 ($\pm$100) nm (30 mins), and the density of NRs also increased. Therefore, when the deposition time increase, the as-synthesized WO_3 thin films became less transparent.

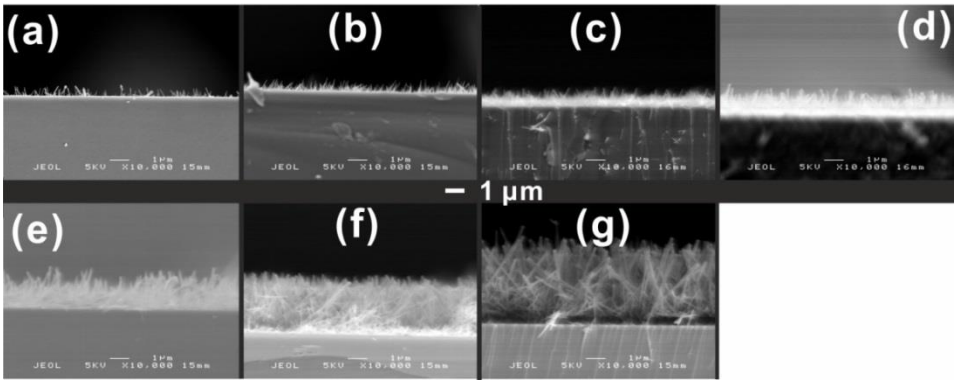

Figure 3.13. Cross-section SEM images of WO3 thin films deposited in 0.5 (a), 1(b), 3(c), 5(d), 10(e), 20(f) and 30 minutes (g) via AACVD.

As shown in Figure 3.14, glancing XRD revealed tungsten oxide with $W_{32}O_{84}$ (discussed in section 3.1). After annealing, substoichiometric tungsten oxide was oxidised and hence monoclinic WO_3 was presented (a=7.306, b=7.540, c=7.692 Å and β=90.881°, PDF# 01-072-0677, Figure 2.54) with the intensity of the dominant reflection (002) becoming stronger and lower intensity peaks emerging as the length of the NRs became longer. The strong (002) reflection of the XRD pattern is in good agreement with the NRs growth along [001] direction observed by TEM as shown in Figure 2.38.

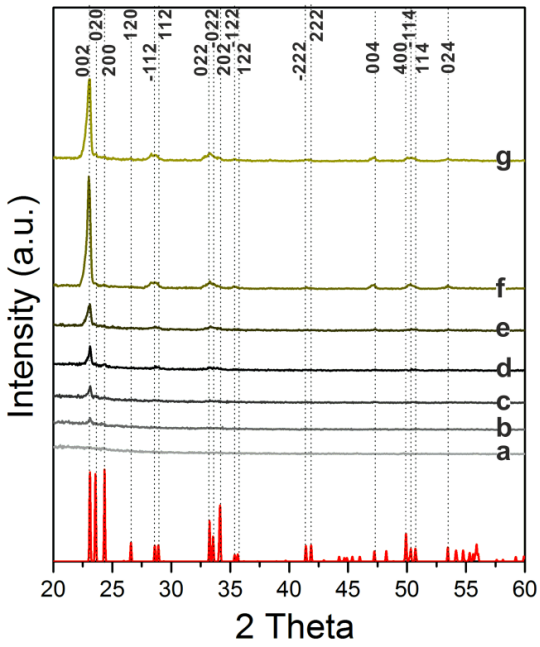

Figure 3.14. Glancing angle XRD patterns of WO_3 thin films deposited after 0.5 (a), 1 (b), 3 (c), 5 (d), 10 (e), 20 (f) and 30 (g) minutes (from bottom to top) via AACVD matching the reference patterns of monoclinic WO_3 (PDF# 01-072-0677) in red (bottom).

As shown in Figure 3.15a, b and c, the optical properties of the films altered systematically with the length and density of the WO_3 NRs which was controlled by the deposition time. Transmittance generally decreased and reflectance and absorbance in the visible region increased with increasing deposition time. Based on the calculated absorbance spectra, the band gap of as-synthesized samples was estimated by Tauc plot giving indirect band gaps from 2.56 - 3.05 eV (Figure 3.15d) and direct band gaps of 2.99 - 3.59 eV (Figure 3.15e) as deposition time deceased. Bulk WO_3 has an indirect band gap of 2.62 eV and a direct band gap of 3.50 eV with ΔE_g (difference bandgap between direct and indirect) of ~ 0.9 eV.[191] The sample deposited for 30 mins had band gap value comparable to the bulk WO_3, however samples deposited at shorter times showed widening of the indirect band gap compared to the bulk (Figure 3.15f). The sample deposited for 30 s with NR length 350 nm and diameter 75 nm showed an indirect band gap of around 3.1 eV, similar to values observed for WO_3 quantum dots with size of 1.4 nm.[7] Moreover, the ΔE_g narrowed (from 0.6 to 0.4 eV) with increasing deposition time.

In section 2.3.3, we observed dislocation loops in the nucleus of the tungsten oxide in the [010] and [100] directions, perpendicular to NR growth [001] direction (Figure 2.38). The

formation of dislocation loops which provide strain fields have been seen to lead to quantum-spatial-confinement (QSC) effects,[188] and this may be the cause of the QCE of widened indirect band gap in both our 1D tungsten oxide NR arrays where the diameter is far larger than the particle size of semiconductors which display a quantum-size-confinement (Q-size) effect (between 1 to 12 nm).[192] As the NRs grow along [001] direction without defects (preferred orientation of (002) shown in XRD patterns in Figure 3.14), the strain fields from dislocation loops in [010] and [100] directions would relax in the NR [001] growth direction leading to a decaying in QSC effect decay and narrowing of the indirect band gap to bulk WO_3.[165]

It is notable that samples WO_3 (30 min), WO_3 (20 min) and WO_3 (10 min) gave an optical absorption peak at NIR region (~ 1000 nm) which was previously observed in WO_3 with V_O in previous reports and attributed to IVCT or small-polaron hopping.[193] A V_O can donate two electrons reducing W^{6+} to W^{4+} and forming small-polaron by short range electron-lattice interactions, creating a potential well with a small-polaron ground state.[162] The energy of incident light needed to excite the excess bound electrons released from that potential well is $2E_p$ (where E_p is the polaron binding energy, also described as the activation energy of polaron-hopping) with consideration of a fast change in potential of atom. Simultaneously phonons is also able to be excited known as a shake-up-effect, hence the maximum energy of absorbed light is ideally at around $4E_p$.[171,193] Based on a small-polaron ground state reported at 0.15 to 0.2 eV below the CB minimum dependent on varying concentration of V_O,[171,194] the maximum NIR absorption peak was calculated approximately between 0.8 to 1.2 eV (1500 to 1000 nm) close to the measured value around 1000 nm (Figure 3.15c).

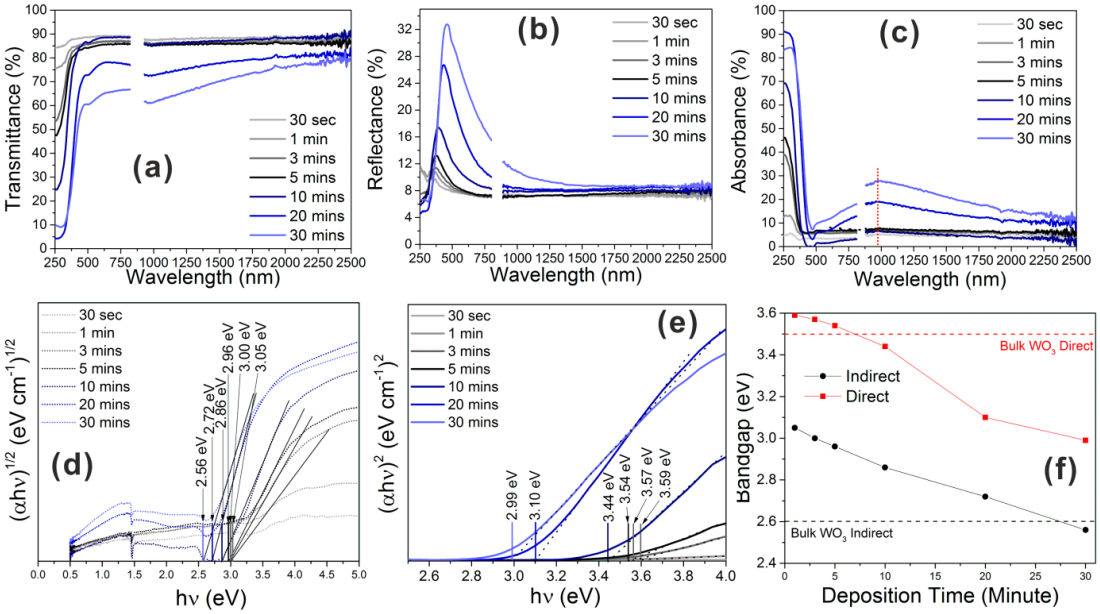

Figure 3.15. The transmittance (a), reflectance (b) and absorbance (c) spectrum (aberant data due to grating change of the UV-Vis spectrometer has been removed) of WO_3 NR arrays deposited on quartz for 0.5 to 30 mins were used to calculate their bandgap E_g (d, indirect) and (e, direct) by tauc plots. (f) the change of indirect and direct E_g of as-synthesized thin films dependent on depositon time (1 to 30 min) compared to indirect (2.62 eV) and direct (3.50 eV) E_g of bulk WO_3.[191] Only samples 10, 20, 30 mins present NIR absorption at around 1000 nm (c).

X-ray photoelectron spectroscopy (XPS) was used to identify the composition of the tungsten oxide NR arrays prepared with 3 to 30 min deposition time. The W 4f region showed two peaks at 35.4 (±0.4) eV and 37.5 (±0.3) eV which were fitted by using software "CasaXPS" showing two components at 35.4 and 34.2 eV (binding energy) attributed to $W_{4f7/2}$ of W^{6+} and W^{4+} respectively.[160,195] Deconvolution of the W 4f region showed both W^{6+} and W^{4+} states, with the relative concentration of W^{4+} increasing from 0 to 8.56 % as deposition time increased (Figure 3.16a). The appearance of W^{4+} was supported by W 5d peaks which were observed in the XPS VB region for deposition time from 10 to 30 min (Figure 3.16b and 3.17) owing to electrons partially fill the W 5d orbitals which are detectable close to the Fermi level (BE = 0 eV) for reduced WO_x. Based on the absence of a detectable W 5d peak in the valence band, the symmetrical (yet broad) W 4f core line XPS peaks, and the absence of a NIR absorption in the optical spectrum (Figure 3.15c), we conclude that only W^{6+} is present for these short deposition time samples, *i.e.* no W^{4+} or other reduced tungsten states are present within the detection limits of the techniques employed. Assuming V_O is not balanced by cations vacancies then the concentration of V_O can be estimated by the concentration of W^{4+} analysed by XPS, and hence

the concentration of V_O increases as the deposition time increases, corresponding to an increase in the length and diameter of the NR (see detail in section 2.3.3) due to NR coalescence. When the coalescence occurs as the NR grows, the individual layers are not lattice matched forming strained layer. The homogeneous strain energy is proportional to the thickness of the strained layer, and when the strained layer is thicker than a critical thickness (e.g. Ge_xSi_{1-x} films growth on Si with crystal thickness in order of 10 – 100 Å) relaxation can occur by producing defects and dislocations.[196] Therefore as the NR diameter increase (more layers coalesce) the V_O concentration increases, in agreement with the XPS results of the V_O concentration increasing as deposition time increases (Figure 3.16a).

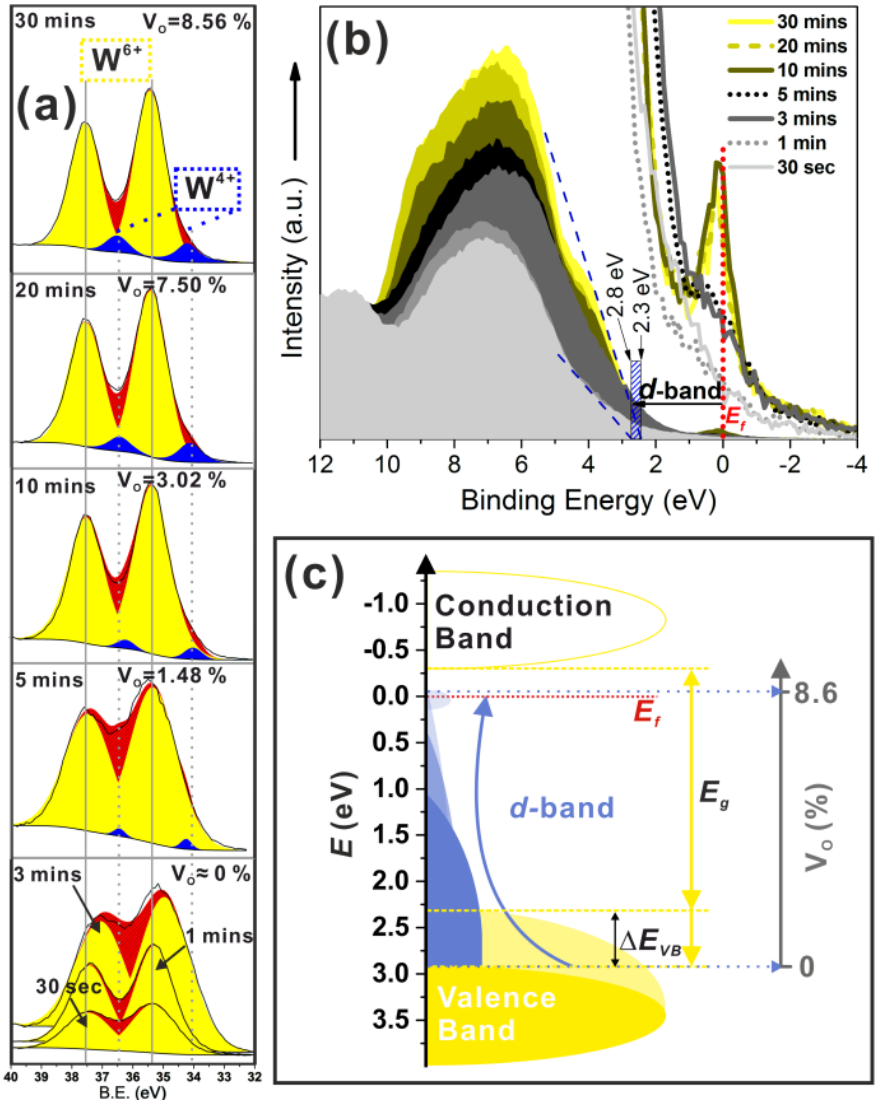

Figure 3. 16. XPS spectra for the W 4f region (a), valance band (b) and schamic band strucutre (c) of WO_3 NR arrays thin film deposited from 0.5 to 30 mins with reference C1s peak calibrated to 284.8 eV and respecting to fermi level (E_f = 0 eV). The expansion of *d*-band of W^{4+} and E_g with red shift of VB is dependent on the increase of V_O (from 0 to 8.6 %).

The gradient and binding energy of the VBM relative to the Fermi level (0 eV), obtained by extrapolating the low binding energy edge of the VB to the spectra baseline depending on the deposition time. The VBM shifted from 2.8 eV to 2.3 eV (at 30 s to 30 min deposition time) (Figure 3.17). As deposition time increased, the VBM shifted up towards the Fermi level. For short deposition times, the VB spectrum has a considerable tail into the band gap. This indicates the presence of a low concentration of filled states, which may be due to surface states or disorder states, as found in black-TiO_2.[197,198] However, in contrast to black-TiO_2, these disorder states are of much lower XPS spectral intensity and do not cause optical absorption. This may be due to the lower density of these disorder states. Therefore, the schematic band structure of all the as-synthesized thin films (Figure 3.16c) illustrated that the expansion of the indirect bandgap at short deposition times from 2.6 to 3.1 eV can be mainly accounted for by the downward shift of the VBM from 2.3 to 2.8 eV below the Fermi level. In this case, assuming the indirect optical transition is at the fundamental bandgap, CBM is situated 0.2-0.3 eV above the Fermi level for all samples.

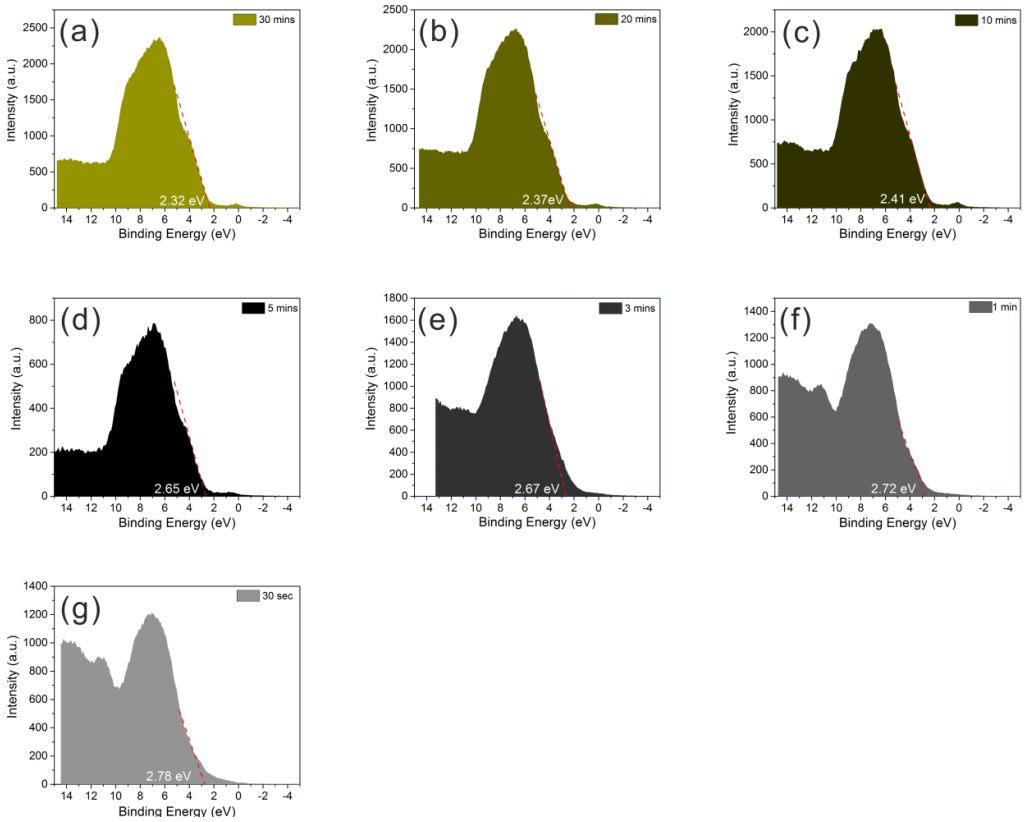

Figure 3.17. XPS spectra for the valance band of WO_3 thin films with NRs structure deposited on quartz after 30 mins to 30 seconds (a to g) with reference C1s peak calibrated to 284.8 eV.

In summary, the band structures of WO_3 NR array thin films were modified by V_O *via* forming small-polarons and dislocation loops controlled by deposition time. Consequently, the photocatalytic activities of those thin films were evaluated by photodegradation of stearic acid (SA) under UVA irradiation (Philips, TL-D 18W BLB, maximum at 365 nm with spectra from 340 to 410 nm, Figure 3.11) and are reported in terms of formal quantum efficiency (FQE). This is defined as the amount of SA molecules photodegraded per incident photon, estimated by linear regression of the initial 30 to 40% steps (Figure 3.18a).[139] Surprisingly the WO_3 film (5 mins) with the (joint) wider indirect bandgap $E_g \approx 3.0$ eV, i.e. the sample absorbing least photons, gave the highest activity amongst all samples, with the activity decreasing as the bandgap decreases (Figure 3.18b), i.e. activity decreased as the number of photons absorbed increased. As the deposition time increased, the density and length of NR increased, and hence the sample WO_3 (30 min) was expected to give the highest activity of photodegradation of SA. Although the indirect bandgap of WO_3 (5 min) expanded ~0.4 eV This was due to VB shifting downward and not shifting the CB upwards and hence this would be no change in the potential relative to O_2/H^+ reduction photo-reaction 1 (Figure 3.9). The lower photocatalytic degradation of SA under UVA found in those samples deposited for longer time 5 mins maybe due to the increased concentration of V_O forming more dislocation loops which are capable of spatially localizing carrier diffusion in the undefected point rather than point defects elsewhere outside the dislocation loops attributed to enhanced radiative recombination.[188]

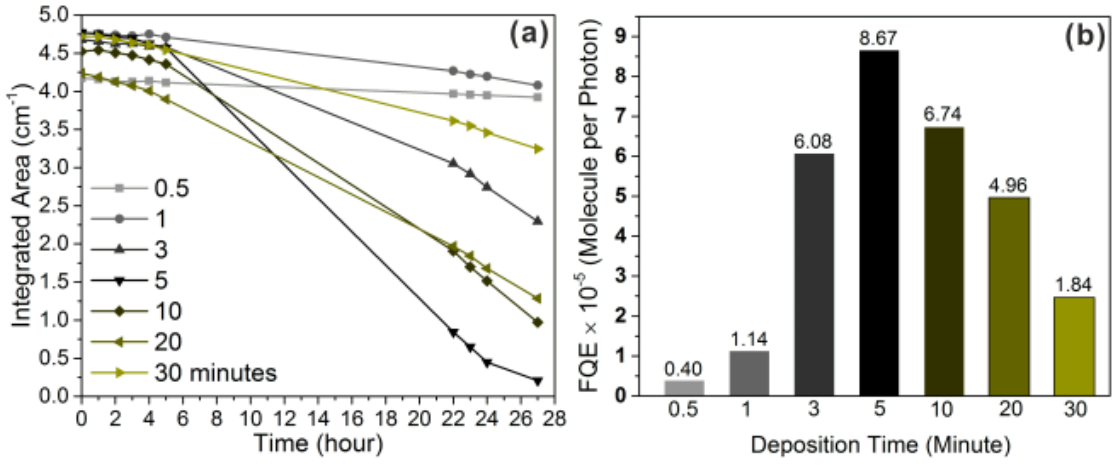

Figure 3.18. Integrated areas of stearic acid bands (a) were estimated during UVA light (4.2 mW cm^{-2}) irradiation of SA coated as-synthesized WO_3 thin. Formal quantum efficiencies(b), given as degraded SA molecules by per incident photon in unit (molecule photon^{-1}), were calculated from the initial rates of photodegradation of SA (a).

3.3 Conclusion

In chapter 2, V_O defects were found in tungsten NR witnessed by the optical absorption in NIR described as intervalence charge transfer or/and small-polaron hopping. Therefore, in section 3.1, the NIR absorption of WO_x NR thin films were studied for use as a solar heat-filter coating. Hence, in order to find out the best candidate for a NIR shielding coating simulated NIR absorption experiments were conducted, varying the density and length of WO_x NR by varying the deposition time from 30 s to 30 min. A WO_x thin film deposited for 10 min is a potential candidate for a NIR shielding coating giving around 70 % visible light transparent and 40 % NIR absorption (1500 nm), reducing the internal temperature by 4.5 ℃.

Subsequently, the change of band structures of as-synthesized WO_3 nanorod (NR) array thin films by AACVD dependent on deposition time were studied. As the deposition time increased, the length and diameter of NR increased leading to V_O increasing due to NR coalescence during growth inducing strained layer relaxation, producing more defects and dislocations. The appearance of oxygen vacancy (V_O) was able to modify their band structure *via* forming small-polarons and creating dislocation-loops. The small-polaron hopping gave rise to an optical absorption peak in the NIR and appearance of a partially occupied *d*-band extending to fermi level (binding energy = 0 eV). The dislocation-loops (diameter 0.4 to 1.5 nm) created in [010] and [100] directions perpendicular to NR growth direction [001] provided spatial strain inducing quantum-spatial-confinement leading to bandgap expansion (3.1 eV in 0.5 and 1 min sample compared to 2.6 eV in bulk WO_3) giving the suggestion for quantum confinement effect of WO_3 NR with large size (length > 350 and diameter > 73 nm), and can also increase radiation recombination by spatially localizing carrier diffusion in the undetected point rather than point defects elsewhere outside the dislocation-loops resulting the direct bandgap narrowing (3.0 eV in 30 min sample compared to 3.5 in bulk WO_3) implying an indirect-direct semiconductor transition which provide an explanation for the previous observation of WO_3 NR with strong photoluminescence at room-temperature.[199,200]

CHAPTER 4: TUNGSTEN OXIDE-BASED HYBRID NANOSTRUCTURED THIN FILM MATERIALS: DESIGN, SYNTHESIS, CHARATERISATION AND APPLICATION

In this chapter, AACVD is used to fabricate noble metal nanoparticle (NP) (Au, Pt, Pd or Ru) decorated WO_3 nanorod (NR) hybrid nanostructured thin films. After subsequent oxidative treatment noble metal oxide NPs/WO_3 NR hybrid nanostructured heterojunction thin films are obtained for PdO/WO_3 or RuO_2/WO_3. Their photocatalytic activity is evaluated by photodegradation of stearic acid.

4.1 Noble Metal (Au, Pt, Pd or Ru) or Noble Metal Oxide (PdO or RuO_2) Nanoparticle decorated Tungsten Oxide Nanorod Films

4.1.1 Introduction

Noble metal nanoparticles (NPs) e.g. Au, Pt, Pd and Ru with diameter smaller than 2-3 nm have been found to be catalytically active (e.g. CO oxidation, hydrogenation of allyl alcohol),[109,201,202] have applications in photocatalysis (e.g. organic pollutant degradation, CO_2 reduction, hydrogen production),[203] and NPs of their oxide such as PdO and RuO_2 are utilized as catalysts for oxygen reduction reaction and oxygen evolution reactions respectively.[122,204] If metal NPs are decorated on a metal oxide support then metal/metal oxide semiconductor hybrid nanostructured materials are formed which have potential applications in catalysis, electrocatalysis, photocatalysis, solar cell, plasmon-enhanced spectroscopy and biotechnology, with the metal-oxide interaction radically enhancing the performance of supported catalysts due to the so-called 'strong metal-support interaction'.[203,205,206] For example, supported Au NPs on active (e.g. TiO_2) or inert (e.g. BN, SiO_2) substrates demonstrate enhanced catalytic properties if their diameters fall below 4 nm, dependent on the substrate.[105,207]

Generally, synthesis of metal NPs in solution requires organic agents such as stabilisers, dendrimer templates and reducing agents which typically lead to a layer of organic compound encapsulating the nanoparticles or to contamination with foreign anions.[105,109,203,208] Despite progress, e.g. recently a hydrothermal method for fabricating metal/$WO_{2.72}$ hybrids without organic agents was reported,[91] the restriction of this method is the reducing support which must be strong enough to reduce the metal salt to be metallic NPs.

Our aim was to directly deposit metal NPs on thin film supports without the introduction of foreign organic agents or requirement for a reducing support, whilst also being able to tune the NP size. Here we describe a method for growth of noble metal (Au, Pt, Pd or Ru) or their oxide (PdO or RuO_2) NPs supported on tungsten oxide nanorod (NR) array thin films, with NP size simply controlled by the deposition time during aerosol-assisted chemical vapour deposition (AACVD). The use of AACVD as a variant of the conventional chemical vapour deposition

(CVD) process is crucial because it utilises solvent aerosols to transport precursors and hence can be used with many relatively cheap commercially available metal precursors not suitable for traditional CVD.[209]

4.1.2 Experimental

The synthesis of WO_3 NR array thin film (AM375q) is described in the experimental of section 2.2.2, with a deposition time of 5 minutes showing the best photocatalytic activity for degradation of stearic acid under UV light irradiation (see detail in section 3.2). The precursor $W(CO)_6$ (Aldrich with 99% purity) was dissolved in a mixture of acetone and methanol in a 2 : 1 ratio, and an aerosol created by an ultrasonic humidifier operated at 2 MHz. The aerosols were transported to the reactor by N_2 carrier gas (99.99%, BOC, flow rate 300 cm^3/min) controlled by a mass flow controller (MFC, Brooks), decomposed and reacted over a quartz substrate (1 mm thickness) at 375 ℃ and then samples were annealed in air at 500 ℃ for 2 hours.

The metal NPs were decorated on the as-synthesized WO_3 NR thin films with the parameters shown in Table 4.1 via the AACVD process described above, with different deposition times in order to alter the noble metal NP size on the WO_3 NR. The obtained metal NPs/WO_3 NRs hybrid nanostructure thin films are denoted as M/WO_3 (t minute), where 't' is the deposition time for the metal precursor during AACVD, for example Au/WO_3 (1 min) implying that the deposition time of Au precursor on WO_3 NR array is 1 min.

The obtained noble metal NPs/WO_3 NR hybrid nanostructure thin films were oxidised by annealing at 500 ℃ in air for 2 hours in order to obtain metal oxide NPs/WO_3 NR hybrid nanostructured thin films (e.g. PdO/WO_3 and RuO_2/WO_3).

The noble metal and noble metal thin films were deposited on plain quartz substrate for 45 mins using the same amount of the metal precursors in order to obtain the valence band energy for estimating the band structure of the hybrid nanostructure samples.

Table 4.1. The deposition parameters of metal nanoparticles/WO_3 nanorods hybrid nanostructured thin films.

Sample	Precursor /g	Solvent /mL	Temperature /°C	N_2 Flow Rate /SCCM
Au/WO3	$HAuCl_4$ /0.001	Methanol /15 mL	350	300
Pd/WO3	$(NH_4)_2PdCl_4$/0.001	Methanol /15 mL	350	300
Ru/WO3	$Ru_3(CO)_{12}$ /0.001	Methanol /15 mL	350	400
Pt/WO3	H_2PtCl_6 /0.001	Methanol /15 mL	350	300

As shown in Figure 4.1, The general pathway includes three processes as follows: (I) the support material is deposited first, e.g. a nanorod (NR) structured sub-stoichiometric tungsten oxide, WO_x ($3 > x > 2$), thin film was fabricated on quartz by AACVD;[91,153] (II) the support materials can be further treated, e.g. the as-synthesised WO_x NR thin film was annealed at 500 ℃ in air for 2 hour in order to obtain fully oxidised tungsten trioxide WO_3; (III) the metal NPs were grown on the synthesized WO_3 NR thin film support *via* thermally activated AACVD;[209] (IV) metal NPs grown on the support can be further treated, e.g. the oxidation of metal, *via* annealing at 500 ℃ in air for 2 hours.[210] The mean particle size of noble metals is obtained by counting NPs (>200 particles) from many different WO_3 NRs in TEM images. The number concentration of NPs is estimated by counting the number of NPs on a WO_3 NR and then dividing by the surface area of that NR. The coverage of NPs on a WO_3 NR surface was estimated by the equation $[n\pi(0.5d)^2]/(0.5S)$ where n is the number concentration, d is the mean size of NPs and S is the surface area of that NR.

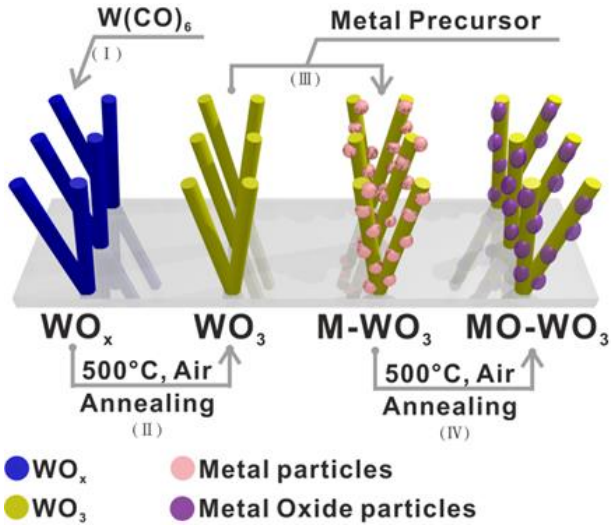

Figure 4.1. Schematic processes for fabrication of metal or metal oxide nanoparticles supported on a tungsten oxide nanorod array on quartz substrate *via* AACVD.

The photodegradation of stearic acid (SA) was detected by Fourier transform infrared (FTIR) (Perkin Elmer RX-I) spectroscopy scanning in the range 2700–3000 cm^{-1}. A thin layer of stearic acid was dip-coated onto the as-synthesized WO_3 films from a 0.05 M stearic acid solution in chloroform (Figure 3.10), and then irradiated by UV light in spectra range of 340 to 410 nm (maximum at 365 nm) (4 mW cm^{-2}) (Figure 3.11) with area of the samples being 0.78 cm^2. Consequently, the IR spectra were recorded in absorbance mode and the integrated areas of typical C - H bands of the acid at 2958, 2923 and 2853 cm^{-1} recorded for a series of radiation times. These bands give an estimation of the number of molecules of stearic acid degraded using a conversion factor reported in the literature (1 $cm^{-1} \equiv 9.7 \times 10^{15}$ mol)[134]. Finally, the formal quantum efficiency (FQE) value can be obtained as $FQE\ (SA) = \frac{rate\ of\ removal\ of\ SA\ (molecules/s)}{rate\ of\ incident\ light\ (photons/s)}$ in order to compare the photocatalytic efficiency of different samples.

4.1.3 Results and Discussion

The as-synthesized thin film WO_3 (5 min) (AM375q ann) is white and transparent as shown in Figure 3.2.2. After noble metals were deposited on undecorated thin film WO_3 (5 min), the colour of noble metal NPs/WO_3 NR hybrid nanostructure thin films were changed. As shown in Figure 4.2, (a) the colour of Au/WO_3 thin films became pink as the deposition time of Au precursor increase from 30 s to 20 mins, (b) the colour of Pd/WO_3 thin films became yellow as the deposition time of Pd precursor increase from 5 to 35 mins, (c) the colour of Pt/WO_3 thin films became yellow as the deposition time of Pt precursor increase from 1 to 20 mins, (d) the colour of Ru/WO_3 thin films became brown as the deposition time of Ru precursor increase from 1 to 36 mins from white (undecorated WO_3 thin film). The colour of noble metal/WO_3 thin films became darker as the deposition time of noble metal precursors increases. After annealing at 500 ℃ in air for 2 hours, Pd or Ru NPs on WO_3 NRs were oxidised to PdO or RuO_2

respectively, forming PdO/ WO_3 or RuO_2/ WO_3 hybrid nanostructure thin films of which became yellow or brown in colour (Figure 4.2e and 4.2f).

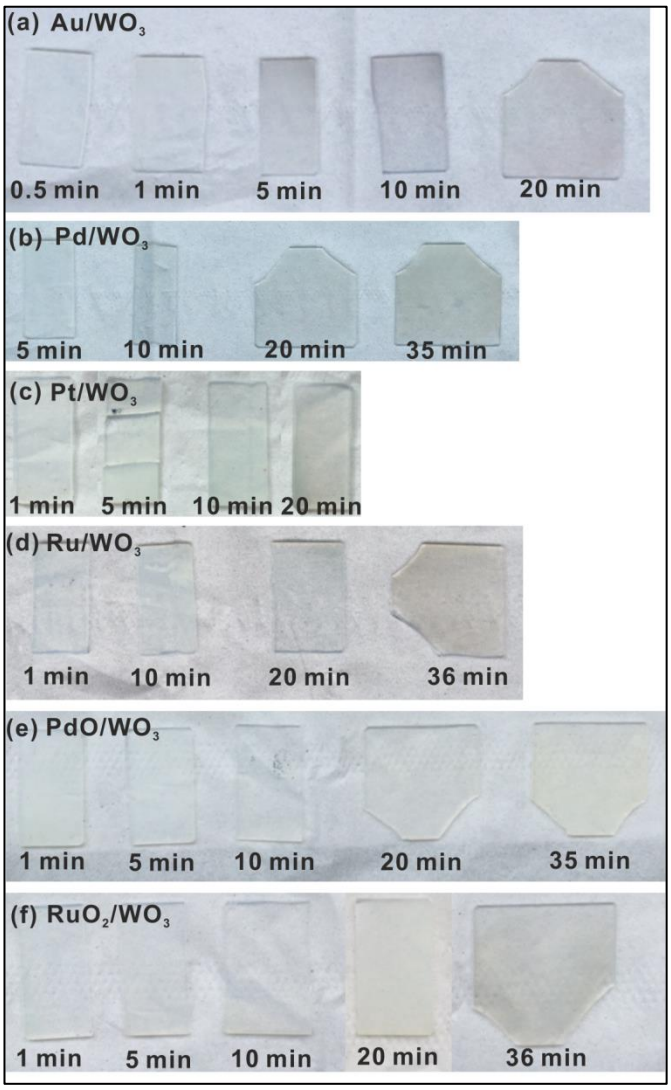

Figure 4.2. The photographs of thin films: (a) Au/WO_3, (b) Pd/WO_3, (c) Pt/WO_3, (d) Ru/WO_3, (e) PdO/WO_3, (f) RuO_2/WO_3.

The WO_3 NR array thin films (AM375q) deposited for 5 mins were characterised by glancing angle XRD as monoclinic WO_3 (m-WO_3) (PDF 072-0677, a=7.306, b=7.540, c=7.692 Å and α=90 °, β=90.881 °, γ=90 °) with a dominant (002) reflection (Figure 4.3a). Thin films decorated by noble metals or noble metal oxides NPs, even for relatively long deposition times showed a similar pattern to that of the undecorated WO_3 NR array support, e.g. Au//WO_3 (20 min), Pt//WO_3 (20 min), Pd/WO_3 (35 min), Ru/WO_3 (36 min), PdO/WO_3 (35 min) and RuO_2/WO_3

(36 min) (Figure 4.3b to 4.3g). This is likely due to the loading and long range order of NPs being too low to be observed by XRD, in agreement with previous study,[211] thus XRD was unable to detect the noble metal or their oxide on those films.

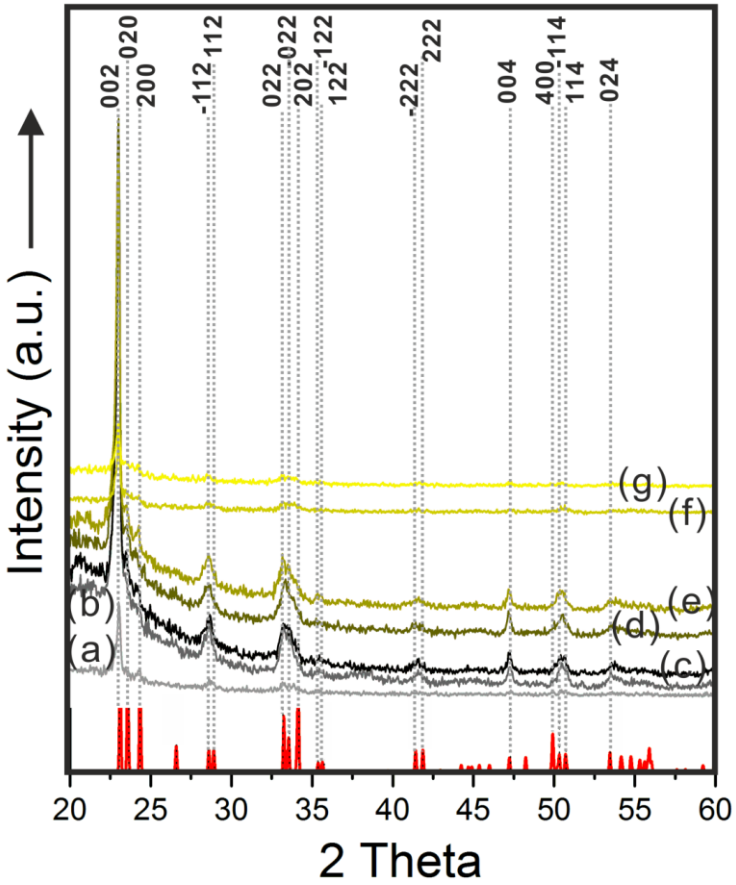

Figure 4.3. XRD patterns of (a) WO_3, (b) Au/WO_3 (20 min), (c) Pt//WO_3 (20 min), (d) Pd/WO_3 (35 min), (e) Ru/WO_3 (36 min), (f) PdO/WO_3 (35 min) and (g) RuO_2/WO_3 (36 min) which matches the monoclinic WO_3 reference pattern (red colour) (PDF 072-0677, *a*=7.306, *b*=7.540, *c*=7.692 Å and α=90 °, β=90.881°, γ=90 °).

X-ray photoelectron spectroscopy (XPS) confirmed the sample Au/WO_3 (20 min) contained Au (0) with the Au $4f_{7/2}$ peak at 84.0 eV (Figure 4.4a).[212] The sample of Pd/WO_3 (35 min) possessed Pd (0) and Pd (II) ionisations (Figure 4.4c) with Pd $3d_{5/2}$ peaks corresponding to Pd metal (335.8 eV) and $PdCl_2$ (338.4 eV) respectively.[213,214] The presence of $PdCl_2$ is surprising, but may indicate incomplete decomposition of the precursor $(NH_4)_2PdCl_4$. The NPs of Ru/WO_3 (36 min) are comprised of both states Ru (0) and Ru (IV), with Ru $3d_{5/2}$ peaks apparent for Ru metal (280.1 eV) and RuO_2 (280.8 eV) respectively (Figure 4.4d).[215,216] The sample of Pt/WO_3 (20 min), showed only Pt (0) in the XPS spectra (Figure 4.4b) with the Pt $4f_{7/2}$ peak

corresponding to Pt metal (71.2 eV).[217] After annealing Pd/WO_3 (35 min) the sample PdO/WO_3 (35 min) contains PdO with the Pd $3d_{5/2}$ peak shifting to higher binding energy, matching the reference of PdO (337.2 eV) (Figure 4.4e),[218] and the sample RuO_2/WO_3 (36 min) contained not just Ru (IV) but also Ru (VI), with the Ru $3d_{5/2}$ peaks shifting to higher binding energy, matching the reference value for RuO_2 (280.6 eV) and RuO_x (281.9 eV) respectively (Figure 3f).[219,220]

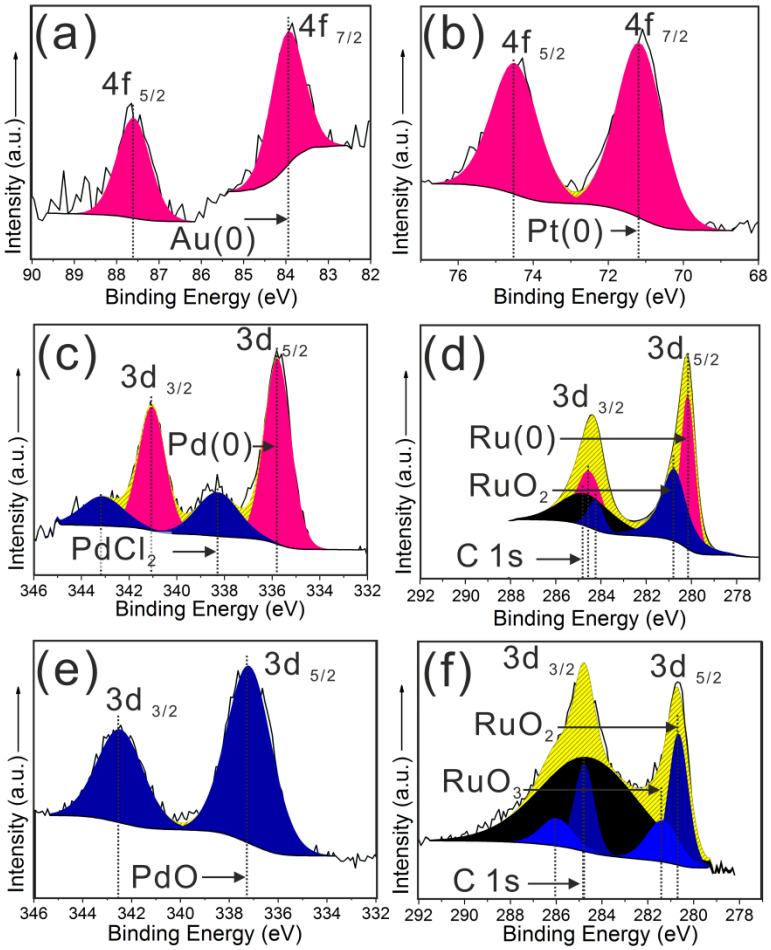

Figure 4.4. XPS spectra of the as-synthesized hybrid nanostructure thin films: (a) Au/WO_3 (20 min), (b) Pt/WO_3 (20 min), (c) Pd/WO_3 (35 min), (d) Ru/WO_3 (36 min), (e) PdO/WO_3 (35 min), (f) RuO_2/WO_3 (36 min). The peaks of metal, metal oxide or carbon are in pink, blue or carbon.

The NPs are able to be observed by the HR-TEM decorating the tungsten oxide NRs (Figure 4.5). As shown in Figure 4.5b (inset) for Au/WO_3, a NP possesses an interplanar spacing of 0.23 (± 0.01) nm corresponding to the (111) plane of Au metal, in agreement with the XPS result that Au (0) was found (Figure 4.4a). The mean size in diameter of Au NPs on the NRs increases

from 2.4 to 6.8 nm as the deposition time increases from 0.5 to 20 min (Figure 4.5a to 4.5e). The amount of those NPs also rises resulting in more surface area of the NRs being occupied by Au NPs.

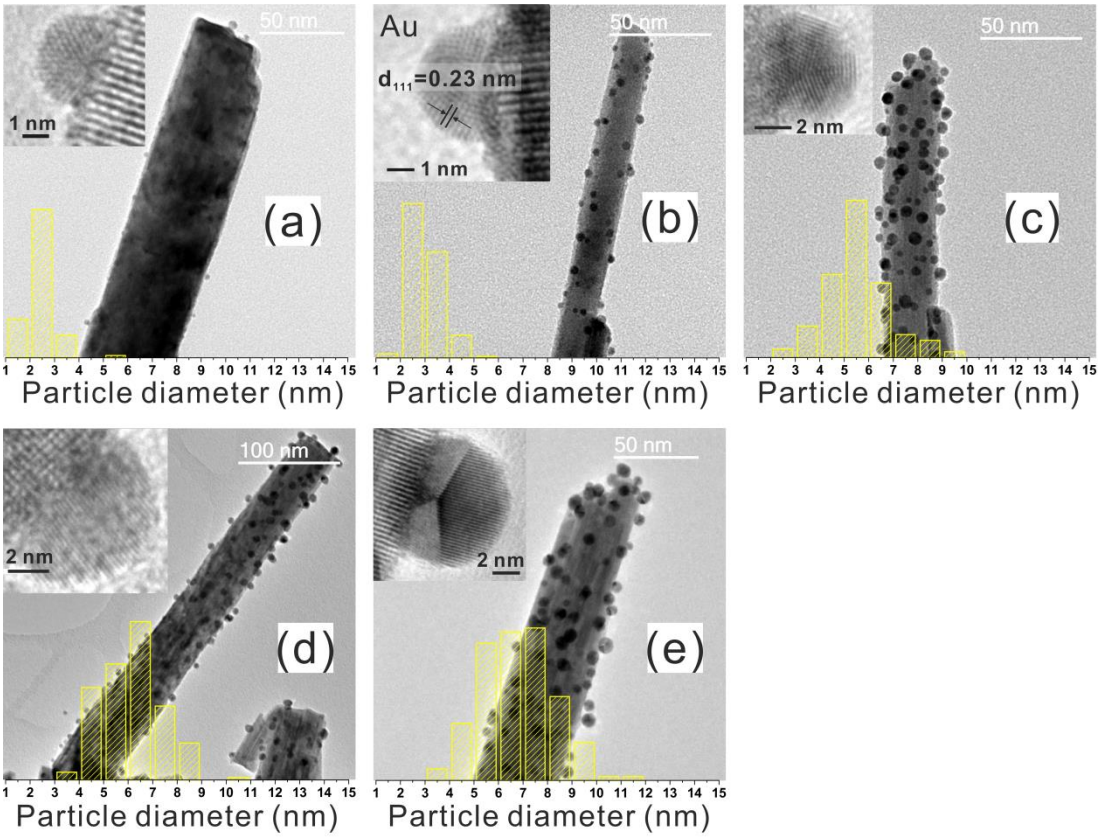

Figure 4.5. TEM images of the Au/WO_3 hybrid nanostructure thin films: (a) Au/WO_3 (0.5 min), (b) Au/WO_3 (1 min), (c) Au/WO_3 (5 min), (d) Au/WO_3 (10 min), (e) Au/WO_3 (20 min) with NP size distributions on WO_3 NR. The Au NPs with interplanar spacing of 0.23 nm corresponding to (111) plane (b inset).

For Pd/WO_3, HRTEM shows the NPs decorating the WO_3 NRs have an interplanar spacing of 0.22 ($\pm$0.01) nm (Figure 4.6a, inset) corresponding to the (111) plane of Pd metal, in agreement with the XPS result that Pd (0) was found (Figure 4.4d). As the deposition time increases from 1 to 36 min (Figure 4.6a to 4.6d), the mean size in diameter of Pd NPs on the NRs increases from 1.9 to 4.1 nm. The amount of those NPs also rises resulting in more surface area of NRs occupied by Pd NPs.

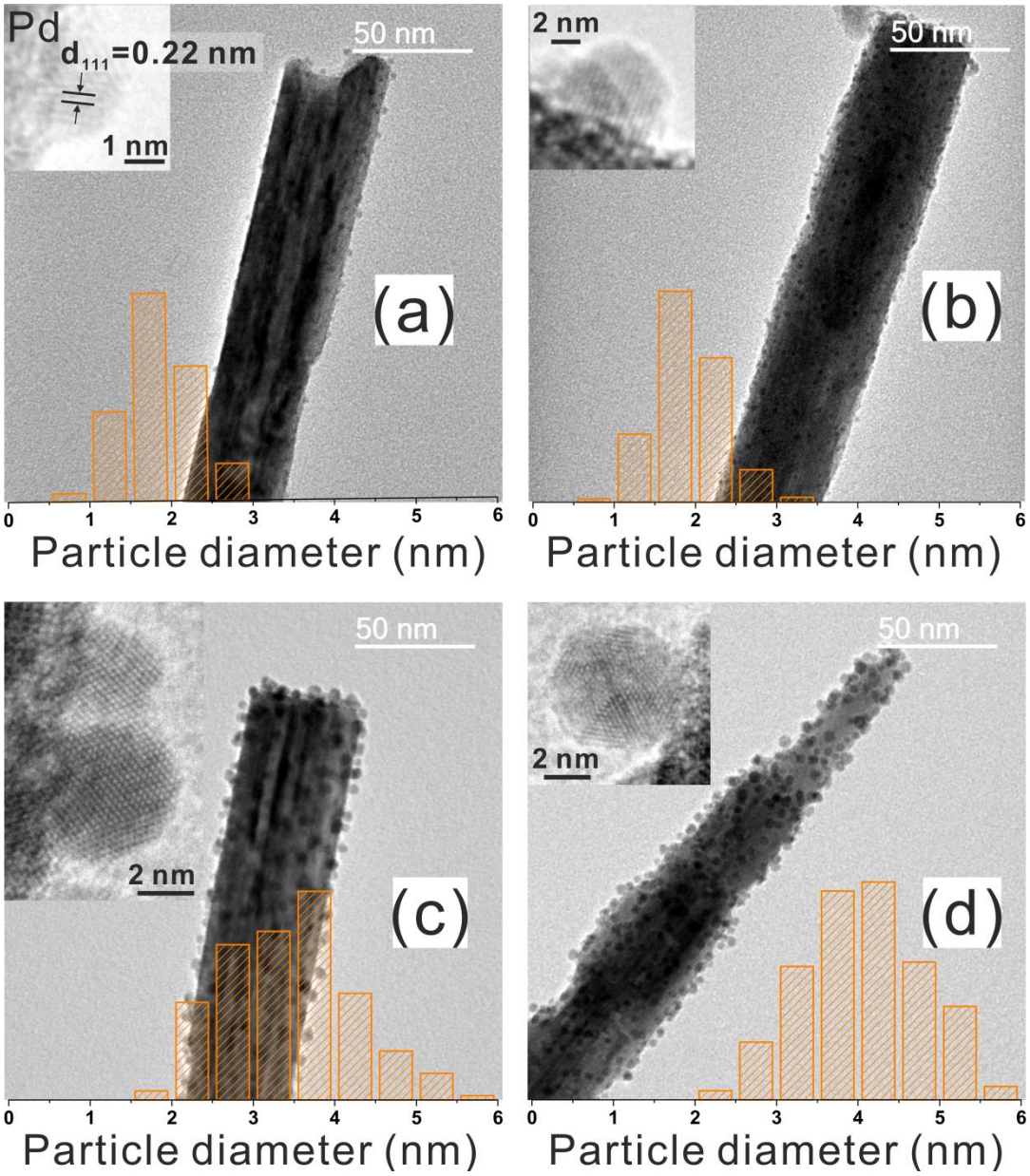

Figure 4.6. TEM images of Pd/WO_3 hybrid nanostructure thin film: (a) Pd/WO_3 (5 min), (b) Pd/WO_3 (10 min), (c) Pd/WO_3 (20 min), (d) Pd/WO_3 (35 min) with NP size distributions on WO_3 NR and insect zoom-in images of Pd NP. NPs with interplanar spacing of 0.22 nm correspond to (111) plane of Pd (a, inset).

For Ru/WO_3 the NPs were found on the WO_3 NRs (Figure 4.7) possessed an interplanar spacing of 0.21 (±0.01) nm (Figure 4.7d, inset) corresponding to the (002) plane of Ru metal, in agreement with the XPS showings that Ru (0) (Figure 4.4c). As the deposition time increases from 1 to 36 min the mean diameter of Ru NPs on the NRs increases from 1.6 to 2.9 nm, and also the mount of Ru NPs increases (Figure 4.7a to 4.7d).

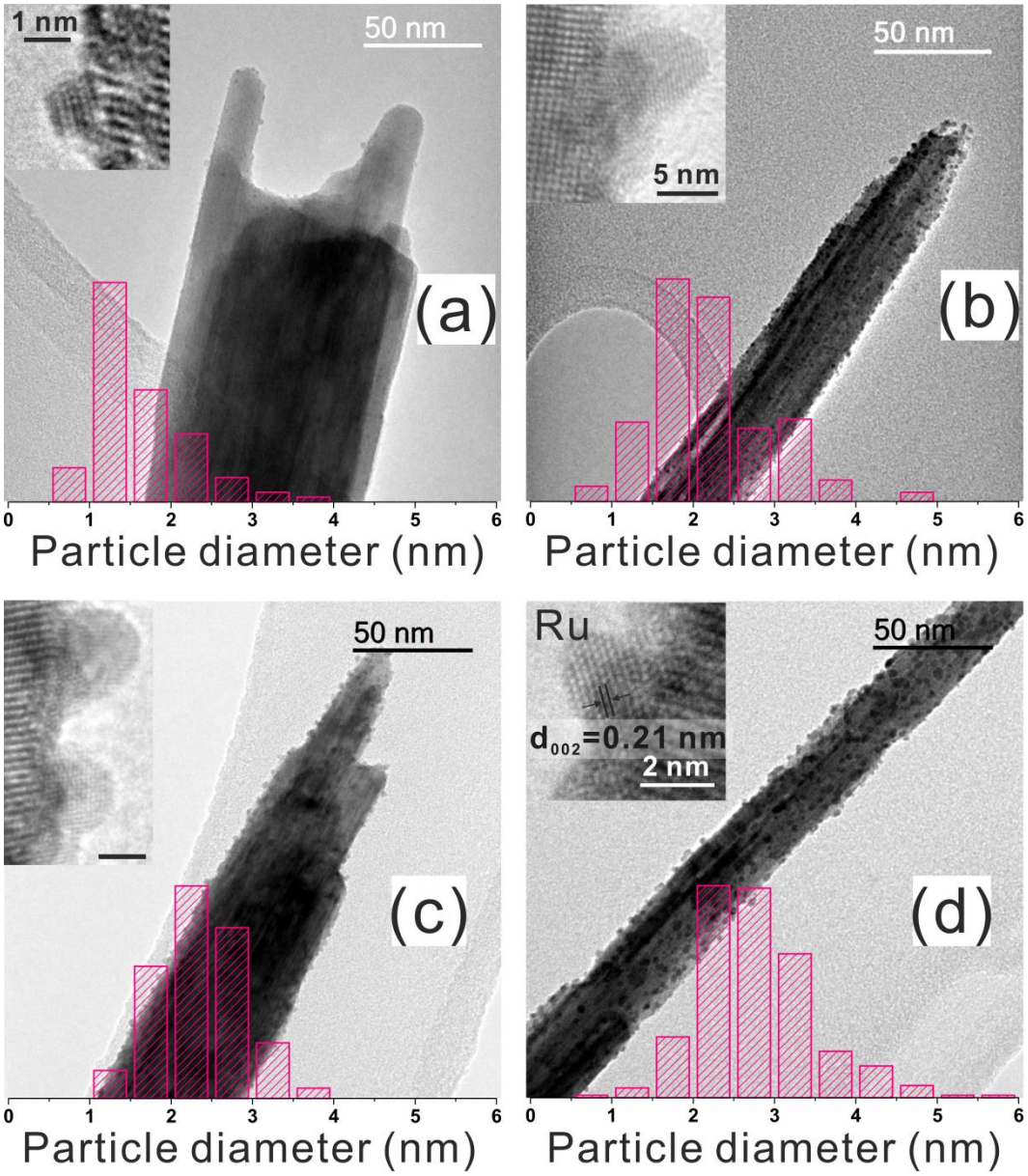

Figure 4.7. TEM images of Ru/WO_3 hybrid nanostructure thin film: (a) Ru/WO_3 (1 min), (b) Ru/WO_3 (10 min), (c) Ru/WO_3 (20 min), (d) Ru/WO_3 (36 min) with NP size distributions on WO_3 NR and insect zoom-in images of Ru NP. NPs with interplanar spacing of 0.21 nm correspond to (002) plane of Ru (d, inset).

In Pt/WO_3 the NPs on WO_3 NRs (Figure 4.8) showed an interplanar spacing of 0.22 (± 0.01) nm (Figure 4.8c, inset) corresponding to the (111) plane of Pt metal, in agreement with the XPS results that Pt metal can be found (Figure 4.4b). As the deposition time increases from 1 to 20 min the mean diameter of Pt NPs on the NRs increases from 3.0 to 7.1 nm, and also the mount of Pt NPs increases (Figure 4.8a to 4.8d).

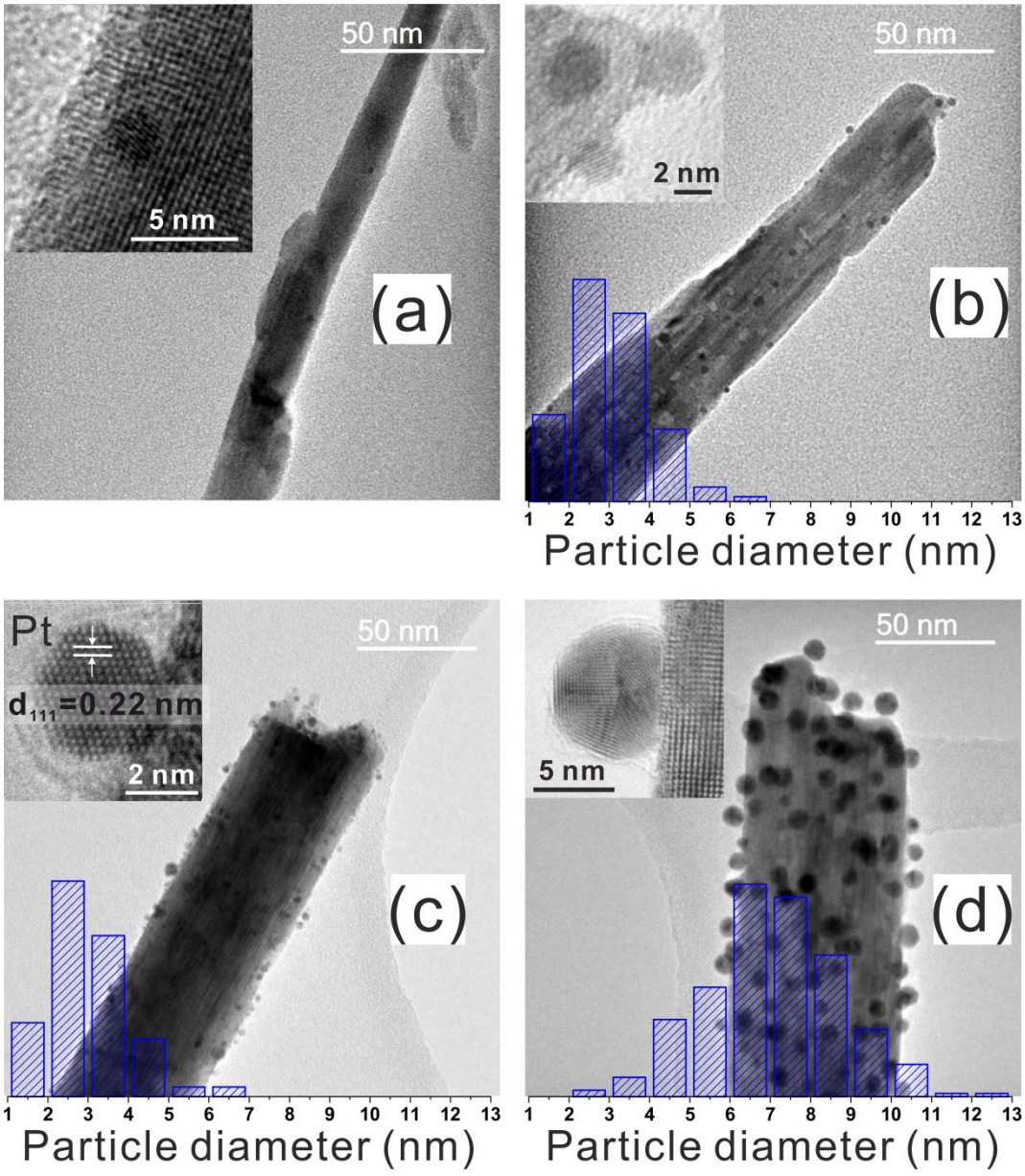

Figure 4.8. TEM images of Pt/WO_3 hybrid nanostructure thin film: (a) Pt/WO_3 (1 min), (b) Pt/WO_3 (5 min), (c) Pt/WO_3 (10 min), (d) Pt/WO_3 (20 min) with NP size distributions on WO_3 NR and insect zoom-in images of Ru NP. NPs with interplanar spacing of 0.22 nm correspond to (111) plane of Pt (c, inset).

After annealing Pd/WO_3, the NPs found on the WO_3 NRs by HR-TEM (Figure 4.9) show an interplanar spacing of 0.27 ($\pm$ 0.01) nm (Figure 4.9b, inset) corresponding to the (002) plane of PdO metal in agreement with the XPS result that Pd (II) was found (Figure 4.4c). The mean diameter of the PdO NPs was larger than the Pd metal NPs (5.6 to 6.5 nm) with no significant change as the deposition time increased, but the number concentration of NP on the NR (Table 4.2) decrease compared to the counterpart before annealing. Therefore, the NP enlargement is attributed to particle oxidation and/or coalescence during the annealing process.

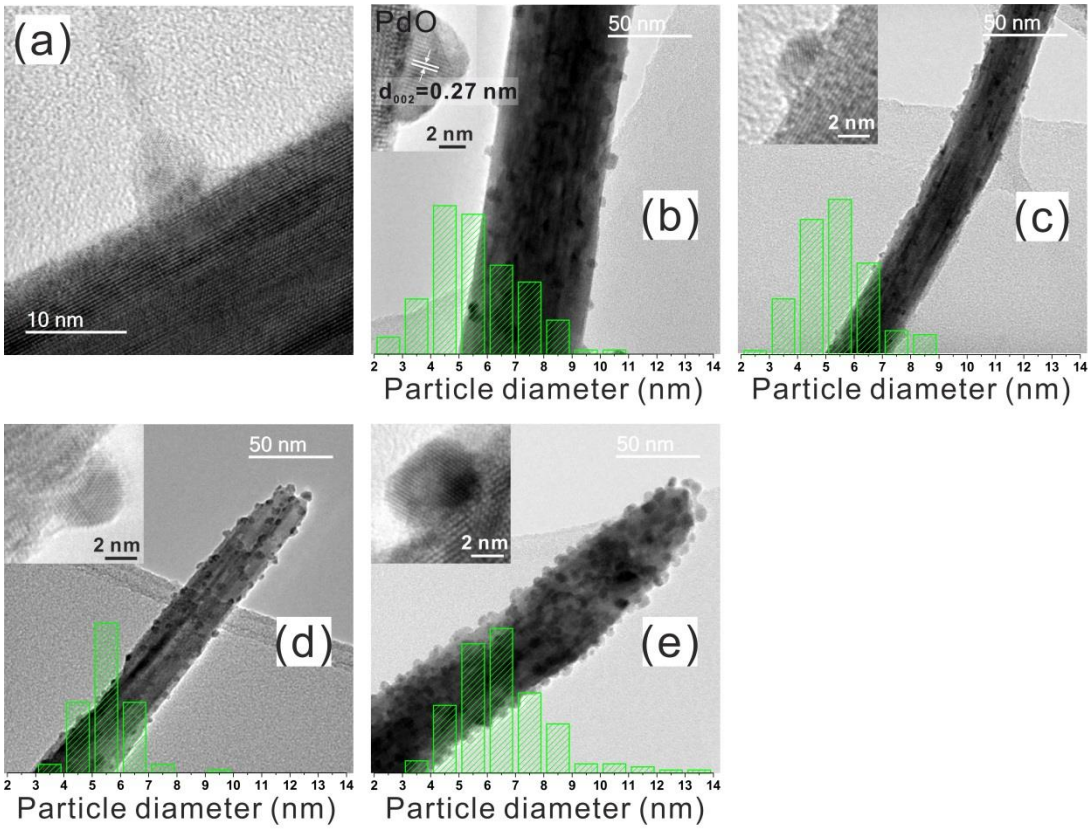

Figure 4.9. TEM images of PdO/WO_3 hybrid nanostructure thin film: (a) PdO/WO_3 (1 min), (b) PdO/WO_3 (5 min), (c) PdO/WO_3 (10 min), (d) PdO/WO_3 (20 min), (e) PdO/WO_3 (35 min) with NP size distributions on WO_3 NR and insect zoom-in images of PdO NP. NPs with interplanar spacing of 0.27 nm correspond to (002) plane of PdO (b, inset).

After annealing Ru/WO_3, the NPs found on the WO_3 NRs by HR-TEM (Figure 4.10) show an interplanar spacing of 0.22 ($\pm$0.01) nm (Figure 4.10e, inset) corresponding to the (002) plane of RuO_2 metal, in agreement with the XPS result that Ru (IV) was found (Figure 4.4d). The mean diameter of the RuO_2 NPs was larger than that for Ru NPs (3.7 to 5.1 nm) with litter change as the deposition time increased, ascribed to particle oxidation and/or coalescence during the annealing process showing lower number concentration of NP on the NR than the counterpart before annealing (Table 4.2).

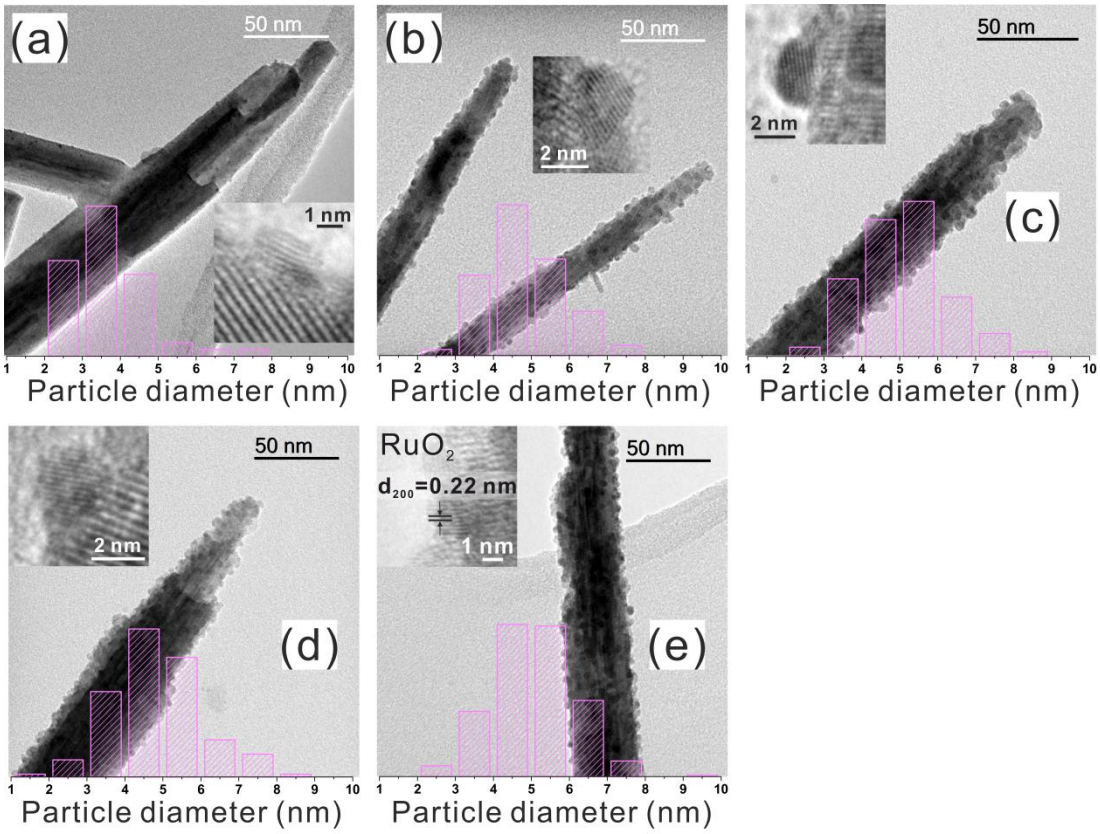

Figure 4.10. TEM images of RuO_2/WO_3 hybrid nanostructure thin film: (a) RuO_2/WO_3 (1 min), (b) RuO_2/WO_3 (10 min), (c) RuO_2/WO_3 (20 min), (d) RuO_2/WO_3 (36 min) with NP size distributions on WO_3 NR and insect zoom-in images of RuO_2 NP. NPs with interplanar spacing of 0.22 nm correspond to (200) plane of RuO_2 (e, inset).

In summary, the size and concentration of noble metal NPs decorated on WO_3 NRs are able to be altered by deposition time, leading to larger particle size and higher particle amount on NRs during AACVD process (Table 4.2). After annealing, the noble metal NPs (Pd or Ru) can be oxidised to noble metal oxide NPs (PdO or RuO_2) with larger particle mean size due to particle oxidation and/or coalescence during annealing without significant change as deposition time increase.

Table 4.1. The NPs size and number concentration and coverage % of metal and metal oxide loaded on surface of WO_3 NRs dependent on the deposition time during AACVD.

Sample	Depos. Time [Minute]	Mean [nm][a)]	Mini. [nm]	Max. [nm]	Concentration [NPs·nm^{-2}][b)] ×10^{-3}	Coverage[c)]
Au/WO_3	0.5	2.4	1.5	5.2	1.29	0.6%
	1	3.0	1.7	5.0	5.23	3.7%
	5	5.5	2.8	9.9	1.62	3.9%
	10	6.1	3.6	10.2	1.74	5.1%
	20	6.8	4.3	11.1	2.46	8.8%
	35	7.3	5.0	14.7	3.61	15.1%
Pd/WO_3	5	1.9	0.8	3.0	3.54	1.0%
	10	1.9	0.9	3.4	4.32	1.2%
	20	3.4	1.7	5.9	7.14	6.6 %
	35	4.1	2.1	5.7	11.12	14.3%
Pt/WO_3	1	--	--	--	trace	--
	5	3.0	1.2	6.1	0.85	0.6%
	10	3.0	1.4	6.5	3.69	2.6%
	20	7.1	2.8	12.9	1.85	7.3%
Ru/WO_3	1	1.6	0.7	3.6	3.54	0.7%
	10	2.2	0.5	4.9	11.91	4.6%
	20	2.3	1.1	3.9	11.96	5.1%
	36	2.9	0.9	5.7	10.83	6.5%
PdO/WO_3	1	--	--	--	trace	--
	5	5.6	3.2	10.0	0.56	1.4%
	10	5.3	2.9	7.4	2.92	6.5%
	20	5.5	3.7	9.8	3.76	9.0%
	35	6.5	3.3	13.7	3.85	12.8%
RuO/WO_3	1	3.7	2.2	7.1	2.36	2.5%
	5	4.8	2.7	7.9	6.11	11.2%
	10	5.1	2.5	8.9	6.28	12.8%
	20	4.8	1.7	8.4	6.97	12.7%
	36	5.1	2.4	9.4	6.44	13.2%

[a)]The mean particle size is obtained by counting NPs (>200 particles) from many different WO_3 NRs in TEM images; [b)]The number concentration of NPs is estimated by counting the number of NPs on a WO_3 NR and then divided by the surface area of that NR; [c)]The coverage of NPs on a WO_3 NR surface estimated by the equation $[n\pi(0.5d)^2]/(0.5S)$ where n is the number concentration, d is the mean size of NPs and S is the surface area of that NR.

The optical properties of all the noble metal or noble metal NPs/WO_3 NR hybrid nanostructure thin films were characterised by UV-Vis in transmittance, reflectance and calculated absorbance as shown in Figure 4.11. All the films showed a similar change in transmittance, reflectance and absorbance with increasing deposition time. While the size and concentration of NPs on the NRs increased as the deposition time increased (Table 4.2), the transmission of those thin films firstly decreased and then increased, though is always lower than for undecorated WO_3 NR thin films. The reflectance for NP modified samples is higher

than for undecorated WO_3 NR thin films when concentration of NPs on the NR is low, but with increasing concentration the reflectance decreases below that of an undecorated WO_3 thin film, leading to an increase in the calculated absorption compared to undecorated WO_3 thin film. The interpretation of optical properties of the hybrid nanostructure thin films relates to the shape, size, dielectric environment, and aggregation or isolation of NPs and their interactions with WO_3 NRs.[221] When the NPs had very small size and low concentration and appeared isolated on the NRs (observed by TEM shown in Figure 4.5 to 4.10) the films showed enhanced reflection compared to undecorated WO_3 thin films. The mechanism of how the isolated tiny metal NPs increasing the reflection of WO_3 NRs is still unclear. When the NPs grew larger with higher concentration achieved by increasing deposition time (above 20 mins in our experiments), the coalescence of NPs on NRs occurred forming a rough optical slab on the surface of the WO_3 NRs. When light strikes the rough and granular slab, this incident light will be bounce off and reflect in all directions (known as diffuse reflection) which reduce the measured reflection compared to undecorated WO_3 thin films. The calculated absorbance of all hybrid nanostructure thin films increased as the deposition time increased owing to the reflectance decreased but diffuse reflection effect increased. It is notable that the samples Au/WO_3, Ru/WO_3, Pt/WO_3 and PdO/WO_3 deposited for less than 20 min showed NIR absorption. This phenomenon is still unclear, although some previous literatures suggested this is attributed to localized surface plasmon resonance (LSPR) of isolated NPs.[222] However, only Au, Ag and Cu have been reported LSPR.[223]

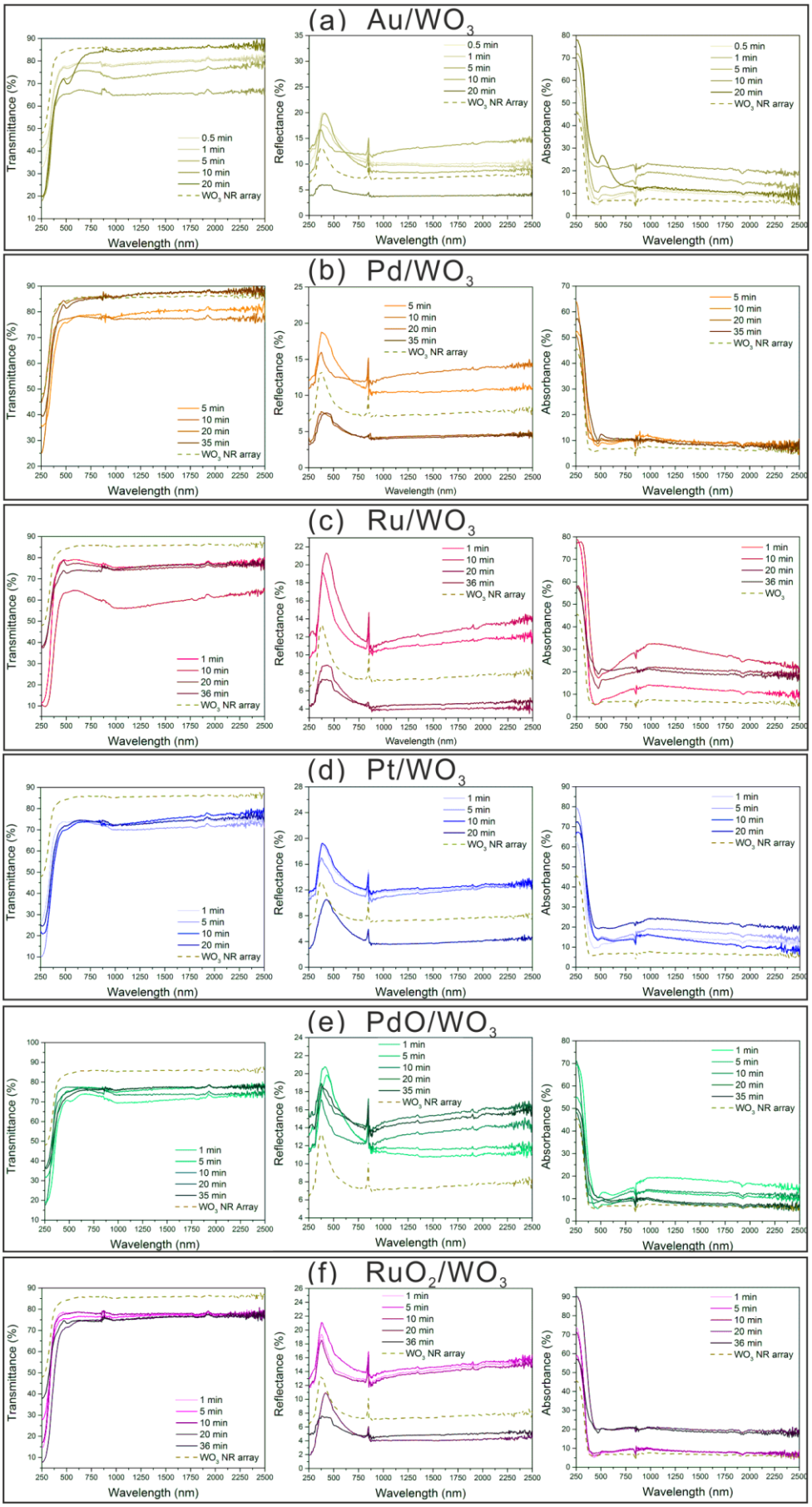

Figure 4.11. The transmittance (left row), reflectance (middle row) and absorbance (right row) spectrum (the noise peak at 865 nm due to grating change of the UV-Vis spectrometer) of (a) Au/WO_3, (b) Pd/WO_3, (c) Pt/WO_3, (d) Ru/WO_3, (e) PdO/WO_3, (f) RuO_2/WO_3 thin films deposited for various time.

In chapter 3, the photocatalytic activity of WO_3 NR array thin films deposited for 0.5 to 30 min was discussed. The thin film deposited for 5 min (WO_3 (5 min)) showed the best activity for photodegradation of SA under UVA light, with an FQE of 8.67×10^{-5}. After the WO_3 NRs were functionalized by Au NPs, not all the Au/WO_3 hybrid nanostructure thin films showed enhanced photocatalytic degradation of SA, with only the sample Au/WO_3 (1 min) with particle mean size 3.0 nm and relative high concentration of NPs decorating on the surface of NRs giving higher photocatalytic activity (a FQE of 11.00×10^{-5}) compared to undecorated WO_3 (5 min) (8.67×10^{-5}) (Figure 4.12a). Previously Au NPs below 3 nm have been reported as catalytically active for the partial oxidation of styrene by dissociation of chemisorbed O_2 to produce O adatoms,[105] which would help produce superoxide radicals and then activate photoreaction II (Figure 3.9) enhancing the photodegradation of SA. Although the sample Au/WO_3 (0.5 min) possessed NP of 2.4 nm diameters, small than Au/WO_3 (1 min), the very low coverage of Au NPs on NRs (0.6 %) may be too low to improve the photocatalytic activity. When the mean particle size of Au NP was larger than 3.0 nm, the photocatalytic degradation of SA became lower (Figure 3.9).

When WO_3 (5 min) was functionalised by Pd NPs, the Pd/ WO_3 samples showed lower photocatalytic degradation of SA than undecorated WO_3 (5 min) (Figure 4.12b). As the particle size and concentration of Pd NPs on NRs increased, the activity reduced. This contradicts previous literature that TiO_2 supported Pd NPs showed enhanced photocatalysis,[224] possibly owing to $PdCl_2$ found in the Pd metal by XPS (Figure 4.4c) in the samples of Pd/ WO_3.

Ru/WO_3 showed similar photocatalytic activity to Pd/WO_3, i.e. lower than undecorated WO_3 (5 min) which decreased as deposition time increased. There is very little literature concerning use of a Ru NP functionalized semiconductor to improve H_2 evolution or O_2 reduction, but Ru NPs have been used as catalyst for enhanced H_2 in a Ru/$SrTiO_3$:Rh system, where only loading of Ru upto a 1.5 wt% presented enhanced photocatalytic activity, with higher amount may leading to increased recombination.[225] Also, TiO_2 functionalised with Ru NPs have demonstrated enhanced O_2 oxidation.[226] Therefore, the mechanism of Ru NPs on WO_3 NRs

hindering photocatalytic degradation of SA is not clear, but increasing amount of Ru NPs on WO_3 NR deceased photocatalytic degradation of SA is possibly owing to increasing recombination by Ru NPs.

After Pt NPs were deposited on the WO_3 NRs only the sample Pt/WO_3 (10 min) with particle mean size 3.0 nm and 2.6 % coverage, showed enhanced photocatalytic degradation of SA (FQE = 11.28×10^{-5}) compared to undecorated WO_3 (5 min) (Figure 4.12d. Samples deposited for 1, 5 or 20 min with very low coverage (< 0.6 %) or larger particle size (> 7 nm) showed reduced activity. Pt NPs can act as a catalyst for promoting O_2 reduction into H_2O_2 and superoxide radicals and enhance charge separation, e.g. Pt NPs with particle size < 5 nm loaded on tungsten oxide have shown high efficient photocatalytic activity for decomposition of organic compounds.[227]

None of the Pd/WO_3 samples showed improved photocatalytic properties, though after annealing the sample PdO/WO_3 (5 min) with particle mean size 5.6 nm and 1.4 % coverage gave enhanced photocatalytic degradation of SA (FQE=13.21×10^{-5}) (Figure 4.12e). Previous literature indicated a PdO/TiO_2:F,N hybrid nanostructure material gave enhanced photocatalytic degradation of organic pollutants due to PdO NPs trapping electrons and hence decreasing the electron-hole recombination.[228]

When WO_3 (5 min) was functionalised with RuO_2 NPs, the photocatlytic degradation of SA was reduced, decreasing as the deposition time increased, corresponding to the particle size and coverage of RuO_2 NPs increasing (Figure 4.12f). RuO_2 has been reported as a good oxidation catalyst for O_2 evolution,[229] However, whereas Au, Pt and PdO NPs can act as a catalyst for O_2 reduction showing enhancement of photocatalytic degradation of SA, therefore, this may relate to why the all RuO_2/WO_3 samples showed no improvement of photocatalytic degradation of SA.

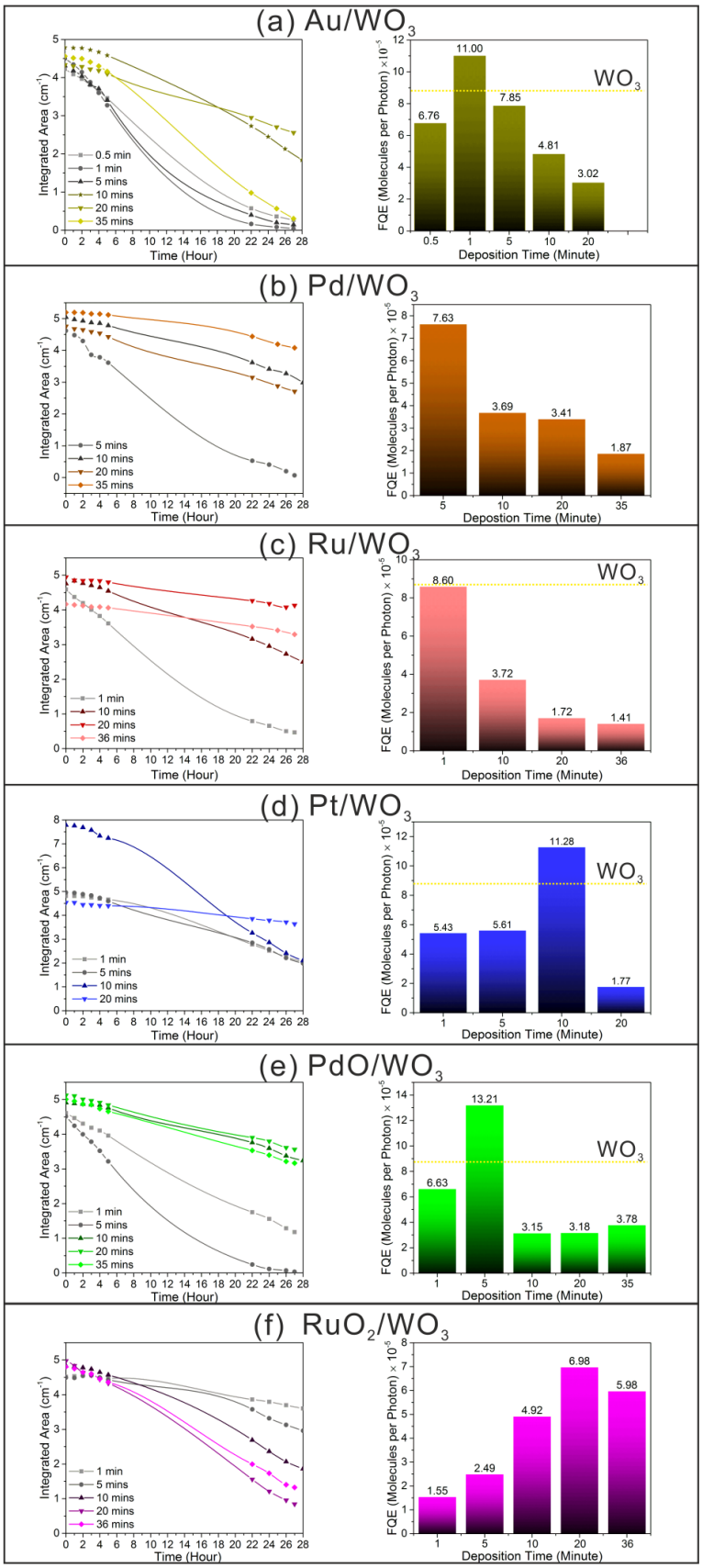

Figure 4.12. The photocatalytic activity of (a) Au/WO_3, (b) Pd/WO_3, (c) Pt/WO_3, (d) Ru/WO_3, (e) PdO/WO_3, (f) RuO_2/WO_3 thin films deposited for various time evaluated by formal quantum efficiencies (right row), given as degraded SA molecules by per incident photon in unit (molecule photon^{-1}), were calculated from the initial rates of photodegradation of SA (left row), compared to undecorated WO_3 NR thin films (FQE = 8.67 $\times$ 10^{-5}).

The XPS valence band regions of noble metal NPs thin film (Au, Pd, Ru and Pt) on plain quartz substrates showed the VBM of the NPs located around the fermi level (BE = 0 eV) (Figure 4.13a to d), attributed to their metallic property. After annealing, PdO NPs had a more positive VBM (-0.25 eV) than Pd NPs (- 1.4 eV), but RuO_2 NPs possessed a similar VBM to Ru NPs (-0.5 to -0.6 eV) (Figure 4.13e and f). Previous literatures reported PdO can act as a p-type semiconductor with bandgap down to 0.5 eV,[119] and RuO_2 showing high electronic conductivity.[123]

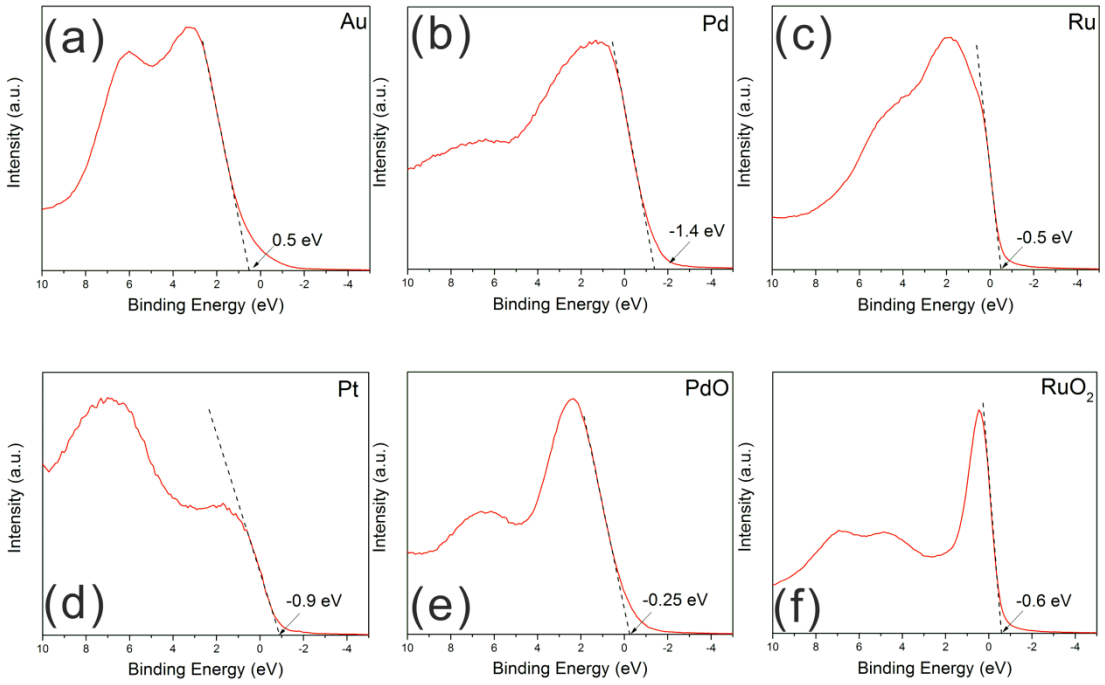

Figure 4.13. The XPS valence band region of (a) Au, (b) Pd, (c) Ru, (d) Pt, (e) PdO and (f) RuO_2 thin films were deposited on quartz substrate for 45 min *via* AACVD, respecting to fermi level (BE=0 eV) and referencing to C 1s (284.8 eV).

Based on the band structure of sample WO_3 (5 min) discussed in Chapter 3 with indirect bandgap 3.0 eV and VBM at 2.65 eV and the VBM of noble metal/noble metal oxide thin film (Figure 4.13) and previous reports,[230,231] the band alignment is generally illustrated in Figure 4.14. The band structure of WO_3 with bandgap of 2.6 to 2.8 eV indicates a good photocatalyst for OER due to its VBM around 1.6 eV more positive than $E(O_2/H_2O)$, but is not active for HER because of a more positive CB level (~0.2 eV) than $E(H^+/H_2)$.[141] Although the bandgap of WO_3 NRs was expanded to 3.0 eV *via* controlled the deposition time of 5 min, the CBM did not move upward more negative than $E(H^+/H_2)$ and/or $E(O_2\,;\,HO_2/O_2)$. Therefore, the sample WO_3

(5 min) only can generate intermediate hydroxyl (OH) by oxidising H_3O due to VBM more positive than *E(OH /H_2O)* at ~2.8 eV vs. NHE. However, photocatalytic degradation of organic pollutants can only proceed indefinitely when the same number of photogenerated electrons and holes are consumed in reducing O_2 and oxidising H_2O leading to intermediate hydroxyl (·OH), superoxide (O_2 ·) and hydroperoxy (HO_2 ·) radicals with *E(O_2 ; HO_2 /O_2)* at ~0.1 eV vs. NHE and *E(OH /H_2O)* at ~2.8 eV vs. NHE corresponding to photocatalytic reactions I and II as shown in Figure 4.14.[32,133] This results in much lower photocatalytic activity for WO_3 compared to anatase (TiO_2),[139] which has one of the highest activities among semiconductor metal oxides due to the potentials of the CB and the VB being sufficiently negative and positive to drive photocatalytic reactions I and II simultaneously.[140] Therefore, if the decorated NPs on WO_3 NRs can act as a catalyst for reducing O_2 generating intermediate $O_2 \cdot$ and $HO_2 \cdot$ radicals driving photocatalytic reaction II, the enhancement of photocatalytic activity is able to be achieved. As shown in Figure 4.14a, Au and Pt NPs can accept the electrons photogenerated from WO_3 NR for reducing O_2 to initiate photocatalytic reaction II. The PdO also can act as acceptor, reducing O_2 and producing $HO_2 \cdot$radicals, [230] and because PdO is found to be a p-type semiconductor the formation of a p-n junction can promote electron-hole separation and production of $HO_2 \cdot$radicals. [119] However, the reasons why the Pd, Ru or RuO_2 decorated on WO_3 NRs show a decrease in photocatalytic degradation of SA are unclear, but possibly due to contamination from carbon layers, presence of foreigner ions (e.g. Cl^-) or/and acting as ORR catalyst.

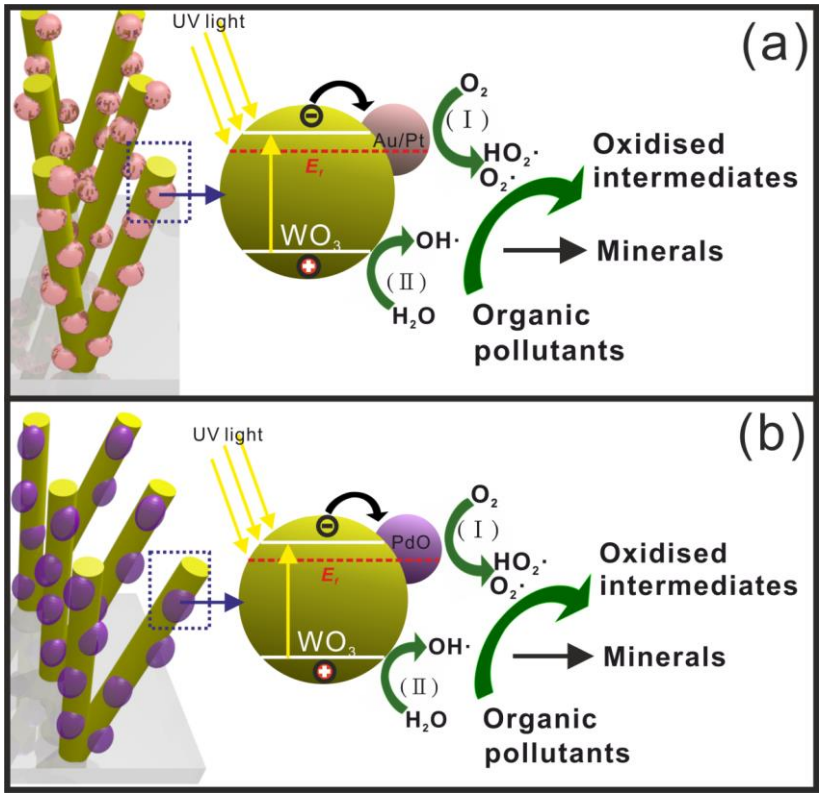

Figure 4.14. Illustration of the possible band alignment of (a) noble metal (Au/Pt) NPs/WO_3 NRs and (b) PdO NPs/WO_3 NRs hybrid nanostructure, and the mechanism of electron-hole separation of those samples activating general reactions for the photocatalytic degradation of organic pollutant: (I) the reduction reaction of O_2 producing superoxide radicals (O_2·) and/or hydroperoxy radical (HO_2·), (II) the oxidation reaction of H_2O creating hydroxyl radical (OH·) based on the previous literatures. [133,141,189,230,231]

4.2 Metal Oxide (TiO_2, Co_2O_3 or CuO_x) and Tungsten Oxide Nanorod Array Hybrid Structured Thin Films

4.2.1 Introduction

Recently heterojunctions constructed from the interface of two solid materials including between semiconductor–semiconductor, semiconductor–metal, and semiconductor–carbon have attracted much attentions.[232,233] By far the most commonly reported heterojunction is that between two semiconductors. In particular combining a p-type and an n-type semiconductor to form a p-n junction leads to a space-charge region and an electric field at the interface. This promotes the flow of electron carriers to the CB of the n-type semiconductor and the flow of hole carriers to the VB of the p-type semiconductor, leading to more efficient separation, and hence longer lifetimes of charge carrier.[233]

Nanostrucutred semiconductors have been the focus of research in this field due to their high surface area. Previous studies have shown that semiconductor-semiconductor heterojunction based on 1D structures have enhanced gas sensor, photocatalytic and photoelctrochemical water splitting.[234,235]

In the above section, the synthesis of noble metal NP/WO_3 NR hybrid nanostructure thin films by AACVD was discussed. After annealing, the samples Pd/WO_3 and Ru/WO_3 can be oxidised to PdO/WO_3 and RuO_3/WO_3 respectively. PdO/WO_3 contains a p-n heterojunction, and showed enhanced photocatalytic degradation of stearic acid (by more than 50 %) compared to an optimised undecorated WO_3 NR array thin film deposited for 5 min. An attractive strategy is to use the AACVD to deposit transition metal oxides directly on the WO_3 NR to form transition metal oxide/WO_3 NR hybrid structured thin films. Herein, we introduce using AACVD to fabricate other metal oxide (TiO_2, Co_2O_3 or CuO_x)/WO_3 NR hybrid nanostructure thin film constructing heterojunctions.

4.2.2 Experimental

The TiO_2, Co_2O_3 and CuO_x were deposited on the WO_3 NR array films (AM375q-ann for 5 min) with parameters as shown in Table 4.3 *via* AACVD, following the procedure as shown in Figure 4.1. The synthesis of WO_3 NR array thin film was discussed in section 2.2.2.

Table 4.2. The deposition parameters of metal oxide nanoparticles/WO_3 nanorods hybrid nanostructured thin films.

Sample	Precursor /g	Solvent /mL	Temperature /˚C	N_2 Flow Rate /SCCM
TiO_2/WO_3	Ti diisoproxide bis(acetylacetonate) /0.0025	Methanol /15 mL	350	300
Co_2O_3/WO_3	Co acetate/0.001	Methanol /15 mL	350	300
CuO_x/WO_3	Cu acetylacetonate/0.001	Toluene/15 mL	375	300

4.2.3 Results and Discussion

As shown in Figure 4.15, the colour of as-synthesised thin films after deposition using transition metal precursors is slightly different from the undecorated WO_3 NR array, which was white

(Figure 4.15a). After deposition of the Co precursor on WO_3 NR array for 50 min, the as-synthesized thin film was yellow (Figure 4.15b) and after deposition of the Cu precursor for 65 min, the as-synthesized thin film was a light yellow colour (Figure 4.15c), similar to deposition using the Ti precursor for 50 min which was also light yellow in colour (Figure 4.15d).

Figure 4.15. The photographs of thin films: (a) WO_3 NR array (5 min), (b) Co_2O_3/WO_3 (50 min), (c) CuO_x/WO_3 (65 min), (d) TiO_2/WO_3 (50 min).

After 50 min deposition of Co precursor, 65 min deposition of Cu precursor or 50 min deposition of Ti precursor (on a WO_3 NR array thin film, the XRD pattern of samples Co_2O_3/WO_3 (50 min), CuO_x/WO_3 (65 min) and TiO_2/WO_3 (50 min) were similar to that of an undecorated WO_3 NR array (Figure 4.16). This may be because the loading of the metal oxides on WO_3 NRs were very low concentration, similar to the samples of noble metal and noble metal oxide/WO_3 (Figure 4.3).[211]

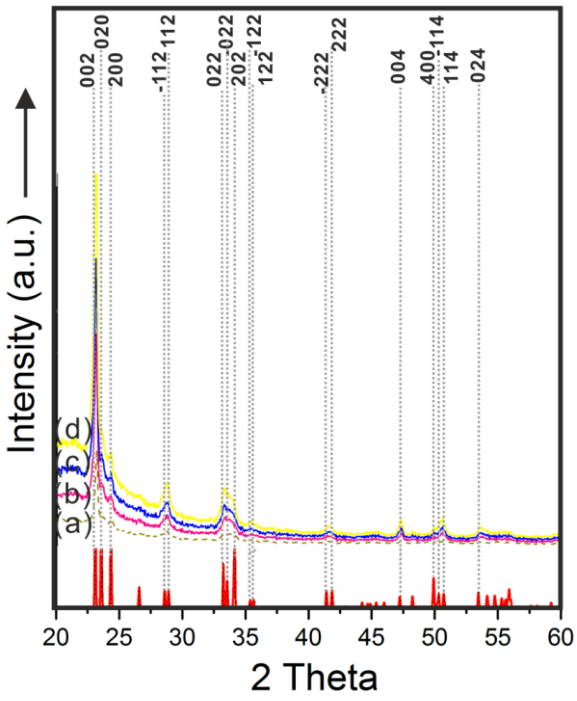

Figure 4.16. XRD patterns of (a) WO_3, (b) Co_2O_3/WO_3 (50 min), (c) TiO_2/WO_3 (50 min), (d) CuO_x/WO_3 (65 min) with matches the monoclinic WO_3 reference pattern (red colour) (PDF 072-0677, a=7.306, b=7.540, c=7.692 Å and α=90 °, β=90.881°, γ=90 °).

The XPS spectrum of Co_2O_3/WO_3 (50 min) (Figure 4.17) showed Co $2p_{3/2}$ and $2p_{1/2}$ at 781.4 and 797.4 eV corresponding to Co (III) in Co_2O_3 (781.3 and 797.1 eV respectively),[236] with the peaks at 787 and 803 eV attributed to the satellite peaks of Co_2O_3.[236] Hence, Co_2O_3 was presented in the sample Co_2O_3/WO_3 (50 min), although no for Co_2O_3 were found in that sample by XRD.

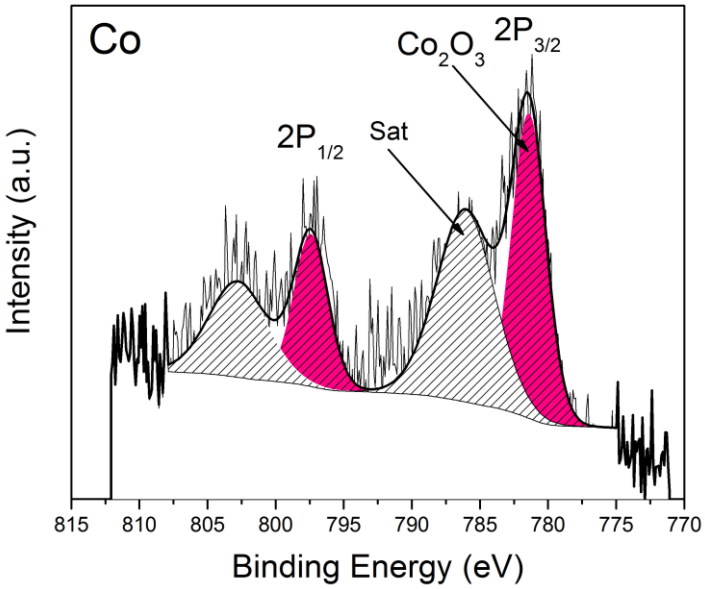

Figure 4.17. XPS spectra of the Co_2O_3/WO_3 (50 min) hybrid nanostructure thin films show Co-(III) state relating to Co_2O_3 and the satellite peaks of Co_2O_3.

The XPS spectrum of CuO_x/WO_3 (65 min) (Figure 4.18) showed both Cu (0) and Cu (II) after fitting with binding energies of 932.8 and 934.9 eV respectively, matching the literatures for Cu metal and CuO (932.8 and 934.6 eV respectively).[237,238] The satellite peaks of CuO are found at 943.4 eV in agreement with previous report (943.0 eV).[238] Hence, Cu and CuO are found in the sample CuO_x/WO_3 (65 min), although neither Cu nor CuO were observed in XRD.

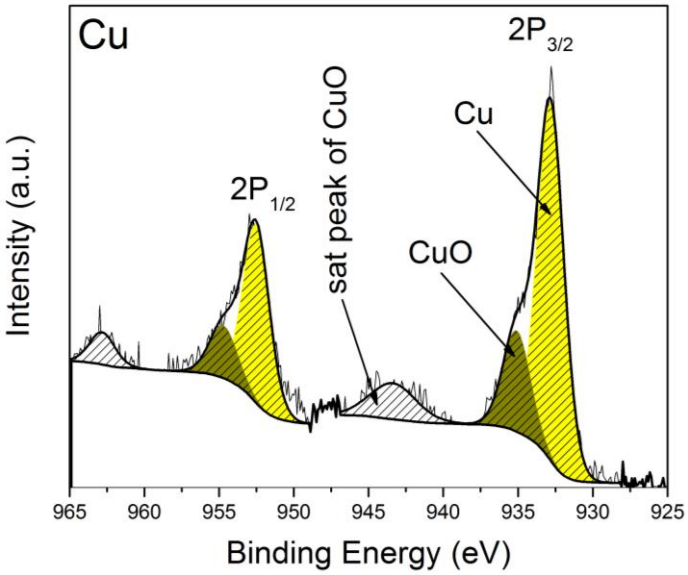

Figure 4.18. XPS spectra of the CuO_x/WO_3 (65 min) hybrid nanostructure thin films show Cu-(0) and Cu-(II) states relating to Cu and CuO and the satellite peaks of CuO.

The XPS spectrum of TiO_2/WO_3 (50 min) (Figure 4.19) showed only Ti (IV) peak with Ti $2p_{3/2}$ and $2p_{1/2}$ at 459.0 and 464.7 eV respectively in good agreement with the literature for TiO_2 (459.0 and 464.7 eV respectively).[239] Hence TiO_2 was presentd in the sample TiO_2/WO_3 (50 min), although it is not apparent from XRD.

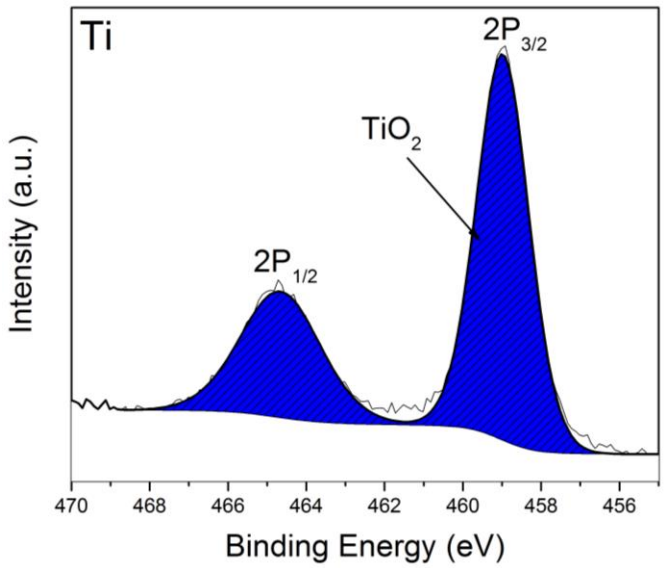

Figure 4.19. XPS spectra of the TiO_2/WO_3 (50 min) hybrid nanostructure thin films show Ti-(IV) state relating to TiO_2.

As shown in Figure 4.20, EDX line scans were used to analyse the composition and distribution of elements on the WO_3 NRs. The EDX line scan results for Co_2O_3/WO_3 (50 min) (Figure 4.20a) show the presence of Co, W and O elements in the NR with wt% 1.5, 38.9 and 12.6 respectively, results for CuO_x/WO_3 (65 min) (Figure 4.20b) show the presence of Cu, W and O elements in the NR with wt% 5.9, 27.8 and 9.3 respectively, and results for TiO_2/WO_3 (50 min) (Figure 2.52c) show the presence of Ti, W and O elements in the NR with wt% 1.4, 22.2 and 6.8 respectively. Therefore, all the transition metal oxide/WO_3 samples showed the corresponding transition metal in the EDX line scan. The distribution of those transition metals can be observed lower in the edge and higher in the centre of NR with the similar trend of W and O elements, where the expectation was that the edge of the NR would show higher distribution if the transition metal deposit as NPs or a shell covering the WO_3 NR. Subsequently, HRTEM was needed to observe the transition metal oxide/WO_3 hybrids.

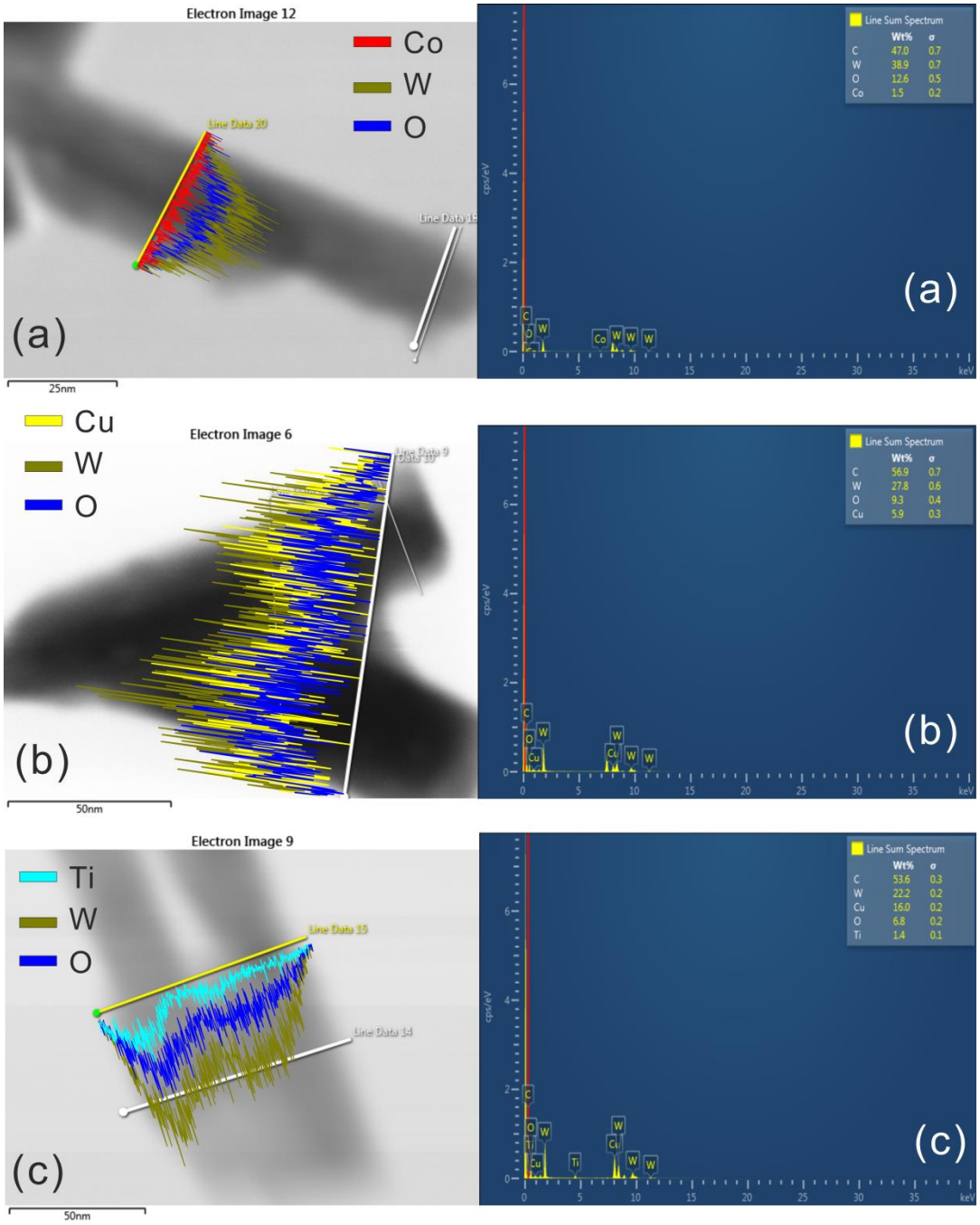

Figure 4.20. The EDX line scan of element of samples (a) Co_2O_3/WO_3 (50 min), (b) CuO_x/WO_3 (65 min) and (c) TiO_2/WO_3 (50 min) showing the element distribution on NR structure with the EDX spectra of (d) Co_2O_3/WO_3 (50 min) showing W (38.9 at%), O (12.6 at%), Co (1.5 at%), (e) CuO_x/WO_3 (65 min) showing W (27.8 at%), O (9.3 at%), Cu (5.9 at%), (f) TiO_2/WO_3 (50 min) showing W (22.2 at%), O (6.8 at%), Ti (1.4 at%).

Using HR-TEM it is able to observe the transition metal oxide decorating the surface of WO_3 NR as NPs as shown in Figure 4.21. The Co_2O_3 NPs ranging from 5 to 20 nm in diameter can be found on the surface of WO_3 NR in sample Co_2O_3/WO_3 (50 min), and the marked interplanar space is 0.28 nm corresponding to (220) face of Co_2O_3 as shown in Figure 4.21a.[240] The CuO

NPs ranging in size from 3 to 5 nm can be found on the surface of the WO_3 NRs in sample CuO_x/WO_3 (65 min), with interplanar spacing of 0.23 nm corresponding to the (111) face of CuO as shown in Figure 4.21b.[241] The TiO_2 NPs range in size from 30 to 60 nm, and the interplanar spacing is 0.23 nm corresponding to the (101) face of TiO_2 (anatase) as shown in Figure 4.21c.[242] Therefore, the transition metal oxides decorated the WO_3 NR similar to the noble metal and noble metal oxides which also decorated the WO_3 NR as NPs. The loading of the NPs on the NRs is very low and possibly why XRD did not detect the NPs. The distribution of those NPs on NRs was in very low concentration, and hence it is difficult for linear scan of STEM with relatively low resolution to select a region with the transition metal oxide NPs on both side of NRs leading to our expectation result of more metal elements found in the edge of NR than at the centre rather than those results shown in Figure 4.20.

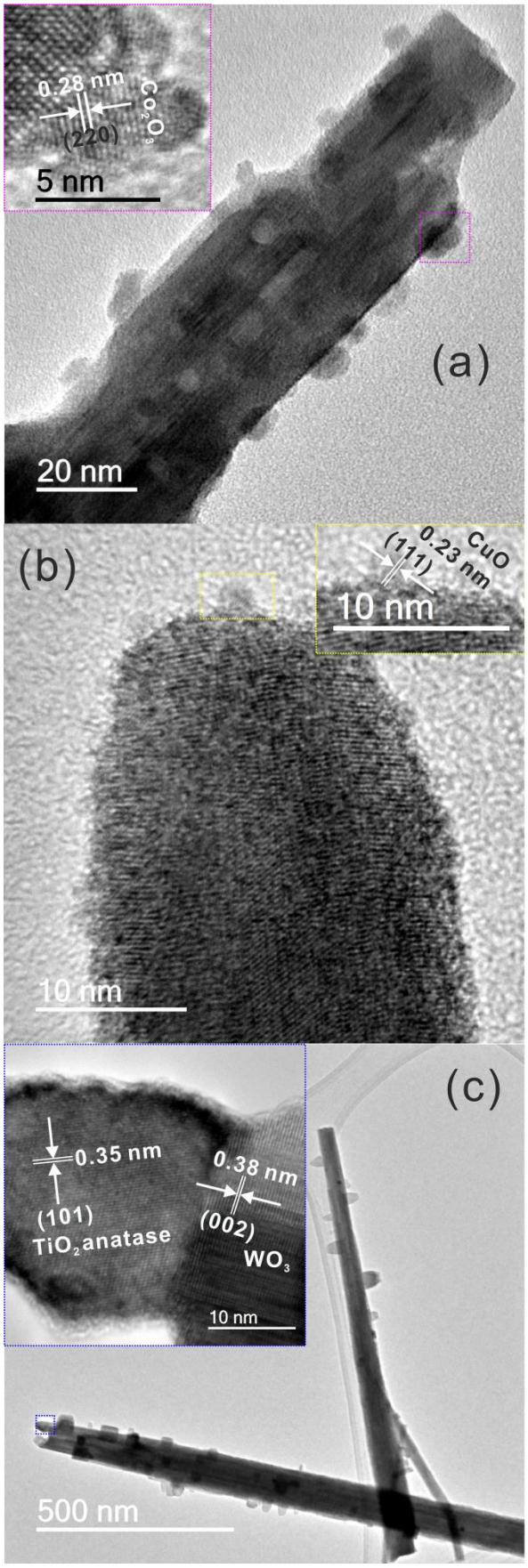

Figure 4.21. TEM images of (a) Co_2O_3/WO_3 (50 min), (b) CuO_x/WO_3 (65 min) and (c) TiO_2/WO_3 (50 min).

As shown in Figure 4.22a, all the samples of transition metal oxide/WO_3 show lower transmittance compared to an undecorated WO_3 NR array. Metal oxide metal NPs loaded on WO_3 NR is expected to reduce the transmittance. The sample TiO_2/WO_3 (50 min) shows the lowest UV transmittance, though the sample CuO_x/WO_3 (65 min) shows similar UV transmittance to undecorated WO_3. The sample Co_2O_3/WO_3 (50 min) shows similar transmittance to that of TiO_2/WO_3 (50 min).

The reflectance of samples decreases after transition metal oxide NPs are loaded on the NRs, lower than undecorated WO_3. This is similar to the samples of noble metal or their oxide NP/WO_3 deposited for longer than 20 min (Figure 4.11) possibly owing to diffuse reflection caused by spherical NPs on NRs and/or a thin carbon layer formed on the NPs. The sample Co_2O_3/WO_3 (50 min) shows the lowest reflectance in the regions from UV to NIR, presented in Figure 4.22b.

In the calculated absorbance spectrum (Figure 4.22c), the sample TiO_2/WO_3 (50 min) shows highest absorption in the regions from UV to NIR, possibly owing to the high bandgap of TiO_2 (~3.2 eV),[189] the sample Co_2O_3/WO_3 (50 min) shows increased UV light absorption,[243] though the sample CuO_x/WO_3 (65 min) shows UV absorption similar to the undecorated WO_3. Therefore, the transition metal oxide/WO_3 hybrid nanostructured thin film show different UV-Vis spectra from undecorated WO_3 NR array.

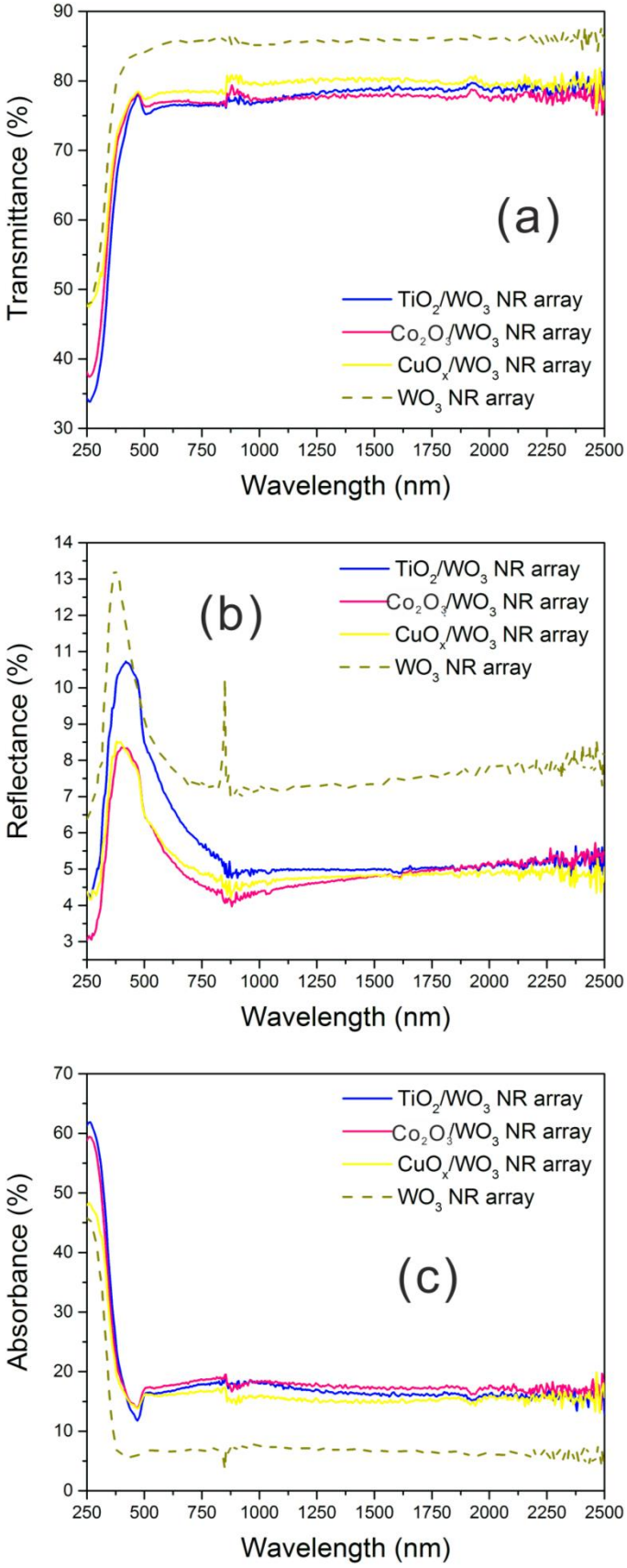

Figure 4.22. The transmittance (a), reflectance (b) and absorbance (c) spectrum (the noise peak at 865 nm due to grating change of the UV-Vis spectrometer) of Co_2O_3/WO_3 (50 min), CuO_x/WO_3 (65 min) and TiO_2/WO_3 (50 min).

4.3 Conclusion

AACVD has been demonstrated as a versatile tool to fabricate metal (M) nanoparticle (NP)/WO_3 nanorod (NR) thin films without requirement of additional agents or catalysts. Metallic Au/WO_3, Pd/WO_3, Pt/WO_3 and Ru/WO_3 hybrid nanostructured thin films were successfully fabricated, although the NPs of Pd and Ru also contain oxidised states of Pd-(II) and Ru-(IV) respectively.

The NP size of the noble metal is tuned simply by altering the deposition time. When the deposition time is short, the mean size of NPs is small and amount of NPs loading is low, whilst as the deposition time increases the mean size and amount of NPs loading also increases. This method is suitable for depositing a wide range of metal and metal oxide NPs on various support thin films fabricated by different methods (e.g. Au NPs on flat TiO_2 support), and also for developing simple routes to heterojunctions for application in photovoltaic, photocatalysis, catalysis and surface enhanced Raman spectroscopy.

The size and the amount of noble metal loading on WO_3 NR array affect its optical properties and also its photocatalytic activity. The photodegradation of SA was used to evaluate a functional property of the noble metal NPs/WO_3 NR array hybrid thin film. The photodegradation rate of SA (Figure 4.12) was increased over the hybrid nanostructures of Au/WO_3 (1 min, with particle mean size 3.0 nm) and Pt/WO_3 (10 min, 3.0 nm) compared to undecorated WO_3 NR array thin films, and in particular Pt NPs with mean particle size 3.0 nm increases the rate by more than 50 % which is attributed to Pt as a good catalyst for oxygen reduction reaction.[122,204] However Pd/WO_3, Ru/WO_3 show lower activity compared to undecorated WO_3 possibly due to contamination from forming carbon layers or foreigner ions (e.g. Cl^-) or/and acting as ORR catalyst.

After annealing the Pd or Ru NPs on WO_3 NRs were able to be oxidised as PdO or RuO_2 NPs respectively. the sample PdO/WO_3 (5 min) gave an FQE of photodegradation SA higher than undecorated WO_3 NR array by 60%, and better photocatalyst than Au (1 min, 11.0) and Pt (10 min, 11.3) possible owing to forming a p-n heterojuction between PdO NPs and WO_3 NRs.

Consequently, the transition metal oxide NPs of Co_2O_3, CuO_x and TiO_2 were successfully loaded onto WO_3 NR forming Co_2O_3/WO_3 (50 min), CuO_x/WO_3 (65 min) and TiO_2/WO_3 (50 min) hybrid nanostructured thin film *via* AACVD without further oxidation treatment e.g. annealing in the furnace in high temperature.

Therefore, AACVD demonstrated as a versatile tool to fabricate metal or metal oxide NPs/metal oxide hybrid nanostructure thin films with tunable NP size *via* controlling the deposition time and forming heterojunctions for enhanced photocatalyst.

CHAPTER 5: SUMMARY AND FUTURE WORK

In Chapter 1, literatures about (a) the properties, application, synthesis and growth mechanism of tungsten oxide with nanorod (NR) structure; (b) the mechanism and applications of aerosol assisted chemical vapour deposition (AACVD); (c) the synthesis, property and application of noble metals, were discussed. However, the recent growth mechanism of 1D structure (e.g. Vapour-Liquid-Solid and Vapour-Solid) focused on the reasons of 1D structure formed based on different driven force and was unable to tell, for example, at which temperature the 1D structure can form. The growth processes of tungsten oxide NR *via* AACVD was unknown, and the origin of the quantum confinement effect (QCE) in tungsten oxide NR with length up to the microscale unclear.

In Chapter 2, the deposition conditions e.g. precursor, solvent, substrate, and deposition temperature, were studied in order to fabricate tungsten oxide thin films with NR structure. As shown in Table 5.1, the deposition conditions affected the morphologies of tungsten thin films *via* AACVD. In order to identify the relation between deposition conditions and morphologies of as-synthesised thin films, the tungsten oxide thin films deposited under different conditions (e.g. temperature and the concentration of precursor) were characterised. The change of morphologies of tungsten oxide thin film was attributed to the competition for arrival adatoms on substrate between nucleation and growth along the direction perpendicular to substrate. Hence a "Kinetic competition" mechanism was proposed to predict the morphology of tungsten oxide as planar or NR dependent on the deposition temperature and the concentration of precursor.

Table 5.1. Deposition conditions of tungsten oxide thin films relating to nanostructure.

Precursor (g)	Solvent (mL)	Substrate	Deposition Temp.(°C)	Nanostructure	Nanostructure After annealing
$W(OPh)_6$ (0.075)	Acetone (15)	Glass	450	Yes	Yes
$W(OPh)_6$ (0.075)	Acetone (15)	B-glass	450	No	Yes
$W(OPh)_6$ (0.075)	Acetone (15)	Alumina	450	No	No
$W(OPh)_6$ (0.075)	Acetone(10) and Toluene(5)	B-Glass	450	Odd	No
$W(OPh)_6$ (0.075)	Toluene(15)	B-Glass	450	Yes	Yes
$W(OPh)_6$ (0.075)	Acetone(15)	B-Glass	450	Yes	Yes
$W(OPh)_6$ (0.150)	Toluene (15)	B-glass	300	Odd	No
$W(OPh)_6$ (0.150)	Toluene (15)	B-glass	325	No	No
$W(OPh)_6$ (0.150)	Toluene (15)	B-glass	350	Yes	No
$W(OPh)_6$ (0.150)	Toluene (15)	B-glass	375	Yes	Yes
$W(OPh)_6$ (0.075)	Toluene (15)	B-glass	400	Yes	Yes
$W(OPh)_6$ (0.075)	Toluene (15)	B-glass	425	Yes	Yes
$W(OPh)_6$ (0.075)	Toluene (15)	B-glass	450	Yes	Yes
$W(OPh)_6$ (0.075)	Toluene (15)	B-glass	500	Yes	Yes
$W(CO)_6$ (0.06)	Toluene (15)	Quartz	375	Yes	Yes
$W(CO)_6$ (0.06)	Acetone (15)	Quartz	375	No	-
$W(CO)_6$ (0.06)	Methanol (15)	Quartz	375	Yes	-
$W(CO)_6$ (0.06)	Acetone(10) and Methanol(5)	Quartz	375	Odd	-
$W(CO)_6$ (0.06)	Acetone(10) and Toluene(5)	Quartz	375	Yes	-
$W(CO)_6$ (0.06)	Methanol(10) and Toluene(5)	Quartz	375	No	-
$W(CO)_6$ (0.06)	Acetone(10) and Methanol(5)	Quartz	350	Yes	-
$W(CO)_6$ (0.06)	Acetone(10) and Methanol(5)	Quartz	375	Yes	Yes

As shown in Figure 5.1, the competition between nucleation rate (J) and nucleus perpendicular growth rate (r_{perp}) results in different morphologies. The thin film growth (thickness increase) is contributed to r_{perp} and r_i (layered growth rate of nucleus, $r_i \propto J$) leading to a wave-like surface of the thin film due to the difference between r_{perp} and r_i. As the ratio of r_{perp} to r_i reaches 7.1 (r_{perp} is 7.1 times faster than r_i), the tungsten oxide grows as a NR structure, otherwise a planar structure results in agreement of the observation by SEM as shown in Figure 5.2.

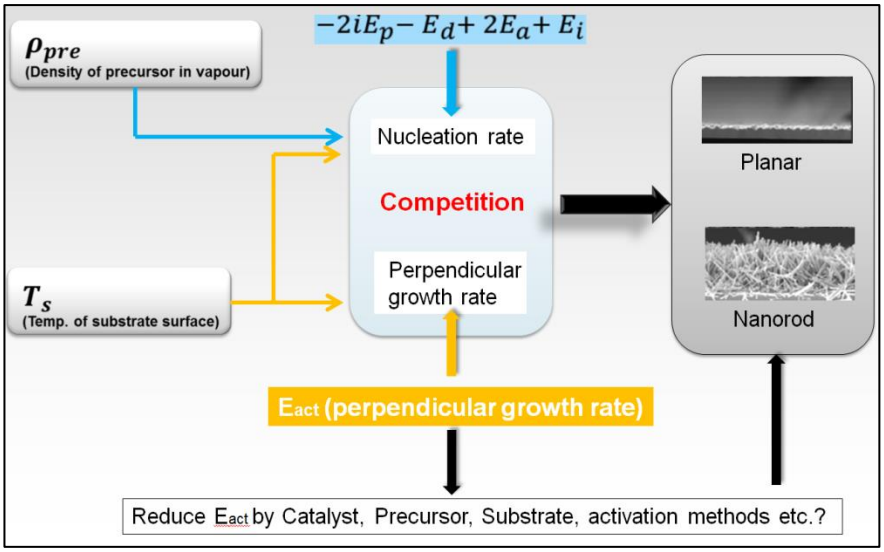

Figure 5.1. The "Kinetic Competition" between nucleation rate and perpendicular rate dependent on deposition temperature and concentration of precursor leads to planar or nanorod structure of tungsten oxide thin film.

Hence, based on the Venables' kinetic theory, the 'Kinetic competition' equation was deduced as Equation 2.29 which could be used to estimate the required temperature for 1D nanostructure formation during AACVD after the constant calculated *via* conducting a small series depositions. The 'Kinetic competition' equation also describes that decrease E_{act} (activation energy for growth along the direction perpendicular to substrate) can reduce temperature for fabricating 1D structures e.g. introducing catalysts, using plasma and different precursors.[79,244,245]

The E_{act} of growth is comprised of E_{act} of absorption and pyrolysis of precursor, surface diffusion, adsorption, binding and nucleation of adatoms. After nucleation as shown in Figure 5.2, the NR extrudes from a certain facet of the nucleus, whilst other directions parallel to substrate grow with relatively low rate. This is possibly due to a relatively high E_{act}, which could be attributed to V_O found increasing the E_{act} of adsorption and binding on those facets suppressing the growth along those directions. As the length of NRs grows, their diameter also increases due to the coalescence of NRs resulting in a reduction of the concentration of V_O which is a function of the deposition time with reciprocal relationship. The ability of the V_O to act as n-type donor was first reported in 2007,[246] and an V_O can donate two electrons reducing

W^{6+} to W^{4+}.[162] Therefore, controlling the concentration of V_O *via* controlling the growth of tungsten oxide NR by deposition time during AACVD is the example of V_O doping of a tungsten oxide NR array to modify its band structure.

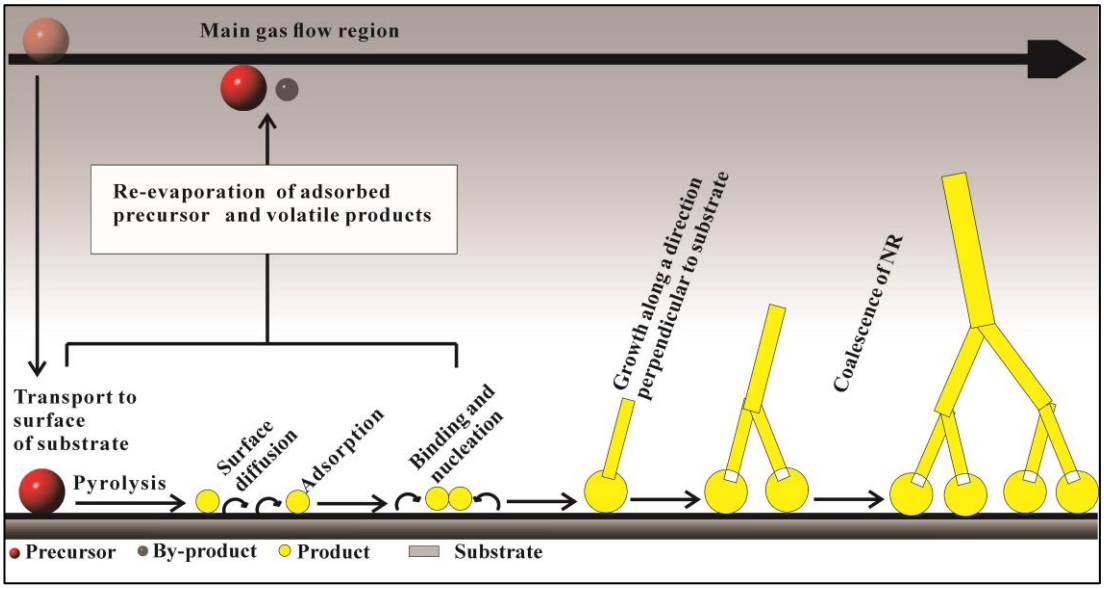

Figure 5.2. Growth mechanism of AACVD from precursor to tungsten NRs.

In Chapter 3, tungsten oxide NR arrays with an $W_{32}O_{84}$ ($WO_{2.63}$) phase showed strong NIR absorption arising from small-polarons hopping and/or intervalence charge transfer owing to the presence of a high concentration of reduced tungsten states (W^{4+}) induced by V_O. Therefore, sub-stoichiometric tungsten oxide (WO_x) thin films have potential in NIR shielding and heat filter coatings. A sample of $WO_{2.63}$ deposited for 30 min was able to reduce interior temperature by around 10 ℃, and sample deposited for 10 min can lower temperature by 4.5 ℃ with 70 % visible light transparency in a simulated NIR absorption experiment.

After annealing at 500 ℃ in air for 2 hours, the sample of $WO_{2.63}$ converts to be monoclinic WO_3 (m-WO_3). When the concentration of defects (V_O) is low (0 to 1.48 %, length of NR from 1.0 to 1.5 μm deposited for 3 and 5 min) no NIR absorption was observed and bandgap widens (3.0 eV compared to bulk WO_3, 2.6 eV) shown in Figure 5.3 and Table 5.2. We attribute the observed bandgap widening to the formation of dislocation loops. It has previously been found that strain fields introduced by the presence of dislocation loops lead to quantum-spatial-

confinement (QSC) effects, which in the case of silicon can increase the bandgap energy by 325 to 750 meV due to the stress formed at the edge of dislocation loops.[188] We observed dislocation loops by HRTEM imaging with diameters between 0.4 and 1.5 nm in the nanorod nucleates from which the WO_3 NRs grow. At higher defects (V_O) (3.0 to 8.6 %, length of NR from 2.5 to 4.5 μm deposited in 10 and 30 min) (Table in 5.2) NIR absorption was observed and the bandgap narrows from 2.9 to 2.6 eV (Figure 5.3). This has previously been observed in WO_3.[193]

Table 5.2. A summary of the XPS results, which relate changes in indirect bandgap, concentration (at. %) of W^{4+}, VBM position and the peak maxima of NIR absorption with deposition time.

Deposition time (minute)	Indirect Bandgap (eV)	W^{4+} (at. %)	VBM (eV)	NIR absorption peak (nm)
30	2.6	8.56	2.32	986
20	2.7	7.50	2.37	970
10	2.9	3.02	2.41	968
5	3.0	1.48	2.65	n/a
3	3.0	trace	2.67	n/a
1	3.1	trace	2.72	n/a
0.5	3.1	trace	2.78	n/a

Therefore, here the 1D quantum confinement effect of tungsten oxide NR arrays can be attributed to QSC induced by dislocation loops rather than quantum-size-confinement. The dislocation loops were created by V_O which also introduced small-plasmons inducing small-plasmon-hopping contributing to the NIR absorption. Hence, the V_O modified the band structure and optical property of tungsten oxide NR arrays *via* forming dislocation loops and small-plasmons.

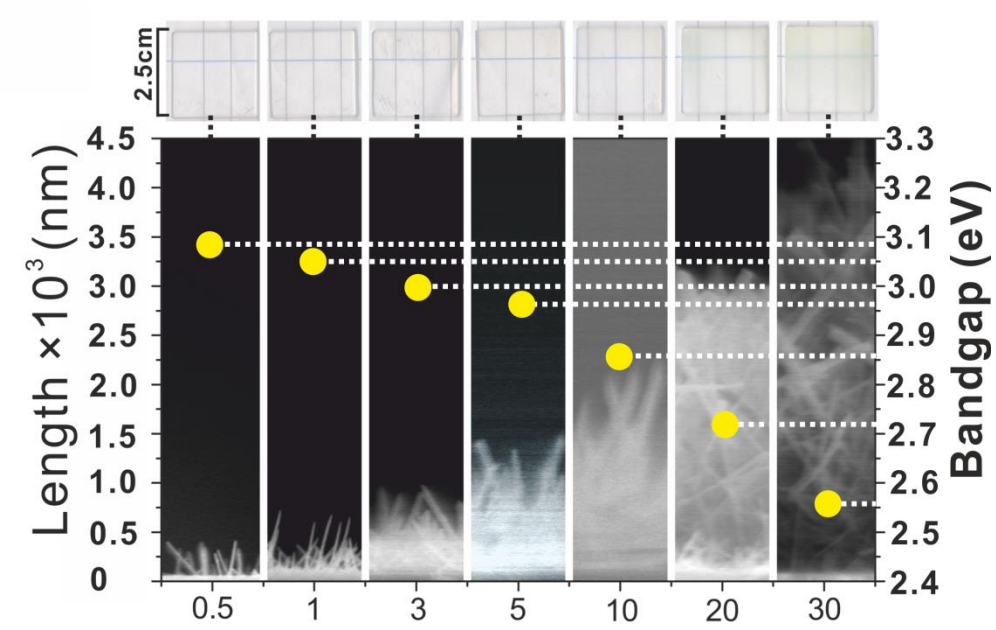

Figure 5.3. Photographs of WO_3 thin films (2.5 * 2.5 cm) deposited after 0.5, 1, 3, 5, 10, 20 and 30 minutes (from left to right) *via* AACVD (top) corresponding to change in length of NRs from around 400 to 4500 nm (images of cross-section SEM, middle) and in the optical direct band gap E_g from 3.0 to 3.6 eV (yellow square).

The modification of band structure of WO_3 NR arrays by V_O doping is evaluated by photodegradation of stearic acid (SA) under UVA irradiation (365 nm). The 5 min growth time sample showed the best activity amongst all the samples, possibly due to bandgap expansion, leading to increased oxidation potential. The presence of V_O can cause charge carriers to be strongly localized, and hence inhibit their movement to the material surface where they can react.[247,248] Consequently the photocatalytic performance of our WO_3 NRs decreased with an increase in V_O, found in samples with growth times greater than 5 minutes.

In Chapter 4, the direct growth of noble metal NPs supported on WO_3 NR array thin films, without the introduction of foreign agents (organic and/or inorganic) or requirement for supports as a reducer, was introduced noble metal (Au, Pt, Pd and Ru) NP/WO_3 NR hybrid structured thin films were successfully fabricated, and the mean particle size of Au, Pt, Pd and Ru loading on the surface of WO_3 was tailored from 2 to 7 nm simply by controlling the deposition time from 0.5 to 36 min.

With subsequent oxidative treatment, Pd and Ru NPs loaded on WO_3 NR were oxidised to PdO and RuO_2 NPs forming PdO/WO_3 and RuO_2/WO_3 hybrid structured thin films.

The photocatalytic activity of the noble metal or noble metal oxide/WO_3 hybrid nanostructured thin films was evaluated by photo-degradation of SA. As shown in Figure 5.4, the photodegradation rate of SA was increased over the hybrid nanostructures of Au/WO_3 (1 min, with particle mean size 3.0 nm), Pt/WO_3 (10 min, 3.0 nm) and PdO/WO_3 (5 min, 5.6 nm) compared to undecorated WO_3 NR array thin films, and in particular PdO NPs increase the rate by more than 50 %.[122,204] However Pd/WO_3 (5 min, 1.9 nm), Ru/WO_3 (36 min, 2.8 nm) and RuO_2/WO_3 (36 min, 5.1 nm) show lower activity compared to undecorated WO_3 most likely due to a lack of catalytic activity for oxygen reduction reaction in the metal or oxide NPs, and the loss of surface area by covering the surface of the WO_3 NRs.

The transition metal oxide NPs of Co_3O_4, CuO_x and TiO_2 were loaded on WO_3 NR forming Co_3O_4/WO_3, CuO_x/WO_3 and TiO_2/WO_3 hybrid nanostructured thin film *via* AACVD without further oxidative treatment e.g. annealing in the furnace in high temperature.

Therefore, AACVD can be used to construct different type of metal or metal oxide/metal oxide with 1D structure hybrid materials to improve properties of catalysis and photocatalysis.

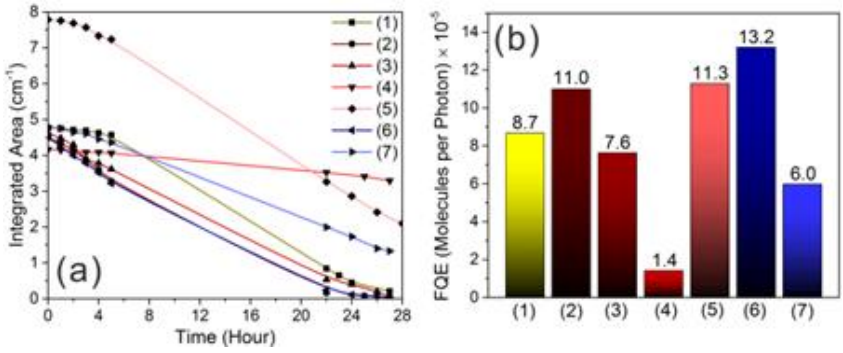

Figure 5.4. Integrated areas of stearic acid bands (a) were estimated during UVA light (4.2 mW cm^{-2}) irradiation of SA coated as-synthesized M/WO_3 and MO/WO_3 hybrid nanostructure thin films: (1) plain WO_3 NR array (2) Au/WO_3 (1 min), (3) Pd/WO_3 (5 min), (4) Ru/WO_3 (36 min), (5) Pt/WO_3 (10 min), (6) PdO/WO_3 (5 min), (7) RuO_2/WO_3 (36 min). Formal quantum efficiencies (b), given as degraded SA molecules by per incident photon in unit (molecule photon^{-1}), were calculated from the initial rates of photodegradation of SA (a).

For future work, firstly the AACVD will be used to fabricate N doped tungsten oxide and tungsten nitride which are efficient hydrogen evolution cathode,[249,250] with 1D nanostructure *via* introducing ammonia in precursor solution or in carrier gas, and annealing in ammonia gas at high temperature > 600 ℃. If this strategies work, more metal nitride or/and non-metal doped metal oxide composite materials with 1D nanostructure could be synthesized by AACVD.

Secondly, the tungsten oxide NR array thin films based hybrid materials will continue studying. Metal, metal oxide, metal nitride or polymer/tungsten oxide NR array core-shell hybrid materials will try to be constructed by combining AACVD with other techniques (e.g. CVD, PVD or hydrothermal synthesis).

The V_O can affect the band structure and optical properties of tungsten oxide NR arrays *via* creating dislocation loops and small-plasmons. In future, the band structure and optical properties of other metal oxide 1D arrays would try to be modified by 'doping V_O' *via* annealing in reductive gas e.g. H_2 or in vacuum to figure out their application in photocatalysis and water splitting.

In 'kinetic competition' mechanism, the competition between nucleation and thin film growth leading to various morphologies from planar to 1D, however, there are still unclear why the V_O formed along certain direction suppressing the growth, hence crystal can grow along one direction forming 1D structure, and the relationship between growth activation energy and facet surface energy or the atom arrangement in that facet. Therefore, in future, the exposure facets of nucleus can be estimated by thermodynamics theory,[251] and the growth activation energy along facets could relate to their surface energy possibly *via* RRKM thory.[252] subsequently, combing with kinetic competition' mechanism, the various nanostructure dependent on deposition conditions can be predicted from ab initio calculation.

REFERENCES

1. Cora, F. & Stachiotti, M. Transition metal oxide chemistry: Electronic structure study of WO3, ReO3, and NaWO3. *J. Phys. Chem. B* **101,** 3945–3952 (1997).
2. Diehl, R., Brandt, G. & Salje, E. The crystal structure of triclinic WO3. *Acta Crystallogr. Sect. B* **34,** 1105–1111 (1978).
3. Zheng, H. *et al.* Nanostructured Tungsten Oxide - Properties, Synthesis, and Applications. *Adv. Funct. Mater.* **21,** 2175–2196 (2011).
4. Gerand, B., Nowogrocki, G., Guenot, J. & Figlarz, M. Structural study of a new hexagonal form of tungsten trioxide. *J. Solid State Chem.* **29,** 429–434 (1979).
5. Woodward, P. M., Sleight, A. W. & Vogt, T. Ferroelectric Tungsten Trioxide. *J. Solid State Chem.* **131,** 9–17 (1997).
6. Woodward, P. M., Sleight, A. W. & Vogt, T. Structure refinement of triclinic tungsten trioxide. *J. Phys. Chem. Solids* **56,** 1305–1315 (1995).
7. Loopstra, B. O. & Rietveld, H. M. Further refinement of the structure of WO3. *Acta Crystallogr. Sect. B Struct. Crystallogr. Cryst. Chem.* **25,** 1420–1421 (1969).
8. Salje, E. The orthorhombic phase of WO3. *Acta Crystallogr. Sect. B Struct. Crystallogr. Cryst. Chem.* **33,** 574–577 (1977).
9. Kehl, W. L., Hay, R. G. & Wahl, D. The Structure of Tetragonal Tungsten Trioxide. *J. Appl. Phys.* **23,** 212 (1952).
10. Suetin, D. V., Shein, I. R. & Ivanovskii, A. L. Structural, electronic, and magnetic properties of tungsten oxycarbides WC1-xOx and WO3-xCx from first principles calculations. *Phys. status solidi* **248,** 2884–2892 (2011).
11. Ashraf, S., Blackman, C. S., Palgrave, R. G., Naisbitt, S. C. & Parkin, I. P. Aerosol assisted chemical vapour deposition of WO3 thin films from tungsten hexacarbonyl and their gas sensing properties. *J. Mater. Chem.* **17,** 3708 (2007).
12. Vallejos, S., Umek, P. & Blackman, C. Aerosol Assisted Chemical Vapour Deposition Control Parameters for Selective Deposition of Tungsten Oxide Nanostructures. *J. Nanosci. Nanotechnol.* **11,** 8214–8220 (2011).
13. Roussel, P., Labbé, P. & Groult, D. Symmetry and twins in the monophosphate tungsten bronze series (PO 2) 4 (WO 3) 2 m (2 ≤ m ≤ 14). *Acta Crystallogr. Sect. B Struct. Sci.* **56,** 377–391 (2000).
14. Fahlman, B. D. *Materials Chemistry*. (Springer, 2011).
15. Barabanenkov, Y. A. Structure Of Wo2. 625 (W32o81) Tungsten-Oxide. *Zhurnal Neorg. Khimii* **37,** 19–24 (1992).
16. Sundberg, M. *et al.* Two high-pressure tungsten oxide structures of W 3 O 8 stoichiometry deduced from high-resolution electron microscopy images. *Acta Crystallogr. Sect. B Struct. Sci.* **49,** 951–958 (1993).
17. LAMIRE, M., LABBE, P., GOREAUD, M. & RAVEAU, B. Réaffinement et nouvelle analyse de la structure de W18O49. *Rev. Chim. minérale* **24,** 369–381
18. Dobson, M. M. & Tilley, R. J. D. A new pseudo-binary tungsten oxide, W 17 O 47. *Acta Crystallogr. Sect. B Struct. Sci.* **44,** 474–480 (1988).
19. McColm, I. J., Steadman, R. & Wilson, S. J. Iron-promoted phases in the tungsten-oxygen system. *J. Solid State Chem.* **23,** 33–42 (1978).
20. Magnéli, A. Structures of the ReO 3 -type with recurrent dislocations of atoms: `homologous series' of molybdenum and tungsten oxides. *Acta Crystallogr.* **6,** 495–500 (1953).
21. Sundberg, M. The crystal and defect structures of W25O73, a member of the homologous series WnO3n−2. *Acta Crystallogr. Sect. B Struct. Crystallogr. Cryst. Chem.* **32,** 2144–2149 (1976).
22. Gebert, E. & Ackermann, R. J. Substoichiometry of Tungsten Trioxide; the Crystal Systems of WO 3.00 , WO 2.98 , and WO 2.96. *Inorg. Chem.* **5,** 136–142 (1966).
23. Housecroft, C. E. & Sharpe, A. G. *Inorganic Chemistry*. (Pearson College Div, 2012).
24. Busca, G. The surface acidity of solid oxides and its characterization by IR spectroscopic methods. An attempt at systematization. *Phys. Chem. Chem. Phys.* **1,** 723–736 (1999).
25. HERRERA, J. *et al.* Synthesis, characterization, and catalytic function of novel highly dispersed tungsten oxide catalysts on mesoporous silica. *J. Catal.* **239,** 200–211 (2006).
26. Yoffe, A. D. Low-dimensional systems: quantum size effects and electronic properties of semiconductor microcrystallites (zero-dimensional systems) and some quasi-two-dimensional systems. *Adv. Phys.* **42,** 173–

262 (1993).

27. May, R. A., Kondrachova, L., Hahn, B. P. & Stevenson, K. J. Optical Constants of Electrodeposited Mixed Molybdenum-Tungsten Oxide Films Determined by Variable-Angle Spectroscopic Ellipsometry. *J. Phys. Chem. C* **111,** 18251–18257 (2007).

28. Watanabe, H., Fujikata, K., Oaki, Y. & Imai, H. Band-gap expansion of tungsten oxide quantum dots synthesized in sub-nano porous silica. *Chem. Commun. (Camb).* **49,** 8477–9 (2013).

29. Darwent, J. R. & Mills, A. Photo-oxidation of water sensitized by WO3 powder. *J. Chem. Soc. Faraday Trans. 2* **78,** 359 (1982).

30. Yan, J. *et al.* Tungsten oxide single crystal nanosheets for enhanced multichannel solar light harvesting. *Adv. Mater.* **27,** 1580–6 (2015).

31. Cross, W. B. & Parkin, I. P. Aerosol assisted chemical vapour deposition of tungsten oxide films from polyoxotungstate precursors: active photocatalysts. *Chem. Commun.* 1696 (2003). doi:10.1039/b303800a

32. Mills, A. & Le Hunte, S. An overview of semiconductor photocatalysis. *J. Photochem. Photobiol. A Chem.* **108,** 1–35 (1997).

33. Cross, W. B. & Parkin, I. P. Aerosol assisted chemical vapour deposition of tungsten oxide films from polyoxotungstate precursors: active photocatalysts. *Chem. Commun. (Camb).* 1696–1697 (2003). doi:10.1039/b303800a

34. Lee, W., Lai, C. & Hamid, S. One-Step Formation of WO3-Loaded TiO2 Nanotubes Composite Film for High Photocatalytic Performance. *Materials (Basel).* **8,** 2139–2153 (2015).

35. Hjelm, A., Granqvist, C. G. & Wills, J. M. Electronic structure and optical properties of WO 3 , LiWO 3 , NaWO 3 , and HWO 3. *Phys. Rev. B* **54,** 2436–2445 (1996).

36. Faughnan, B. W., Crandall, R. S. & Lampert, M. A. Model for the bleaching of WO3 electrochromic films by an electric field. *Appl. Phys. Lett.* **27,** 275 (1975).

37. Granqvist, C. G. Electrochromics for smart windows: Oxide-based thin films and devices. *Thin Solid Films* **564,** 1–38 (2014).

38. Lee, S.-H. *et al.* Raman spectroscopic studies of gasochromic a-WO3 thin films. *Electrochim. Acta* **46,** 1995–1999 (2001).

39. Georg, A. Mechanism of the gasochromic coloration of porous WO3 films. *Solid State Ionics* **127,** 319–328 (2000).

40. Makarov, V. O. & Trontelj, M. Sintering and electrical conductivity of doped WO3. *J. Eur. Ceram. Soc.* **16,** 791–794 (1996).

41. Aguir, K., Lemire, C. & Lollman, D. B. . Electrical properties of reactively sputtered WO3 thin films as ozone gas sensor. *Sensors Actuators B Chem.* **84,** 1–5 (2002).

42. Ponzoni, A. *et al.* Ultrasensitive and highly selective gas sensors using three-dimensional tungsten oxide nanowire networks. *Appl. Phys. Lett.* **88,** 203101 (2006).

43. Stoycheva, T. *et al.* Important considerations for effective gas sensors based on metal oxide nanoneedles films. *Sensors Actuators B Chem.* **161,** 406–413 (2012).

44. Santato, C., Odziemkowski, M., Ulmann, M. & Augustynski, J. Crystallographically Oriented Mesoporous WO 3 Films: Synthesis, Characterization, and Applications. *J. Am. Chem. Soc.* **123,** 10639–10649 (2001).

45. Breedon, M. *et al.* Synthesis of Nanostructured Tungsten Oxide Thin Films: A Simple, Controllable, Inexpensive, Aqueous Sol−Gel Method. *Cryst. Growth Des.* **10,** 430–439 (2010).

46. Lakshmi, B. B., Dorhout, P. K. & Martin, C. R. Sol−Gel Template Synthesis of Semiconductor Nanostructures. *Chem. Mater.* **9,** 857–862 (1997).

47. Li, X.-L., Lou, T.-J., Sun, X.-M. & Li, Y.-D. Highly sensitive WO3 hollow-sphere gas sensors. *Inorg. Chem.* **43,** 5442–9 (2004).

48. Sadakane, M. *et al.* Preparation of 3-D ordered macroporous tungsten oxides and nano-crystalline particulate tungsten oxides using a colloidal crystal template method, and their structural characterization and application as photocatalysts under visible light irradiation. *J. Mater. Chem.* **20,** 1811 (2010).

49. Walton, R. I. Subcritical solvothermal synthesis of condensed inorganic materials. *Chem. Soc. Rev.* **31,** 230–238 (2002).

50. Einarsrud, M.-A. & Grande, T. 1D oxide nanostructures from chemical solutions. *Chem. Soc. Rev.* **43,** 2187–99 (2014).

51. Song, X., Zhao, Y. & Zheng, Y. Hydrothermal synthesis of tungsten oxide nanobelts. *Mater. Lett.* **60,** 3405–3408 (2006).

52. Yayapao, O., Thongtem, T., Phuruangrat, A. & Thongtem, S. CTAB-assisted hydrothermal synthesis of

tungsten oxide microflowers. *J. Alloys Compd.* **509,** 2294–2299 (2011).

53. Poinern, G. E. J., Le, X. T., Hager, M., Becker, T. & Fawcett, D. Electrochemical Synthesis, Characterisation, and Preliminary Biological Evaluation of an Anodic Aluminium Oxide Membrane with a pore size of 100 nanometres for a Potential Cell Culture Substrate. *American Journal of Biomedical Engineering* **3,** 119–131 (2013).

54. Mukherjee, N., Paulose, M., Varghese, O. K., Mor, G. K. & Grimes, C. A. Fabrication of nanoporous tungsten oxide by galvanostatic anodization. *J. Mater. Res.* **18,** 2296–2299 (2011).

55. Fanny Béron, L.-P. C. D. M. and A. Y. *Electrodeposited Nanowires and their Applications*. (InTech, 2010). doi:10.5772/2799

56. Baeck, S. H., Jaramillo, T., Stucky, G. D. & McFarland, E. W. Controlled Electrodeposition of Nanoparticulate Tungsten Oxide. *Nano Lett.* **2,** 831–834 (2002).

57. Reichelt, K. & Jiang, X. The preparation of thin films by physical vapour deposition methods. *Thin Solid Films* **191,** 91–126 (1990).

58. Dai, Z. R., Pan, Z. W. & Wang, Z. L. Novel Nanostructures of Functional Oxides Synthesized by Thermal Evaporation. *Adv. Funct. Mater.* **13,** 9–24 (2003).

59. Smith, A. M., Kast, M. G., Nail, B. A., Aloni, S. & Boettcher, S. W. A planar-defect-driven growth mechanism of oxygen deficient tungsten oxide nanowires. *J. Mater. Chem. A* **2,** 6121–6129 (2014).

60. Alfonso, J. E., Torres, J. & Marco, J. F. Influence of the substrate bias voltage on the crystallographic structure and surface composition of Ti6A14V thin films deposited by rf magnetron sputtering. *Brazilian J. Phys.* **36,** 994–996 (2006).

61. Nanba, T. *et al.* Characterization of amorphous tungsten trioxide thin films prepared by rf magnetron sputtering method. *J. Non. Cryst. Solids* **178,** 233–237 (1994).

62. Choy, K. Chemical vapour deposition of coatings. *Prog. Mater. Sci.* **48,** 57–170 (2003).

63. Chi, Y. *et al.* Fluorinated aminoalkoxide CuII complexes: new CVD precursors for deposition of copper metal. *J. Mater. Chem.* **12,** 3541–3550 (2002).

64. Lo Nigro, R., Toro, R. G., Malandrino, G. & Fragalà, I. L. Morphological and structural control of nanostructured <100> oriented CeO2 films grown on random metallic substrates. *J. Mater. Chem.* **15,** 2328 (2005).

65. Blackman, C. S. & Parkin, I. P. Atmospheric Pressure Chemical Vapor Deposition of Crystalline Monoclinic WO 3 and WO 3 - x Thin Films from Reaction of WCl 6 with O-Containing Solvents and Their Photochromic and Electrochromic Properties. *Chem. Mater.* **17,** 1583–1590 (2005).

66. Tracy, C. E. Preparation of amorphous electrochromic tungsten oxide and molybdenum oxide by plasma enhanced chemical vapor deposition. *J. Vac. Sci. Technol. A Vacuum, Surfaces, Film.* **4,** 2377 (1986).

67. Seman, M. & Wolden, C. A. Investigation of the role of plasma conditions on the deposition rate and electrochromic performance of tungsten oxide thin films. *J. Vac. Sci. Technol. A Vacuum, Surfaces, Film.* **21,** 1927 (2003).

68. Venables, J. A. Atomic processes in crystal growth. *Surf. Sci.* **299–300,** 798–817 (1994).

69. Venables, J. A., Spiller, G. D. T. & Hanbucken, M. Nucleation and growth of thin films. *Reports Prog. Phys.* **47,** 399–459 (1984).

70. Zhang, Z. Atomistic Processes in the Early Stages of Thin-Film Growth. *Science (80-.).* **276,** 377–383 (1997).

71. Ratsch, C. & Venables, J. Nucleation theory and the early stages of thin film growth. *J. Vac. Sci. Technol. …* (2003). at <http://scitation.aip.org/content/avs/journal/jvsta/21/5/10.1116/1.1600454>

72. Burton, W. K., Cabrera, N. & Frank, F. C. The Growth of Crystals and the Equilibrium Structure of their Surfaces. *Philos. Trans. R. Soc. A Math. Phys. Eng. Sci.* **243,** 299–358 (1951).

73. Myers-Beaghton, A. & Vvedensky, D. Generalized Burton-Cabrera-Frank theory for growth and equilibration on stepped surfaces. *Phys. Rev. A* **44,** 2457–2468 (1991).

74. Venables, J. A. Nucleation growth and pattern formation in heteroepitaxy. *Phys. A Stat. Mech. its Appl.* **239,** 35–46 (1997).

75. Venables, J. A., Spiller, G. D. T. & Hanbucken, M. Nucleation and growth of thin films. *Reports Prog. Phys.* **47,** 399 (1984).

76. Bloem, J. Nucleation and growth of silicon by CVD. *J. Cryst. Growth* **50,** 581–604 (1980).

77. Lu, J. G., Chang, P. & Fan, Z. Quasi-one-dimensional metal oxide materials—Synthesis, properties and applications. *Mater. Sci. Eng. R Reports* **52,** 49–91 (2006).

78. Smith, A. M., Kast, M. G., Nail, B. A., Aloni, S. & Boettcher, S. W. A planar-defect-driven growth

mechanism of oxygen deficient tungsten oxide nanowires. *J. Mater. Chem. A* **2,** 6121–6129 (2014).

79. Wagner, R. S. & Ellis, W. C. Vapor - Liquid - Solid Mechanism Of Single Crystal Growth. *Appl. Phys. Lett.* **4,** 89–90 (1964).

80. Liu, F. *et al.* A Catalyzed-Growth Route to Directly Form Micropatterned WO2 and WO3 Nanowire Arrays with Excellent Field Emission Behaviors at Low Temperature. (2010). at <http://pubs.acs.org/doi/citedby/10.1021/cg100995f>

81. Wu, S. *et al.* Vapor-solid growth of high optical quality MoS_2 monolayers with near-unity valley polarization. *ACS Nano* **7,** 2768–72 (2013).

82. Burton, W. K., Cabrera, N. & Frank, F. C. The Growth of Crystals and the Equilibrium Structure of their Surfaces. *Philos. Trans. R. Soc. A Math. Phys. Eng. Sci.* **243,** 299–358 (1951).

83. Meng, F., Morin, S. A., Forticaux, A. & Jin, S. Screw dislocation driven growth of nanomaterials. *Acc. Chem. Res.* **46,** 1616–26 (2013).

84. Kojima, Y., Kasuya, K., Nagato, K., Hamaguchi, T. & Nakao, M. Solid-phase growth mechanism of tungsten oxide nanowires synthesized on sputtered tungsten film. *J. Vac. Sci. & Technol. B* **26,** 1942–1947 (2008).

85. Zhang, Z. *et al.* Atomic-Scale Observation of Vapor-Solid Nanowire Growth via Oscillatory Mass Transport. *ACS Nano* **10,** 763–9 (2016).

86. Hou, X. & Choy, K.-L. Processing and Applications of Aerosol-Assisted Chemical Vapor Deposition. *Chem. Vap. Depos.* **12,** 583–596 (2006).

87. Cross, W. B. *et al.* Tungsten oxide coatings from the aerosol-assisted chemical vapor deposition of W (OAr) 6 (Ar= C6H5, C6H4F-4, C6H3F2-3, 4); photocatalytically active γ-WO3 films. *Chem. Mater.* **15,** 2786–2796 (2003).

88. Molloy, K. C. & Williams, P. A. AACVD of WO 3 thin films from W(O)(OPr i) 3 [O(CH 2) n NMe 2] (n = 2, 3). *Appl. Organomet. Chem.* **22,** 676–683 (2008).

89. Vallejos, S., Umek, P. & Blackman, C. Aerosol Assisted Chemical Vapour Deposition Control Parameters for Selective Deposition of Tungsten Oxide Nanostructures. *J. Nanosci. Nanotechnol.* **11,** 8214–8220 (2011).

90. Kim, H. *et al.* Aerosol-assisted chemical vapor deposition of tungsten oxide films and nanorods from oxo tungsten(VI) fluoroalkoxide precursors. *ACS Appl. Mater. Interfaces* **7,** 2660–7 (2015).

91. Xi, G. *et al.* In situ growth of metal particles on 3D urchin-like WO3 nanostructures. *J. Am. Chem. Soc.* **134,** 6508–11 (2012).

92. Vallejos, S. *et al.* Au nanoparticle-functionalised WO3 nanoneedles and their application in high sensitivity gas sensor devices. *Chem. Commun. (Camb).* **47,** 565–7 (2011).

93. Vallejos, S. *et al.* Single-Step Deposition of Au- and Pt-Nanoparticle-Functionalized Tungsten Oxide Nanoneedles Synthesized Via Aerosol-Assisted CVD, and Used for Fabrication of Selective Gas Microsensor Arrays. *Adv. Funct. Mater.* **23,** 1313–1322 (2013).

94. Annanouch, F. E. *et al.* Aerosol-assisted CVD-grown WO_3 nanoneedles decorated with copper oxide nanoparticles for the selective and humidity-resilient detection of H_2S. *ACS Appl. Mater. Interfaces* **7,** 6842–51 (2015).

95. Armor, J. N. A history of industrial catalysis. *Catal. Today* **163,** 3–9 (2011).

96. Parsons, R. The rate of electrolytic hydrogen evolution and the heat of adsorption of hydrogen. *Trans. Faraday Soc.* **54,** 1053–1063 (1958).

97. Greeley, J., Jaramillo, T. F., Bonde, J., Chorkendorff, I. B. & Nørskov, J. K. Computational high-throughput screening of electrocatalytic materials for hydrogen evolution. *Nat. Mater.* **5,** 909–13 (2006).

98. Chen, A. & Holt-Hindle, P. Platinum-based nanostructured materials: synthesis, properties, and applications. *Chem. Rev* **110,** 3767–3804 (2010).

99. Jin, R. The impacts of nanotechnology on catalysis by precious metal nanoparticles. *Nanotechnol. Rev.* **1,** 31–56 (2012).

100. Chen, J., Lim, B., Lee, E. P. & Xia, Y. Shape-controlled synthesis of platinum nanocrystals for catalytic and electrocatalytic applications. *Nano Today* **4,** 81–95 (2009).

101. Hashmi, A. S. K. & Rudolph, M. Gold catalysis in total synthesis. *Chem. Soc. Rev.* **37,** 1766–75 (2008).

102. Hashmi, A. S. K. & Hutchings, G. J. Gold catalysis. *Angew. Chem. Int. Ed. Engl.* **45,** 7896–936 (2006).

103. HARUTA, M. Gold catalysts prepared by coprecipitation for low-temperature oxidation of hydrogen and of carbon monoxide. *J. Catal.* **115,** 301–309 (1989).

104. HUTCHINGS, G. Vapor phase hydrochlorination of acetylene: Correlation of catalytic activity of supported metal chloride catalysts. *J. Catal.* **96,** 292–295 (1985).

105. Turner, M. *et al.* Selective oxidation with dioxygen by gold nanoparticle catalysts derived from 55-atom clusters. *Nature* **454,** 981–983 (2008).

106. Li, Y., Liu, Q. & Shen, W. Morphology-dependent nanocatalysis: metal particles. *Dalton Trans.* **40,** 5811–26 (2011).

107. TARDY, B. Catalytic hydrogenation of 1,3-butadiene on Pd particles evaporated on carbonaceous supports: Particle size effect. *J. Catal.* **129,** 1–11 (1991).

108. Conrad, H., Ertl, G. & Latta, E. E. Adsorption of hydrogen on palladium single crystal surfaces. *Surf. Sci.* **41,** 435–446 (1974).

109. Wilson, O. M., Knecht, M. R., Garcia-Martinez, J. C. & Crooks, R. M. Effect of Pd nanoparticle size on the catalytic hydrogenation of allyl alcohol. *J. Am. Chem. Soc.* **128,** 4510–1 (2006).

110. Grigoriev, S. A., Millet, P. & Fateev, V. N. Evaluation of carbon-supported Pt and Pd nanoparticles for the hydrogen evolution reaction in PEM water electrolysers. *J. Power Sources* **177,** 281–285 (2008).

111. Pattabiraman, R. Electrochemical investigations on carbon supported palladium catalysts. *Appl. Catal. A Gen.* **153,** 9–20 (1997).

112. Tateishi, N., Yahikozawa, K., Nishimura, K. & Takasu, Y. Hydrogen electrode reaction on electrodes of glassy carbon-supported ultrafine Pd particles in alkaline media. *Electrochim. Acta* **37,** 2427–2432 (1992).

113. Xiong, Y. & Xia, Y. Shape-Controlled Synthesis of Metal Nanostructures: The Case of Palladium. *Adv. Mater.* **19,** 3385–3391 (2007).

114. Musser, M. T. Cyclohexanol and Cyclohexanone. *Ullmann's Encyclopedia of Industrial Chemistry* 219 (1987).

115. Maxwell, G. *Synthetic nitrogen products: a practical guide to the products and processes*. (Springer Science & Business Media, 2004).

116. MOGGI, P., ALBANESI, G., PREDIERI, G. & SPOTO, G. Ruthenium cluster-derived catalysts for ammonia synthesis. *Appl. Catal. A Gen.* **123,** 145–159 (1995).

117. AIKA, K. Preparation and characterization of chlorine-free ruthenium catalysts and the promoter effect in ammonia synthesis 3. A magnesia-supported ruthenium catalyst. *J. Catal.* **136,** 126–140 (1992).

118. Ronchin, L. & Toniolo, L. Supported Ru catalysts: a study of the influence of supports, promoters and preparative variables on the catalytic activity and selectivity. *React. Kinet. Catal. Lett.* **78,** 281–289

119. Nilsson, P. O. Optical properties of PdO in the range of 0.5-5.4 eV. *J. Phys. C Solid State Phys.* **12,** 1423–1427 (1979).

120. Zhou, W. *et al.* PdO/TiO2 and Pd/TiO2 heterostructured nanobelts with enhanced photocatalytic activity. *Chem. Asian J.* **9,** 1648–54 (2014).

121. Zhang, H. *et al.* PdO doping tunes band-gap energy levels as well as oxidative stress responses to a Co_3O_4 p-type semiconductor in cells and the lung. *J. Am. Chem. Soc.* **136,** 6406–20 (2014).

122. Sunarso, J. *et al.* Bi-Functional Water/Oxygen Electrocatalyst Based on PdO-RuO2 Composites. *J. Electrochem. Soc.* **160,** H74–H79 (2012).

123. Over, H. Surface chemistry of ruthenium dioxide in heterogeneous catalysis and electrocatalysis: from fundamental to applied research. *Chem. Rev.* **112,** 3356–426 (2012).

124. Uddin, M. T. *et al.* Preparation of RuO 2 /TiO 2 Mesoporous Heterostructures and Rationalization of Their Enhanced Photocatalytic Properties by Band Alignment Investigations. *J. Phys. Chem. C* **117,** 22098–22110 (2013).

125. Ma, S. S. K., Maeda, K., Abe, R. & Domen, K. Visible-light-driven nonsacrificial water oxidation over tungsten trioxide powder modified with two different cocatalysts. *Energy Environ. Sci.* **5,** 8390 (2012).

126. Tauster, S. J., Fung, S. C., Baker, R. T. & Horsley, J. A. Strong interactions in supported-metal catalysts. *Science* **211,** 1121–5 (1981).

127. VANNICE, M. Metal-support effects on the activity and selectivity of Ni catalysts in CO/H2 synthesis reactions. *J. Catal.* **56,** 236–248 (1979).

128. Jin, R. *et al.* Mechanism for catalytic partial oxidation of methane to syngas over a Ni/Al2O3 catalyst. *Appl. Catal. A Gen.* **201,** 71–80 (2000).

129. Maiyalagan, T. & Viswanathan, B. Catalytic activity of platinum/tungsten oxide nanorod electrodes towards electro-oxidation of methanol. *J. Power Sources* **175,** 789–793 (2008).

130. Enache, D. I. *et al.* Solvent-free oxidation of primary alcohols to aldehydes using Au-Pd/TiO2 catalysts. *Science* **311,** 362–5 (2006).

131. Cao, E. *et al.* Reaction and Raman spectroscopic studies of alcohol oxidation on gold–palladium catalysts in microstructured reactors. *Chem. Eng. J.* **167,** 734–743 (2011).

132. Mills, A. & Wang, J. Simultaneous monitoring of the destruction of stearic acid and generation of carbon dioxide by self-cleaning semiconductor photocatalytic films. *J. Photochem. Photobiol. A Chem.* **182,** 181–186 (2006).

133. Mills, A., Davies, R. H. & Worsley, D. Water purification by semiconductor photocatalysis. *Chem. Soc. Rev.* **22,** 417 (1993).

134. Mills, A. & Wang, J. Simultaneous monitoring of the destruction of stearic acid and generation of carbon dioxide by self-cleaning semiconductor photocatalytic films. *J. Photochem. Photobiol. A Chem.* **182,** 181–186 (2006).

135. Quesada-Cabrera, R., Sotelo-Vazquez, C., Darr, J. A. & Parkin, I. P. Critical influence of surface nitrogen species on the activity of N-doped TiO2 thin-films during photodegradation of stearic acid under UV light irradiation. *Appl. Catal. B Environ.* **160–161,** 582–588 (2014).

136. Sotelo-Vazquez, C., Quesada-Cabrera, R., Darr, J. A. & Parkin, I. P. Single-step synthesis of doped TiO2 stratified thin-films by atmospheric-pressure chemical vapour deposition. *J. Mater. Chem. A* **2,** 7082 (2014).

137. Sotelo-Vazquez, C. *et al.* Multifunctional P-Doped TiO 2 Films: A New Approach to Self-Cleaning, Transparent Conducting Oxide Materials. *Chem. Mater.* **27,** 3234–3242 (2015).

138. Noimark, S. *et al.* Functionalised gold and titania nanoparticles and surfaces for use as antimicrobial coatings. *Faraday Discuss.* **175,** 273–87 (2014).

139. Quesada-Cabrera, R., Sotelo-Vazquez, C., Bear, J. C., Darr, J. A. & Parkin, I. P. Photocatalytic Evidence of the Rutile-to-Anatase Electron Transfer in Titania. *Adv. Mater. Interfaces* **1,** 1–7 (2014).

140. Ohtani, B. Preparing Articles on Photocatalysis—Beyond the Illusions, Misconceptions, and Speculation. *Chem. Lett.* **37,** 216–229 (2008).

141. Kudo, A. & Miseki, Y. Heterogeneous photocatalyst materials for water splitting. *Chem. Soc. Rev.* **38,** 253–78 (2009).

142. Cabrera, R. Q. *et al.* Photocatalytic activity of needle-like TiO2/WO3−x thin films prepared by chemical vapour deposition. *J. Photochem. Photobiol. A Chem.* **239,** 60–64 (2012).

143. Hammond, C. *The Basics of Crystallography and Diffraction*. (Oxford University Press Inc., 2001).

144. John F. Watts & Wolstenholme, J. *An Introducton to Surface Analysis by XPS and AES*. (John Wiley and Sons Ltd., 2003).

145. Skoog, D. A., James, H. F. & Crouch, S. R. *Principles of Instrumental Analysis*. (Thomson Brooks/Cole, 2007).

146. Tauc, J., Grigorovici, R. & Vancu, A. Optical Properties and Electronic Structure of Amorphous Germanium. *Phys. status solidi* **15,** 627–637 (1966).

147. McMullan, D. Scanning electron microscopy 1928-1965. *Scanning* **17,** 175–185 (2006).

148. Oura, K., Flfshits, V. G., Saranin, A. A., Zotov, A. V. & Katayama, M. *Surface Science An Introduction*. (Springer-Verlag, 2003).

149. Goldstein, J. & etc. *Scanning Electron Microscopy and X-ray Microanalysis*. (Springer science+bussiness media LLC, 2003).

150. White, R. *Chromatography/Fourier transform infrared spectroscopy and its applications*. (Marcel Dekker, 1990).

151. Kruis, F. E., Fissan, H. & Peled, A. Synthesis of nanoparticles in the gas phase for electronic, optical and magnetic applications—a review. *J. Aerosol Sci.* **29,** 511–535 (1998).

152. Cross, W. B. *et al.* Tungsten Oxide Coatings from the Aerosol-Assisted Chemical Vapor Deposition of W(OAr) 6 (Ar = C 6 H 5 , C 6 H 4 F-4, C 6 H 3 F 2 -3,4); Photocatalytically Active γ-WO 3 Films. *Chem. Mater.* **15,** 2786–2796 (2003).

153. Ling, M. & Blackman, C. Growth mechanism of planar or nanorod structured tungsten oxide thin films deposited via aerosol assisted chemical vapour deposition (AACVD). *Phys. status solidi* **12,** 869–877 (2015).

154. Chen, D. & Ye, J. Hierarchical WO 3 Hollow Shells: Dendrite, Sphere, Dumbbell, and Their Photocatalytic Properties. *Adv. Funct. Mater.* **18,** 1922–1928 (2008).

155. Navío, C. *et al.* Gold clusters on WO3 nanoneedles grown via AACVD: XPS and TEM studies. *Mater. Chem. Phys.* **134,** 809–813 (2012).

156. Blackman, C. S. & Parkin, I. P. Atmospheric pressure chemical vapor deposition of crystalline monoclinic WO3 and WO3-x thin films from reaction of WCl6 with O-containing solvents and their photochromic and electrochromic properties. *Chem. Mater.* **17,** 1583–1590 (2005).

157. Palgrave, R. G. & Parkin, I. P. Aerosol assisted chemical vapour deposition of photochromic tungsten oxide and doped tungsten oxide thin films. *J. Mater. Chem.* **14,** 2864 (2004).

158. Zhou, J. *et al.* Three‐Dimensional Tungsten Oxide Nanowire Networks. *Adv. Mater.* **17,** 2107–2110 (2005).

159. Nefedov, V. I., Salyn, Y. V, Leonhardt, G. & Scheibe, R. A comparison of different spectrometers and charge corrections used in X-ray photoelectron spectroscopy. *J. Electron Spectros. Relat. Phenomena* **10,** 121–124 (1977).

160. Biloen, P. & Pott, G. T. X-ray photoelectron spectroscopy study of supported tungsten oxide. *J. Catal.* **30,** 169–174 (1973).

161. Greiner, M. T. *et al.* Universal energy-level alignment of molecules on metal oxides. *Nat. Mater.* **11,** 76–81 (2012).

162. Wang, F., Di Valentin, C. & Pacchioni, G. Semiconductor-to-metal transition in WO 3 − x : Nature of the oxygen vacancy. *Phys. Rev. B* **84,** 73103 (2011).

163. Koffyberg, F. P., Dwight, K. & Wold, A. Interband transitions of semiconducting oxides determined from photoelectrolysis spectra. *Solid State Commun.* **30,** 433–437 (1979).

164. Berak, J. M. & Sienko, M. J. Effect of oxygen-deficiency on electrical transport properties of tungsten trioxide crystals. *J. Solid State Chem.* **2,** 109–133 (1970).

165. Chatten, R., Chadwick, A. V, Rougier, A. & Lindan, P. J. D. The oxygen vacancy in crystal phases of WO(3). *J. Phys. Chem. B* **109,** 3146–56 (2005).

166. Gunnar A. Niklasson, C. G. G. Electrochromics for smart windows: thin films of tungsten oxide and nickel oxide, and devices based on these. at <http://citeseerx.ist.psu.edu/viewdoc/summary?doi=10.1.1.456.6128>

167. Bechinger, C., Burdis, M. S. & Zhang, J.-G. Comparison between electrochromic and photochromic coloration efficiency of tungsten oxide thin films. *Solid State Commun.* **101,** 753–756 (1997).

168. de Wijs, G. A. & de Groot, R. A. Structure and electronic properties of amorphous WO3. *Phys. Rev. B* **60,** 16463–16474 (1999).

169. Zhang, J.-G. Chromic Mechanism in Amorphous WO[sub 3] Films. *J. Electrochem. Soc.* **144,** 2022 (1997).

170. Berggren, L., Azens, A. & Niklasson, G. A. Polaron absorption in amorphous tungsten oxide films. *J. Appl. Phys.* **90,** 1860 (2001).

171. Larsson, A. Optical absorption of Li-intercalated polycrystalline tungsten oxide films: comparison to large polaron theory. *Solid State Ionics* **165,** 35–41 (2003).

172. Kim, H. *et al.* Aerosol-Assisted Chemical Vapor Deposition of Tungsten Oxide Films and Nanorods from Oxo Tungsten (VI) Fluoroalkoxide Precursors. *ACS Appl. Mater. Interfaces* (2015).

173. *The Chemistry of Metal CVD*. (Wiley-VCH Verlag GmbH, 1994). doi:10.1002/9783527615858

174. Lewis, K. E., Golden, D. M. & Smith, G. P. Organometallic bond dissociation energies: laser pyrolysis of iron pentacarbonyl, chromium hexacarbonyl, molybdenum hexacarbonyl, and tungsten hexacarbonyl. *J. Am. Chem. Soc.* **106,** 3905–3912 (1984).

175. Bloem, J. Nucleation and growth of silicon by CVD. *J. Cryst. Growth* **50,** 581–604 (1980).

176. Wei, W.-C. J. & Lo, M.-H. Processing and properties of (Mo,Cr) oxycarbides from MOCVD. *Appl. Organomet. Chem.* **12,** 201–220 (1998).

177. Ziegler, T., Tschinke, V. & Ursenbach, C. Thermal stability and kinetic lability of the metal carbonyl bond. A theoretical study on M(CO)6 (M = chromium, molybdenum, tungsten), M(CO)5 (M = iron, ruthenium, osmium), and M(CO)4 (M = nickel, palladium, platinum). *J. Am. Chem. Soc.* **109,** 4825–4837 (1987).

178. Lewis, K. E., Golden, D. M. & Smith, G. P. Organometallic bond dissociation energies: laser pyrolysis of iron pentacarbonyl, chromium hexacarbonyl, molybdenum hexacarbonyl, and tungsten hexacarbonyl. *J. Am. Chem. Soc.* **106,** 3905–3912 (1984).

179. Xu, S. & Diao, L. Study of tungsten oxidation in O2/H2/N2 downstream plasma. *J. Vac. Sci. & Technol. A* **26,** 360–364 (2008).

180. Gibou, F., Ratsch, C. & Caflisch, R. Capture numbers in rate equations and scaling laws for epitaxial growth. *Phys. Rev. B* **67,** 155403 (2003).

181. Venables, J. A. Atomic processes in crystal growth. *Surf. Sci.* **299,** 798–817 (1994).

182. Jensen, K. F. in *Chemical Vapour Deposition principle and applicaiton* (ed. M.L. Hitchman, K. F. J.) 38 (Academic Press Inc., 1993).

183. Guo, C., Yin, S., Huang, Y., Dong, Q. & Sato, T. Synthesis of W18O49 nanorod via ammonium tungsten oxide and its interesting optical properties. *Langmuir* **27,** 12172–12178 (2011).

184. Takeda, H. & Adachi, K. Near infrared absorption of tungsten oxide nanoparticle dispersions. *J. Am. Ceram. Soc.* **90,** 4059–4061 (2007).

185. Walter, M. G. *et al.* Correction to Solar Water Splitting Cells. *Chem. Rev.* **111,** 5815–5815 (2011).

186. Hoffmann, M. R., Martin, S. T., Choi, W. & Bahnemann, D. W. Environmental Applications of Semiconductor Photocatalysis. *Chem. Rev.* **95,** 69–96 (1995).

187. Walsh, A. *et al.* Nature of the band gap of In2O3 revealed by first-principles calculations and x-ray spectroscopy. *Phys. Rev. Lett.* **100,** 167402 (2008).

188. Ng, W. L. *et al.* An efficient room-temperature silicon-based light-emitting diode. *Nature* **410,** 192–194 (2001).

189. Mills, A. & Le Hunte, S. An overview of semiconductor photocatalysis. *J. Photochem. Photobiol. A Chem.* **108,** 1–35 (1997).

190. Philips, K. Product information TL-D Blacklight Blue. *Koninklijke Philips* (2015). at <http://www.lighting.philips.co.uk/prof/lamps/fluorescent-lamps-and-starters/tl-d/tl-d-blacklight-blue/928048010805_EU/product>

191. Sun, Q. *et al.* Appearance of bulk properties in small tungsten oxide clusters. *J. Chem. Phys.* **121,** 9417–22 (2004).

192. LIN, H. *et al.* Size dependency of nanocrystalline TiO2 on its optical property and photocatalytic reactivity exemplified by 2-chlorophenol. *Appl. Catal. B Environ.* **68,** 1–11 (2006).

193. Triana, C. A., Granqvist, C. G. & Niklasson, G. A. Electrochromism and small-polaron hopping in oxygen deficient and lithium intercalated amorphous tungsten oxide films. *J. Appl. Phys.* **118,** 24901 (2015).

194. Johansson, M. B., Zietz, B., Niklasson, G. A. & Österlund, L. Optical properties of nanocrystalline WO3 and WO3-x thin films prepared by DC magnetron sputtering. *J. Appl. Phys.* **115,** 213510 (2014).

195. Ho, S. F., Contarini, S. & Rabalais, J. W. Ion-beam-induced chemical changes in the oxyanions (Moyn-) and oxides (Mox) where M = chromium, molybdenum, tungsten, vanadium, niobium and tantalum. *J. Phys. Chem.* **91,** 4779–4788 (1987).

196. People, R. Physics and applications of GexSi1-x/Si strained-layer heterostructures. *IEEE J. Quantum Electron.* **22,** 1696–1710 (1986).

197. Hu, Y. H. A highly efficient photocatalyst--hydrogenated black TiO2 for the photocatalytic splitting of water. *Angew. Chem. Int. Ed. Engl.* **51,** 12410–2 (2012).

198. Naldoni, A. *et al.* Effect of nature and location of defects on bandgap narrowing in black TiO2 nanoparticles. *J. Am. Chem. Soc.* **134,** 7600–3 (2012).

199. Lee, K., Seo, W. S. & Park, J. T. Synthesis and optical properties of colloidal tungsten oxide nanorods. *J. Am. Chem. Soc.* **125,** 3408–9 (2003).

200. Feng, M. *et al.* Strong photoluminescence of nanostructured crystalline tungsten oxide thin films. *Appl. Phys. Lett.* **86,** 141901 (2005).

201. Hvolbæk, B. *et al.* Catalytic activity of Au nanoparticles. *Nano Today* **2,** 14–18 (2007).

202. Joo, S. H. *et al.* Size effect of ruthenium nanoparticles in catalytic carbon monoxide oxidation. *Nano Lett.* **10,** 2709–13 (2010).

203. Jiang, R., Li, B., Fang, C. & Wang, J. Metal/Semiconductor hybrid nanostructures for plasmon-enhanced applications. *Adv. Mater.* **26,** 5274–309 (2014).

204. Hull, R. V., Li, L., Xing, Y. & Chusuei, C. C. Pt Nanoparticle Binding on Functionalized Multiwalled Carbon Nanotubes. *Chem. Mater.* **18,** 1780–1788 (2006).

205. Tauster, S. J., Fung, S. C., Baker, R. T. & Horsley, J. A. Strong interactions in supported-metal catalysts. *Science* **211,** 1121–5 (1981).

206. Vayssilov, G. N. *et al.* Support nanostructure boosts oxygen transfer to catalytically active platinum nanoparticles. *Nat. Mater.* **10,** 310–5 (2011).

207. Haruta, M. Size- and support-dependency in the catalysis of gold. *Catal. Today* **36,** 153–166 (1997).

208. Poon, K. C. *et al.* Newly developed stepwise electroless deposition enables a remarkably facile synthesis of highly active and stable amorphous Pd nanoparticle electrocatalysts for oxygen reduction reaction. *J. Am. Chem. Soc.* **136,** 5217–20 (2014).

209. Marchand, P., Hassan, I. A., Parkin, I. P. & Carmalt, C. J. Aerosol-assisted delivery of precursors for chemical vapour deposition: expanding the scope of CVD for materials fabrication. *Dalton Trans.* **42,** 9406–22 (2013).

210. Tsukamoto, D. *et al.* Gold nanoparticles located at the interface of anatase/rutile TiO2 particles as active plasmonic photocatalysts for aerobic oxidation. *J. Am. Chem. Soc.* **134,** 6309–15 (2012).

211. Palgrave, R. G. & Parkin, I. P. Aerosol Assisted Chemical Vapor Deposition of Gold and Nanocomposite Thin Films from Hydrogen Tetrachloroaurate(III). *Chem. Mater.* **19,** 4639–4647 (2007).

212. Seah, M. P., Smith, G. C. & Anthony, M. T. AES: Energy calibration of electron spectrometers. I?an

absolute, traceable energy calibration and the provision of atomic reference line energies. *Surf. Interface Anal.* **15,** 293–308 (1990).

213. Tressaud, A., Khairoun, S., Touhara, H. & Watanabe, N. X-Ray Photoelectron Spectroscopy of Palladium Fluorides. *Z.anorg.allg.Chem.* **540,** 291–299 (1986).

214. Militello, M. C. Palladium Chloride (PdCl2) by XPS. *Surf. Sci. Spectra* **3,** 402 (1994).

215. Hrbek, J. Carbonaceous overlayers on Ru(001). *J. Vac. Sci. Technol. A Vacuum, Surfaces, Film.* **4,** 86 (1986).

216. Huang, C. S., Houalla, M., Hercules, D. M., Kibby, C. L. & Petrakis, L. Comparison of catalysts derived from oxidation of ruthenium-thorium (Ru3Th7) with impregnated ruthenium/thoria catalysts. *J. Phys. Chem.* **93,** 4540–4544 (1989).

217. Wagner, C. D. Chemical shifts of Auger lines, and the Auger parameter. *Faraday Discuss. Chem. Soc.* **60,** 291 (1975).

218. Militello, M. C. Palladium Oxide (PdO) by XPS. *Surf. Sci. Spectra* **3,** 395 (1994).

219. Shen, J. Y., Adnot, A. & Kaliaguine, S. An ESCA study of the interaction of oxygen with the surface of ruthenium. *Appl. Surf. Sci.* **51,** 47–60 (1991).

220. Sarma, D. D. & Rao, C. N. R. XPES studies of oxides of second- and third-row transition metals including rare earths. *J. Electron Spectros. Relat. Phenomena* **20,** 25–45 (1980).

221. Kelly, K. & Coronado, E. The optical properties of metal nanoparticles: the influence of size, shape, and dielectric environment. *J. Phys. …* (2003). at <http://pubs.acs.org/doi/abs/10.1021/jp026731y>

222. Li, J. F. *et al.* Shell-isolated nanoparticle-enhanced Raman spectroscopy. *Nature* **464,** 392–5 (2010).

223. Mayer, K. M. & Hafner, J. H. Localized surface plasmon resonance sensors. *Chem. Rev.* **111,** 3828–57 (2011).

224. Lacerda, A. M., Larrosa, I. & Dunn, S. Plasmon enhanced visible light photocatalysis for TiO2 supported Pd nanoparticles. *Nanoscale* **7,** 12331–12335 (2015).

225. Kuo, Y. & Klabunde, K. J. Hydrogen generation from water/methanol under visible light using aerogel prepared strontium titanate (SrTiO3) nanomaterials doped with ruthenium and rhodium metals. *Nanotechnology* **23,** 294001 (2012).

226. Ohno, T., Tanigawa, F., Fujihara, K., Izumi, S. & Matsumura, M. Photocatalytic oxidation of water by visible light using ruthenium-doped titanium dioxide powder. *J. Photochem. Photobiol. A Chem.* **127,** 107–110 (1999).

227. Abe, R., Takami, H., Murakami, N. & Ohtani, B. Pristine simple oxides as visible light driven photocatalysts: highly efficient decomposition of organic compounds over platinum-loaded tungsten oxide. *J. Am. Chem. Soc.* **130,** 7780–1 (2008).

228. Li, Q. & Shang, J. K. Composite photocatalyst of nitrogen and fluorine codoped titanium oxide nanotube arrays with dispersed palladium oxide nanoparticles for enhanced visible light photocatalytic performance. *Environ. Sci. Technol.* **44,** 3493–9 (2010).

229. Teramura, K. *et al.* Characterization of ruthenium oxide nanocluster as a cocatalyst with (Ga(1-x)Zn(x))(N(1-x)Ox) for photocatalytic overall water splitting. *J. Phys. Chem. B* **109,** 21915–21 (2005).

230. Zhou, W., Guan, Y., Wang, D. & Zhang, X. PdO/TiO2 and Pd/TiO2 Heterostructured Nanobelts with Enhanced Photocatalytic Activity. *Chem. Asian* **9,** 1648–1654 (2014).

231. Zhou, N. *et al.* Plasmon-enhanced light harvesting: applications in enhanced photocatalysis, photodynamic therapy and photovoltaics. *RSC Adv.* **5,** 29076–29097 (2015).

232. Wang, H. *et al.* Semiconductor heterojunction photocatalysts: design, construction, and photocatalytic performances. *Chem. Soc. Rev.* **43,** 5234–44 (2014).

233. Moniz, S., Shevlin, S. A., Martin, D., Guo, Z. & Tang, J. Visible-Light Driven Heterojunction Photocatalysts for Water Splitting– A Critical Review. *Energy Environ. Sci.* **8,** 731–759 (2015).

234. Miller, D. R., Akbar, S. A. & Morris, P. A. Nanoscale metal oxide-based heterojunctions for gas sensing: A review. *Sensors Actuators B Chem.* **204,** 250–272 (2014).

235. Su, J., Guo, L., Bao, N. & Grimes, C. A. Nanostructured WO_3/$BiVO_4$ heterojunction films for efficient photoelectrochemical water splitting. *Nano Lett.* **11,** 1928–33 (2011).

236. Tan, B. J., Klabunde, K. J. & Sherwood, P. M. A. XPS studies of solvated metal atom dispersed (SMAD) catalysts. Evidence for layered cobalt-manganese particles on alumina and silica. *J. Am. Chem. Soc.* **113,** 855–861 (1991).

237. Capece, F. M. *et al.* 'Copper chromite' Catalysts: XPS structure elucidation and correlation with catalytic activity. *J. Electron Spectros. Relat. Phenomena* **27,** 119–128 (1982).

238. Parmigiani, F., Pacchioni, G., Illas, F. & Bagus, P. S. Studies of the Cu O bond in cupric oxide by X-ray

photoelectron spectroscopy and ab initio electronic structure models. *J. Electron Spectros. Relat. Phenomena* **59,** 255–269 (1992).

239. Sullivan, J. L., Saied, S. O. & Bertoti, I. Effect of ion and neutral sputtering on single crystal TiO2. *Vacuum* **42,** 1203–1208 (1991).

240. Douin, M., Guerlou-Demourgues, L., Goubault, L., Bernard, P. & Delmas, C. Evolution Mechanism of the Na[sub 0.6]CoO[sub 2] Conductive Additive during Cycling in the Alkaline Electrolyte of Ni–MH Batteries. *J. Electrochem. Soc.* **156,** A459 (2009).

241. Zhang, X. *et al.* Nanoparticle-aggregated CuO nanoellipsoids for high-performance non-enzymatic glucose detection. *J. Mater. Chem. A* **2,** 10073 (2014).

242. Ballirano, P. & Caminiti, R. Rietveld refinements on laboratory energy dispersive X-ray diffraction (EDXD) data. *J. Appl. Crystallogr.* **34,** 757–762 (2001).

243. Mordi, C., Eleruja, M. & Taleatu, B. Metal organic chemical vapour deposited thin films of cobalt oxide prepared via cobalt acetylacetonate. *J. Mater.* (2009). at <http://scholar.oauife.edu.ng/sites/default/files/bdntaleatu/files/mordi_et_al._2009-_jmst.pdf>

244. Sun, D. C., Senz, S. & Hesse, D. Topotaxial formation of Mg 4 Ta 2 O 9 and MgTa 2 O 6 thin films by vapour-solid reactions on MgO (001) crystals. *J. Eur. Ceram. Soc.* **24,** 2453–2463 (2004).

245. Simon, Q. *et al.* Vertically oriented CuO/ZnO nanorod arrays: from plasma-assisted synthesis to photocatalytic H 2 production. *J. Mater. Chem.* **22,** 11739–11747 (2012).

246. Lany, S. & Zunger, A. Dopability, intrinsic conductivity, and nonstoichiometry of transparent conducting oxides. *Phys. Rev. Lett.* **98,** 45501 (2007).

247. Rettie, A. J. E., Chemelewski, W. D., Emin, D. & Mullins, C. B. Unravelling Small-Polaron Transport in Metal Oxide Photoelectrodes. *J. Phys. Chem. Lett.* **7,** 471–9 (2016).

248. M. A. Louren ço, M. S. A. Siddiqui, G. Shao, R. M. Gwilliam, K. P. H. in *Towards the First Silicon Laser* 11–20 (Springer Netherlands, 2003).

249. Brian Cole, *,† *et al.* Evaluation of Nitrogen Doping of Tungsten Oxide for Photoelectrochemical Water Splitting. (2008). doi:10.1021/JP077624C

250. Shi, J. *et al.* Tungsten nitride nanorods array grown on carbon cloth as an efficient hydrogen evolution cathode at all pH values. *Electrochim. Acta* **154,** 345–351 (2015).

251. Li, X. L., Wang, C. X. & Yang, G. W. Thermodynamic theory of growth of nanostructures. *Prog. Mater. Sci.* **64,** 121–199 (2014).

252. Berne, B. J., Borkovec, M. & Straub, J. E. Classical and modern methods in reaction rate theory. *J. Phys. Chem.* **92,** 3711–3725 (1988).

APPENDIX

Publications

1. F. Di Maggio, **M. Ling**, A. Tang; J. Covington, J. Saffell, C. Blackman. Aerosol-Assisted CVD Synthesis, Characterisation and Gas-sensing Application of Gold-Functionalised Tungsten Oxide. *Journal of Sensors and Sensor Systems*. **2014**, 3, 325-330.

2. **M. Ling**, C. Blackman. Growth Mechanism of Planar or Nanorod Structured Tungsten Oxide Thin Films Deposited via Aerosol Assisted Chemical Vapour Deposition. *Physica Status Solidi C*. **2015**, 12, 869-877.

3. A. Kafizas, X. Wang, S. Pendlebury, P. Barnes, **M. Ling**, C. Sotelo-Vazquez, RQ. Cabrera, C. Lin, I. Parkin, J. Durrant. Where Do Photo-Generated Holes Go In Anatase : Rutile TiO_2? A Transient Absorption Spectroscopy Study of Charge Transfer and Lifetime. *The Journal of Physical Chemistry A. **2016**, 120 (5), 715-723*.

4. F.E. Annanouch, Z. Haddi, **M. Ling**, S. Vallejos, T. Shujah, P. Umek, C. Bittencourt, C. Blackman and E. Lobet. Aerosol-assisted CVD –grown PdO nanoparticle-decorated tungsten oxide nanoneedles extremely sensitive and selective to hydrogen. *ACS Applied Materials & Interfaces. **2016,** 2016, 8 (16), pp 10413–10421*.

5. Kaipei Qiu, Guoliang Chai, Chaoran Jiang, **M. Ling**, Junwang Tang and Zhengxiao Guo. Maghemit Embedded in Nitrogen-Doped Hierarchical Graphene Framework: Strategic Development of Efficient Fe-N-C Based Oxygen Reduction Catalysts in Alkaline Media. *ACS Catalysis*, **2016**, 6 (6), pp 3558–3568.

6. Carlos Sotelo-Vazquez, Raul Quesada-Cabrera, **M.Ling**, David O Scanlon, Pardeep Kumar Thakur, Tien-Lin Lee, Andreas Kafizas, Alaric Taylor, Robert G Palgrave, Chris Blackman, and Ivan P Parkin. Nanostructured WO3/TiO2 Heterojunction Films: A Facile Solution to Deliver Up-scalable Coatings with Outstanding Photocatalytic Properties. Submitted.

7. **M. Ling**, C. Blackman. Growth of Nobel Metal or Oxide Nanoparticle/WO3 Nanorods Hybrid Structured Thin Films with Size-Tunability for Enhanced Photocatalysis. Submitted.

8. **M. Ling**, C. Blackman, R. Palgrave, A. Kafizas. Correlation of Optical Properties, Electronic Structure and Photocatalytic Activity in Nanostructured Tungsten Oxide. Submitted.

Conference and Symposium Attending

1. 20th Biennial European Conference on Chemical Vapour Deposition (EuroCVD 20), Sempach, Switzerland, July 12 – 17, 2015, (Oral)

2. Early Career Researchers' Symposium "Solar Fuels: Moving from Materials to Devices", Imperial College, London, UK, 6th July 2015.

3. The 3rd Thomas-Young-Centre energy workshop "Theory and Simulation of Electrochemical Energy Storage Material", UCL, London, UK, 10 – 12 September 2014.